1-1-2013

Experimental and Numerical Study of Free Convection in a Vertical Channel with Opposing Buoyancy Forces

Derek Roeleveld
Ryerson University

EXPERIMENTAL AND NUMERICAL STUDY OF FREE CONVECTION IN
A VERTICAL CHANNEL WITH OPPOSING BUOYANCY FORCES

by

Derek Roeleveld

B.Eng., Ryerson University, Toronto, 2005

M.A.Sc., Ryerson University, Toronto, 2007

A dissertation

presented to Ryerson University

in partial fulfillment of the

requirements for the degree of

Doctor of Philosophy

in the Program of

Mechanical Engineering

Toronto, Ontario, Canada, 2013

©(Derek Roeleveld) 2013

AUTHOR'S DECLARATION

FOR ELECTRONIC SUBMISSION OF A DISSERTATION

I hereby declare that I am the sole author of this dissertation. This is a true copy of the dissertation, including any required final revisions, as accepted by my examiners.

I authorize Ryerson University to lend this dissertation to other institutions or individuals for the purpose of scholarly research

I further authorize Ryerson University to reproduce this dissertation by photocopying or by other means, in total or in part, at the request of other institutions or individuals for the purpose of scholarly research.

I understand that my dissertation may be made electronically available to the public.

EXPERIMENTAL AND NUMERICAL STUDY OF FREE CONVECTION IN
A VERTICAL CHANNEL WITH OPPOSING BUOYANCY FORCES

Derek Roeleveld

Doctor of Philosophy

Department of Mechanical & Industrial Engineering

Ryerson University, Toronto, Ontario, Canada, 2013

Abstract

Free convective heat transfer inside a vertical channel was studied both experimentally and numerically. An experimental model of an isothermally, asymmetrically heated vertical channel was constructed to study various cases of opposing buoyancy forces. Many studies in the literature have investigated buoyancy forces in a single direction. The study presented here investigated opposing buoyancy forces, where one wall is warmer than the ambient and the other wall is cooler than the ambient. Five different temperature ratios were studied using four different channel spacings between the two channel walls. A Mach-Zehnder interferometer provided temperature field visualization. In addition, local and average heat transfer measurements were made with the interferometer. Flow visualization was conducted to determine the flow pattern inside the channel. The measured local and average Nusselt number data were compared to numerical solutions obtained using ANSYS FLUENT. A steady laminar model and a steady k-ε turbulence model with two different wall functions were used. Numerical solutions were obtained for a Prandtl number of 0.71 and Rayleigh numbers ranging from the laminar fully developed flow regime to the turbulent isolated boundary layer regime.

Acknowledgements

I would like to thank Dr. David Naylor and Dr. Wey Leong for their insight and support with this dissertation. Without their persistence, guidance, and enthusiasm, this dissertation would not have been possible.

I would also like to acknowledge the support of the Natural Sciences and Engineering Research Council of Canada for the funding of this research.

I would also like to thank Alan Machin for his time and assistance in designing and building the experimental model.

I would also like to thank my friends and family for their support. Special thanks to my parents for their encouragement and understanding. I would also like to thank the various graduate students in the lab for the inspiring research related discussions we had.

Table of Contents

List of Tables

List of Figures

Nomenclature

A	aspect ratio
b	channel spacing, m
B	pre-entry plenum size, m
c	speed of light, m/s
c_0	speed of light in a vacuum, m/s
c_p	specific heat of fluid, J/kgK
C_μ, $C_{\varepsilon 1}$, $C_{\varepsilon 2}$, $C_{\varepsilon 3}$	k-ε model constants
D	amplitude of a wave
D_0	maximum amplitude of wave
F	rate of change of phase
g	gravity, m/s^2
G	Gladstone-Dale constant, m^3/kg
G_b	production of kinetic turbulent energy due to buoyancy, N/m^{2}s
G_k	production of kinetic turbulent energy due to shearing, N/m^{2}s
Gr_b	Grashof number based on the channel spacing
I	pixel intensity
I_0	mean pixel intensity
k	turbulent kinetic energy, m^2/s^2
K	thermal conductivity of fluid, W/mK
K_s	thermal conductivity of fluid at the surface temperature, W/mK
L	channel length, m
n	index of refraction
Nu	overall channel average Nusselt number
Nu_{fd}	fully developed flow Nusselt number
Nu_H	hot wall average Nusselt number
Nu_C	cold wall average Nusselt number
Nu_y	local Nusselt number
P	absolute pressure, Pa
P_k	pressure defect, Pa

Pr	Prandtl number
Pr_T	turbulent Prandtl number
q	heat flux, W/m^2
q_y	instantaneous heat flux, W/m^2
R	gas constant, J/kgK
Ra	Rayleigh number
Ra(b/L)	modified Rayleigh number
Ra_C	Critical Rayleigh number
R_T	temperature ratio
t	time, s
T	temperature, °C or K
T_s	surface temperature, K
$\overline{\Delta T}$	average channel wall temperature difference, °C
u, v	fluid velocity in x-, y-direction, m/s
u_t	tangential component of velocity, m/s
V	dimensionless y-velocity
W	channel width, m
x, y, z	Cartesian coordinate system, m
x_1	location of first pixel, m
X	dimensionless distance
y^+	dimensionless distance from the wall

Greek Symbols

β	volumetric thermal expansion coefficient, 1/K
ε	fringe shift order (Chapter 3)
ε	turbulent kinetic energy dissipation rate (Chapter 4), m^2/s^3
θ	dimensionless temperature
λ	wavelength of light, m
$λ_0$	wavelength of light in a vacuum, m
μ	dynamic viscosity of fluid, Ns/m^2
$μ_T$	dynamic turbulent viscosity, Ns/m^2

ρ	density of fluid, kg/m^3
σ_k	turbulent Prandtl number for k
σ_ε	turbulent Prandtl number for ε
τ_w	shear stress at the wall
ϕ	phase shift

Subscripts

C	cold wall
f	bulk temperature
H	hot wall
REF	reference beam
TEST	test beam
∞	ambient

Chapter 1
General Review

1.1 Introduction

In natural or free convection, the fluid motion is caused by buoyancy forces within the fluid. This is in contrast to forced convection, where the fluid motion is applied externally such as from a pump or fan. These buoyancy forces are caused by a body force acting on the fluid. This body force acts upon the density gradient of the fluid. In most cases, the body force is gravitational and the density gradient is due to a temperature gradient.

Generally, the heat transfer and velocity of the fluid are much lower in natural convection than in forced convection. However, natural convection is an important mode of heat transfer in many applications. Some advantages of natural convection are that it is inexpensive, reliable and quiet. Also, natural convection can have a strong influence on the total heat transfer rate of many systems because it can often be the source of the largest thermal resistance.

There are many applications of natural convection for a wide range of geometries. The geometry of interest in this study is a vertical channel, with two channel walls providing the temperatures to induce buoyancy driven flow. Natural convection in a heated vertical channel is a classical heat transfer problem that has received a great deal of attention in the literature. Symmetrical or asymmetrical heating of a vertical channel where the buoyancy driven flow is in a single direction, upwards or downwards, has been extensively studied.

This general problem has many heat transfer engineering applications. Electronics cooling is one application, where heated computer chips are arranged in vertical channels and cooled by natural convection in air in order to provide an inexpensive cooling option. Most electronics cooling applications involve symmetrical or asymmetrical heating with buoyancy forces in a single direction. Other applications include the simulation of flow inside nuclear reactors, where heated vertical channels are sometimes cooled by natural convection in water. The problem that motivated the current work is the application to fenestration systems (window and blinds). A window and blind can be approximated as a vertical channel as shown in Figure 1.1. By using this approximation, correlations of natural convection in a heated vertical channel can used in

simplified models of fenestration systems to approximate the convective heat transfer between the window and blinds.

The current study will investigate free convection in a vertical channel with opposing buoyancy forces. A schematic of opposing buoyancy forces in a heated vertical channel is shown in Figure 1.2. This problem is complex in that the fluid is flowing in two directions inside the vertical channel. One of the channel walls is heated above ambient temperature, so the fluid will flow up along the hot wall. On the other side of the channel, the wall is cooled below ambient temperature, so the fluid will flow down the cold wall. The countercurrent flows create an area in the center of the channel where the flows will mix and possibly create eddies and unsteadiness.

There are many studies that have developed correlations to predict the heat transfer from a vertical channel for buoyancy forces in a single direction. However, in the current study, the convective heat transfer caused by an opposing buoyancy-driven flow inside a vertical channel will be studied, which has rarely been investigated in the literature. The current study will characterize the flow utilizing flow visualization. Classical interferometry will be used to visualize the temperature field inside the vertical channel and measure the convective heat flux
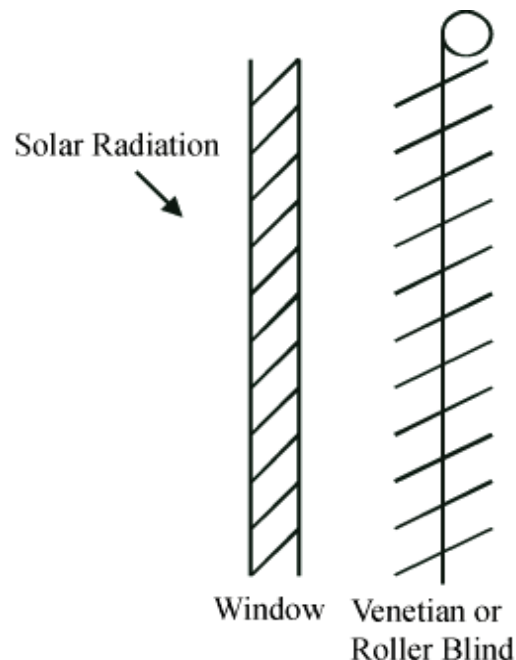
Figure 1.1: Schematic of a blind mounted next to the indoor window surface.
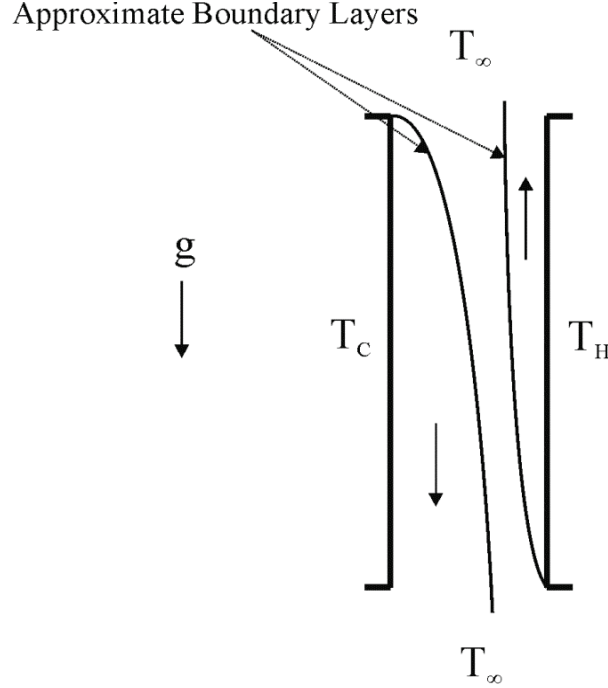
Figure 1.2: Schematic of opposing buoyancy forces inside a vertical channel at high Rayleigh number.

distributions on the channel walls. These experimental results will be compared to Computational Fluid Dynamics (CFD) solutions and additional numerical predictions will be obtained over a wider range of variables.

1.2 Dimensionless Numbers

The problem geometry is given in Figure 1.3. For consistency, in this thesis the cold wall will always be on the left hand side and the hot wall will be on the right hand side. An open-ended channel is formed by two vertical isothermal walls of height L and channel spacing b, giving a channel aspect ratio A = L/b. The hot wall has temperature T_H and the cold wall has temperature T_C. The fluid above and below the channel is quiescent and at the ambient temperature of T_∞.

Before reviewing the literature, there are some dimensionless numbers used in natural convection that need to be defined. These are the standard dimensionless numbers that are used for natural convection in a vertical channel or a vertical cavity and are presented in any

3
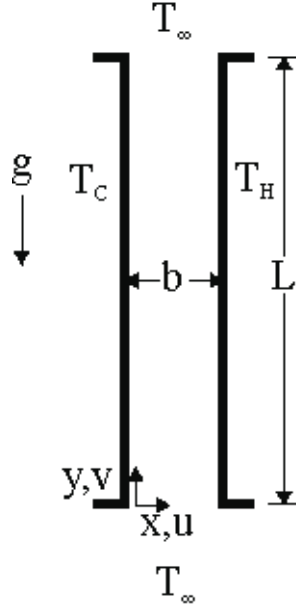
Figure 1.3: Vertical channel problem geometry and coordinate system.

undergraduate textbook, such as Incropera and DeWitt (2002). In natural convection, the Grashof number indicates the ratio of the buoyancy force to the viscous force acting on the fluid. It plays a similar role in natural convection as the Reynolds number does in forced convection. It is defined as:

$$Gr_b = \frac{g\beta\Delta T\rho^2 b^3}{\mu^2} \qquad (1.1)$$

where β is the volumetric thermal expansion coefficient of the fluid, ρ is the density of the fluid, μ is the dynamic viscosity of the fluid, b is the channel spacing, and ΔT is the characteristic temperature difference. The characteristic temperature difference will be discussed later in this section. All the fluid properties are evaluated at the film temperature T_f, which is (Raithby and Hollands 1998):

$$T_f = \left[\frac{T_H + T_\infty}{2} + \frac{T_C + T_\infty}{2}\right]\Big/2 = \left[\frac{T_H + T_C}{2} + T_\infty\right]\Big/2 \qquad (1.2)$$

The Prandtl number is the ratio of momentum and thermal diffusivities of the fluid. It is defined as:

4

$$Pr = \frac{\mu c_p}{K} \tag{1.3}$$

where c_p is the specific heat at constant pressure of the fluid and K is the conductivity of fluid.

A discussion is needed on the characteristic temperature difference. For this study, there are two different characteristic temperature differences used. The average channel wall temperature difference $\overline{\Delta T}$ is one of the characteristic temperature differences and it is defined as (Aung et al. 1972):

$$\overline{\Delta T} = \frac{T_H + T_C}{2} - T_\infty \tag{1.4}$$

This is the standard temperature difference used to characterize the total convective heat transfer from a channel. Another temperature difference used is the hot wall temperature subtracted from the cold wall temperature $T_H - T_C$. This is the standard temperature difference that is used to describe the convective heat transfer from one of the channel walls or when studying natural convection in a tall enclosure.

In this study, two different Rayleigh numbers are used. For natural convection in a heated channel, the modified Rayleigh number Ra(b/L) is used and it is defined as:

$$Ra(b/L) = Gr_b\, Pr\, \frac{b}{L} = \frac{g\beta\overline{\Delta T}\rho^2 b^3}{\mu^2}\, Pr\, \frac{b}{L} \tag{1.5}$$

where the characteristic temperature difference is $\overline{\Delta T}$. The non-modified Rayleigh number is also used in this study:

$$Ra = Gr_b\, Pr = \frac{g\beta\left(T_H - T_C\right)\rho^2 b^3}{\mu^2}\, Pr \tag{1.6}$$

where the characteristic temperature difference is $T_H - T_C$. This Rayleigh number is also used in studies on natural convection in a tall vertical enclosure.

The convective heat transfer rates are presented in terms of two Nusselt numbers. The Nusselt number is the ratio of heat transferred by convection to the heat transferred by conduction. For

natural convection in a heated vertical channel, the overall channel average Nusselt number is defined as:

$$Nu = \frac{(q_H + q_C)b}{2K\overline{\Delta T}} \qquad (1.7)$$

where q_H and q_C are the average heat fluxes from the hot and cold walls of the channel. The hot wall average Nusselt number is also used:

$$Nu_H = \frac{q_H b}{K(T_H - T_C)} \qquad (1.8)$$

Another Nusselt number of interest is the cold wall average Nusselt number:

$$Nu_C = \frac{q_C b}{K(T_H - T_C)} \qquad (1.9)$$

For clarification, when discussing natural convection in a vertical channel, the modified Rayleigh number $Ra(b/L)$ and overall channel average Nusselt number Nu are used. Natural convection inside a tall vertical cavity uses the Rayleigh number Ra and hot wall average Nusselt number Nu_H. Due to complexities that will be discussed later, when analyzing the anti-symmetrical channel cases, the Rayleigh number Ra and hot wall average Nusselt number Nu_H are used.

1.3 Literature Review

The primary interest of this study is natural convection in a heated vertical channel, which has been extensively studied in the literature. A brief overview of published studies is provided. When studying the anti-symmetrical cases, the flow pattern was observed to behave similar to natural convection in a tall vertical enclosure. A tall enclosure is considered to be when the aspect ratio $A > 20$. There are many papers published on this topic, but only a brief summary of related literature on tall cavities is given.

1.3.1 Natural Convection in a Heated Vertical Channel

Elenbaas (1942) was one of the first to study the heat flow of a symmetrically, isothermally heated vertical channel (in the symmetrical case: $T_H = T_C$). Using two square plates separated by various channel spacings, he was able to obtain experimental data for a wide range of Rayleigh numbers. The non-dimensional general-case correlation was developed through some analytical and experimental work. The overall channel average Nusselt number was determined to be:

$$Nu = \frac{1}{24} Ra(b/L)\left(1 - e^{\frac{-35}{Ra(b/L)}}\right)^{\frac{3}{4}} \tag{1.10}$$

Figure 1.4 shows a plot of some experimental data and the empirical correlation. It is important to note that the experimental data and correlation curve have upper and lower asymptotic limits. The upper limit asymptote is the isolated flat plate limit and the lower asymptote is fully developed flow.
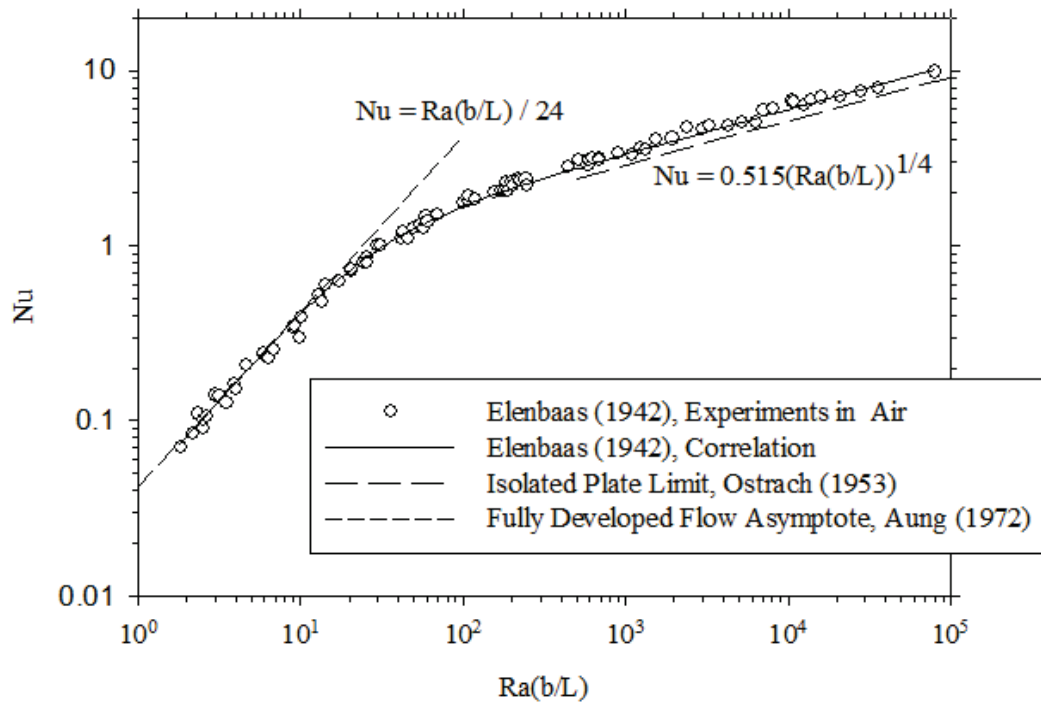
Figure 1.4: Plot of Elenbaas' (1942) experimental data and empirical correlation showing the upper and lower asymptotes.

Bodia and Osterle (1962) developed a finite difference numerical solution for free convection in a symmetrically heated channel. They used boundary-layer approximations, so the governing equations were parabolic and assumed that the fluid enters the channel with ambient temperature and a flat velocity profile. A range of solutions was acquired for a Prandtl number of 0.7, where two asymptotes were discovered at high and low modified Rayleigh numbers. The results were in good agreement with Elenbaas' work, except at low Rayleigh number where Elenbaas' results were slightly higher due to edge effects of his apparatus.

Aung et al. (1972) studied the conditions of a uniform heat flux and a uniform wall temperature in an asymmetrically heated vertical channel. A finite difference method using the boundary-layer approximation similar to Bodia and Osterle (1962) was used to obtain numerical solutions and some experimental work was performed to verify the results. They showed that, for uniform wall temperature, a nearly universal curve can be used to relate the Nusselt numbers and the modified Rayleigh numbers for a wide range of temperature ratios. This is the case if the Nusselt numbers and modified Rayleigh numbers are defined appropriately by using the average channel wall temperature difference defined in Equation (1.4). The temperature ratio is defined as:

$$R_T = \frac{T_C - T_\infty}{T_H - T_\infty} \qquad (1.11)$$

This temperature ratio R_T is used to define the entire range of possible asymmetrically heated channel cases. However, the results of this work only apply to the cases where the buoyancy forces are in a single direction inside the channel. These cases are where both channel walls are either heated at or above the ambient temperature or both cooled at or below the ambient temperature. In their study, both channel walls were heated above the ambient temperature.

Aung (1972) also investigated the fully developed flow of an asymmetrically heated channel. This was an analytical solution to the parabolic Navier-Stokes and energy equations. It was found that at low Rayleigh numbers (Ra(b/L) < 2), the asymptote of the Nusselt number varied depending on the temperature ratio. The average Nusselt number at the fully developed limit can be expressed as:

$$Nu_{fd} = \frac{4R_T^2 + 7R_T + 4}{90(1 + R_T)^2} Ra(b/L) \qquad (1.12)$$

Also, they determined the velocity and temperature profiles of the fully developed flow. The velocity profile is:

$$V = (R_T - 1)\frac{X^3}{6} - R_T \frac{X^2}{2} + (2R_T + 1)\frac{X}{6} \qquad (1.13)$$

and the temperature profile is:

$$\theta = (1 - R_T)X + R_T \qquad (1.14)$$

where V is the dimensionless y-velocity, θ is the dimensionless temperature, and X is the dimensionless distance. They are defined as:

$$X = \frac{x}{b}, V = \frac{b\rho v}{\mu Gr_b}, \theta = \frac{T - T_\infty}{T_H - T_\infty} \qquad (1.15)$$

Miyatake and Fujii (1973a) numerically investigated natural convection inside an isothermally heated vertical channel. They studied multiple temperature ratios over a range of Ra(b/L) for both air and water. This numerical method used a finite difference method with a forward marching implicit scheme. As with previous numerical studies, they assumed a flat velocity profile at the channel entrance and neglected any flow reversal in the channel. An overall channel average Nusselt number correlation for air was determined to be:

$$Nu = C[Ra(b/L)]^{\frac{1}{4}} \qquad (1.16)$$

where

$$C = 0.58(1 + 0.165R_T^{0.36}) \qquad (1.17)$$

Similar to Aung et al. (1972), they also determined that all data for multiple temperature ratios could be plotted on the same curve using a shifting factor. Numerical data was also plotted for the hot and cold wall average Nusselt numbers over a range of Ra(b/L). Their numerical results for the symmetrical heating case were in good agreement with experimental data from the literature. Miyatake and Fujii (1973b) also studied natural convection in an isoflux heated vertical channel, using unequal fluxes on the two channel walls. They used a similar numerical

method to the previous study in order to determine the local Nusselt numbers. This study considered only positive values of surface heat flux, so that the buoyancy forces in the channel were in a single directional.

Bar-Cohen and Rohsenow (1984) used analytical expressions for the asymptotes at low and high Rayleigh numbers to develop correlations for various channel heating configurations. By using the curve fitting methods of Churchill and Usagi (1972), they developed correlations for four different cases: symmetrically heated, isothermal plates; one plate isothermally heated, the other insulated; symmetrically heated, isoflux plates; and one wall isoflux heated, the other insulated. The new correlations were developed to fit various experimental and numerical data and the approach was validated against the work of Elenbaas (1942), Miyatake and Fujii (1972b) and others. For the isothermal, symmetrically heated channel walls case the overall channel Nusselt number is:

$$ \text{Nu} = \left(\frac{576}{[\text{Ra}(b/L)]^2} + \frac{2.873}{\sqrt{\text{Ra}(b/L)}} \right)^{-\frac{1}{2}} \tag{1.18} $$

and for the asymmetric case, with one channel wall isothermally heated and the other channel wall insulated (q = 0):

$$ \text{Nu} = \left(\frac{144}{[\text{Ra}(b/L)]^2} + \frac{2.873}{\sqrt{\text{Ra}(b/L)}} \right)^{-\frac{1}{2}} \tag{1.19} $$

This paper also determined the optimal spacing of the channel walls for all four cases studied.

Sparrow et al. (1984) investigated a vertical channel with the hot wall isothermally heated and the cold wall unheated ($T_C = T_\infty$, $R_T = 0$). They conducted a flow visualization study using Thymol blue to study flow reversal in the top of the channel. The experimental model was set up in water at ambient temperature in which the Thymol blue was injected. They observed that in a channel with an aspect ratio of 15.2 at Ra(b/L) = 5270, some ambient water was drawn in from the top of the channel and flowed down about 25% of the cold wall. This flow then recirculated with the air flowing up the hot wall. The percentage of backflow on the cold wall varied depending on the aspect ratio and Rayleigh number of the channel. Generally, flow reversal

10

occurs when Ra(b/L) is greater than 2300. The fluid flowing close to the hot wall draws mass towards the wall as it accelerates up the channel. When there is insufficient mass within the channel, fluid is drawn into the channel from the top of channel, adjacent to the cold wall. They also used both experimental and numerical models to determine the hot wall average Nusselt numbers in this study. The experiments were conducted in water, but numerically they studied multiple Prandtl numbers of 0.7 to 10 over a range of $200 < \text{Ra}(b/L) < 10^5$. The numerical solution was similar to existing numerical models in that it did not include flow reversal. When comparing with the experimental data, the numerical predictions showed that not including flow reversal did not affect the average Nusselt numbers.

Sparrow and Azevedo (1985) also performed an experimental and numerical study spanning the fully developed limit to the single-plate boundary-layer limit. The case studied was similar to Sparrow et al. (1984), with one channel wall heated and the other wall unheated. The main focus was to study the effect of channel spacing on the heat transfer. Over 50 different channel spacings were studied, giving an aspect ratio range of $2 < A < 90$. They also studied a wide range of Rayleigh numbers from $2 < \text{Ra}(b/L) < 10^8$ using water as the fluid of interest. They determined that all the Nusselt numbers for different aspect ratios fall onto the same curve when plotted using Ra(b/L).

A review of all the correlations was performed by Raithby and Hollands (1998). It was determined that the best correlation for the overall channel average Nusselt number for isothermally heated channel walls is:

$$\text{Nu} = \left[\left(\text{Nu}_{\text{fd}} \right)^{-1.9} + \left(0.618 \left[\text{Ra}(b/L) \right]^{\frac{1}{4}} \right)^{-1.9} \right]^{\frac{1}{-1.9}} \tag{1.20}$$

where Nu_{fd} is determined from Equation (1.13) by Aung (1972).

Currie and Newman (1970) investigated a symmetrically heated vertical channel in air using three different aspect ratios of 72, 90 and 120 over $10 < \text{Ra}(b/L) < 100$. They reported the velocity and temperature profiles for all these cases. The heat transfer results were in agreement with the experimental work of Elenbaas (1942). Martin et al. (1991) conducted a numerical study of the low Rayleigh number asymptote for a symmetrically heated vertical channel. They

11

determined that the heat transfer at low Rayleigh numbers will depend on the shape and boundary conditions of the inlet and outlet plenums. They determined that in order for the fully developed asymptote to be valid, the channel length and the inlet plenum must be large. Kazeminejad (2005) studied natural convection in a heated vertical channel numerically. He used the full elliptical Navier-Stokes equations along with the energy equation to study the effect of various parameters. The range of parameters examined were $Ra = 10$ to 10^3, $A = 10$ to 10^3, $Pr = 0.72$ and 5, and $R_T = 0$, 0.5, and 1. The velocity profiles, temperature profiles and heat fluxes were reported over this range of variables.

Roeleveld et al. (2009) presented numerical predictions of natural convection in an isothermally, asymmetrically heated vertical channel. Numerical data was obtained over $0.1 < Ra(b/L) < 10^5$ for $0 \leq R_T < 1$. Semi-empirical correlations were developed from some existing experimental data and numerical solutions that allow separate calculation of the average Nusselt numbers for each channel wall. The hot wall average Nusselt number correlation uses a blended temperature difference, which varies with Rayleigh number. The hot wall and overall channel average Nusselt number correlations were used in a heat balance to determine the cold wall average Nusselt number correlation. Suárez et al. (2011) also studied the heat flux for each channel wall separately using a numerical model. They were also interested in obtaining the mass flow rate because of its application to determine the performance of open ventilated facades. Correlations for the average Nusselt number on each channel wall and the non-dimensional mass flow rate were presented. A numerical study conducted by Terekhov and Ekaid (2011) examined asymmetrical heating of a vertical channel. They obtained solutions for a Prandtl number of 0.71, $A = 10$, $0.1 < Ra(b/L) < 10^5$, and $0 < R_T < 1$. Velocity profiles and temperature profiles were presented, as well as the local and average heat fluxes for the overall channel and the hot and cold walls individually.

There have also been studies on turbulent natural convective flow inside an asymmetrically, isothermally heated vertical channel. Federov and Viskanta (1997) used a low Reynolds number k-ε turbulence model to investigate two-dimensional turbulent natural convection in a heated vertical channel. Rayleigh numbers between 1800 and 10^4 were examined using an aspect ratio of 80 for $R_T = 0$. The computational domain did not include any pre-entry plenums at the entrance or exit of the channel. The numerical results showed some disagreement with the

experimental data from the literature. But, it was concluded that the low Reynolds number k-ε turbulence model was capable of predicting the velocity, temperature and heat fluxes.

Badr et al. (2006) studied turbulent natural convection in a symmetrically heated channel ($R_T = 1$) numerically. The numerical model was validated against the velocity distributions of some experimental data from the literature. Rayleigh numbers over a range of $10^5 < Ra < 10^7$ were investigated using aspect ratios of 12.5 to 100. A low Reynolds number k-ε turbulence model was used to study both isothermal and isoflux surfaces. The velocity and temperature profiles, isotherms and average Nusselt numbers were determined from the numerical solutions. Two different correlations for the average Nusselt numbers at higher Rayleigh numbers were obtained. Yilmaz and Gilchrist (2007) studied turbulent flow in a heated vertical channel both experimentally and numerically. One channel wall was heated by a heat flux and the other wall was adiabatic. Three Ra(b/L) values of 1.91×10^7, 2.74×10^7 and 3.19×10^7 were used with an aspect ratio of 20. A laser-Doppler anemometer was used to obtain velocity measurements and a thermocouple was used to measure the temperature field. The numerical model did not consider any pre-entry plenums and the numerical results had some small discrepancies with the experimental data. The numerical solution used a low Reynolds number k-ε turbulence model. The low Reynolds number k-ε turbulence model was capable of predicting the mean temperature field, but it grossly overestimated the velocity field especially in the core region of the channel.

Other studies have been performed on natural convective flow in an isothermally heated vertical channel. Kettleborough (1971) and Nakamura et al. (1982) performed some transient numerical solutions for a symmetrically heated vertical channel. Other studies have been conducted experimentally by Guo et al. (1988) and numerically by Burch et al. (1985), Chappidi and Eno (1990) and Naylor et al. (1991).

There are also numerous studies on symmetrical and asymmetrical uniform channel wall heat flux, which are of less direct interest to the proposed study. Lauber and Welch (1966) studied fully developed flow in an asymmetrically, isoflux heated vertical channel analytically. They determined that the solution is only applicable for Ra(b/L) < 150. Wirtz and Stutzman (1982) investigated a symmetrically, isoflux heated vertical channel with air as the fluid. They developed correlations for the local heat transfer along the channel over a Rayleigh number range of 17.7 < Ra(b/L) < 2414. The results showed good agreement with the numerical data of

Aung et al. (1972). Webb and Hill (1989) examined experimentally the effects of higher modified Rayleigh numbers on a vertical channel with one wall heated with a uniform heat flux and the other wall insulated. The Rayleigh number was set between 500 and 1.75×10^7 and their results compared favorably with previous experimental and numerical work from the literature. Lau et al. (2012) developed a numerical model to study natural convective flow in an isoflux heated vertical channel with specific boundary conditions applicable to passive cooling in building-integrated photovoltaics.

Ospir et al. (2012) conducted flow visualization of natural convection inside an asymmetrically heated channel. The channel was placed in water, with one wall heated with a constant heat flux and the other wall adiabatic. Laser tomography was used with dye tracers and Particle Tracking Velocimetry to determine the flow patterns within the channel. A Rayleigh number range of $4.3 \times 10^5 < \text{Ra}(b/L) < 4.5 \times 10^6$ was used with three aspect ratios of 5.2, 6 and 6.9. A transient study was performed, recording the flow patterns until steady-state was reached. An upward boundary layer formed on the heated wall and reverse flow developed on the adiabatic wall from the top of the channel. Similar to Sparrow et al. (1984), water was drawn into the top of the channel, creating a separation point on the adiabatic wall and a recirculating cell inside the channel. As the Rayleigh number was increased, the separation point moved higher up the adiabatic wall and there was less recirculation inside the channel. Other studies using isoflux heated channel walls have been conducted experimentally by Auletta et al. (2001) and numerically by Kim et al. (1990), Ramanathan and Kumar (1991), and Campo et al. (2006).

Some other variations of the classic vertical channel problem have been studied. Other areas of interest include unheated entrances (Dyer 1978 and Campo et al. 2005) and obstructions on the channel walls (Desrayaud and Fichera 2002 and Wang and Pepper 2009). Investigations of convergent and divergent channel walls have been investigated by Sparrow and Ruiz (1988), Sahoo and Sastri (1997), Bianco and Nardini (2005), and Marcondes et al. (2006). Boudebous et al. (2001) studied a vertical channel where the channel walls curve in a hyperbolic shape. Many other sources study the effects of various heated objects inside a vertical channel. Studies include a singular heat source (Higuera and Ryazantsev 2002), heated cylinder (Marsters 1975 and Karim et al. 1986), heated square cylinder (Khodary and Bhattacharyya 2006) and heated auxiliary plate (Andreozzi et al. 2002).

1.3.2 Opposing Buoyancy Forces inside a Heated Vertical Channel

To the author's knowledge only four studies have considered the case of $R_T < 0$, where there are opposing buoyancy forces. This thermal condition is the focus of the current work. So, these studies will be discussed in detail.

Lee et al. (1982) studied an asymmetrically heated vertical channel, with one wall porous so that carbon dioxide could be injected into the channel. Since CO_2 is heavier than air, this caused opposing buoyancy forces inside the channel. The porous plate was maintained at 7.5 °C above ambient and the solid plate was maintained at 30 ºC above ambient temperature, giving $R_T = 0.25$. They used a Mach-Zehnder interferometer and a traversing thermocouple probe to determine the temperature and CO_2 concentration profiles inside the channel. A numerical model was also developed to determine the velocity profiles at various points in the channel. Rayleigh numbers between 35 and 315 were investigated using aspect ratios of 10 and 15 and two carbon dioxide injection rates of 0.1 m/s and 0.2 m/s. The results showed that at low Rayleigh number, the flow is almost entirely in a negative y-direction. As the Rayleigh number is increased, air flows up the solid wall, while CO_2 continues to flow down the porous wall, creating recirculating flow inside the channel. The temperature field and flow patterns in this study are similar to the negative R_T results of the current thesis.

Habib et al. (2002) studied turbulent flow in a symmetrically ($R_T = 1$) and anti-symmetrically ($R_T = -1$) heated vertical channel with a channel aspect ratio of 3.125 and air as the test fluid. The anti-symmetric case ($R_T = -1$) is where the temperature difference between the hot wall and the ambient is the same as the temperature difference between the ambient and the cold wall (i.e. $T_H - T_\infty = T_\infty - T_C$). The symmetrical case was set at $Ra(b/L) = 1.0 \times 10^4$, with both channel walls heated 20 ºC above the ambient. The anti-symmetrical case was set at $Ra = 2.6 \times 10^4$, with the hot wall 10 ºC above ambient and the cold wall 10 ºC below ambient. Velocity profiles of the flow were determined with a Laser Doppler Anemometer. It was determined that in the symmetrical case, there was a high velocity gradient near the walls and a region of reversed flow in the center region of the channel. The anti-symmetrical case showed a circulation effect inside the channel, with greater velocity in the upwards direction at the entrance, and greater velocity in the downwards direction at the top. The middle was symmetrical, with equal flow moving up the hot wall and down the cold wall. This created a small reverse vortex in the center of the channel.

They also observed that even at relatively low Rayleigh number there is a high amount of unsteadiness in the flow.

Two aspect ratios of 6.25 and 12.5 and two temperature differences of $T_H - T_C = 15$ and 30 ºC were used to investigate turbulent flow in the anti-symmetrical ($R_T = -1$) heating of a vertical channel by Ayinde et al. (2008). These conditions gave Rayleigh numbers of 1.0×10^5 to 1.6×10^6. A Particle Image Velocimeter (PIV) was used to determine velocity profiles and a correlation for dimensionless flow rate in the channel was developed. The results indicated that the flow entering at the top and bottom of the channel got mixed with the recirculated flow inside the channel before exiting the other side of the channel. The results also showed that the flow pattern inside the channel was similar to an enclosure. An unsteadiness analysis was performed and fluctuations as much as 150% of the average velocity were found in the center of the channel.

Collins (2001) examined the effects of a Venetian blind present on the indoor surface of a window. As shown in Figure 1.1, this geometry is closely related to a vertical channel. This study is of interest because it examined convective heat transfer in a similar geometry to a vertical channel. The indoor window surface was approximated as an aluminum plate that was heated or cooled using a constant temperature water bath. The Venetian blinds were heated with thin foil electric heaters to simulate solar loading. The convective heat transfer rates and temperature field were determined using a Mach-Zehnder interferometer. Eight cases were investigated, with four cases studying $R_T = 0$ and four studying R_T between -0.2 to -0.4. In the negative temperature ratio cases, the plate was cooled 15 °C below the ambient temperature and the blinds were heated by a constant heat flux of 125 W/m^2. Thermocouples were placed on the surfaces of the blind slats to record the average blind temperatures, which were between 3 ºC to 6 ºC above ambient temperature. Various blind angles and blind to plate spacings were studied. A numerical solution was also obtained for each case studied for comparison. The results showed that the heat flux distribution along the plate was periodic due to the blind slats and was dependent on the blind slat angle and spacing between the plate and blinds. Near the top of the geometry, the numerical model showed some discrepancies with the experimental data, which were due to the boundary conditions used above and below the plate. Additional numerical

results for a wide range of variables were also obtained, which included other negative temperature ratio cases.

As discussed above, only four previous studies have considered free convection in a channel with opposing buoyancy forces. In these experimental studies, velocity field measurements were made for the anti-symmetric case, in relatively low aspect ratio channels. In contrast, the present work investigates the convective heat transfer rates in higher aspect ratio channels over a wide range of negative temperature ratios.

1.3.3 Natural Convection in a Tall Vertical Enclosure

As discussed in the previous section, the flow field in the channel for the anti-symmetrical case ($R_T = -1$) is similar to that of a tall enclosure (a tall enclosure is where $A > 20$). So, for this thermal condition, comparisons will be made with results for free convection in enclosures. For this reason, a review of several relevant studies of tall enclosures is presented below.

Eckert and Carlson (1961) used a Mach-Zehnder interferometer to obtain local heat transfer results of air in a tall vertical cavity. They proposed that there are conduction, transition, and boundary layer regimes when studying laminar natural convection. In the conduction regime, there is a large single cell flow inside the cavity, with fluid travelling up the hot wall and down the cold wall. At low Rayleigh numbers ($Ra < 10^3$), the heat transfer across the cavity is primarily due to conduction between the counter-flowing streams, resulting in a linear temperature profile ($Nu_H = 1$). As the Rayleigh number is increased ($10^4 < Ra < 10^5$), the flow develops into boundary layers on the cavity walls, separated by a core region. Due to convection in the boundary layers, higher temperature gradients exist on the walls than in the core region. The temperature profile is no longer linear and the core region shows almost no temperature gradient. This results in higher heat transfer rates in the boundary layer regime ($Nu > 1$). In between these two regimes is the transition regime. The temperature profile across the enclosure is not linear in this case either, but the heat transfer is a combination of convection and conduction across the core region. There is a critical value of Rayleigh number, in which the flow leaves the conduction regime, and it was determined to be a function of the aspect ratio of the cavity.

ElSherbiny et al. (1982) studied natural convection in a tall vertical enclosure experimentally with air as the fluid. Using a Rayleigh number range of 100 to 2.0×10^7 and six aspect ratios between 5 and 110, the heat transfer rates were determined. The Rayleigh number was varied independent of the aspect ratio, which permitted the role of aspect ratio to be clearly defined. A correlation for the hot wall average Nusselt number was determined to be:

$$\mathrm{Nu}_1 = 0.0605 \mathrm{Ra}^{\frac{1}{3}}$$

$$\mathrm{Nu}_2 = \left[1 + \left[\frac{0.104 \mathrm{Ra}^{0.293}}{\left(1 + \left(\frac{6310}{\mathrm{Ra}} \right)^{1.36} \right)} \right]^3 \right]^{\frac{1}{3}} \tag{1.21}$$

$$\mathrm{Nu}_3 = 0.242 \left(\frac{\mathrm{Ra}}{\mathrm{A}} \right)^{0.272}$$

$$\mathrm{Nu}_\mathrm{H} = \left[\mathrm{Nu}_1, \mathrm{Nu}_2, \mathrm{Nu}_3 \right]_{\max}$$

where the maximum value of Nu_1, Nu_2 and Nu_3 should be used.

Shewen et al. (1996) investigated large aspect ratios at high Rayleigh numbers. They used aspect ratios of 40, 60 and 110 over a Rayleigh number range $10^3 < \mathrm{Ra} < 10^6$. The results agreed with the experimental data of ElSherbiny et al. (1982). Using both sets of data, they developed a correlation for A > 40, Pr = 0.7, and Ra < 10^6. Wright (1996) also used the data from ElSherbiney et al. (1982) and Shewen et al. (1996) to develop a new correlation for large aspect ratios (A > 25) that are useful for a variety of window applications. These correlations are intended for much larger aspect ratios than are considered in the current thesis.

A detailed flow visualization study was conducted by Wright et al. (2006) using smoke patterns and interferometry. The experiments covered the transition from fully laminar to fully turbulent flow (4850 < Ra < 54,800), with an aspect ratio of A = 40. Slow and stable unicellular flow was observed in the conduction regime of Ra = 4850 to 6220. At Ra = 6800, a secondary flow was observed, where the primary flow is unicellular along the walls and secondary cells form in the

core region. The primary flow was stable along the walls, but the secondary cells slowly moved inside the enclosure. The onset of the secondary cells was in agreement with the critical Rayleigh number predicted by Korpela et al. (1982):

$$\text{Ra}_c = 8000 \left(1 + \frac{5}{A} \right) \text{Pr} \qquad (1.22)$$

As the Rayleigh number is increased beyond Ra = 10^4, the flow became irregular and the core region became increasingly unsteady and three dimensional. Eddies were seen moving up the hot wall and down the cold wall, with smaller ones forming inside the larger ones as the Rayleigh number is further increased.

1.4 Application to Fenestration Systems

One application of the current work is to implement empirical correlations of opposing buoyancy forces into a simplified model of fenestration systems (window and blinds). As discussed previously, Collins (2001) has studied a few winter daytime conditions where negative temperature ratios exist. If a simplified model of a fenestration system can predict the heat transfer over the full range of conditions, they can be implemented into building energy simulation programs in order to more accurately calculate the heating and cooling loads of a building.

Building energy simulation programs, such as ESP-r (2005) and TRNSYS (2000), are used to determine the heating and cooling loads of a building. These programs can be used to analyze buildings with various types of building materials, such as exterior siding, framing, insulation, and windows. Other programs, such as VISION3 (Wright 1992) offer a center-glass analysis of windows under different indoor and outdoor conditions. Various sizes and types of windows can be implemented in these programs, but currently they have limited capability to shading devices, such as blinds. In reality, shading devices are usually added to windows for privacy and occupant comfort, but they also can have a significant impact on the thermal performance of the window. Simplified models for fenestration systems are being developed for implementation into these programs to include the effects of blinds on the windows. These models use a

simplified thermal model for the convective and radiative heat transfer through a window with a blind. Kotey et al. (2009) developed a solar optical model for determining the radiative heat transfer. Lomanowski and Wright (2005) and Roeleveld et al. (2010) have used a simplified convective model with this radiative model to determine the total heat transfer of blinds mounted adjacent to the indoor glazing surface of a window.

Figure 1.1 shows a schematic diagram of a blind mounted next to the indoor surface of a window, creating a vertical channel. For a typical summer day, the window will be heated above room temperature and the blind will also be heated above the room temperature due to solar radiation. This can be approximated by natural convection in an asymmetrically heated vertical channel. Roeleveld et al. (2010) used empirical correlations from the literature as the convective heat transfer model in a simplified model for fenestration systems. It should be noted that the simplified model uses a Venetian type blind, but that the blind is approximated as a solid wall for the convective model.

The simplified model of Roeleveld et al. (2010) was compared with the experimental data collected by Machin (1997) and Collins (2001) for Venetian blinds mounted on an indoor window surface. Machin (1997) investigated cases where the window surface was heated above the ambient room temperature, but the blinds were unheated. Collins (2001) studied cases where both the blinds and the window surface were heated above the ambient. These cases have a single upwards buoyancy force inbetween the window and blind. Even though the geometry of a Venetian blind is much more complex than a flat channel wall, Roeleveld et al. (2010) have shown that this approximation in a simplified model compares within 10% to 30% of the experimental data. This approach has limitations, especially in certain conditions where there is flow across the permeable Venetian blinds at higher blind temperatures.

As discussed previously, there were also some cases studied numerically by Collins (2001) that represent winter daytime conditions, where the indoor window surface will be colder than the ambient room temperature and the blind will be hotter than the ambient room temperature due to solar radiation. In these cases, there are opposing buoyancy forces between the blind and window. Roeleveld et al.'s (2010) simplified model breaks down in these cases because there are no empirical correlations in the literature that can predict heat transfer rates for opposing buoyancy forces inside a vertical channel.

It should be noted that a center-glass region approximation is commonly used when studying fenestration systems. In the center-glass region, the temperatures are isothermal and this region neglects any end effects such as the window frame. This center-glass region approximation is used in VISION3 (Wright 1992) and other simplified models, such as Roeleveld et al. (2010) and Lomanowski and Wright (2005).

1.5 Scope of Research

Most existing studies of natural convection in vertical channels are only concerned with a temperature ratio in the range of $0 \leq R_T \leq 1$, where the buoyancy forces inside the channel act only in a single direction. The current study investigates the opposing buoyancy forces cases, where the temperature ratio is in the range of $-1 \leq R_T \leq 0$. Both experimental and numerical models are used to obtain data for a range of modified Rayleigh numbers.

Flow visualization and laser interferometry are used to characterize the flow and temperature fields inside the vertical channel. The experimental model covers a range of different negative temperature ratios, aspect ratios, and Rayleigh numbers. Smoke is introduced into the channel to visualize the streamlines inside the channel. A Mach-Zehnder interferometer (MZI) is used to visualize the temperature field and measure the local convective heat flux distributions on the channel walls. The flow and temperature field visualization will be used to determine the effects of opposing buoyancy forces and when the flow turns unsteady. The experimental data is analyzed to determine the local and average Nusselt numbers. The effect of negative temperature ratios on the local and average convective heat transfer rates will also be investigated, with some emphasis on the effect on the overall channel average Nusselt numbers.

General purpose CFD software ANSYS FLUENT (2010) is used to develop a numerical model of natural convection inside an asymmetrically heated vertical channel. Both laminar and turbulent solutions are obtained and the experimental data is used to validate the numerical predictions. A parametric study is conducted to obtain data for $-1 \leq R_T \leq 0$, over a Rayleigh number range of $0.1 < Ra(b/L) < 10^4$ ($100 < Ra < 10^6$ for $R_T = -1$).

Chapter 2
Experimental Equipment and Apparatus

2.1   Introduction

There are many different optical techniques used to measure temperature and heat transfer (Goldstein 1976). Some of these techniques can be used to measure convection. The current study uses an optical technique to measure convective heat transfer rates with a Mach-Zehnder Interferometer (MZI). The interferometer output is a pattern of constructive and deconstructive interference fringes that is related to changes in the refractive index field of the test fluid. For a constant pressure environment, the refraction index variation is related to the temperature field.

A Mach-Zehnder interferometer has advantages and disadvantages over other measurement techniques. Some advantages are that the technique is non-intrusive to the temperature and flow field. Light has no thermal inertia, so "real time" rapid transients can be studied. Also, a large area of the temperature field can be studied simultaneously. Finally, in comparison to other interferometers, the Mach-Zehnder interferometer has a large displacement between the reference and test beams, which allows the reference beam to pass through a uniform field. This allows for high quality and accurate interference. Some disadvantages are that the optics are sensitive to vibrations and dirt. A clean environment with minimal vibration is required. The optics are high precision, expensive and delicate, requiring careful handling. The test fluid must be transparent to light, which is air in this study. (Other issues arise when the flow has a significant pressure variation as well, where lines of constant density can no longer be related to temperature.) Another area of concern is dealing with turbulent and three dimensional flows. Laser interferometry is ideal for two dimensional flows, as the laser light beam averages the temperature field in the direction of the light beam propagation. Three-dimensional unsteady or turbulent flow can still be studied as will be discussed in Chapter 3. Further information on interferometry can be found in the literature (Hauf and Grigull 1970 and Naylor 2003).

2.2   Interferometer

The Mach-Zehnder interferometer was used both for visualization and to obtain experimental data. This instrument was used because it is a non-intrusive method that gives temperature field visualization and can also be used to measure local and average convective heat transfer rates. The fluid of interest is air, which is suitable for this application since it is transparent to radiation so that only the convective heat transfer component is measured. Air can also be considered an ideal gas, which means the temperature field can be related directly from the density field.

A schematic view of the Mach-Zehnder interferometer is shown in Figure 2.1 and a photograph is shown in Figure 2.2. A 15 mW Helium-Neon laser is used as the light source, which produces monochromatic light at a wavelength of 632.8 nm. The light is first passed through a spatial filter that eliminates any high frequency "noise" and expands the beam onto a parabolic mirror, which produces a collimated beam at a diameter of $\approx$ 20 cm (8 inc hes). The light passes through the first beam splitter (BS_1 in Figure 2.1), which creates two light beams of approximately the same intensity and in the same phase. One light beam reflects off first surface mirror M_{REF} and passes through the ambient air at room temperature. This is called the reference beam. The other light beam reflects off another first surface mirror M_{TEST} and passes through the experimental model. This is called the test beam. The experimental model causes the air to be heated (or cooled), which changes the index of refraction of the test fluid. Hence the test beam becomes out of phase with the reference beam. The two light beams are then recombined at the second beam splitter BS_2, which produces an interference pattern in the output. A spherical mirror focuses the output onto a small flat first surface mirror, which reflects the image into a still image camera or high-speed movie camera for recording.

Some major upgrades were made to the Mach-Zehnder Interferometer (MZI) prior to this study. Two new digital cameras were purchased. (More information on the new cameras will be presented in Section 2.3.4). In addition, the main optical components were over twenty years old and degraded in quality. New optics were purchased and installed in the MZI to improve the quality of the output captured by the new digital cameras. Full specifications of the optics can be found in Appendix A.1. All optics are 20 cm (8 inches) in diameter. The parabolic mirror has a focal length of 1.63 m (64 inches) and the spherical mirror has a focal length of 0.61 m
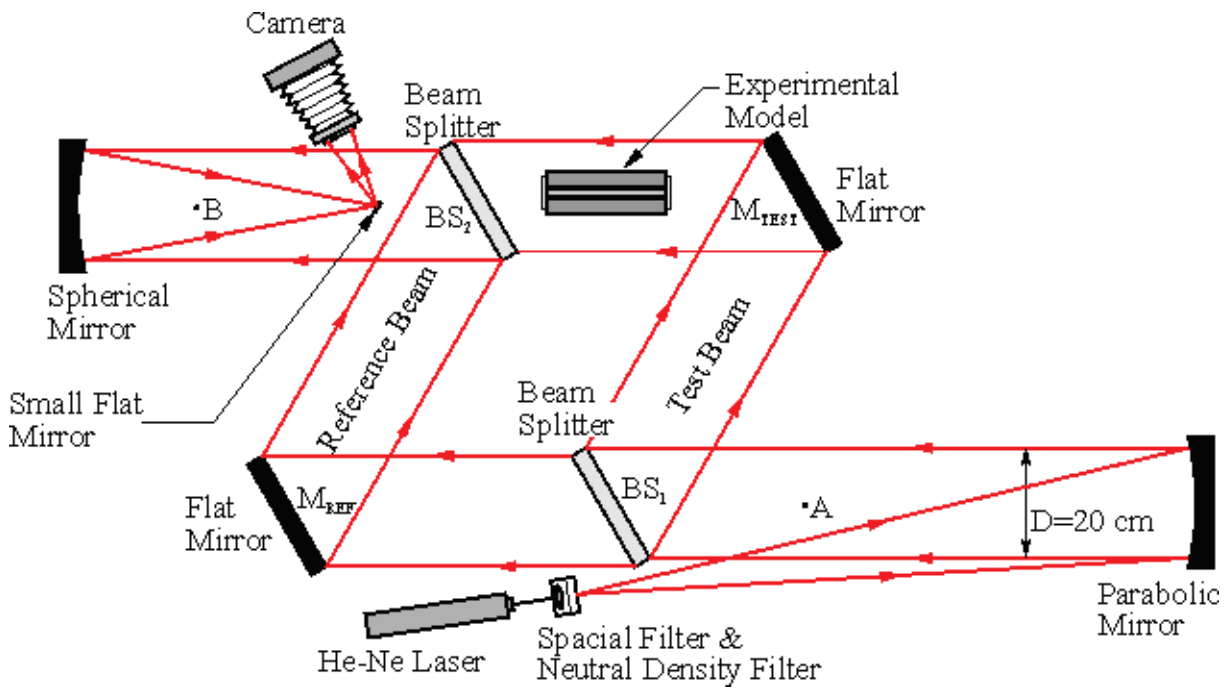
Figure 2.1: Schematic of the Mach-Zehnder interferometer.

Figure 2.2: Photograph of the Mach-Zehnder interferometer.

(24 inches). The two beam splitters have a flatness of $\lambda/20$ ($\lambda = 632.8$ nm) over the central 90% of the optic and have surface parallelism to 1 arc second. The first surface mirrors also have a flatness of $\lambda/20$ over the central 90% of the optic. A few notes on the interferometer optics are:

1) Each beam splitter has an A and B side. The A side is 50% reflective and 50% transmissive and the B side has an anti-reflective coating. To get the best image quality, it is very important to make sure that the beam splitters are installed correctly. In the interferometer, the A side of BS_1 is facing the parabolic mirror, so that the light does not pass through the glass before being reflected, which would result in the reflected light passing through BS_1 twice. The A side of BS_2 is installed facing the spherical mirror for the same reason. There is a second output of the interferometer from the B side of BS_2, but this output is not as high quality because the reflected light has passed through the beam splitter glass twice.

2) Surface flatness and parallelism are important for a MZI because of the wave front error they could introduce. If the optic surfaces are not parallel, the light will travel through more glass in the thicker part of the optic and will be out of phase with the light going through the thinner part of the optic. Similarly, variations in the surface finish cause changes in the local optical path length through the optic, which will result in wave front distortions.

3) Precise optical alignment of the MZI is also necessary to obtain a high quality output. The optics must also be aligned with each other in both the near field and far field. If an object is placed at point A in Figure 2.1 and the optics are not aligned, the shadow of the object from the reference beam will not align with the shadow of the object from the test beam. Flat mirror M_{REF} must be adjusted both horizontally and vertically until these two shadows are coincident in the interferometer output. This is called far-field beam alignment. Another object is then placed at point B and the two shadows are again aligned using beam splitter BS_2. This is called near-field focusing. In practice, this is an iterative process, as adjusting the optics at one point brings the object slightly out of alignment at the other point.

The MZI was mounted on an optical bench manufactured by Newport Corporation. It is 800 lb (364 kg), 1.22 m × 3.05 m (4 feet × 10 feet) with ¼ - 20 NC tapped holes equally spaced on 25.4 mm (1 inch) centers. In order to reduce external vibrations from the floor, the table was placed on 8 inflated tire inner tubes. As shown in the schematic in Figure 2.1, the laser, parabolic mirror, BS_1 and M_{TEST} were all mounted on the optical table. BS_2 and M_{REF} were mounted on extensions that were cantilevered off the side of the optical bench. The extensions were modified from the existing ones to provide more clearance for the experimental model of this thesis. They were made of 3/8 inch and ½ inch thick steel sheet bolted together with ¼ - 20 NC holes for mounting purposes. Mechanical drawings of the new extensions are shown in Appendix B.1. Also, a new small flat mirror mounting system was constructed, which is described in Appendix B.1. The MZI is enclosed inside a room of size 3.66 m × 6.10 m × 2.44 m (12 feet × 20 feet × 8 feet), that is designed to reduce outside air currents and exterior light.

2.3 Experimental Model

The experimental model consists of two isothermal vertical flat plates that are separated by an air gap, creating a vertical channel. The dimensions of the entire model are approximately 40.6 × 45.7 × 76.2 cm (16 × 18 × 30 inches). A photograph and three-dimensional SolidWorks (2008) drawing of the entire experimental model assembly is given in Figure 2.3.

2.3.1 Hot and Cold Isothermal Plates

The hot and cold walls of the vertical channel are similar and each consists of two plates, the front plate and back plate. The mechanical drawings of the front plates are shown in Figures 2.4 and 2.5 and Figure 2.6 shows the back plates. Each plate is ¾ inch thick and made of aluminum. The walls were designed to be 26.4 cm (10.4 inches) tall so that when in the interferometer only two images were needed to study the entire channel and the entrance and exit regions. The width of the walls was determined based on the sensitivity of the interferometer. A width of 35.5 cm (13.98 inches) was sufficient to obtain 5 to 15 interference fringes inside the channel depending on the temperature conditions being studied.

(a)   (b)
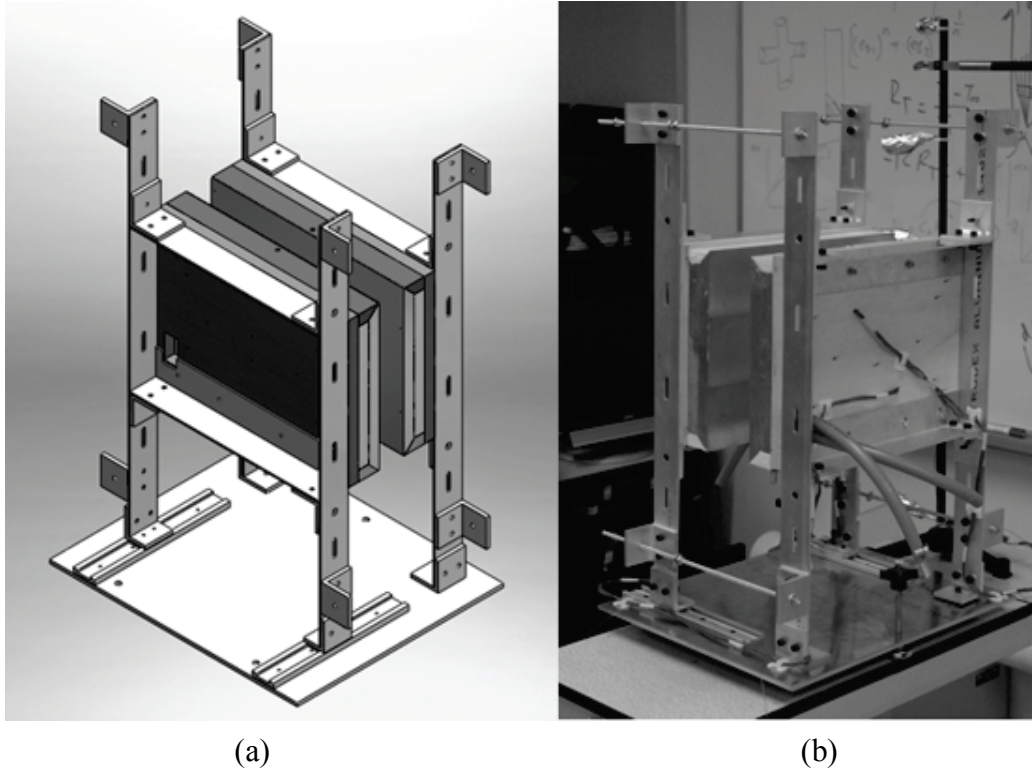
Figure 2.3: (a) SolidWorks (2008) drawing and (b) photograph of the experimental model.

The aluminum plates were machined to their required dimensions on a computer numerical control (CNC) milling machine. The front surface of the plates was milled in the beam direction to a flatness within ±0.12 mm. The improved flatness yields better results in the interferometer due to increased accuracy in aligning the test beam. Eight holes were drilled in the front plate at precise locations for locating pins to also be used for alignment in the interferometer. The walls are heated or cooled using a constant temperature water bath (Model: Lauda Proline RP 1845 see specifications in Appendix A.2). The water is pumped through the plates in a ½" (12.7 mm) flow channel of depth ¼" (6.35 mm), which is milled into the surface of the back plates. The flow channels follow a coil pattern with the inlet following the outlet to the center of the channel. This promotes isothermal conditions within the plate. Pressure loss calculations were performed to check that the flow rate through the model would be at least 6 L/min. At this flow rate the temperature of the fluid was calculated not to rise more than 0.02 °C as it passed through the model.

Figure 2.4: Mechanical drawing of the cold wall front plate.

Back View

TC holes X12

R0.25

#10-32x0.5 depth X30

0.661

Ø0.25

1.50 equally spaced

1.49
0.75
1.50

3.25

3.00

2.20

0.75
1.50

0.75

0.24

0.95
1.50
1.50
1.25

1.20

0.49

0.18x0.105 depth
(1/8" O-Ring Gasket)

Side View

0.04
(1 mm)

0.375

45°

0.75

Front View

10.40
5.15
2.625

13.98

0.25

2.625
0.75

4.50

5.90

2.625

7.775

9.65

Ø1/16 X8
(Locating Pins)
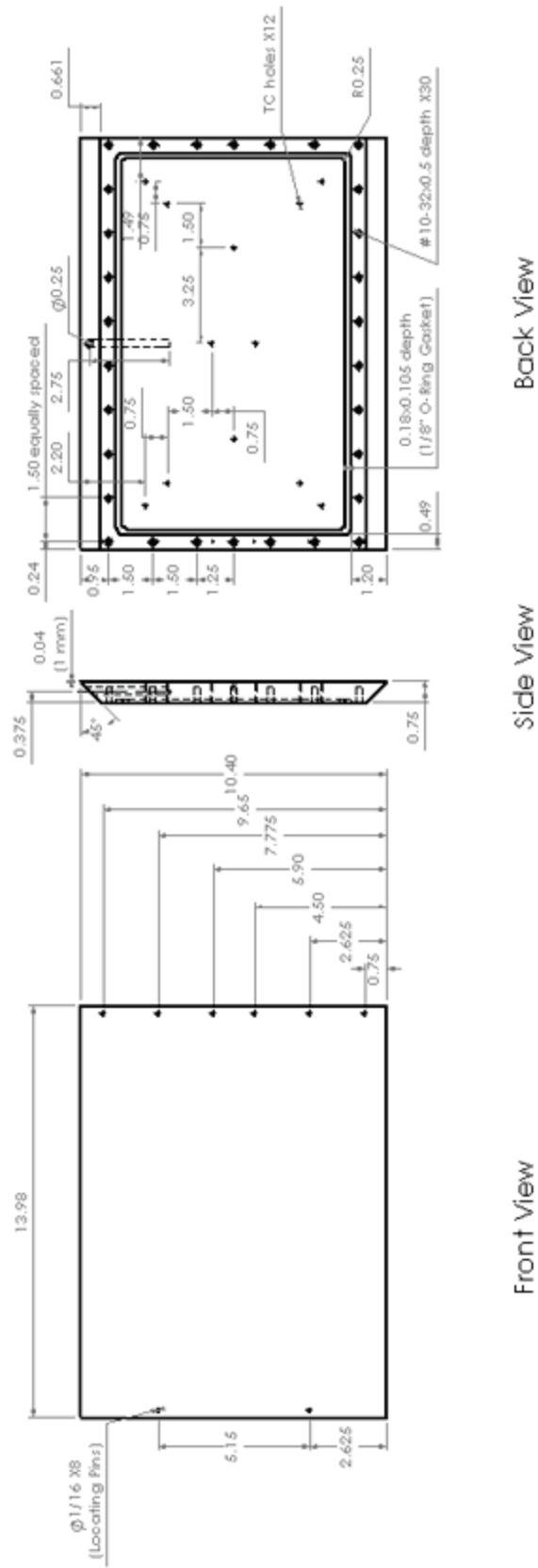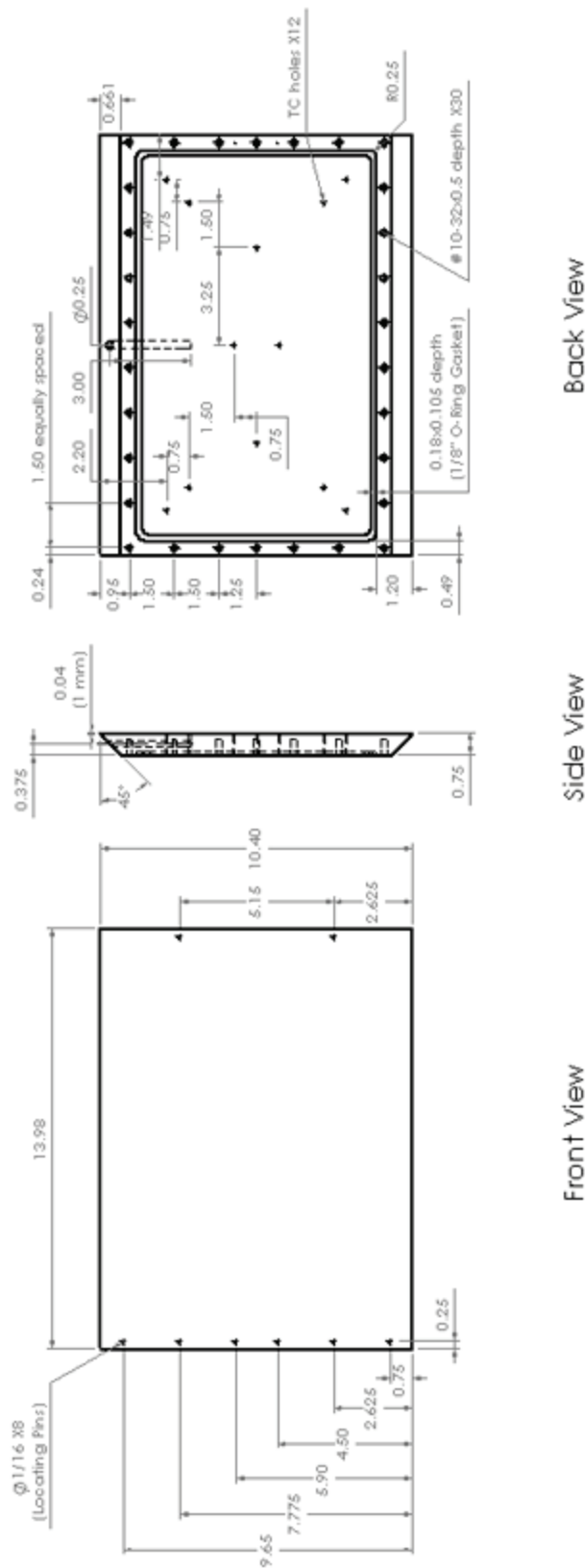
Front Plate Hot (1 required)
14" x 10.5" x 0.75" aluminum
All measurements in inches

1. Front surface of plate shall be precision flat milled
    2. TC hole at 11/16" depth
3. Layout of holes on Back View is symmetrical

Figure 2.5: Mechanical drawing of the hot wall front plate.
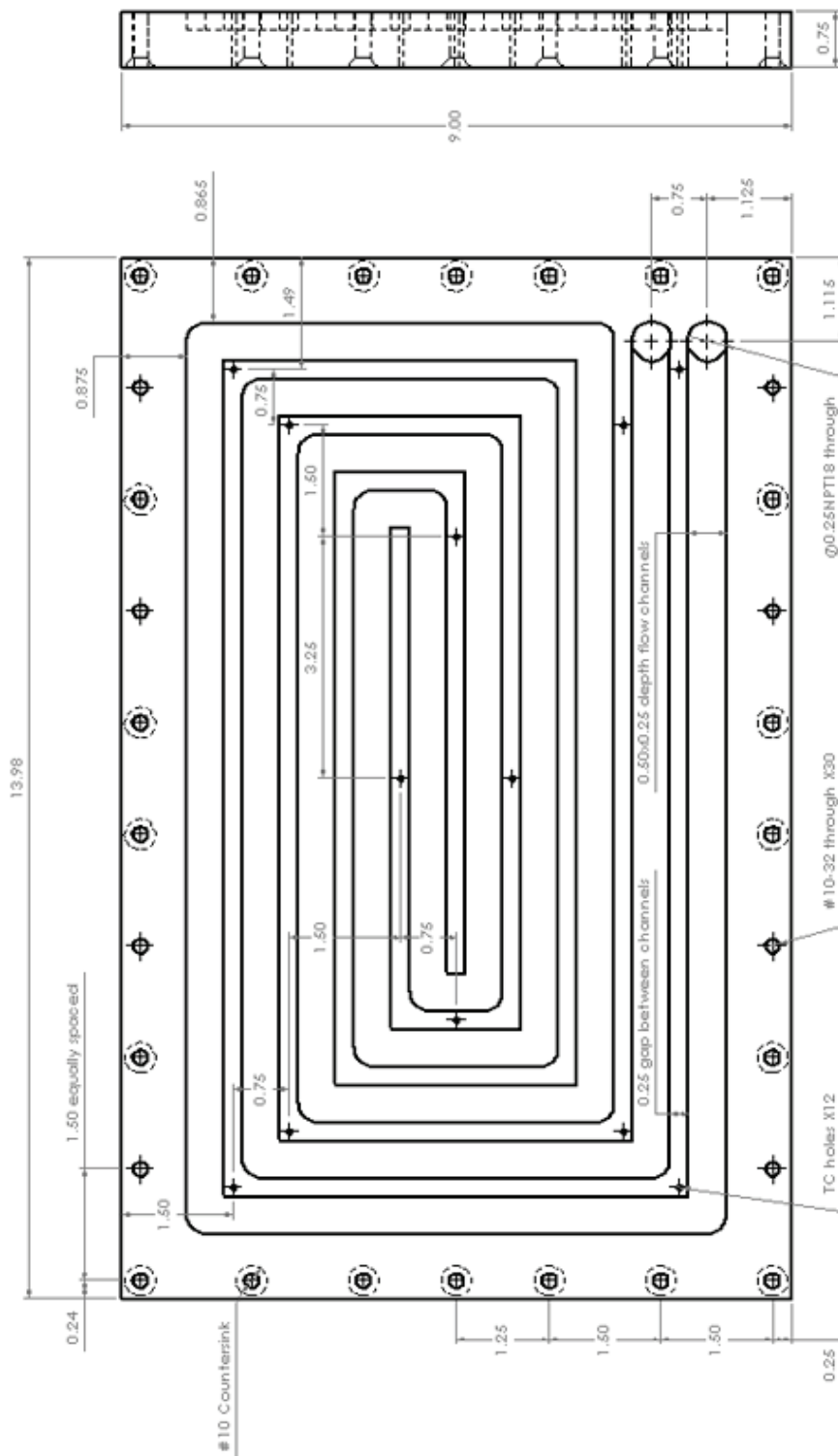
30

Figure 2.6: Mechanical drawing of the back plates.

The two plates were sealed together by a 3.175 mm (1/8") diameter O-ring gasket (McMaster Carr #9407K12) and held together with twenty two #10-32 screws around the perimeter of the plates. An additional eight #10-32 fibreglass reinforced screws (McMaster Carr #91221A710) were used to mount the plates to the wood backing plate and support frame in order to reduce heat transferring from the plates to the support frame. Each wall had twelve holes drilled through the front and back plate to within 1.59 mm (1/16") of the surface of the front plate for the thermopiles and thermocouples. All twelve of these holes were sealed with silicone after the thermocouples/thermopiles were installed. The two front plates also had a 7.62 cm (3") hole drilled vertically through the bevelled edge to hold the probes for the platinum resistance thermometers. More information on the temperature monitoring will be discussed in Section 2.3.3.

2.3.2 Model Assembly

The assembled model is shown in Figure 2.3. The hot and cold walls were mounted to wood backing plates to insulate the support frame from the isothermal plates. A simple 1-D calculation showed that the back surface of the wood would not deviate more than 0.1 °C from ambient when the plates were heated or cooled. Foam insulation was also added to the top and bottom edges of each wall to create 90° edges at the entrance and exit of the channel. These wall assemblies were attached to aluminum angle (5.08 × 5.08 × 0.32 cm) (2 × 2 × 1/8 inch) using the fibreglass reinforced screws, which were also used to insulate the support frame from the walls. The aluminum angle was attached to aluminum bar (5.08 × 0.32 cm) (2 × 1/8 inch), which are the main support pieces, using brackets made from aluminum angle (5.08 × 5.08 × 0.64 cm) (2 × 2 × ¼ inch). These were attached to a ¼ inch (0.64 cm) aluminum base plate. Mechanical drawings for all these parts are shown in Appendix B.2.

The cold plate was fixed to the base plate with screws and the hot wall was attached to the base plate with a track and sliders (McMaster Carr #6723K31 and #6723K12) that allow movement in the x-direction to adjust the width of the channel. The base plate was also fitted with adjustable legs for levelling the entire model. The width of the channel can be adjusted with four threaded rods attached to brackets from the edges of the model. Two of these rods are located at the top

of the model and two are located near the base. These threaded rods are adjusted with precision gauge blocks located in between the two channel walls to ensure an accurate channel width.

In order to promote a two-dimensional flow, an optical window assembly was mounted on both sides of the vertical channel. These windows prevented air from being entrained from the sides. Two 20 cm (8 inch) optical windows were mounted in Plexiglas mounts. Each optical window has parallelism to within 5 arc seconds and a surface flatness to within $\lambda/20$. The specifications of the optical windows are given in Appendix A.1. The mechanical drawings of the Plexiglas mounts are shown in Appendix B.3. These mounts were attached to the experimental model support frame such that they could be adjusted both vertically and horizontally. The apparatus was designed such that the temperature field of the entire channel could be captured in two images. So, the optical windows could be mounted in two positions to cover the entire model. Foam weather stripping was used between the optical window mounts and the aluminum frame of the vertical channel to seal the sides of the vertical channel and prevent the optical windows from being scratched.

Since the model is open to the environment at the top and the bottom of the vertical channel, an "eddy tent" was constructed. This is used to dampen the disturbances in the room, so that they do not affect the air around the experimental model and affect the data. The eddy tent was constructed out of 1×2 inch wood and sheer fabric (The fabric still allows air to move through it, but dampens any large disturbances). It is roughly 61 cm wide by 91 cm long by 122 cm high ($2 \times 3 \times 4$ feet), such that it can be placed over the experimental model without interfering with the model, the instrumentation wiring or the optics. Holes were cut in the fabric on the ends in alignment with the optical windows to allow the laser beam to pass through the eddy tent. The other two side panels of fabric were attached with Velcro so that the fabric could be removed to work on the experimental model and also to make removal of the eddy tent easier. A photo of the apparatus with the eddy tent in the MZI is shown in Figure 2.7.

2.3.3 Temperature Monitoring

The temperatures of the two walls were measured using thermopiles and thermocouples. The cold wall had 6 thermocouples strategically located in holes on the back of the plates. The

thermocouples were handmade Type T using 20 gauge Teflon coated copper and constantan wire with special limits of error (Omega Engineering Inc. TFCC-020 and TFCU-020) and an oxy-acetylene torch with a very fine tip to create a small bead (approximately 2 mm) on the ends. The thermocouples were calibrated in an isothermal bath against a precision glass thermometer calibrated against national standards. The thermocouples were checked over multiple temperatures, starting at 15 °C and heating up to 40 °C at 5 °C intervals, and then cooling back down to 15 °C. A correction was then applied to each thermocouple based on the calibration. The corrections are shown in Table G.1 in Appendix G.1. To electrically insulate the wires, the thermocouples were coated in a thin layer of epoxy and then placed inside holes in the plates, which were sealed with silicone. The thermocouples were connected to a thermocouple reader, where the cold wall temperatures were monitored.

Two thermopiles were also constructed to measure the temperature difference between the ambient air and the hot wall, and the temperature difference between the hot and cold walls. A thermopile was used instead of thermocouples because of its greater accuracy in measuring temperature differences, which is very important for these experiments. These thermopiles were

Figure 2.7: Photograph of the experimental model with the "eddy tent" in the interferometer.

constructed using the same Type T 20 gauge Teflon coated copper and constantan wire with special limits of error used to construct the thermocouples. Each thermopile had 12 junctions that were welded together using an oxy-acetylene torch leaving a small bead on the ends. The thermopiles were tested in two isothermal baths against a precision glass thermometer calibrated against national standards. Again the temperature differences between the two baths were adjusted from 0 °C to 20 °C in 5 °C increments. The thermopile voltage was measured and the NIST standard tables were used to check that the thermopiles were working properly. The first thermopile TP_1 is located between the hot and cold walls, 6 leads were placed strategically in the back of the hot wall, and 6 leads were placed strategically in the back of the cold wall. Again, the ends were coated in a thin layer of epoxy and placed inside holes in the plates, which were sealed using silicone. The second thermopile TP_2 is located between the hot wall and the ambient air, 6 leads placed in the hot wall and 6 leads located in the ambient above and below the experimental model. The leads in the ambient thermopile were attached to a moveable pole and each thermopile end was covered in a tin foil shield to prevent radiation from affecting the temperature of the beads. Each thermopile had two leads that attached to digital multimeters (Fluke 8846A see Appendix A.2 for specifications) for measurement. These are 6.5 digit precision digital multimeters that are necessary to record the output of the thermopiles in micro-volts.

A spreadsheet was used to determine the proper temperatures required for each case of interest. The average temperature of the cold wall is first recorded using the thermocouples. This temperature is converted into a voltage. The voltages of the two thermopiles are recorded onto the spreadsheet. In order to get the hot wall temperature, the voltage of TP_1 is added to voltage of the average cold wall temperature multiplied by the number of leads in the cold wall (6 in this case) and that number is divided by the number of leads in the hot wall (6 in this case). A sample calculation for a thermopile is given in Appendix D.2. Similarly, the voltage of TP_2 is recorded and the ambient temperature can be determined. Once all three temperatures are known, the temperature difference can be determined and adjusted as needed.

As a method of double checking the temperatures, a platinum resistance thermometer (Omega DP97 with two DP97-PROBE1) was also used. Two probes were used, one in each wall of the vertical channel. The platinum resistance thermometer can measure the absolute temperatures of

the hot wall and the cold wall, and it can measure the temperature difference between the two probes, which will give the temperature difference between the two channel walls.

2.3.4 Cameras and Data Acquisition

Along with the new optics for the interferometer, there are two new cameras. The output of the interferometer used to be captured by a large format Polaroid film camera, but the Polaroid film is no longer being produced. A Phase One P45 digital back with a resolution of 39 megapixels was purchased to replace the film camera. The full specifications of the digital back are presented in Appendix A.2. This digital back is still used with a view camera that is fitted with a lens with a focal length of 180 mm.

The digital back uses software (Capture One Pro 2008) to export the raw image file into a usable TIFF file. There are many features and functions of Capture One Pro. For experiments it is important that the proper settings are used so that the raw picture data are not corrupted. Extensive testing was conducted to find the best settings in the software to reduce the error in the output.

Also, an Integrated Design Inc. MotionPro X-3 Monochrome high speed digital movie camera is used to measure the unsteady temperature field. It has a resolution of 1.3 mega pixels and can take up to 1040 fps at the maximum resolution. It should be noted that the camera can support higher frame rates if the resolution of the images is reduced, but for the current experiments a frame rate of 120 fps was found to be more than sufficient. The specifications of this camera are also in Appendix A.2. The technique used with this camera was fully described by Poulad et al. (2011).

Since the high-speed movie camera is of a lower resolution than the still camera, multiple captures are required to record the entire output from the interferometer. It is mounted on three Velmex A40 Unislide translating devices so that the camera can be moved through the output beam without moving the entire tripod. The translating devices can move the camera in the x-, y- and z-directions.

2.4 Flow Visualization

A different experimental model was used for flow visualization, which was constructed by Lai (2004). This apparatus was designed to be used as a tall enclosure with heated blinds between the two plates, but it was adapted for use as a vertical channel. The experimental model was constructed of two aluminum plates mounted vertically separated by a channel spacing b to create a vertical channel. The height of the aluminum plates was L = 400 mm. The aspect ratio was adjusted to obtain data at different Rayleigh numbers. The cold wall was cooled using a constant temperature water bath. The hot wall was heated using six electric strip heaters attached to the back surface of the aluminum plate. Thermocouples were used to monitor the temperatures of the two aluminum plates and these were used to determine the temperature ratio, R_T.

A separate room was constructed out of clear plastic and 2 by 4 inch lumber to create a "smoke room", so that outside drafts would not affect the air flow around the experimental model. The smoke room had sufficient room for a large table with enough room so that the operator could walk around to work with the apparatus. The plastic covered the four sides and top of the smoke room, with an opening for access that could be closed. The camera was setup on a tripod outside the smoke room and a small hole was cut in the plastic for the camera. This hole also allowed the operator to introduce smoke into the experimental model from outside the smoke room.

A 50 mW laser was used with a line generating optic to illuminate a cross section of the smoke inside the experimental model. The laser illuminated a cross section located about $1/3^{rd}$ from the front of the model. The line of laser light generated was approximately 1 mm in thickness and only illuminates a plane of smoke. This technique is excellent for viewing vertical flows that are heavily seeded with smoke. A schematic of the flow visualization setup is shown in Figure 2.8.

A Dräger tube (item #CH25301) was used as the source of the smoke. Moisture from the air reacts with contents of the Dräger tube and a sulphuric acid aerosol emerges in the form of white smoke. The Dräger tube content is toxic, so some safety precautions were taken. The smoke was introduced into the model from outside the "smoke room" so that the operator was not breathing the aerosol and it was allowed to dissipate before re-entering the "smoke room". The smoke was introduced into the experimental model using hoses that directed the smoke to the top

and bottom of the channel. The Dräger tube was connected to the hoses outside the smoke room with a hand pump. This pump was used to slowly blow air through the Dräger tube and the hoses into the experimental model. The disturbance caused by the smoke injection was then allowed to settle. A dense stream of smoke is desirable for photographs, but a leaner stream is more neutrally buoyant and beneficial in natural convection.

A digital single-lens reflex (DSLR) camera was used to capture images of steady flow. A Tamron DP Di 180 mm lens was used on the camera with a remote shutter release. The camera was mounted on a tripod outside the smoke room and placed approximately 2.5 m from the focal plane. For unsteady flow a video camera was used to record the flow for one minute. It was also placed on a tripod outside the smoke room. It should be noted that an item was placed in the experimental model at the location of the laser line and the camera was focused onto this item, so that the camera was focused on the illuminated smoke.
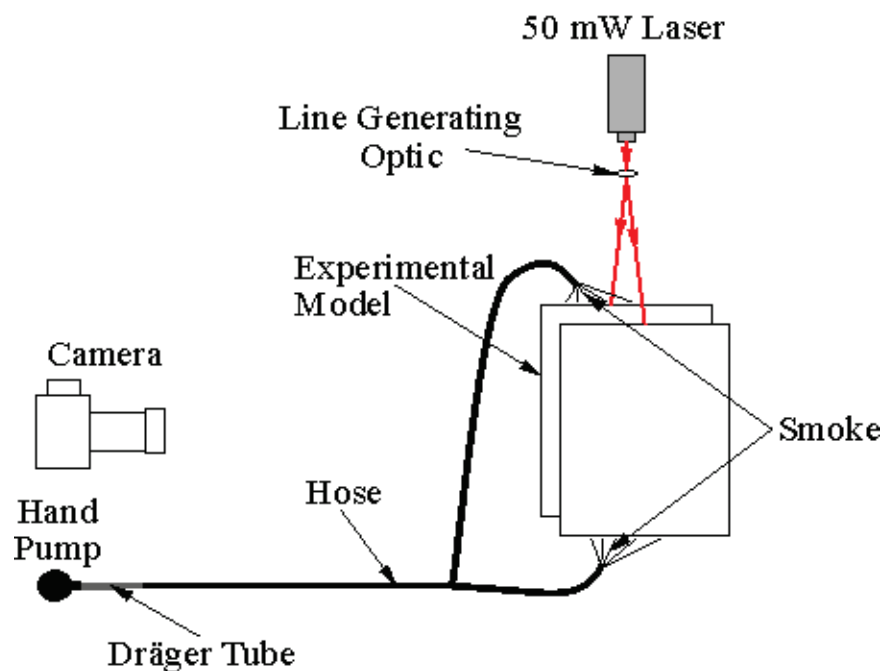
Figure 2.8: Schematic of the flow visualization apparatus.

Chapter 3

Experimental Procedure and Analysis

3.1 Introduction

A total of 54 finite fringe interferograms and 30 infinite fringe interferograms were used for analysis. Fifteen different cases were studied using the still image camera and two cases were conducted using the high speed movie camera. The range of variables used in this study was:

R_T = 1, 0, −0.5, −0.75, and −1

A = 26.4, 17.6, 13.2, and 8.8

The cold wall temperature was maintained at 7.5 ºC below the ambient temperature, except for the R_T = 0 cases, where T_C = T_∞ and the R_T = 1 cases, where T_C = T_H. The experiments were carried out in winter, spring and summer, so the temperature and relative humidity in the lab varied from day to day. If we assume that the typical relative humidity in the lab is 50% and the typical temperature is 24 °C, then the dew point is 13 °C. The cold wall temperature was set 7.5 °C below ambient temperature in order to not fall below the dew point of the air and create condensation on the surface of the channel walls. The hot wall temperatures were set between 7.5 and 15 ºC above the ambient temperature. These temperatures were used to obtain sufficient interference fringes in the output of the interferometer. The aspect ratios were based on the four channel spacings of 10, 15, 20 and 30 mm. These channel spacings were chosen to study the range of Rayleigh number of interest.

For each experiment with the still image camera, both infinite and finite fringe interferograms were taken. With the high speed movie camera, only the finite fringe interferograms were taken. The infinite fringe setting requires that the test beam and reference beam be almost perfectly parallel when they are recombined at the second beam splitter. In the infinite fringe mode, the interference fringes are isotherms. In the finite fringe setting, the reference and test beams are purposely misaligned by a small angle at the second beam splitter. In this setting, a constant fringe gradient in the y-direction is superimposed upon the fringe field that is produced by the temperature field. Figure 3.1 shows a comparison between the finite and infinite fringe

interferograms of both the unheated and heated experimental model. The local heat transfer analysis was conducted with the finite fringe interferograms and the infinite fringe interferograms were used for visualization of the temperature field. This chapter outlines the procedure and analysis used to obtain the heat transfer results presented in Chapter 5.

3.2 Experimental Procedure

The experimental procedure outlined here is adapted from Machin (1997), but has been updated to reflect the current experimental model and some updates to the Mach-Zehnder interferometer. A checklist is included in Appendix C.1 that was used when conducting the experiments.

The first step is the coarse alignment of the interferometer. The instructions for setting up the interferometer optics are given in Appendix C.2. Once the coarse alignment was completed, the experimental model was prepared for the experiments. The experimental model was placed on an adjustable table, so that the model could be translated vertically for the two image captures necessary to encompass the entire channel height. This table was also easily moved into and out of the test beam in the interferometer, so that adjustments could be made to the interferometer or experimental model. Before beginning the experiments, the aluminum plates were polished with an all purpose metal polish to remove any oxidation and increase the reflectivity. Increasing the reflectivity makes aligning the plates in the interferometer easier. Polishing also reduces the emissivity of the plates, which gives the secondary effect of reducing the radiation and therefore the total heat transfer and the plates will be more isothermal. (It should be noted that the interferometer does not measure radiation, so reducing the emissivity of the plates is not necessary.)

Before placing the experimental model into the interferometer, the plates were adjusted to the correct channel spacing and checked with gauge blocks at all four corners of the plates. The hoses from the constant temperature water baths were attached to the back of the channel walls. Then the thermocouples were attached to a portable thermocouple reader and the two thermopiles were each connected to a precision digital multimeter. The platinum resistance thermometer probes were placed into the top of each channel wall and attached to the reader.
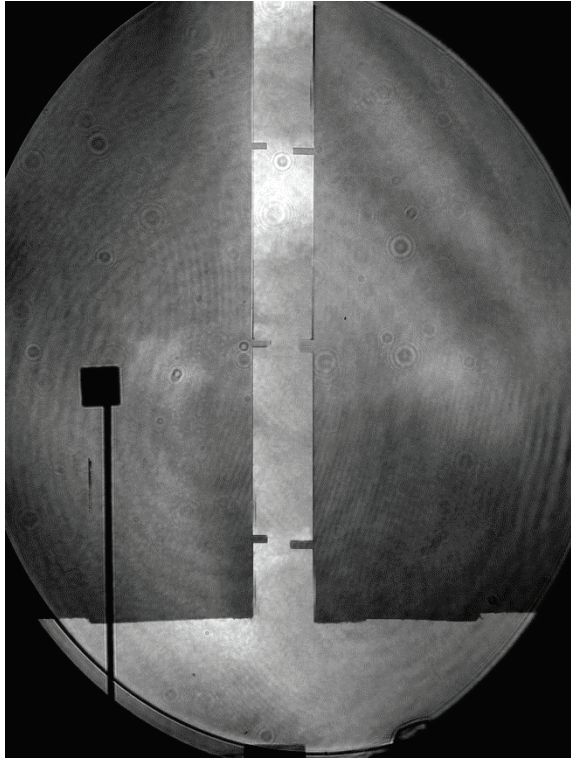
(a) Infinite fringe mode unheated experimental model
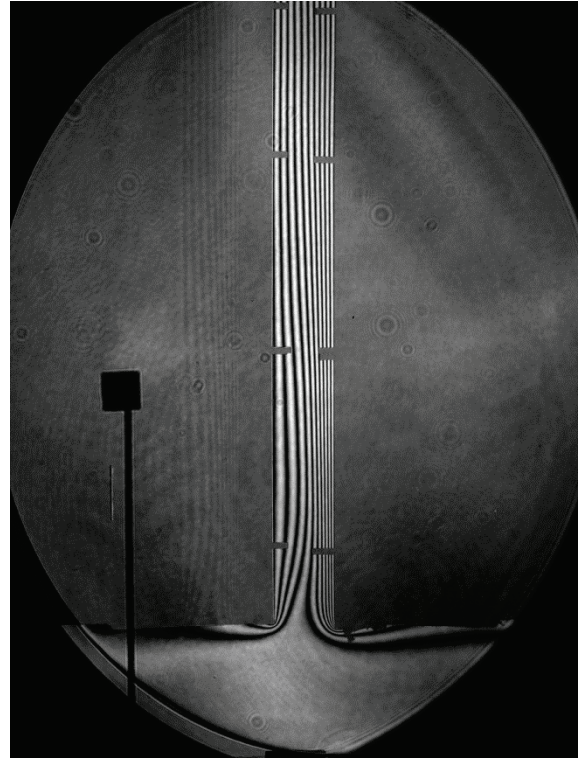
(b) Infinite fringe mode heated experimental model
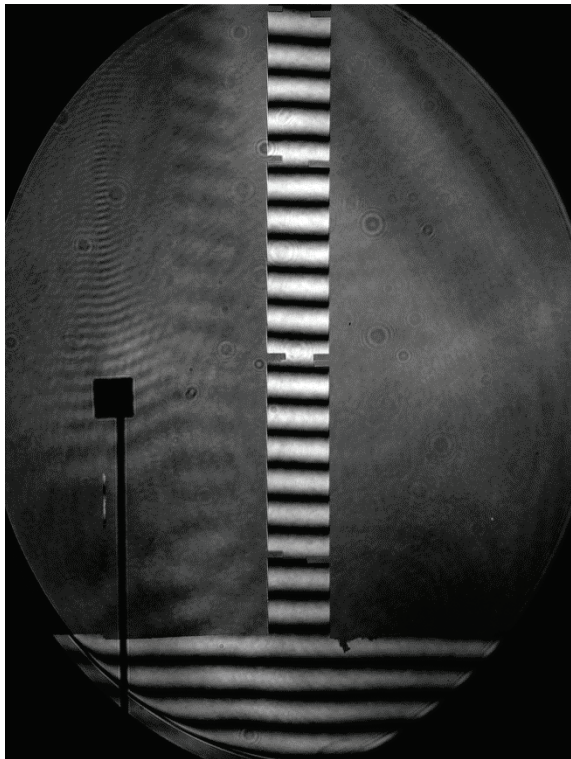
(c) Finite fringe mode unheated experimental model
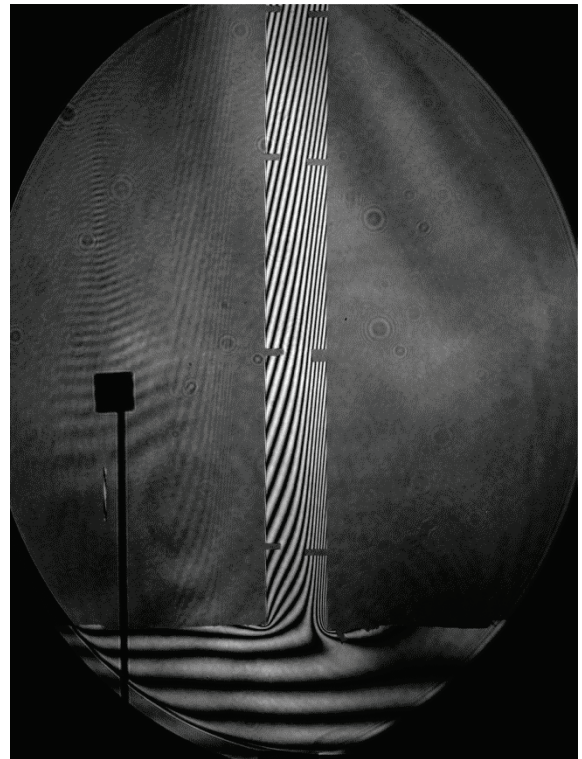
(d) Finite fringe mode heated experimental model

Figure 3.1: Sample interferograms at $R_T = -0.5$, $A = 17.6$, and $Ra(b/L) = 66.6$ in both infinite and finite fringe modes, with an unheated and heated experimental model.

The optical windows were then attached and aligned with each other on both sides of the experimental model.

The experimental model on the table was then carefully moved into the test beam of the interferometer. The table height and location were adjusted so that the optical windows on the experimental model were aligned with the test beam. The model was then levelled horizontally using a spirit level and vertically using a plumb bob by adjusting the legs on the base plate. The "eddy tent" was carefully placed over the experimental model on the table.

The fine alignment of the interferometer was next, which is discussed in Appendix C.3. This involved aligning the test beam with the experimental model and then obtaining the desired fringe pattern by near field - far field focusing. Each case involved an image of the upper and lower portions of the experimental model, which involved moving the optical windows on the experimental model. Every time the optical windows were moved, the alignment procedure and the setting of the fringe pattern were repeated. It should be noted that a higher level of precision was used in setting the optics for the finite fringe pictures because they were used for analysis. Since the infinite fringe pictures were for visualization only and it is harder to set, the optics were adjusted when the model was "hot" in order to obtain the best images for presentation.

The camera was positioned and photographs of the experimental model were taken. There are two slightly different procedures for the still camera and the high-speed movie camera. Appendix C.4 outlines the still camera procedure. The still image camera was aligned such that the entire interferometer output beam was captured on the CCD array of the camera. All the images were taken at a shutter speed $1/400^{th}$ of a second. The finite fringe images were taken first because they required more precision and then the infinite fringe images were taken. Once the photographs were taken, they were processed through a custom MATLAB (2010) image processing code to extract the fringe spacing data and analyzed with a spreadsheet.

The high-speed movie camera procedure is given in Appendix C.5. The high speed camera does not use a lens, so the output is focused directly onto the CCD array. Because this camera has a lower resolution, it cannot capture the entire output of the MZI. Therefore, the camera is mounted to an X-Y-Z translating device so that multiple locations can be used to obtain images. For this study, it was determined that 6 locations were needed for each half of the channel, so a

total of 12 captures were required for the entire channel height. The high speed movie camera was setup to record a sequence of images at a frame rate of 120 fps for 20 seconds. Once the images were obtained, again they were processed through a custom MATLAB image processing code. The thermocouple and thermopile readings, the atmospheric pressure, and the output from the MATLAB code were used in a spreadsheet in order to calculate the local and average heat transfer rates.

The ambient pressure was measured using a mercury barometer with a calibration traceable to national standards. It was corrected for local gravity and thermal expansion effects according to the manufacturer's specifications.

3.3 Interferogram Analysis

In general, an interferometer measures the phase shift between two light waves. As described in Chapter 2, the interferometer splits the laser beam into two beams, one of which passes through the experimental model. The density of the air changes due to the changing air temperature because of the experimental model being heated/cooled. This change in air density causes a small change in the index of refraction of the air, which changes the speed of the laser light as it passes through this region. This causes the test beam to be out of phase with the reference beam. When these two beams are recombined, an interference pattern is created in the output. A complete overview of interferometry is given by Goldstein (1976), Merzkirch (1987) and Naylor (2003) and a brief overview is given here.

Interferometry uses the wave nature of light. Laser light is monochromatic and its amplitude can be expressed as:

$$D = D_0 \sin\left(\frac{2\pi}{\lambda}(ct - z)\right) \qquad (3.1)$$

where D_0 is the maximum amplitude, λ is the wavelength, c is the speed of light, t is the time, and z is the position. The amplitude of the reference beam at a fixed point is:

$$D = D_{0,REF} \sin\left(\frac{2\pi ct}{\lambda}\right) \qquad (3.2)$$

and the amplitude of the test beam is:

$$D = D_{0,TEST} \sin\left(\frac{2\pi ct}{\lambda} - \phi\right) \qquad (3.3)$$

where ϕ is the phase shift between the two waves due to the differences in the index of refraction of the air caused by the experimental model. Given that the amplitude of these two waves are equal ($D_{0,REF} = D_{0,TEST}$), they recombine in the output of the interferometer as:

$$D = D_0 \left(\sin\left(\frac{2\pi ct}{\lambda}\right) + \sin\left(\frac{2\pi ct}{\lambda} - \phi\right) \right) \qquad (3.4)$$

From Equation (3.4), constructive interference (bright lines in the output) occurs when $\phi/2\pi$ is an integer and deconstructive interference (dark lines in the output) occurs when $\phi/2\pi + 1/2$ is an integer. So between the two beams a phase difference of one wavelength exists from fringe center to fringe center. The phase shift between the two beams is related to the difference in the number of waves in the two beams, as follows

$$\varepsilon = \frac{\phi}{2\pi} = \int_{REF} \frac{dz}{\lambda_{REF}} - \int_{TEST} \frac{dz}{\lambda} \qquad (3.5)$$

where ε is the fringe shift order, λ is the local wavelength of the light and dz is the path length of the beam of light. An interferometer measures the phase shift between two light waves, which is caused by changes in the refractive index in the experimental model. The index of refraction of a medium is defined as:

$$n = \frac{c_0}{c} = \frac{\lambda_0}{\lambda} \qquad (3.6)$$

where c_0 is the speed of light in a vacuum and c is the speed of light in the medium (i.e. air in this study); λ_0 is the wavelength of the laser light in a vacuum and λ is the wavelength of the laser light in the medium. Using a 2-D assumption and neglecting end effects, the fringe shift order becomes:

$$\varepsilon = \frac{1}{\lambda_0} \int_0^W (n_{REF} - n) \, dz \qquad\qquad (3.7)$$

where W is the width of the experimental model over which the refractive index varies. Equation (3.7) shows that the Mach-Zehnder interferometer integrates the change in refractive index along the beam. In a steady analysis, the index of refraction is constant along a line of constant density. The index of refraction can be related to density using the Gladstone-Dale equation:

$$n = \rho G + 1 \qquad\qquad (3.8)$$

where G is the Gladstone-Dale constant, which depends on the wavelength of light and the type of fluid. For this study, using air and a Helium-Neon laser (λ_0 = 6.328 $\times$ 10^{-7} m), G = 0.226 $\times$ 10^{-3} m^3/kg. In this study, air is considered to behave like an ideal gas (the compressibility factor of air at 300 K is 0.9999). Therefore the relationship between the density and the absolute temperature (T) is:

$$n = \frac{PG}{RT} + 1 \qquad\qquad (3.9)$$

where P is the absolute pressure and R is the gas constant (R = 287 J / kg K for air). Substituting this into Equation (3.7):

$$\varepsilon = \frac{WPG}{R\lambda_0} \left(\frac{1}{T_{REF}} - \frac{1}{T} \right) \qquad\qquad (3.10)$$

Rearranging to solve for temperature gives:

$$T = \frac{T_{REF}}{1 - \dfrac{\varepsilon R \lambda_0 T_{REF}}{WPG}} \qquad\qquad (3.11)$$

where in this study, T_{REF} is taken as one of the channel wall temperatures, depending on which side of the channel is being analyzed. Equation (3.11) is used to determine the temperature field. The first fringe from the surface does not necessarily represent a full fringe shift, but the

regression technique used to determine the fringe spacing accounts for this to give a more accurate result. The regression technique will be explained in Section 3.3.1.

It should be noted that both infinite and finite fringe modes can be used for analysis, but in this study the finite fringe mode was used for analysis. This is because finite fringe mode is less sensitive to vibrations. The finite fringe pattern was set perpendicular to the channel walls before heating the model. On the heated model pictures, the scans were made perpendicular to the channel walls so that they were parallel to the fringe angle in the ambient.

3.3.1 Local and Average Nusselt Number

In order to calculate the local Nusselt number on each channel wall surface, the direct gradient method is used. For the steady cases, the temperature field is two-dimensional. Consider a two-dimensional field, where the fringe shift is:

$$\varepsilon(x, y) = \frac{W}{\lambda_0}\left(n_{REF} - n(x, y)\right) \tag{3.12}$$

Differentiating Equation (3.12) with respect to x and applying the chain rule gives:

$$\frac{\partial \varepsilon}{\partial x} = -\frac{W}{\lambda_0}\frac{\partial n}{\partial x} = -\frac{W}{\lambda_0}\frac{\partial n}{\partial T}\frac{\partial T}{\partial x} \tag{3.13}$$

and rearranging:

$$\frac{\partial T}{\partial x} = -\frac{\lambda_0}{W}\frac{\partial \varepsilon / \partial x}{\partial n / \partial T} \tag{3.14}$$

Differentiating Equation (3.9) with respect to temperature:

$$\frac{\partial n}{\partial T} = -\frac{PG}{RT^2} \tag{3.15}$$

Substituting Equation (3.15) into Equation (3.14) and applying the result at the surface:

$$\left.\frac{\partial T}{\partial x}\right|_{x=0} = \frac{R\lambda_0 T_s^2}{WPG} \left.\frac{\partial \varepsilon}{\partial x}\right|_{x=0} \tag{3.16}$$

where T_s is the surface temperature of the channel wall being analyzed. The regression technique used in the custom MATLAB image processing code returns the fringe gradient at the surface, $\left.\dfrac{\partial \varepsilon}{\partial x}\right|_{x=0}$, which is then used to calculate the temperature gradient. The heat transfer rates are calculated using:

$$q_C = -K_{s,C} \left.\frac{\partial T}{\partial x}\right|_{x=0} \text{ and } q_H = K_{s,H} \left.\frac{\partial T}{\partial x}\right|_{x=b} \tag{3.17}$$

where q_H and q_C are the heat fluxes from the hot and cold walls, and K_s is the conductivity of the air at the surface temperature. The local Nusselt numbers are defined as:

$$Nu_{y,C} = \frac{q_C b}{\Delta T K} \text{ and } Nu_{y,H} = \frac{q_H b}{\Delta T K} \tag{3.18}$$

where b is the channel spacing, ΔT is the temperature difference, and K is the conductivity of air at the film temperature. The temperature difference depends on which type of case is being studied. For most cases, $\Delta T = \overline{\Delta T}$ except in the anti-symmetrical cases ($R_T = -1$) where $\Delta T = T_H - T_C$. The temperature difference is calculated from the thermopiles and thermocouple readings. Local Nusselt numbers were measured at approximately 100 locations (50 per image) along each channel wall using a uniform increment between measurement locations.

The average Nusselt numbers are determined by integrating the local Nusselt numbers:

$$Nu_H = \frac{1}{L}\int_0^L Nu_{y,H}\,dy \text{ and } Nu_C = \frac{1}{L}\int_0^L Nu_{y,C}\,dy \tag{3.19}$$

where the integrals were solved by using the trapezoidal rule. Combining the hot and cold wall average Nusselt numbers gives the overall channel average Nusselt number:

$$Nu = \frac{1}{2}\left(Nu_H + Nu_C\right) \tag{3.20}$$

47

A complete sample calculation is given in Appendix D. A similar procedure is used when studying unsteady flows, but some special considerations need to be accounted for.

3.3.2 Time-Averaged Local and Average Nusselt Numbers

When studying unsteady cases, the temperature field is three dimensional and time dependent. The output interference fringe pattern of the MZI is two-dimensional, so the temperature field is beam-averaged. The fringe pattern is the spatial integration of the changes in the refractive index of the test fluid (air). The refractive index of the air is integrated along the laser light beam (in the z-direction) from the inlet to the outlet of the test model. If the refraction effects are neglected, the fringe shift is:

$$\varepsilon(x, y, t) = \frac{1}{\lambda_0} \int_0^W \left[n_{REF} - n(x, y, z, t) \right] dz \tag{3.21}$$

Again, assuming air is an ideal gas then the fringe shift can be related to temperature by:

$$\varepsilon(x, y, t) = \frac{PG}{R\lambda_0} \int_0^W \left[\frac{1}{T_{REF}} - \frac{1}{T(x, y, z, t)} \right] dz \tag{3.22}$$

Differentiating Equation (3.22) with respect to x and applying the result at the surface:

$$\left. \frac{\partial \varepsilon}{\partial x} \right|_{x=0} = \frac{PG}{R\lambda_0} \int_0^W \frac{1}{T_s^2} \left. \frac{\partial T}{\partial x} \right|_{x=0} dz \tag{3.23}$$

For measurements on an isothermal surface (as in the current study), the surface temperature can be removed from the integral. Rearranging Equation (3.23), the temperature gradient is:

$$\frac{1}{W} \int_0^W \left. \frac{\partial T}{\partial x} \right|_{x=0} dz = \frac{R\lambda_0 T_S^2}{PG} \left. \frac{\partial \varepsilon}{\partial x} \right|_{x=0} \tag{3.24}$$

Equation (3.24) shows that the beam-averaged surface temperature gradient is being measured in a 3-D field. The instantaneous local heat transfer rates are calculated using:

$$q_{y,C} = -K_s \frac{1}{W} \int_0^W \left. \frac{\partial T}{\partial x} \right|_{x=0} dz \text{ and } q_{y,H} = K_s \frac{1}{W} \int_0^W \left. \frac{\partial T}{\partial x} \right|_{x=b} dz \tag{3.25}$$

Each interferogram that was acquired with the high speed movie camera was analyzed using a custom MATLAB automated image processing algorithm to determine the instantaneous fringe gradient. The fringe gradient was used in Equations (3.24) and (3.25) to determine the instantaneous temperature gradient and instantaneous local heat flux at each time step. The measurements are beam averaged, but they are referred to as instantaneous local heat fluxes. The variations of convective heat flux in the beam direction are averaged by the laser. Therefore the heat flux is averaged in the z-direction, but local with respect to the y-coordinate. The instantaneous heat fluxes were time-averaged using:

$$q = \frac{1}{t} \int_0^t q_y dt \tag{3.26}$$

where the averaging time was sufficiently long to obtain a stationary value. The time-averaged heat flux is used in Equations (3.18), (3.19) and (3.20) in order to determine the time-averaged local and average Nusselt numbers.

3.3.3 Regression Technique

A nonlinear regression technique was used to extract the fringe gradient from the images. This technique was developed by Poulad et al. (2011) based on the nonlinear regression technique of Slepicka and Cha (1995). When the images are scanned, at each location the pixel intensity is extracted perpendicular to the surface. These scans are in the x-direction and long enough to encompass at least one fringe shift. The pixel intensity of a fringe shift approximately follows a sinusoidal pattern if the temperature profile is linear. So, the pixel intensity near the surface can be expressed as:

$$I(x) = I_0 + D_0 \sin\left(F(x - x_1) + \phi\right) \tag{3.27}$$

where I_0 is the mean pixel intensity, D_0 is the amplitude, F is the rate of change of phase, ϕ is the phase shift, and x_1 is the location of the first pixel. Equation (3.27) is fit to the extracted pixel

intensity data closest to the surface over the first full period. The mean pixel intensity is taken as the average intensity over the first full period. The other constants (D_0, F and ϕ) are adjusted iteratively using the least sum of squares best fit between I(x) and the extracted pixel intensity data. The rate of change of phase was then used to calculate the fringe gradient:

$$\left.\frac{\partial \varepsilon}{\partial x}\right|_{x=0} = \frac{F}{2\pi} \tag{3.28}$$

A sample intensity scan is shown in Figure 3.2, which also shows the best fit sine curve. This regression technique was coded in MATLAB, which the images are processed through. The resulting fringe gradient is combined with other measured parameters (temperatures and ambient pressure) in a spreadsheet to calculate the local and average Nusselt numbers.

3.3.4 Experimental Uncertainty

As with any experiment, there is some level of uncertainty in the results. A detailed error analysis of the primary measured and calculated quantities is given in Appendix E. The estimated uncertainty of the Rayleigh numbers is ±5%. The error in the local Nusselt numbers is estimated at ±11%. The integration process averages out the "noise" in the local Nusselt number data. For this reason, the average Nusselt number is more accurate than the individual local Nusselt number data and the estimated uncertainty is ±8%.

3.4 Flow Visualization Procedure

Smoke flow visualization has been used to study flow behaviour in the channel. There are many methods of creating the "ideal" smoke, such as cigar smoke or Dräger tubes, some of which were tested prior to taking any photographs. Dräger tubes were used in this study. These tubes produce a fine sulphuric acid aerosol, which appears as white "smoke". The method used to inject smoke is explained in Section 2.4. The procedure used for flow visualization in this study is described here. This flow visualization is a virtually non-intrusive method of obtaining quantitative information about the entire flow field.
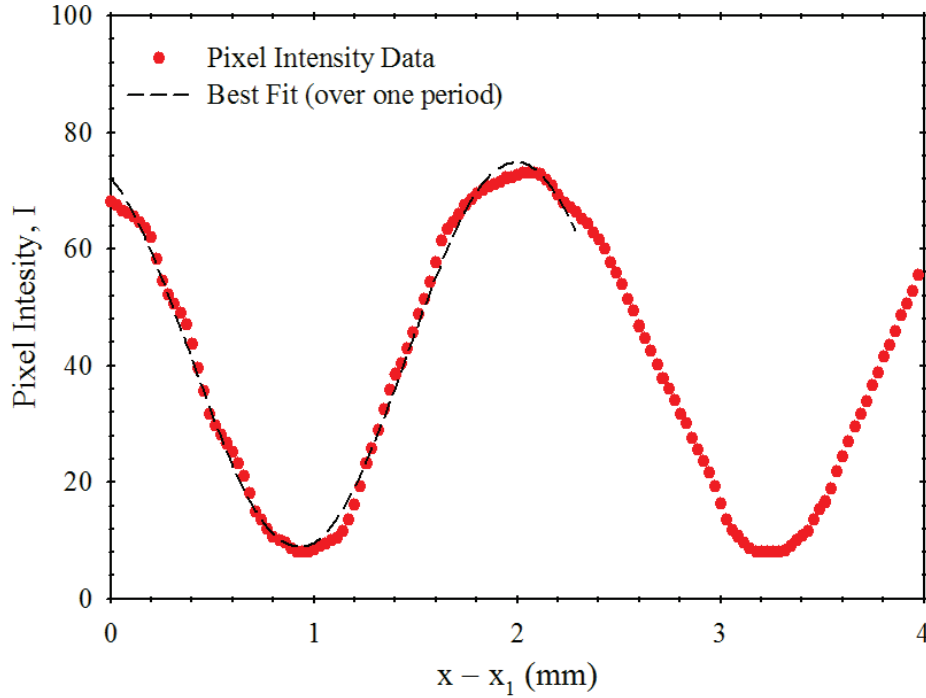
Figure 3.2: Typical near-wall pixel intensity profile and the best fit sine wave over one period used to obtain the fringe shift gradient.

Figure 2.8 shows the apparatus setup for flow visualization. Not all the cases studied with the interferometer were studied with flow visualization, as it was a preliminary experiment and only a few cases of interest were investigated. The spacing between the plates was set and the experimental model was leveled horizontally with a spirit level and vertically with a plumb bob. The laser sheet and the model were adjusted so the line of laser light was perpendicular to the channel walls. The hot wall was heated by six electric strip heaters using a DC power supply and the cold wall was cooled by a constant temperature water bath. The temperatures were monitored with the thermocouples.

The Dräger tube was attached to the hose and a hand pump was used to push air through the hoses and into the model. It should be noted that the air was introduced into the model from outside the "smoke room" so that the operator was not breathing the sulphuric acid aerosol. Air was pumped through the Dräger tube multiple times until the amount of smoke in the model was sufficient according to the judgement of the operator. The smoke was then allowed to settle for a few seconds. So, the flow disturbance associated with the smoke injection process was minimal.

The digital SLR camera was placed outside the "smoke room" and aligned with the experimental model. The camera was focused on the plane of laser light in the experimental model. The typical shutter speed used was 1/5th of a second, with an aperture setting of f/3.5. Three photographs were required to encompass this entire experimental model. The camera was translated up and down on a tripod in order to take images of the top, middle and bottom of the channel. These images were then combined to give a composite image of the flow pattern in the entire channel.

Chapter 4
Numerical Modelling and Solution Procedures

4.1 Problem Geometry

The numerical model is developed to determine the heat transfer of the hot wall, cold wall and overall channel in an asymmetrically, isothermally heated vertical channel with opposing buoyancy forces. The vertical channel geometry is shown in Figure 4.1. The two isothermally heated walls are of height L and separated by a channel width b. The cold wall is set to temperature T_C and the hot wall is at T_H, with the ambient temperature T_∞ at the top and bottom of the channel. The coordinate system is also shown in Figure 4.1. Gravity is in the negative y-direction.

4.2 Governing Equations

A buoyancy force drives the free convective flow in the channel due to the temperature differences between the two channel walls and the ambient temperature. The temperature differences cause fluid density gradients resulting in variation of the gravitational body (buoyancy) force. The laws of mass, momentum, and energy conservation are used to derive these governing equations. The continuity, x-momentum, y-momentum, and energy equations are given below in Equations (4.1) to (4.4) respectively. The viscous dissipation is neglected in the energy equation. The flow is assumed to be laminar, incompressible, two-dimensional, and steady for this solution.

$$\frac{\partial u}{\partial x} + \frac{\partial v}{\partial y} = 0 \tag{4.1}$$

$$\rho\left(u\frac{\partial u}{\partial x} + v\frac{\partial u}{\partial y}\right) = -\frac{\partial P}{\partial x} + \mu\left(\frac{\partial^2 u}{\partial x^2} + \frac{\partial^2 u}{\partial y^2}\right) \tag{4.2}$$

$$\rho\left(u\frac{\partial v}{\partial x} + v\frac{\partial v}{\partial y}\right) = -\frac{\partial P}{\partial y} + \mu\left(\frac{\partial^2 v}{\partial x^2} + \frac{\partial^2 v}{\partial y^2}\right) - \rho g \tag{4.3}$$
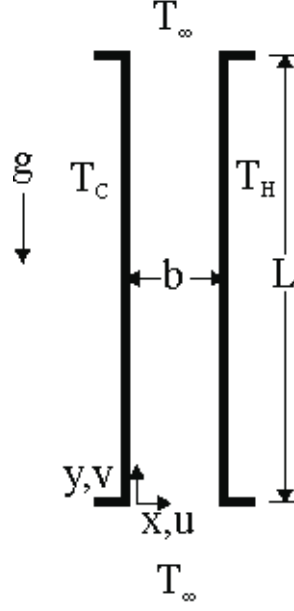
Figure 4.1: Problem geometry and coordinate system.

$$\rho c_p \left(u \frac{\partial T}{\partial x} + v \frac{\partial T}{\partial y} \right) = K \left(\frac{\partial^2 T}{\partial x^2} + \frac{\partial^2 T}{\partial y^2} \right)$$
(4.4)

The fluid properties are assumed to be constant, except for density, which has been treated using the Boussinesq approximation. The Boussinesq approximation is used to include the effects of fluid density variations in the gravitational body force. The Boussinesq approximation only affects the fluid density variations in the gravitational body force term. A pressure defect term is defined between the local pressure and the ambient pressure in the flow field:

$$P_k = P - P_\infty$$
(4.5)

The ambient pressure p_∞ is the hydrostatic pressure measured from some reference point:

$$P_\infty = -\rho_\infty gy + \text{const.}$$
(4.6)

The change in the pressure defect is taken over the x and y directions:

$$\frac{\partial P_k}{\partial x} = \frac{\partial P}{\partial x}$$
(4.7a)

$$\frac{\partial P_k}{\partial y} = \frac{\partial P}{\partial y} + \rho_\infty g \tag{4.7b}$$

The density can be approximated as a linear function of the temperature:

$$\rho = \rho(T) = \rho_\infty + \frac{\partial \rho}{\partial T}(T - T_\infty) \tag{4.8}$$

The volumetric expansion coefficient at constant pressure is:

$$\beta = \frac{1}{V}\frac{\partial V}{\partial T}\bigg|_{P=const.} = \frac{-1}{\rho_\infty}\frac{\partial \rho}{\partial T}\bigg|_{P=const.} \tag{4.9}$$

By combining Equations (4.8) and (4.9), the density defect then becomes:

$$\rho - \rho_\infty = -\rho_\infty \beta(T - T_\infty) \tag{4.10}$$

Equations (4.7a) and (4.10) are substituted back into the x- and y-momentum Equations (4.2) and (4.3):

$$\rho\left(u\frac{\partial u}{\partial x} + v\frac{\partial u}{\partial y}\right) = -\frac{\partial P_k}{\partial x} + \mu\left(\frac{\partial^2 u}{\partial x^2} + \frac{\partial^2 u}{\partial y^2}\right) \tag{4.11}$$

$$\rho\left(u\frac{\partial v}{\partial x} + v\frac{\partial v}{\partial y}\right) = -\frac{\partial P_k}{\partial y} + \mu\left(\frac{\partial^2 v}{\partial x^2} + \frac{\partial^2 v}{\partial y^2}\right) + \rho_\infty \beta(T - T_\infty) \tag{4.12}$$

4.3 Turbulence Model

In order to obtain solutions for the entire Rayleigh number range of interest, a turbulence model was required. For low Rayleigh numbers, steady laminar results were obtained, but the steady laminar model was unable to reach convergence at higher Rayleigh numbers. First an unsteady laminar model was attempted with both fixed and variable time-steps, but the solution was unable to reach convergence over all time-steps. So, it was impossible to obtain a time-averaged Nusselt number from these predictions. Next, a turbulence model was used to obtain results in the higher Rayleigh number range. The standard k-ε model from the commercial CFD code

ANSYS FLUENT (2010) was used in this study. The standard k-ε model uses Reynolds averaging.

In Reynolds averaging, the instantaneous variables are decomposed into the mean and fluctuating components. The velocity, pressure, and temperature become:

$$u = \bar{u} + u', \; v = \bar{v} + v', \; p = \bar{p} + p', \; T = \bar{T} + T' \tag{4.13}$$

The average of these variables is defined as:

$$\bar{u} = \frac{1}{t}\int_0^t u \, dt \tag{4.14}$$

and the average of the fluctuating components are zero:

$$\overline{u'} = \frac{1}{t}\int_0^t u' \, dt = 0 \tag{4.15}$$

Substituting the instantaneous variables into the continuity, x- and y-momentum equations and simplifying gives:

$$\frac{\partial \bar{u}}{\partial x} + \frac{\partial \bar{v}}{\partial y} = 0 \tag{4.16}$$

$$\rho\left(\bar{u}\frac{\partial \bar{u}}{\partial x} + \bar{v}\frac{\partial \bar{u}}{\partial y}\right) = -\frac{\partial \overline{P_k}}{\partial x} + \mu\left(\frac{\partial^2 \bar{u}}{\partial x^2} + \frac{\partial^2 \bar{u}}{\partial y^2}\right) - \rho\left[\frac{\partial}{\partial x}\overline{(u'^2)} + \frac{\partial}{\partial y}\overline{(v'u')}\right] \tag{4.17}$$

$$\rho\left(\bar{u}\frac{\partial \bar{v}}{\partial x} + \bar{v}\frac{\partial \bar{v}}{\partial y}\right) = -\frac{\partial \overline{P_k}}{\partial y} + \mu\left(\frac{\partial^2 \bar{v}}{\partial x^2} + \frac{\partial^2 \bar{v}}{\partial y^2}\right)$$

$$-\rho\left[\frac{\partial}{\partial x}\overline{(u'v')} + \frac{\partial}{\partial y}\overline{(v'^2)}\right] + \rho_\infty \beta\left(\bar{T} - T_\infty\right) \tag{4.18}$$

Equations (4.16) through (4.18) are called the Reynolds averaged Navier-Stokes equations. Again, the flow is assumed to be incompressible, two-dimensional, and steady with constant properties for this solution. As can be seen, there are extra terms compared to the laminar

equations due to the fluctuating velocity components that represent the effects of turbulence. These are called the Reynolds stress terms. Substituting the instantaneous variables into the energy equation and simplifying gives:

$$\rho c_p \left(\overline{u} \frac{\partial \overline{T}}{\partial x} + \overline{v} \frac{\partial \overline{T}}{\partial y} \right) = K \left(\frac{\partial^2 \overline{T}}{\partial x^2} + \frac{\partial^2 \overline{T}}{\partial y^2} \right) - \rho c_p \left[\frac{\partial}{\partial x} \overline{(u'T')} + \frac{\partial}{\partial y} \overline{(v'T')} \right] \tag{4.19}$$

Again, there are extra terms due to the fluctuating velocity and temperature components. In the energy equation, these are the turbulent heat transfer terms.

In order to solve these equations, additional semi-empirical differential equations are used. The standard k-ε turbulence model was used, which is a two equation model. The turbulence kinetic energy k and its dissipation rate ε are obtained from the following two-dimensional transport equations:

$$\rho \left(\overline{u} \frac{\partial k}{\partial x} + \overline{v} \frac{\partial k}{\partial y} \right) = \frac{\partial}{\partial x} \left[\left(\mu + \frac{\mu_T}{\sigma_T} \right) \frac{\partial k}{\partial x} \right] + \frac{\partial}{\partial y} \left[\left(\mu + \frac{\mu_T}{\sigma_T} \right) \frac{\partial k}{\partial y} \right] + G_k + G_b - \rho \varepsilon \tag{4.20}$$

$$\rho \left(\overline{u} \frac{\partial \varepsilon}{\partial x} + \overline{v} \frac{\partial \varepsilon}{\partial y} \right) = \frac{\partial}{\partial x} \left[\left(\mu + \frac{\mu_T}{\sigma_\varepsilon} \right) \frac{\partial \varepsilon}{\partial x} \right] + \frac{\partial}{\partial y} \left[\left(\mu + \frac{\mu_T}{\sigma_\varepsilon} \right) \frac{\partial \varepsilon}{\partial y} \right]$$

$$+ C_{1\varepsilon} \frac{\varepsilon}{k} \left(G_k + C_{3\varepsilon} G_b \right) - C_{2\varepsilon} \rho \frac{\varepsilon^2}{k} \tag{4.21}$$

where G_k is the production of turbulent kinetic energy due to shearing, G_b is the production of turbulent kinetic energy due to buoyancy, μ_T is the turbulent viscosity, σ_T and σ_ε are the turbulent Prandtl numbers for k and ε respectively and $C_{1\varepsilon}$, $C_{2\varepsilon}$ and $C_{3\varepsilon}$ are constants. The turbulent viscosity is defined as:

$$\mu_T = \rho C_\mu \frac{k^2}{\varepsilon} \tag{4.22}$$

where C_μ is a constant.

The production of kinetic energy due to shearing is:

$$G_k = \mu_T \left(\frac{\partial \overline{u}_i}{\partial x_j} + \frac{\partial \overline{u}_j}{\partial x_i} \right) \frac{\partial \overline{u}_i}{\partial x_j} - \frac{2}{3} \rho k \delta_{ij} \frac{\partial \overline{u}_i}{\partial x_j}$$

(4.23)

and the production of turbulent kinetic energy due to buoyancy is:

$$G_b = -g \frac{\mu_T}{\rho \, Pr_T} \frac{\partial \rho}{\partial y}$$

(4.24)

where Pr_T is the turbulent Prandtl number.

The constants used with this model are $C_{1\varepsilon} = 1.44$, $C_{2\varepsilon} = 1.92$, $C_{3\varepsilon} = 0$, $C_\mu = 0.09$, $\sigma_k = 1.0$, $\sigma_\varepsilon = 1.3$, and $Pr_T = 0.85$. The constant $C_{3\varepsilon}$ was set to zero in this model because by default ANSYS FLUENT neglects the effect of buoyancy on the turbulence dissipation rate ε. These constants are the standard values most widely accepted and have been found to work fairly well for a wide range of wall-bounded flows (ANSYS FLUENT Theory Guide 2011 and Versteeg and Malalasekera 1995).

The governing equations can be rewritten in terms of k, ε and the constants:

$$\frac{\partial \overline{u}}{\partial x} + \frac{\partial \overline{v}}{\partial y} = 0$$

(4.25)

$$\rho \left(\overline{u} \frac{\partial \overline{u}}{\partial x} + \overline{v} \frac{\partial \overline{u}}{\partial y} \right) = -\frac{\partial \overline{P}_k}{\partial x} + \frac{\partial}{\partial x} \left[(\mu + \mu_T) \frac{\partial \overline{u}}{\partial x} \right] + \frac{\partial}{\partial y} \left[(\mu + \mu_T) \frac{\partial \overline{u}}{\partial y} \right] - \frac{2}{3} \rho \frac{\partial k}{\partial x}$$

(4.26)

$$\rho \left(\overline{u} \frac{\partial \overline{v}}{\partial x} + \overline{v} \frac{\partial \overline{v}}{\partial y} \right) = -\frac{\partial \overline{P}_k}{\partial y} + \frac{\partial}{\partial x} \left[(\mu + \mu_T) \frac{\partial \overline{v}}{\partial x} \right]$$

$$+ \frac{\partial}{\partial y} \left[(\mu + \mu_T) \frac{\partial \overline{v}}{\partial y} \right] - \frac{2}{3} \rho \frac{\partial k}{\partial y} + \rho_\infty \beta \left(\overline{T} - T_\infty \right)$$

(4.27)

$$\rho c_p \left(\overline{u} \frac{\partial \overline{T}}{\partial x} + \overline{v} \frac{\partial \overline{T}}{\partial y} \right) = \frac{\partial}{\partial x} \left[\left(K + \frac{c_p \mu_T}{Pr_T} \right) \frac{\partial \overline{T}}{\partial x} \right] + \frac{\partial}{\partial y} \left[\left(K + \frac{c_p \mu_T}{Pr_T} \right) \frac{\partial \overline{T}}{\partial y} \right]$$

(4.28)

When using the k-ε turbulence model, wall functions are used to resolve the flow variables close to the walls. This will be discussed in the next section.

4.3.1 Wall Functions

Even when studying turbulence, the velocity is very low close to a solid wall and the flow in this region is essentially laminar. As the distance from the wall increases, the effects of turbulence grow increasingly important and the full turbulent state is eventually reached. This near-wall region can be largely subdivided into three regions. The inner region closest to the wall is the viscous sublayer, where the flow is laminar. The outer layer is the fully-turbulent layer and the region in between is the buffer layer. The dimensionless distance from the wall is defined as:

$$y^+ = \frac{\rho y}{\mu} \sqrt{\frac{\tau_w}{\rho}} \tag{4.29}$$

where y is the distance from the wall and τ_w is the shear stress at the wall. The three layers are then defined as $y^+ < 5$ is the laminar sublayer, $5 < y^+ < 30$ is the buffer layer, and $y^+ > 30$ is the fully turbulent region.

In general, it is impractical to fully resolve the flow patterns in the near-wall regions due to the computational requirements of a finer grid and the inaccuracies of the turbulence models in these regions. Wall functions are used to determine the variables in this near-wall region so that a coarser grid can be used in the domain. The location of the first node from the wall is dependent on which wall functions are to be used. The near wall variations of the solution variables: mean velocity, temperature, k and ε are all calculated with the wall functions. In this study, two different wall functions were used: the standard wall functions (SWF) and the enhanced wall functions (EWF). The details of these two wall functions are in the ANSYS FLUENT Theory Guide (2011).

The standard wall functions are the default wall functions in ANSYS FLUENT and they work reasonably well for a broad range of wall-bounded flows. Generally standard wall functions are applicable for high Reynolds number flows, where there is little to be gained by resolving the viscous sublayer. The first cell from the wall is located in the fully turbulent regime, where

59

$y^+ > 30 - 300$. The standard wall functions use a logarithmic function to determine the velocity from the y^+ value. It was determined that the SWF did not provide reasonable heat transfer results when compared with the experimental data. Therefore, the enhanced wall functions were also used.

The enhanced wall functions were used in the numerical solution because they have been shown to be more accurate when dealing with boundary layer flow over a vertical heated surface (Walsh and Leong 2004). The ANSYS FLUENT User's Guide (2010) also recommends using the enhanced wall functions. The enhanced wall functions were designed to be more universal to the size of the grid, in that they use a blended function to resolve the variables in the near-wall region depending on the location of the first node. This function is based on y^+ and blends a linear equation for the viscous sublayer with a logarithmic equation for the fully turbulent regime. Depending on the y^+ of the first node, the velocity will be determined from this blended function. The EWF are applicable to low Reynolds number flows. It is recommended that the first cell from the wall is located in the viscous sublayer, where $y^+ < 5$. As will be shown in Chapter 5, the enhanced wall functions generally provided reasonable heat transfer predictions when compared with the experimental data.

4.3 Computational Domain and Boundary Conditions

The two-dimensional computational domain is shown in Figure 4.2. The boundary conditions of the computational domain are applied to the solution of the continuity, x- and y-momentum, and energy equations. The boundary conditions are:

$$u = v = 0, T = T_C \qquad \text{for } x = 0, 0 < y < L \qquad \text{(AB)}$$

$$u = v = 0, T = T_H \qquad \text{for } x = b, 0 < y < L \qquad \text{(CD)}$$

$$u = v = 0, \frac{\partial T}{\partial y} = 0 \qquad \text{for } 0 < x < -B + b/2, y = 0 \qquad \text{(HA)}$$

$$u = v = 0, \frac{\partial T}{\partial y} = 0 \qquad \text{for } b < x < B - b/2, y = 0 \qquad \text{(DE)} \qquad \text{(4.30)}$$

$$u = v = 0, \frac{\partial T}{\partial y} = 0 \qquad \text{for } 0 < x < -B + b/2, y = L \qquad \text{(BG)}$$

60

$u = v = 0, \dfrac{\partial T}{\partial y} = 0$ for $b < x < B + b/2, \; y = L$ (CF)

Pressure Outlet   for $-B + b/2 < x < B - b/2, \; 0 < y < -B$ (HE)

Pressure Outlet   for $-B + b/2 < x < B - b/2, \; L < y < L + B$ (GF)

Surfaces AB and CD are the cold wall and hot wall of the channel respectively. They are set to their respective temperatures, with no slip and impermeability. It should be noted that the cold wall temperature is set based on the temperature ratio, R_T. Surfaces HA, DE, BG, and CF are adiabatic walls, with no slip and impermeability. There are two "pre-entry" plenums at either end of the channel as shown in Figure 4.2. A pressure outlet condition has been applied to the semi-circular surfaces HE and GF at the bottom and top of the computational domain. These boundary conditions are used with buoyancy driven flow because the fluid velocities are unknown at the entrances and exits of the computational domain. It should be noted that if the flow reverses direction on a pressure outlet boundary condition, then fluid enters the domain at a specified temperature, the ambient temperature T_∞. This is important for this study because the flow will be moving in both directions inside the channel and the air will need to enter and exit
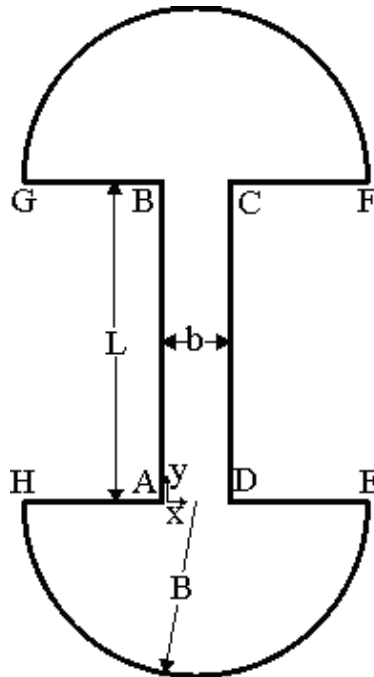
Figure 4.2: Computational domain.

the domain at either end of the channel. On surfaces HE and GF, the fluid enters and exits the channel normal to the boundary, i.e. $u_t = 0$, where u_t is the tangential component of the velocity. The pressure outlet boundary condition uses the specified pressure and extrapolates all other conditions from the interior of the domain. Ideally the pre-entry plenums should be large so that the "pressure outlet" boundary conditions are far enough away from the vertical channel to not affect the flow pattern. But, the plume becomes unstable the further the "pressure outlet" boundary condition is from the top of the channel, so the pre-entry plenum size had to be smaller in order to obtain convergence in the numerical solution.

When the k-ε turbulence model was implemented, the wall functions were used to determine the near-wall boundary conditions. The pressure outlet conditions were the same as above, except that the turbulence kinetic energy and the dissipation rate, k and ε, needed to be defined and were set to 1 m^2/s^2 and 1 m^2/s^3 respectively. These are the default setting as described in the ANSYS FLUENT User's Guide (2010).

The governing equations are solved numerically using the commercial CFD code ANSYS FLUENT (2010). A control-volume formulation with a second-order upwind scheme for evaluation of the convective terms is used in this situation. The PRESTO (Patankar 1980) option was used to discretize the pressure and the SIMPLEC algorithm (Van Doormaal and Raithby 1984) was used for the pressure-velocity coupling. Under-relaxation and incremental loading was required for solutions at higher modified Rayleigh numbers, where the relaxation parameters were between 0.3 and 0.7. The numerical solution was obtained when iterative convergence had been achieved. This occurred when normalized residuals in the continuity, x- and y-momentum equations were reduced to less than 10^{-4} and the normalized residuals in the energy equation were less than 10^{-6}. The normalized residuals in the turbulence kinetic energy and dissipation rate transport equations were also reduced to less than 10^{-4}.

4.5 Grid Sensitivity Study

A sample of the typical structure of the grid used in this study is shown in Figure 4.3. (This is a sample grid of a lower density than was used in this study.) An extensive grid sensitivity study
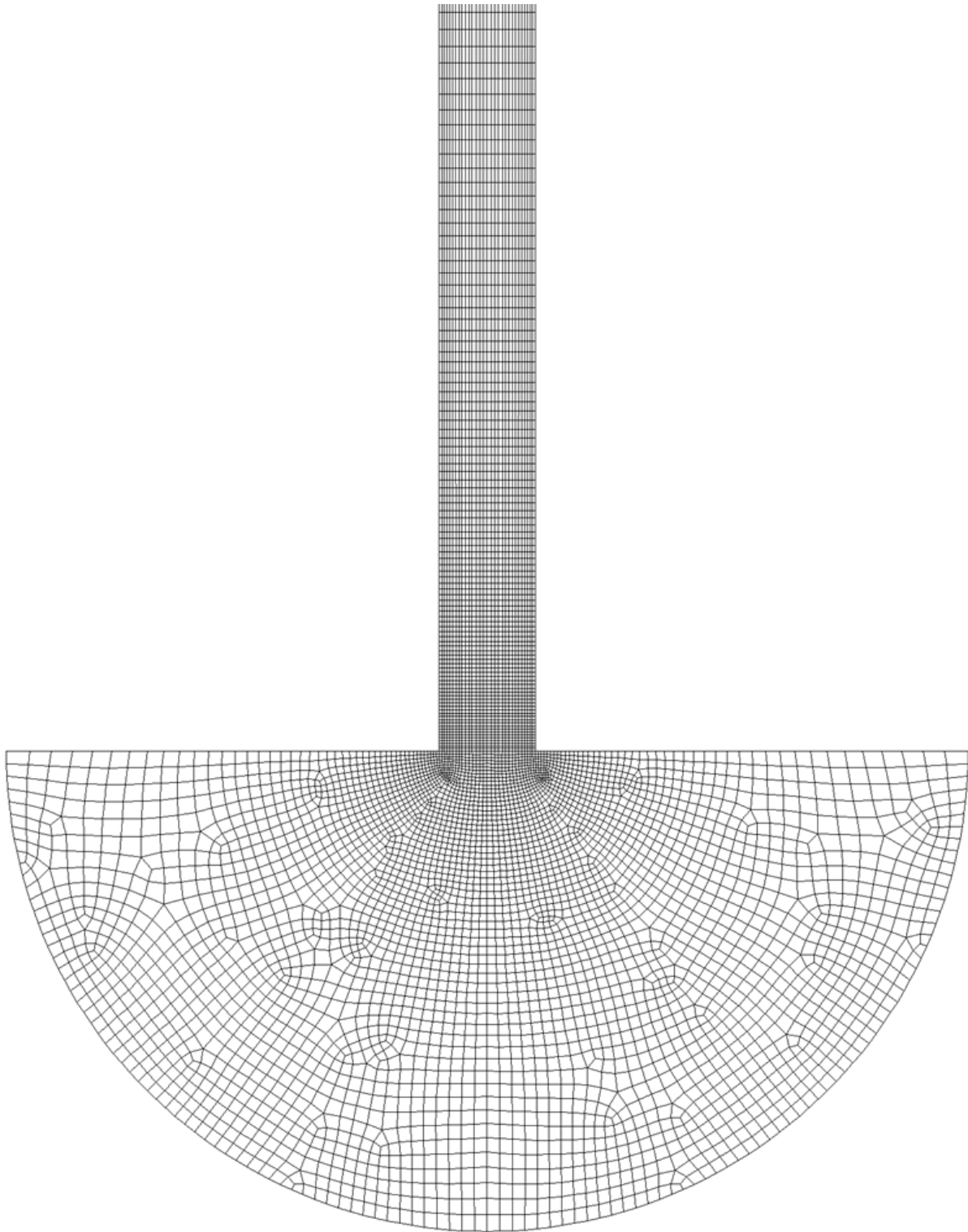
Figure 4.3: Typical structure of the numerical grid (lower portion of the channel and the bottom pre-entry plenum). (Note that this is a lower density grid than was used.)

was conducted to ensure that the numerical solution was grid independent. A non-uniform grid was used, with a higher node density closer to the channel walls and entrance to the channel. Both grid density and far-field boundary conditions were tested.

Table 4.1 shows the grid sensitivity study. The grids were set up with A = 50 and both $R_T = 0$ and $R_T = -0.5$. Three grid sizes of 16670, 30390, and 49390 cells were used to ensure that the solution was grid independent. A grid size of 49390 cells was chosen because for $R_T = 0$, it is 0.02% different from a grid size of 30390 cells and for $R_T = -0.5$, it is 0.08% different from a grid size of 30390 cells. The higher grid size was also chosen because it will give slightly more accurate results and the extra computing power required for the higher grid size is not significant in this study. A Richardson extrapolation (Celik et al. 2008) was performed for both $R_T = 0$ and $R_T = -0.5$. For $R_T = 0$, the numerical uncertainty of the 49390 cell grid is 0.2% and for $R_T = -0.5$, the uncertainty is 0.7%. A detailed calculation of the Richardson extrapolation is in Appendix F.

The far field boundary study is also shown in Table 4.1. Three far field boundary sizes for the entry and exit plenums were studied, B/L = 3, 5 and 10. The same conditions were used as with the grid sensitivity study, where A = 50 and $R_T = 0$ and $R_T = -0.5$. A far field boundary of B/L = 5 was chosen because it is only 0.09% different from B/L = 3 and 0.5% different from B/L = 10 for $R_T = 0$, and 0.06% different from B = 3 and 0.2% different from B/L = 10 for $R_T = -0.5$. Another reason for choosing a pre-entry plenum size of B = 5 is so that the plume exiting the channel does not become unstable due to the plenum size being too large. The numerical grid used in this study has A = 50, 49390 cells, and B/L = 5. This numerical model will be validated in the next section.

4.6 Numerical Validation

Aung (1972) solved analytically fully developed flow solutions for laminar free convection inside an asymmetrically heated vertical channel. This analytical solution presents equations for both the velocity and temperature profiles of the fully developed flow. These equations can be used to validate the numerical model by comparing the velocity and temperature profiles from

Table 4.1: Grid sensitivity and far field boundary study.

Number of Cells	Inlet Boundary Size B/L	Nu ($R_T = 0$)	Nu ($R_T = -0.5$)
16670	5	0.53221	0.22566
30389	5	0.53230	0.22533
49390	5	0.53232	0.22516
49390	3	0.53267	0.22528
49390	10	0.52979	0.22464

the numerical solutions at low Rayleigh numbers. The velocity profile can be determined from Equation (1.14) and the temperature profile can be calculated from Equation (1.15). Figure 4.4 shows the velocity profiles for four different R_T values of $R_T = 0, -0.5, -0.75$, and -1. The Rayleigh number was Ra(b/L) = 0.5 and the location of the velocity profiles was y/L = 0.5. The cold wall is on the left side and the hot wall is on the right side of this graph and the dotted line is zero velocity for reference. The velocity profile data from the numerical solutions is very similar
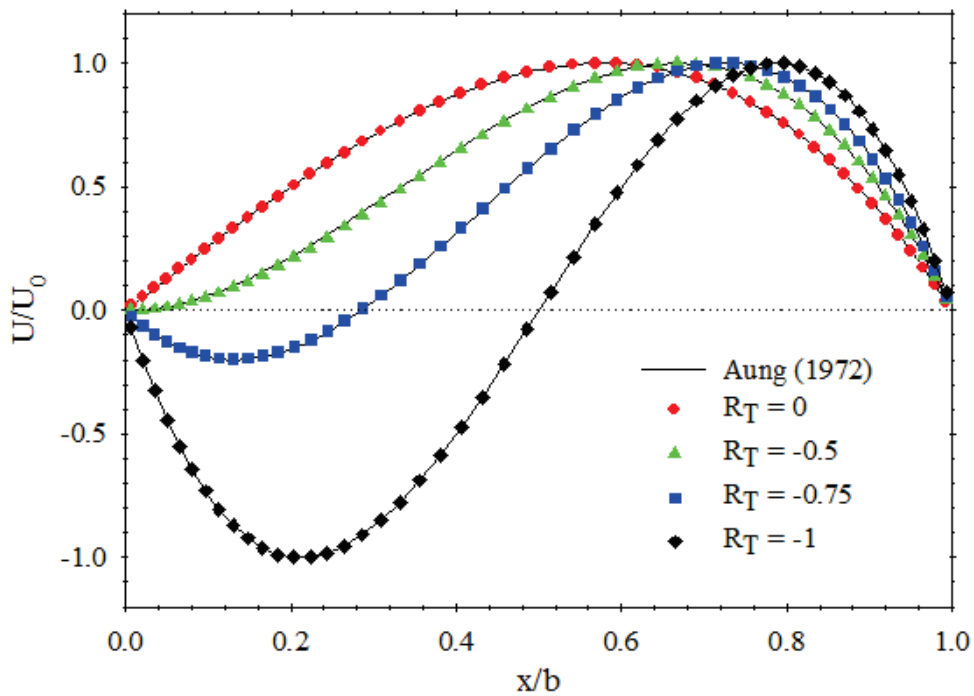
Figure 4.4: Comparison of the velocity profiles at various temperature ratios for fully developed flow at y/L = 0.5 and Ra(b/L) = 0.5 between the numerical results and the correlation by Aung (1972).

to the analytical equation developed by Aung (1972). Using this analytical equation (Equation 1.13) and setting $\dfrac{dV}{dx}$ equal to zero at x = 0, it was determined that reverse flow starts at approximately $R_T = -0.5$ in the fully developed flow regime. At such low Rayleigh numbers, the heat transfers by pure conduction, so the temperature profile is a linear function of distance between the two channel walls. The analytical work was developed for asymmetrically heated vertical channels where both channel walls are heated above the ambient ($0 < R_T < 1$), but these graphs show that the equations can be used for fully developed flows using negative R_T values as well ($-1 < R_T < 0$). Further numerical validation against the current experimental data will be presented in the next chapter.

Chapter 5

Presentation and Discussion of Results

5.1 Introduction

A study of free convection inside an asymmetrically, isothermally heated vertical channel with opposing buoyancy forces was conducted using both flow visualization and interferometry. In free convection, the velocity and temperature field are coupled. So both temperature field and velocity will be investigated experimentally in this study. A preliminary flow visualization investigation was conducted to understand the fluid mechanics better, due to the complex nature of the flow. These results were also needed to plan the interferometry. Some indication of the limits of steady laminar flow was needed for the heat transfer experiments. Composite photographs of smoke seeded inside the channel show streamlines that aid in analyzing the flow. A different experimental model was used for this preliminary study of the flow. A vertical channel of height L = 394 mm was used with two aspect ratios of 39.4 and 19.7. Temperature ratios of R_T = −0.33, −0.67, and −1 were investigated.

The temperature field and heat transfer were determined using a Mach-Zehnder interferometer (MZI). Experiments were conducted on a vertical channel of height L = 264 mm using aspect ratios of 26.4, 17.6, 13.2, and 8.8. Temperature ratios of R_T = 1, 0, − 0.5, −0.75, and −1 were investigated at these different aspect ratios. Infinite fringe interferograms were taken for visualization of the temperature field. The temperature fields are presented as composite interferograms and used in conjunction with the flow field visualization to describe the flow pattern. Finite fringe interferograms were obtained for analysis of the local heat transfer at the various parameters. The local and average Nusselt numbers are presented and compared with numerical solutions. In all the figures that show the vertical channel, the cold wall is on the left side and the hot wall is on the right side.

5.2 Preliminary Flow Visualization Results

A preliminary flow visualization study was conducted using a different experimental model than the one used in interferometry, as discussed in Section 2.4. A few different cases of R_T at different aspect ratios were investigated. Since this was preliminary experimental work to aid in the planning of the interferometric measurements, an exhaustive study was not conducted. The first three cases studied were at an aspect ratio of 39.4 (b = 10 mm) for $R_T = -0.33$, -0.67 and -1. The flow was observed to be steady for all three of these cases. Figures 5.1 and 5.2 show photographs of the flow visualization of two of these cases, $R_T = -0.67$ and -1.

Figure 5.1(a) shows flow visualization for $R_T = -0.67$ with Ra(b/L) = 3.5. A sketch of the flow pattern is shown in Figure 5.1(b). The sketch shows most of the flow coming from the bottom of the channel and leaving the top of the channel on the hot wall side. Some of the air enters at the top of the cold wall and flows to near the bottom of the channel. A separation point is created at y/L = 0.025 where the air flowing down the cold wall changes direction and recirculates with the air flowing up the hot wall inside the channel. This also leaves a node in the center of the channel between the two air flows moving in opposite directions on the hot and cold walls. A node is the zero velocity point in the center of the circulating flow. The flow pattern in this case is similar to what was observed by Sparrow et al. (1984) when studying a vertical channel with the hot wall isothermally heated and the cold wall unheated ($R_T = 0$). They observed that in a channel with an aspect ratio of 15.2 at Ra(b/L) = 5270, some ambient air flowed down about 25% of the cold wall and then recirculated with the air flowing up the hot wall. The reason for backflow in this case was because the fluid adjacent to the hot wall is accelerated by buoyancy forces, which draws the air closer to the hot wall as it flows up the channel. As this happens, the amount of fluid flowing up near the cold wall is depleted and more fluid is needed to fulfill the mass requirements of the fluid near the hot wall. Therefore, fluid is drawn down the cold wall and then recirculates. This partially explains the flow pattern in the negative temperature ratio cases because the hot wall is usually the dominant buoyancy force, which is why the fluid on the cold wall does not completely exit the bottom of the channel. The main reason for fluid flowing down the cold wall in the negative R_T cases is that there is a negative buoyancy force caused by the cold wall. Figure 5.1(c) shows the streamlines from the numerical model. It can be seen that
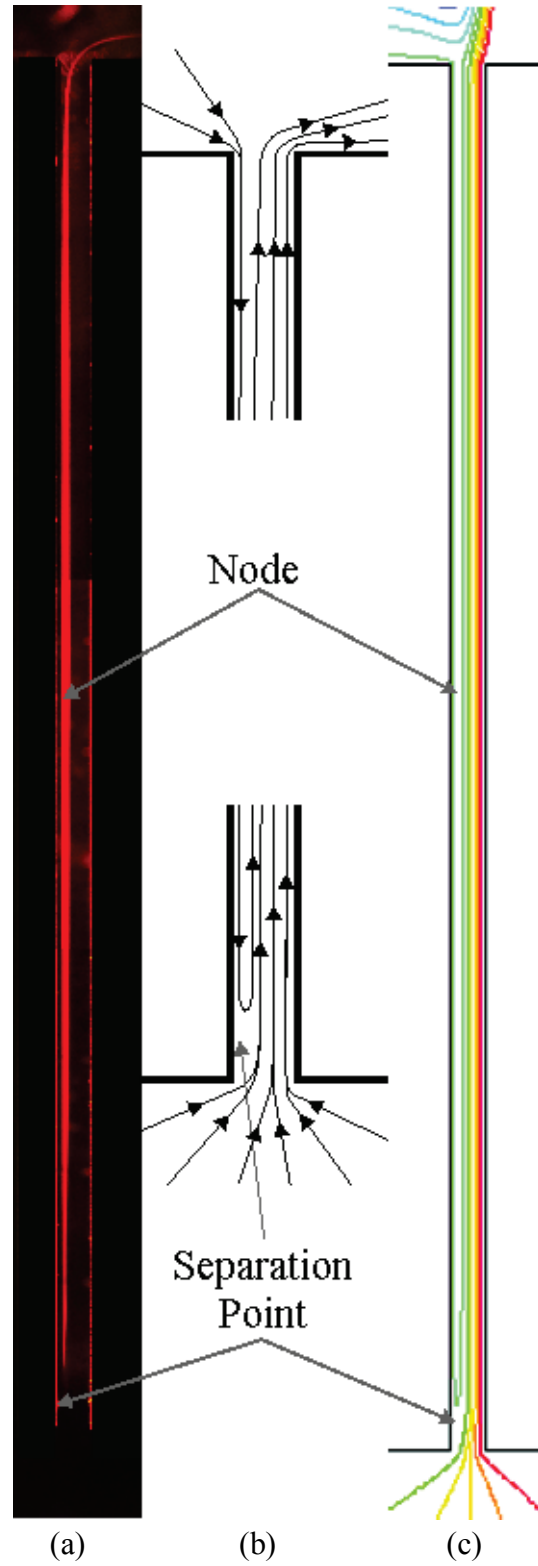
Figure 5.1: (a) Flow visualization, (b) sketch of the flow pattern, and (c) numerical solution streamlines for $R_T = -0.67$, $A = 39.4$, $Ra(b/L) = 3.5$.

the two streamline patterns agree qualitatively, with the separation point and the node located in similar locations.

Another area of interest is at the top of the channel, where the air is exiting the channel. The smoke cell shows that the plume bends abruptly away from the centerline of the channel towards the hot wall side as it exits the channel. This is unexpected because numerical results show the plume exiting straight upwards. This could be due to a few different factors. It could be due to the fact that this experimental model does not have perfectly adiabatic conditions on the horizontal surfaces of the channel walls at the exit of the channel. The numerical solution assumed that these surfaces were perfectly adiabatic. The discrepancy could also be caused by the imperfect nature of the "pressure outlet" boundary conditions applied at the pre-entry plenums in the numerical simulation.

A similar case of $R_T = -0.33$ with $Ra(b/L) = 6.75$ was also studied. A figure is not included of this case, but the flow looked similar to the $R_T = -0.67$ case. Again, most of the air flowed up the hot wall, with some air flowing down the cold wall creating a separation point on the cold wall. The separation point in this case was further up the channel than the $R_T = -0.67$ case at $y/L = 0.25$. Also in this case, the smoke cell was thinner horizontally in the channel than the one shown in Figure 5.1(a) because the hot wall buoyancy force was stronger relative to the cold wall buoyancy force in this case. The plume exiting the top of the channel was also observed to bend away from the centerline of the channel.

The flow visualization of the anti-symmetrical case of $R_T = -1$ and $Ra = 1600$ is shown in Figure 5.2(a). A sketch of the flow is shown in Figure 5.2(b). The flow visualization of this case looks symmetrical, but the air flow near each channel wall is moving in opposite directions. Figure 5.2 does not show the plumes exiting the channel, but it was observed that there was a plume at the top and bottom of the channel. Air enters the bottom of the channel and flows up the hot wall creating a plume out the top of the channel. On the other side of the channel, air enters the top of the channel, flows down the cold wall and creates a plume of air that exits the bottom of the channel. Again, these plumes bend away from the centerline of the channel, unlike the numerical predictions. The plume of air leaving the bottom of the channel bends towards the cold wall and the plume exiting the top of the channel bends towards the hot wall. There is a
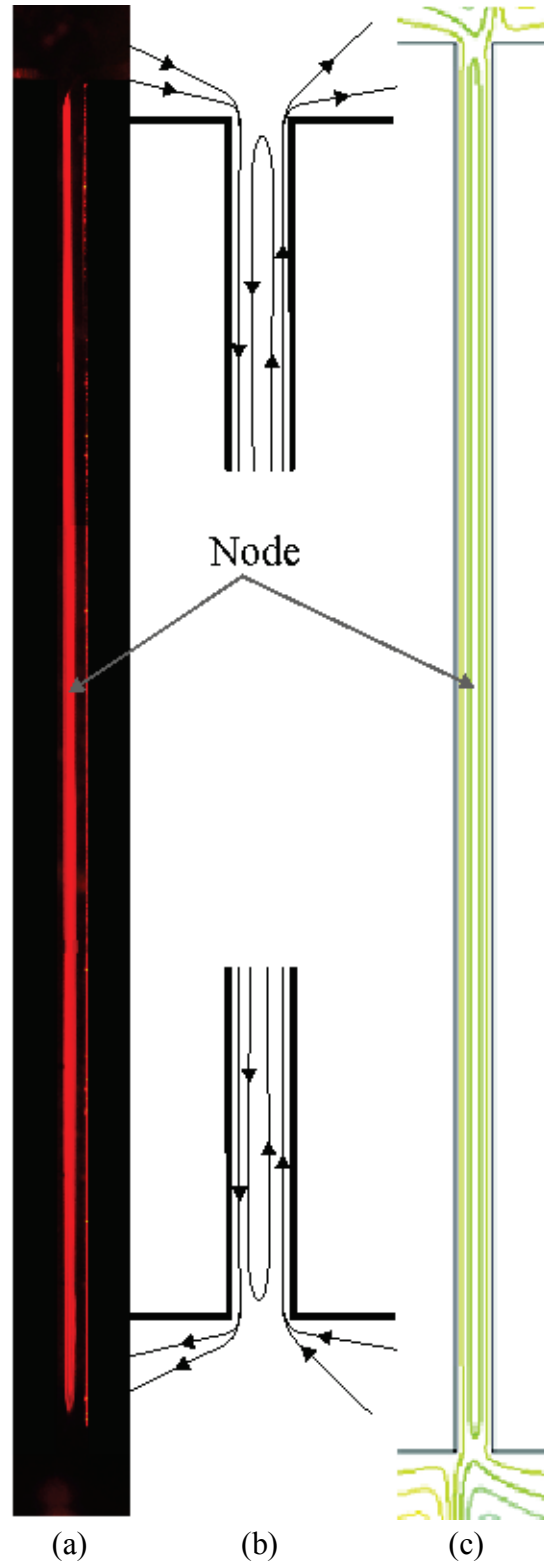
Figure 5.2: (a) Flow visualization, (b) sketch of the flow pattern, and (c) numerical solution streamlines for $R_T = -1$, $A = 37.9$, $Ra = 1600$.

single long cell of re-circulating flow over most of the channel length and a node in the middle of the channel where the smoke can be seen. Again, some of the air reverses direction near the bottom of the channel near the cold wall, but in this case, some air also reverses direction near the top of the channel. The flow pattern of the entire channel in this case is similar to air flow in a tall enclosure (i.e. A > 20) as presented by Wright et al. (2006) and it is consistent with the velocity field observations made by Ayinde et al. (2008). There is a close agreement of the streamlines between the experimental flow visualization and the numerical solution, which is shown in Figure 5.2(c).

The final case investigated with flow visualization was $R_T = -1$ at an aspect ratio of 19.7 and Ra = 13000. This case was observed to be unsteady, so a one-minute video was taken of the flow inside the vertical channel. Eddies were seen moving up and down the channel, with flow moving in a downward direction near the cold wall and in an upwards direction near the hot wall. Again, the flow pattern was observed to be similar to that of a tall enclosure. Similar to the previous case, there are two plumes leaving the channel that bend away from the centerline at the top and bottom of the channel.

5.3 Temperature Field Results

A Mach-Zehnder interferometer was used to obtain temperature field and heat transfer measurements of an isothermally, asymmetrically heated vertical channel. A few different cases of R_T at different aspect ratios were investigated. For each case, two composite interferograms (i.e. total of four images) were obtained, one in infinite fringe mode and the other in finite fringe mode. The finite fringe interferograms were used for analysis to determine the local Nusselt numbers. The infinite fringe interferograms are presented in this section for visualization and discussion purposes. Figure 5.3 shows two composite interferograms at $R_T = 1$ and A = 13.2 illustrating the difference between the infinite fringe and finite fringe modes. Each composite interferogram is divided into two individual images due to the restriction in the size of the optics of the MZI.
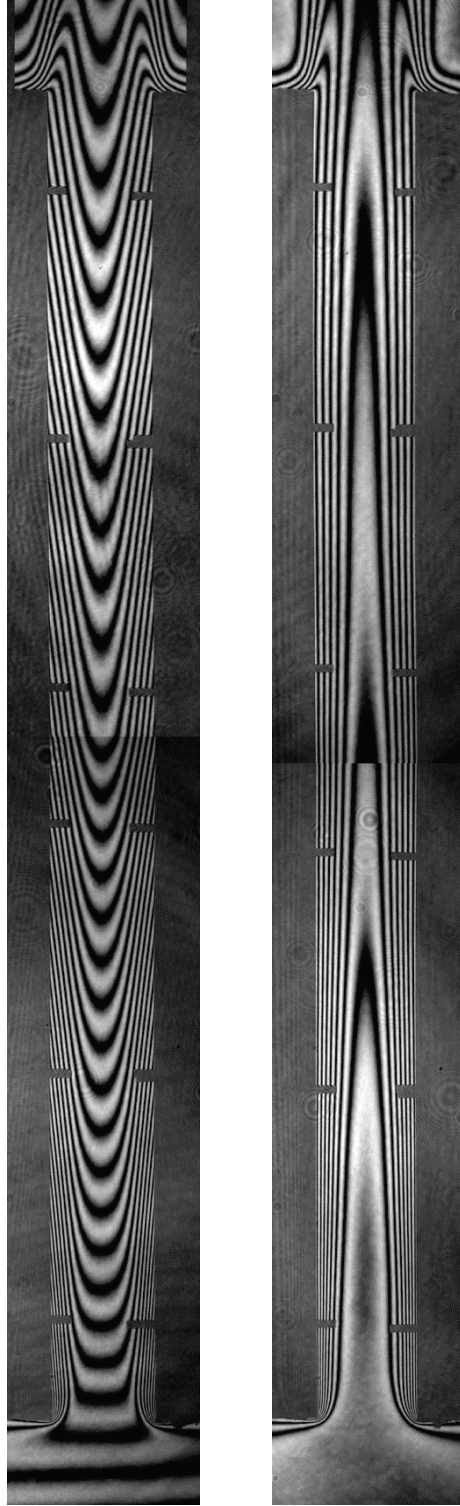
(a) Finite Fringe   (b) Infinite Fringe

Figure 5.3: Composite finite and infinite fringe interferograms at $R_T = 1$ and $A = 13.2$.

Composite infinite fringe interferograms are shown in Figures 5.4, 5.5 and 5.6 for three different aspect ratios and five different temperature ratios. There are also six horizontal pins visible on each channel wall. These small pins were used for model alignment and image locating purposes and have no significant impact on the convection. Temperature ratios of $R_T = 1, 0, -0.5, -0.75$ and -1 and aspect ratios of 26.4, 17.6, and 13.2 are presented in these figures.

Figure 5.4 shows interferograms for an aspect ratio of $A = 26.4$ (b = 10 mm) at the five different temperature ratios and Figure 5.5 shows them for an aspect ratio of 17.6 (b = 15 mm). All of these cases were observed to be steady. Interferograms at an aspect ratio of 13.2 (b = 20 mm) for the five temperature ratios are shown in Figure 5.6. Figures 5.6(a) and (b) were observed to be steady, but Figures 5.6(c), (d), and (e) were observed to be slightly unsteady near the top of the channel in the center region. These three interferograms show that the fringes are wavy in the center region where the unsteadiness was observed.

As was discussed with the flow visualization, the flow recirculates near the bottom of the channel for the negative temperature ratio cases. This flow pattern is evident in the interferograms of the negative R_T cases shown in Figures 5.4, 5.5, and 5.6. The temperature field images show that the isotherms are pulled away from the cold wall near the bottom of the channel, creating a region of low local heat flux. This is where the air flowing down the cold wall separates from the wall and changes direction. In the $R_T = -1$ cases, the same effect is apparent near the top of the channel where the air flowing up the hot wall changes direction to recirculate with the air flowing down the cold wall. This is a similar pattern to those found in interferograms taken by Wright et al. (2006) of a tall enclosure. This effect is stronger as the Rayleigh numbers increase (aspect ratio decreases in the model) and the temperature ratio is decreased.

In the preliminary flow visualization section the behaviour of the plume of warm air exiting the top of the channel was discussed. These figures show that the plume of warm air bends abruptly away from the centerline of the channel when leaving the top of the channel. It can be seen in these interferograms that the horizontal surfaces in the experimental model were not perfectly adiabatic as they were assumed to be in the numerical model. It will be shown later that this effect has a noticeable, but relatively small, impact on the convective heat transfer rates.

(a) $R_T = 1$
Ra(b/L) = 49.3

(b) $R_T = 0$
Ra(b/L) = 24.8

(c) $R_T = -0.5$
Ra(b/L) = 12.3

(d) $R_T = -0.75$
Ra(b/L) = 4.73

(e) $R_T = -1$
Ra(b/L) = 0
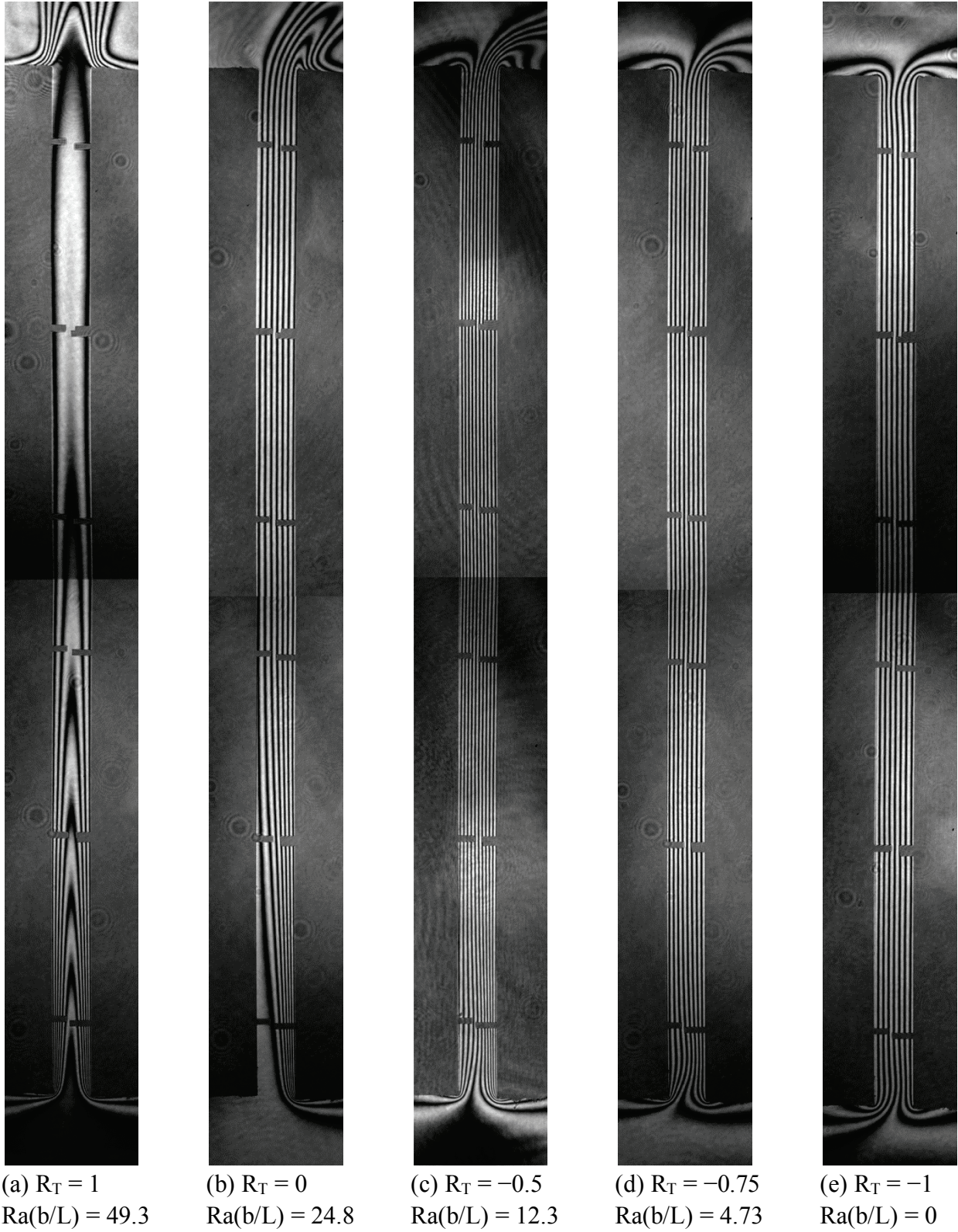
Figure 5.4: Composite interferograms at A = 26.4 for different temperature ratios.

(a) $R_T = 1$
Ra(b/L) = 241

(b) $R_T = 0$
Ra(b/L) = 128

(c) $R_T = -0.5$
Ra(b/L) = 67.0

(d) $R_T = -0.75$
Ra(b/L) = 22.9

(e) $R_T = -1$
Ra(b/L) = 0
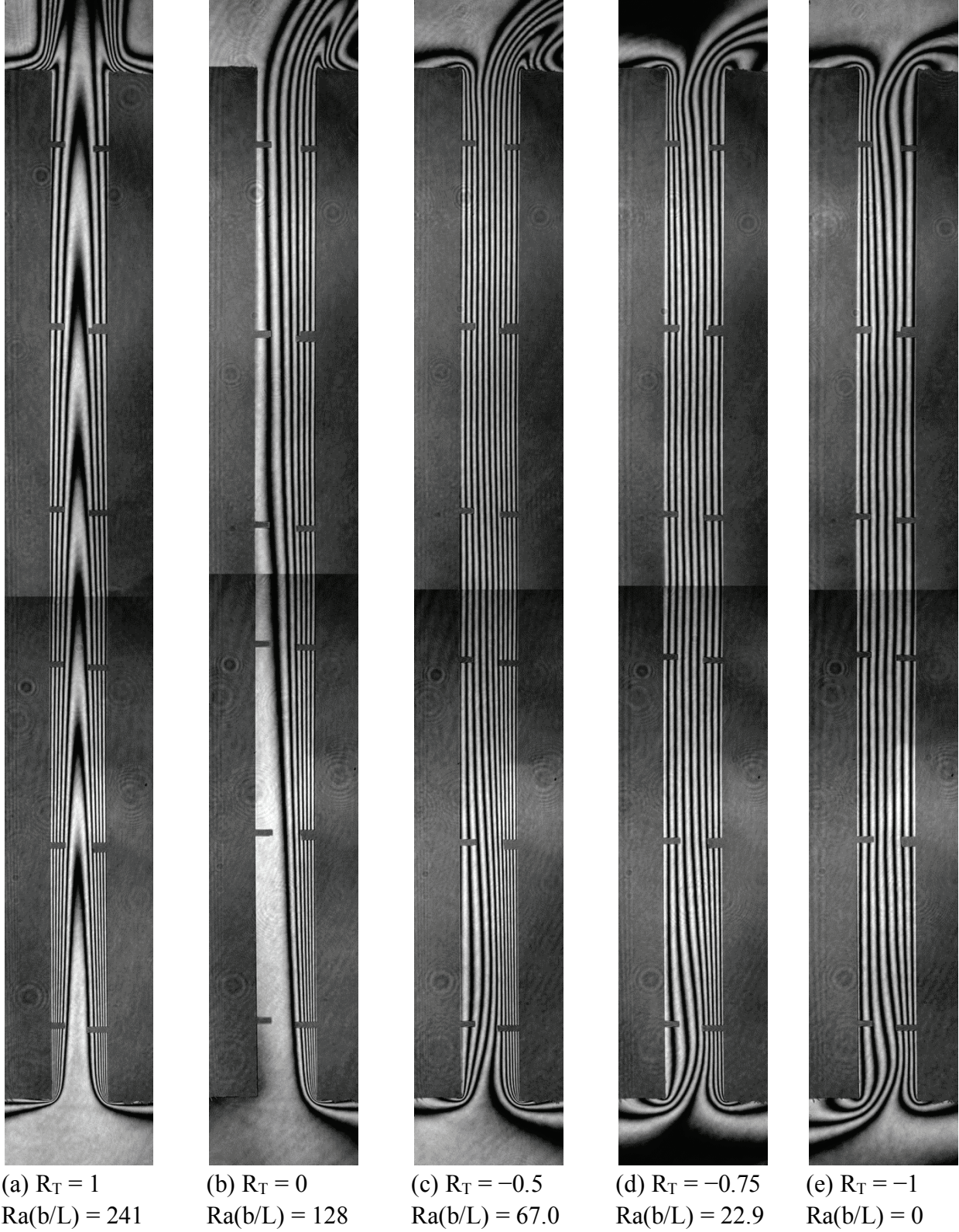
Figure 5.5: Composite interferograms at A = 17.6 for different temperature ratios.

(a) $R_T = 1$
Ra(b/L) = 787

(b) $R_T = 0$
Ra(b/L) = 396

(c) $R_T = -0.5$
Ra(b/L) = 214

(d) $R_T = -0.75$
Ra(b/L) = 75.5

(e) $R_T = -1$
Ra(b/L) = 0
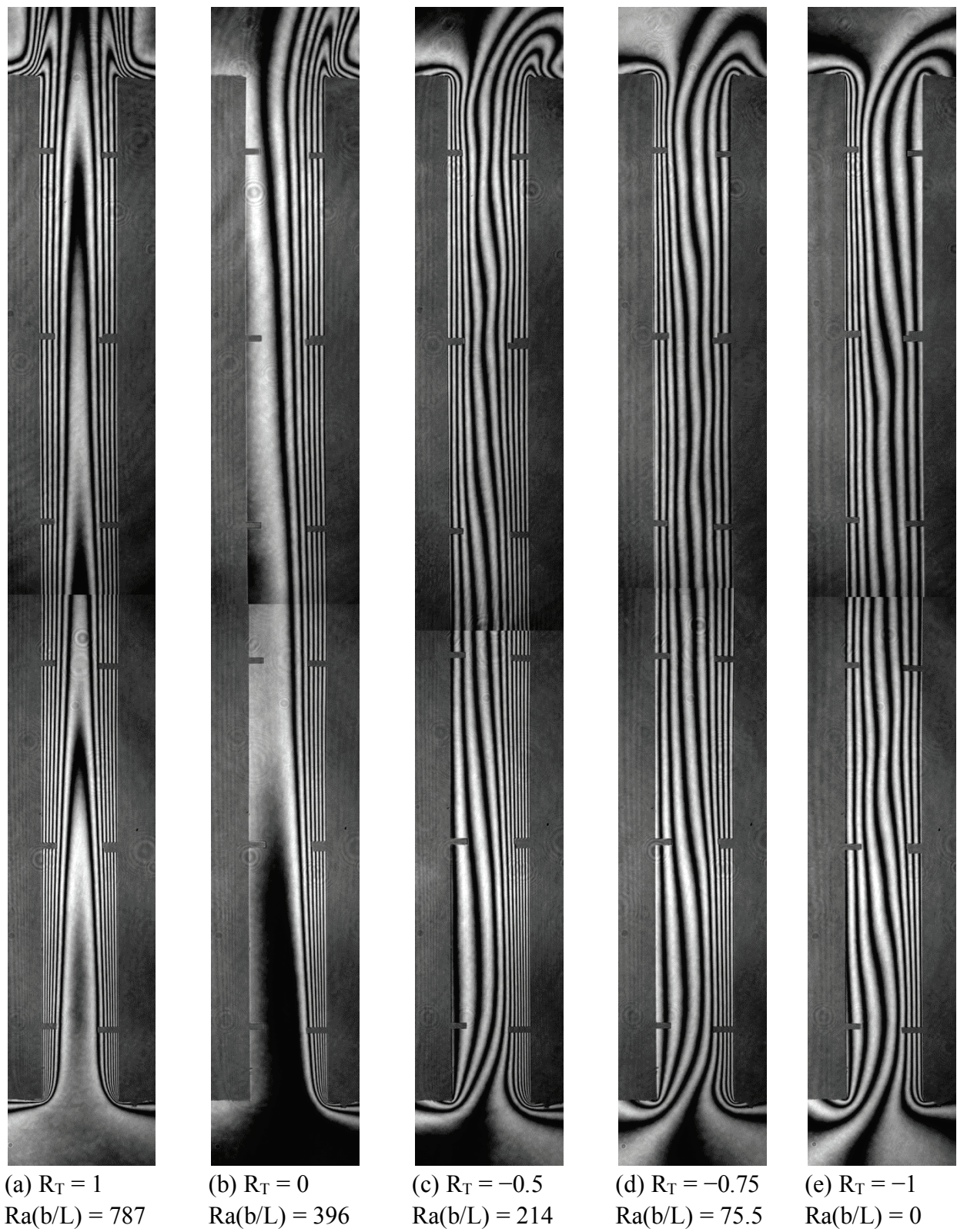
Figure 5.6: Composite interferograms at A = 13.2 for different temperature ratios.

It should be noted that the plume exits the channel straight in the symmetrical cases ($R_T = 1$) as expected from the numerical simulation. This demonstrates that the flow field and temperature field visualization complement each other as together they both fully describe the flow behaviour inside the vertical channel.

The symmetrical heating cases ($R_T = 1$) in Figures 5.4(a), 5.5(a), and 5.6(a), show thermal boundary layers on both channel walls that interact with each other in the center region of the channel. It can be seen that the air enters from the bottom of the channel and exits in a plume from the top of the channel. As the channel spacing is increased, the boundary layers start to merge higher up in the channel. At the highest aspect ratio of 26.4, the isotherms show that there is very low heat flux in the top half of the channel. In this case, the channel Rayleigh number is low and the air in the top section of the channel is almost the same temperature as the channel walls. The lowest aspect ratio of 13.2 shows the boundary layers more clearly as there is less interaction between the two boundary layers as the Rayleigh number increases (aspect ratio decreases in the model).

The $R_T = 0$ cases, shown in Figures 5.4(b), 5.5(b) and 5.6(b) show a boundary layer on the hot wall of the channel. In the highest aspect ratio of 26.4, the boundary layer is apparent in the lower half of the channel and it starts to interact with the cold wall at about a third of the way up the channel. Due to the narrow channel spacing, and corresponding low channel Rayleigh number, the flow appears to be conduction dominated in the top half of the channel. As the channel spacing increases, the boundary layer is seen over the full length of the channel, with less interaction with the cold wall.

Both Figures 5.4 and 5.5 show that as R_T decreases, the boundary layer nature of the flow quickly diminishes and the heat transfer in the center region of the channel becomes increasingly conduction dominated. As the temperature ratio is decreased, the mean buoyancy force becomes zero relative to the ambient, so there is less flow exchanged with the ambient. The flow is more conduction dominated at the higher aspect ratio because of the lower channel Rayleigh number. Also, as the temperature ratio is decreased to $R_T = -1$, less air flows out the top of the channel, but more air flows out the bottom of the channel. The negative R_T cases shown in Figure 5.6 show that as the channel spacing is increased (i.e. Rayleigh number is increased), the flow looks more like boundary layers than conduction.

78

The temperature fields of the anti-symmetrical cases are diagonally symmetric, with the top half of the channel being almost a mirror image of the bottom half of the channel. This looks similar to a temperature field of a tall enclosure (Wright et al. 2006). At $R_T = -1$, except in the widest channel spacing (A = 13.2), the isotherms are uniformly spaced over most of the channel length, i.e. conduction dominated. This might be expected, since the average temperature of the fluid in the channel is equal to the ambient temperature for this condition. As discussed previously, flow visualization showed that for the anti-symmetrical case ($R_T = -1$), there is a single recirculating cell in the channel and only a slight exchange of air with the ambient at the top and bottom of the channel. The temperature difference between the hot wall and ambient is the same as between the ambient and the cold wall (i.e. $T_H - T_\infty = T_\infty - T_C$). Due to these temperature differences being equal, $\overline{\Delta T} = 0$. This causes Ra(b/L) = 0 for all cases of $R_T = -1$, so the non-modified Rayleigh number Ra is used for these cases. Since in the anti-symmetrical case, the net buoyancy force is zero, (i.e $q_H = -q_C$), then Nu = 0 for all cases of Ra. Therefore, the hot wall average Nusselt number Nu_H is reported for the anti-symmetrical ($R_T = -1$) cases.

5.4 Local Convective Heat Transfer Results

The finite fringe interferograms were used for analysis to determine the convective heat transfer rates using the procedure outlined in Sections 3.3. Finite fringe mode was used because it is less sensitive to vibrations and is easier to setup than the infinite fringe mode. Each case consisted of two images to show the entire channel and each image was scanned in 50 locations along each channel wall. Therefore, the local heat transfer data was obtained for approximately 100 locations on each channel wall. The numerical model was solved for each case in order to make comparisons with the experimental data.

Figure 5.7 shows the local Nusselt number distributions for symmetrical heating ($R_T = 1$) of a vertical channel with an aspect ratio of 17.6. This case corresponds to the interferogram in Figure 5.5(a). As expected in the symmetrical heating case, both channel walls have the same local heat transfer data because both walls are at the same temperature. The numerical solution is added to this graph for comparison. The experimental data is slightly below the numerical

Figure 5.7: Graph of local Nusselt number variation versus distance for $R_T = 1$, $A = 17.6$ and $Ra(b/L) = 241$. Experimental: $Nu_H = 2.15$, $Nu_C = 2.17$, CFD: $Nu_H = 2.24$, $Nu_C = 2.24$.

data at the bottom of the channel and this is most likely due to the air being pre-heated before entering the channel, causing the local heat transfer rate to be lower. It can be seen in the interferograms that the horizontal surfaces at the bottom of the experimental model were not perfectly adiabatic as they were assumed to be in the numerical model. The isotherms are not perpendicular to these horizontal surfaces indicating that the air is being pre-heated. Overall the numerical solution shows good agreement with the experimental data.

Symmetrical heating in a vertical channel has been studied in the literature. So, the overall channel average Nusselt number has been compared with a few correlations from the literature. Two different aspect ratios were studied experimentally and are compared in Table 5.1. For symmetrical heating, the experimental data fits best with the correlation by Elenbaas (1942). The overall channel average Nusselt numbers were also determined from the numerical results and they are within 4% of the experimental data.

Table 5.1: Comparison of experimental data, various correlations from the literature, and the numerical solution of the overall channel average Nusselt numbers for symmetrical heating ($R_T = 1$) at two aspect ratios.

	Rayleigh Number	Experimental Data	Raithby and Hollands (1998)		Elenbaas (1942)		Bar-Cohen and Rohsenow (1984)		Numerical Solution	
Aspect Ratio	Ra(b/L)	Nu	Nu	Error	Nu	Error	Nu	Error	Nu	Error
17.6	241	2.16	2.35	8.8%	2.24	3.7%	2.27	5.1%	2.24	3.7%
13.2	787	3.04	3.25	6.9%	3.12	2.6%	3.12	2.6%	3.11	2.3%

The local Nusselt number distribution for $R_T = 0$ at A = 17.6 is shown in Figure 5.8, which corresponds to the interferogram in Figure 5.5(b). The numerical results compare favorably with the experimental data except for some slight error on the bottom of the hot wall due to pre-heating of the air. It should be noted that due to the low heat transfer on the cold wall in the lower portion of the channel in this case (as seen in the interferogram), it was difficult for the image processing code to determine the fringe gradient; therefore the finite fringes were measured manually in this region. Figure 5.8 shows that the lower 40% of the cold wall was measured manually, as can be seen by the greater spacing between data points. Table 5.2 shows a comparison of the overall channel average Nusselt numbers of the $R_T = 0$ case for two different aspect ratios. The numerically predicted overall channel average Nusselt numbers are within 4% and the correlation is within 4% of the experimental data.

The interferogram and the numerical solution isotherms for $R_T = 0$ at A = 17.6 are compared in Figure 5.9. Figure 5.9(b) shows the steady laminar numerical solution as outlined in Chapter 4 using the adiabatic boundary conditions on the horizontal surfaces. The top of the channel shows that the plume exits the channel fairly straight vertically in the numerical prediction. Comparing the isotherms shows that the temperature fields are very close between the numerical prediction and the experimental data. The interferogram shows that the horizontal surfaces at the entrance and exit region of the channel are not perfectly adiabatic, as they were assumed to be in the numerical model. Therefore, another numerical solution was obtained for this case using a

Figure 5.8: Graph of local Nusselt number variation versus distance for $R_T = 0$, $A = 17.6$ and $Ra(b/L) = 128$. Experimental: $Nu_H = 4.46$, $Nu_C = -0.605$, CFD: $Nu_H = 4.63$, $Nu_C = -0.648$.

non-adiabatic boundary condition on these surfaces. A variable temperature was applied to the horizontal surfaces based on the temperature field data in the interferogram to better match the experiment. Figure 5.9(c) shows that the plume still exits the channel straight vertically when using non-adiabatic boundary conditions. This suggests that the "pressure outlet" boundary conditions applied to the pre-entry plenums are imperfect. The heat fluxes were also compared between the non-adiabatic boundary conditions and the experimental data. The local heat

Table 5.2: Comparison of experimental data, various correlations from the literature, and the numerical solution of the overall channel average Nusselt numbers for $R_T = 0$ at two aspect ratios.

	Rayleigh Number	Experimental Data	Raithby and Hollands (1998)		Numerical Solution	
Aspect Ratio	Ra(b/L)	Nu	Nu	Error	Nu	Error
26.4	24.8	0.818	0.846	3.4%	0.788	−3.7%
17.6	128	1.93	1.93	0%	1.99	3.1%

(a)   (b)   (c)
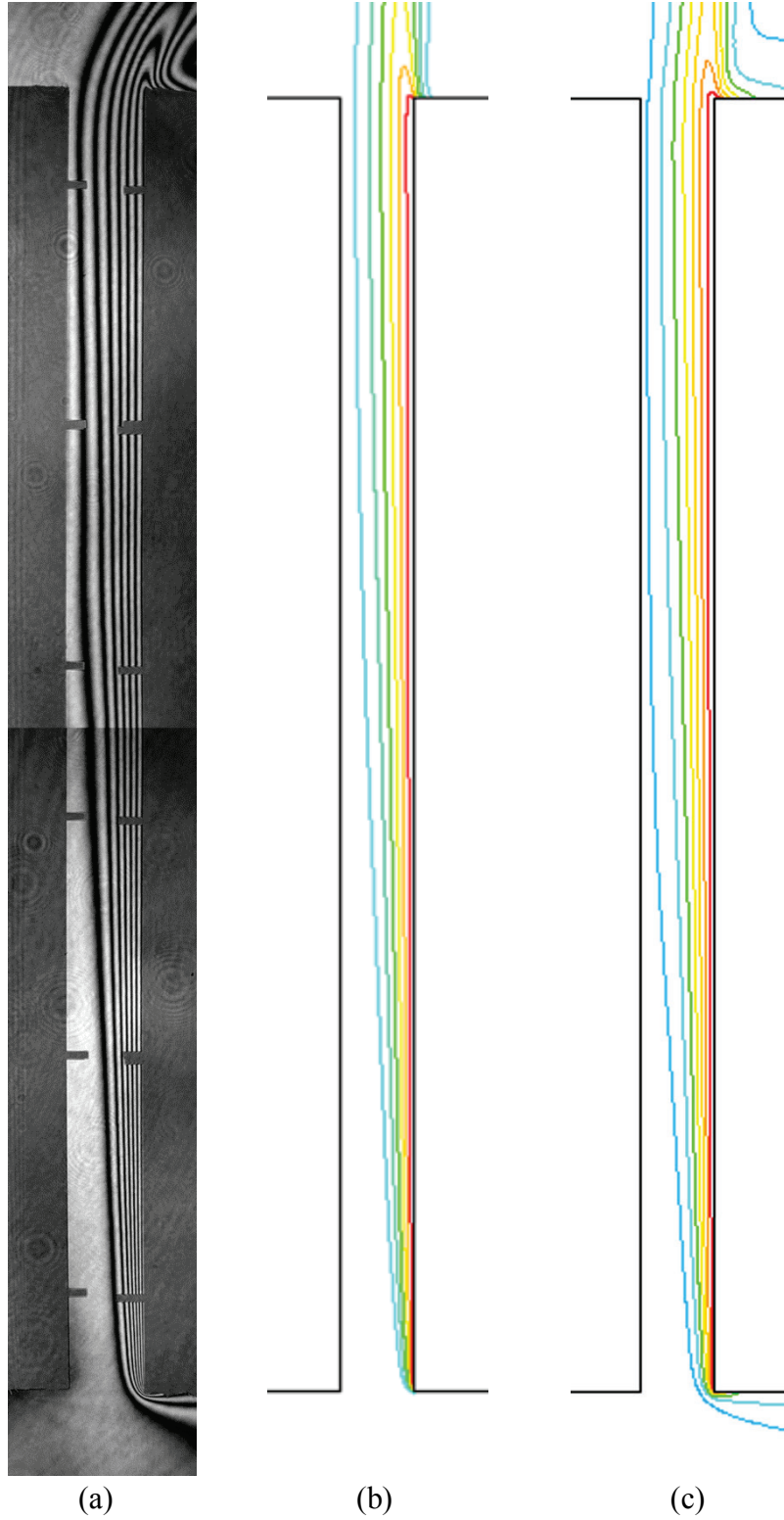
Figure 5.9 Isotherm comparison for $R_T = 0$, $A = 17.6$, and $Ra(b/L) = 128$: (a) experimental, (b) steady laminar numerical model with adiabatic boundary conditions and (c) non-adiabatic boundary conditions.

transfer rate showed better agreement at the bottom of the channel where the pre-heated air enters the channel. The improvement in the heat transfer rate was fairly minor (about 1%), so using the adiabatic boundary condition as an approximation on the horizontal surfaces was sufficient for the numerical model.

Figure 5.10 shows the local Nusselt number distribution for $R_T = -0.5$ at $A = 26.4$, which corresponds to the interferogram in Figure 5.4(c). The numerical prediction is also added to this graph for comparison, which generally shows good agreement. There is a slight over-prediction of the numerical solution at the bottom of the channel on the hot wall. Again, this is most likely due to the air being pre-heated before entering the channel in the experimental model, where the numerical model assumes this is perfectly adiabatic. One-dimensional pure conduction between the walls was also added to the graph for comparison and it can be seen that the heat transfer is conduction dominated in the upper 75% of the channel. A comparison of the isotherms between the interferogram and the numerical predictions are shown in Figure 5.11. The temperature

Figure 5.10: Graph of local Nusselt number variation versus distance for $R_T = -0.5$, $A = 26.4$ and $Ra(b/L) = 12.3$. Experimental: $Nu_H = 6.81$, $Nu_C = -5.46$, CFD: $Nu_H = 7.25$, $Nu_C = -5.86$.

(a)   (b)
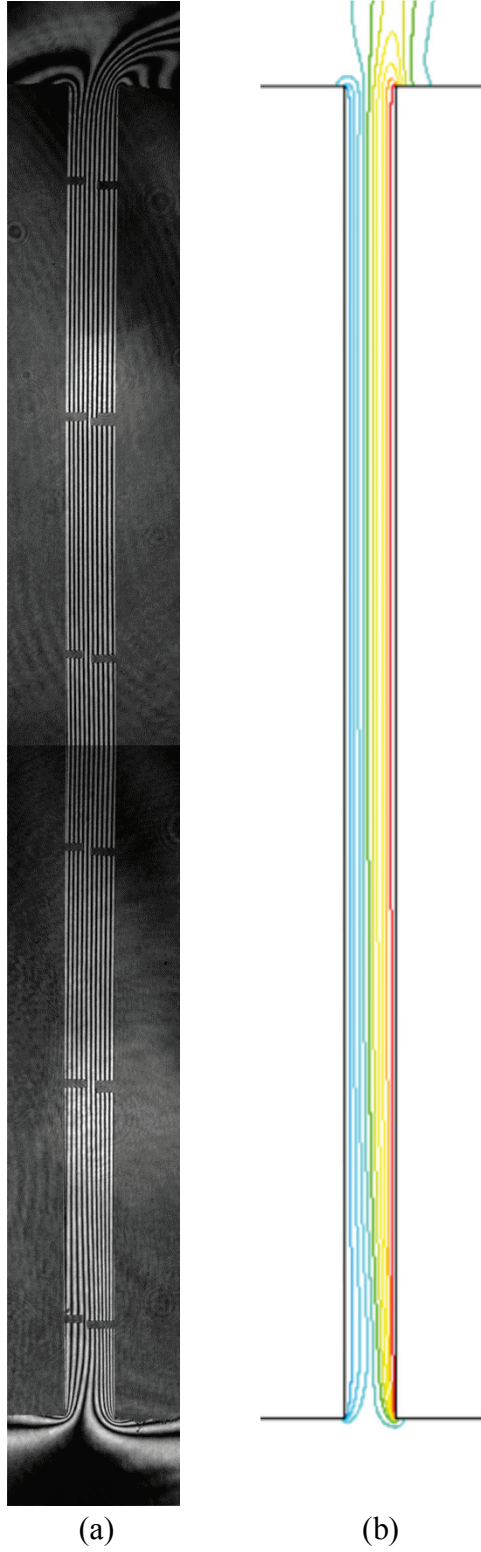
Figure 5.11: (a) Experimental and (b) numerical isotherm comparison for $R_T = -0.5$, $A = 26.4$ and $Ra(b/L) = 12.3$.

fields are very close, but there are some discrepancies between the experiment and numerical solutions. The horizontal surfaces are adiabatic in the numerical model, which are not in the interferograms and they cause the isotherms to be slightly different in the entry and exit regions of the channel. Also, the plume at the top of the channel exits straight vertically in the numerical prediction and bends towards the hot wall in the interferogram. Similar local Nusselt number graphs for $R_T = -0.75$ and $R_T = -1$ for the same aspect ratio are shown in Appendix G.1. These graphs are similar to the one in Figure 5.10, in that most of the channel is conduction dominated.

The local Nusselt number distribution for $R_T = -0.5$ at $A = 17.6$ is shown in Figure 5.12. The interferogram of this case is shown in Figure 5.5(c). This graph shows that the heat transfer is not conduction dominated in this case. Figure 5.13 shows the local Nusselt number distribution for $R_T = -0.75$ at the same aspect ratio, with the corresponding interferogram in Figure 5.5(d). This graph shows that heat tra7nsfer is conduction dominated for approximately 40% of the channel. Finally, the $R_T = -1$ case is shown in Figure 5.14 for the same aspect ratio, with the interferogram shown in Figure 5.5(e). This case shows that the heat transfer is pure conduction
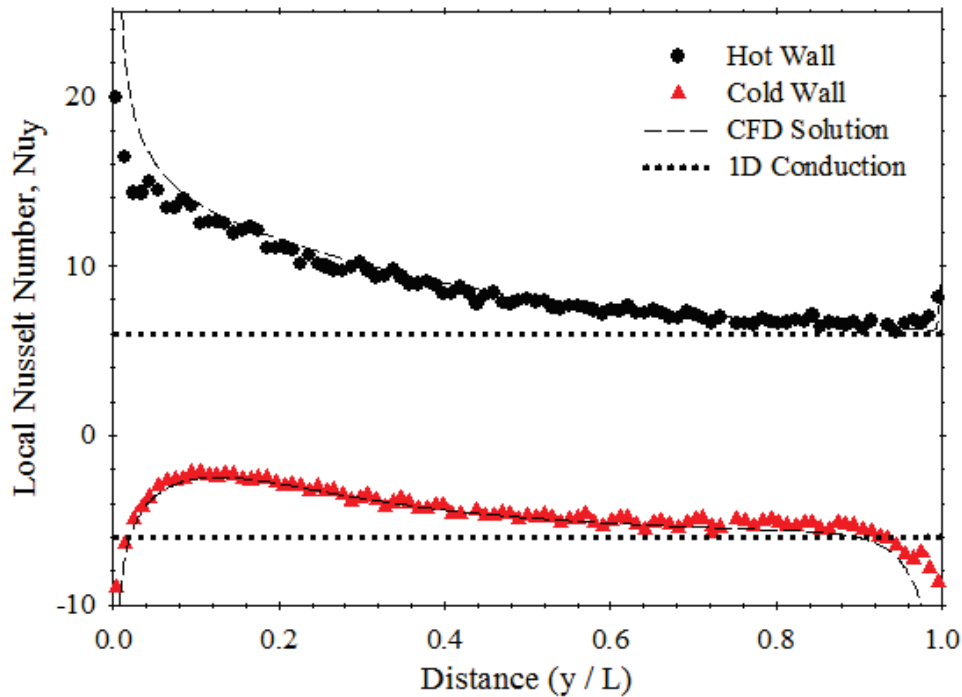
Figure 5.12: Graph of local Nusselt number variation versus distance for $R_T = -0.5$, $A = 17.6$ and $Ra(b/L) = 66.6$. Experimental: $Nu_H = 8.95$, $Nu_C = -4.57$, CFD: $Nu_H = 9.56$, $Nu_C = -5.02$.
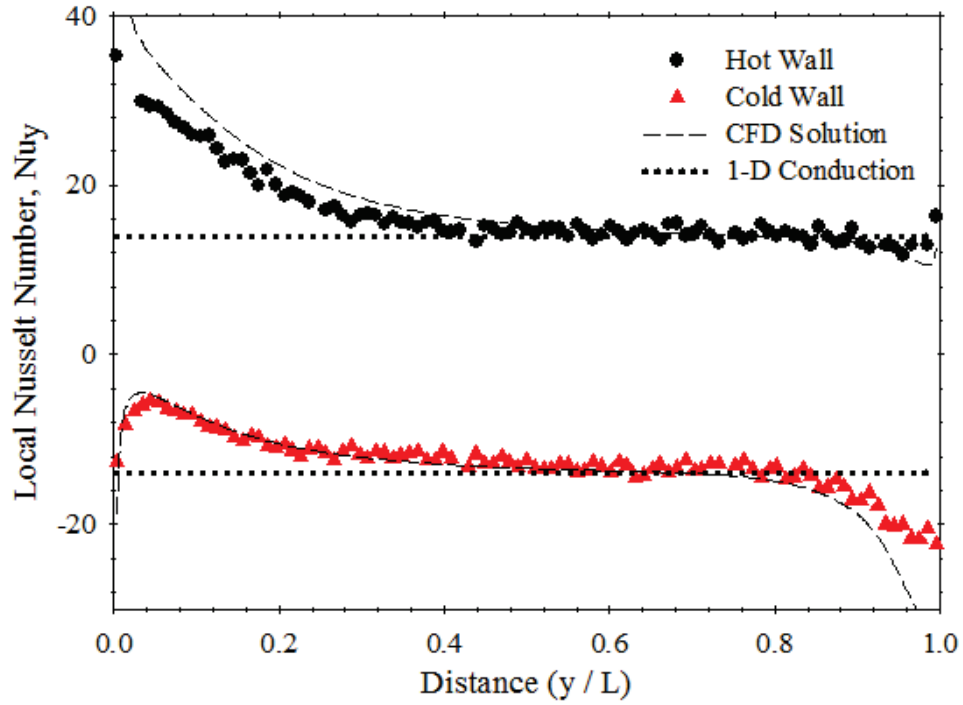
Figure 5.13: Graph of local Nusselt number variation versus distance for $R_T = -0.75$, $A = 17.6$ and $Ra(b/L) = 22.9$. Experimental: $Nu_H = 17.1$, $Nu_C = -12.7$, CFD: $Nu_H = 18.6$, $Nu_C = -14.1$.
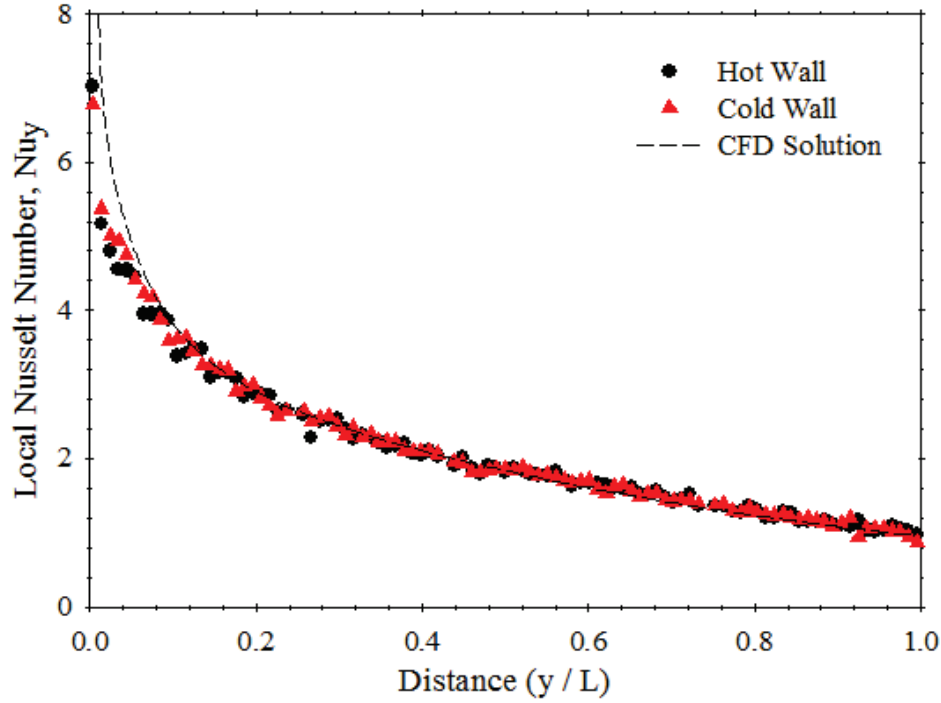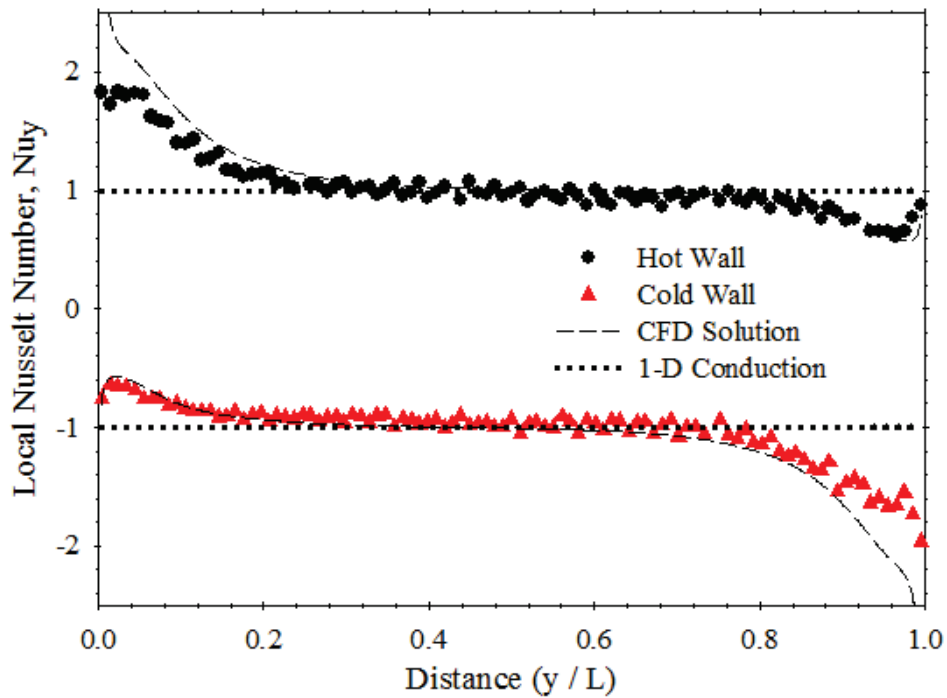

Figure 5.14: Graph of local Nusselt number variation versus distance for $R_T = -1$, $A = 17.6$ and $Ra = 4788$. Experimental: $Nu_H = 1.04$, $Nu_C = -1.03$, CFD: $Nu_H = 1.11$, $Nu_C = -1.11$.

for almost 60% of the channel. These three graphs show that as the temperature ratio is decreased, the heat transfer becomes increasingly conduction dominated for the same aspect ratio. All three graphs show that the numerical solution and the experimental data were in agreement, except for some pre-heating of the air at the bottom of the hot wall. In Figures 5.13 and 5.14, there is also some similar error on the top of the cold wall that could be due to some pre-cooling of the air before it enters the top of the channel or due to the plume bending as discussed in the previous section. Figure 5.15 shows a comparison of the isotherms between the numerical solution and the interferogram for $R_T = -1$ at A = 17.6. Overall, the temperature fields compare favorably. This figure shows that plumes exit both the top and bottom of the channel, with the top plume bending towards the hot wall and bottom plume bending towards the cold wall. In the numerical solution, both plumes exit straight vertically. Also, there are some discrepancies on the horizontal surfaces due to the adiabatic boundary conditions on these surfaces in the numerical model.

The next aspect ratio of 13.2 shows some interesting heat transfer results. Figure 5.16 shows the $R_T = -0.5$ case, with the interferogram in Figure 5.6(c). The graph has the numerical prediction added, which generally shows good agreement. It should be noted that for this case, a steady laminar model was solved for the numerical results. Again, there is some slight error at the bottom of the hot wall due to the pre-heating of the air, but the top of the channel shows another area of interest. Both the hot wall and cold wall show some disagreement with the numerical solution. As previously discussed, this is most likely due to the plume bending to the hot wall side of the channel when it exits the top of the channel. This draws air towards the hot wall as it leaves the top of the channel, increasing the heat transfer. Figure 5.17 shows a comparison of the temperature fields of the numerical model and the experimental interferogram. The streamlines from the numerical model are also shown in Figure 5.17(c). The plume in the numerical solution exits the channel straighter, leaning slightly towards the cold wall and is much larger than in the interferogram. This shows that the air entering the top of the channel is forced closer to the cold wall, which explains why the heat transfer is much lower on the cold wall in this region with the numerical prediction. This comparison also shows that for the majority of the channel, the isotherms are very similar between the interferogram and numerical prediction. The flow is

(a)   (b)
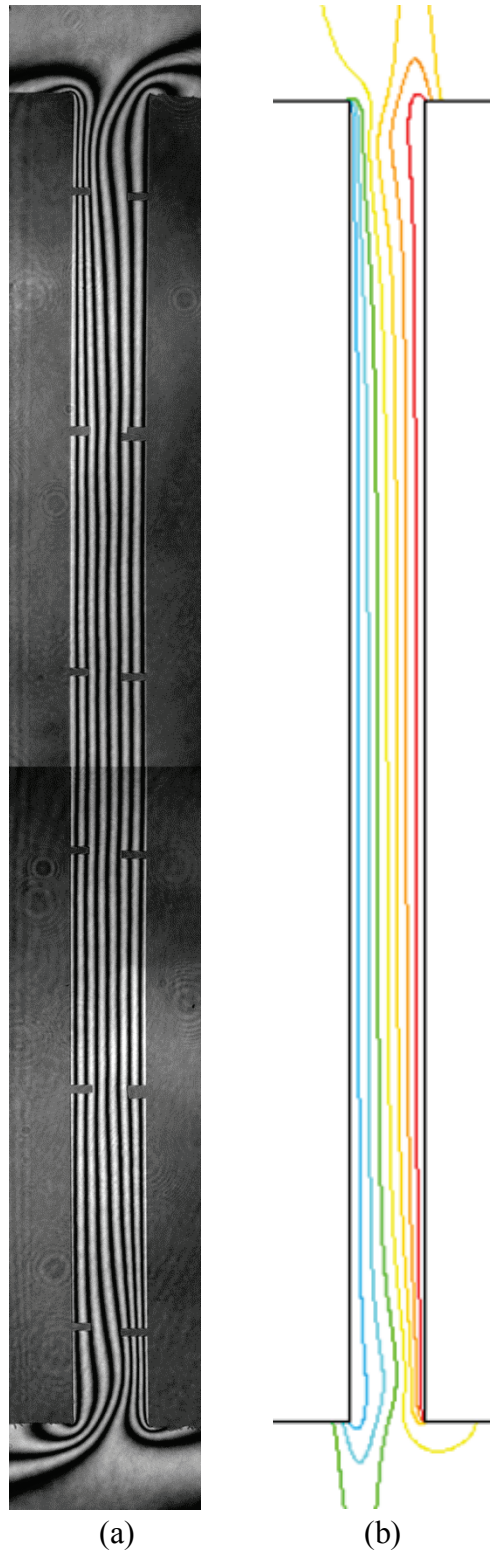
Figure 5.15: (a) Experimental and (b) numerical isotherm comparison for $R_T = -1$, $A = 13.2$ and $Ra = 4786$.
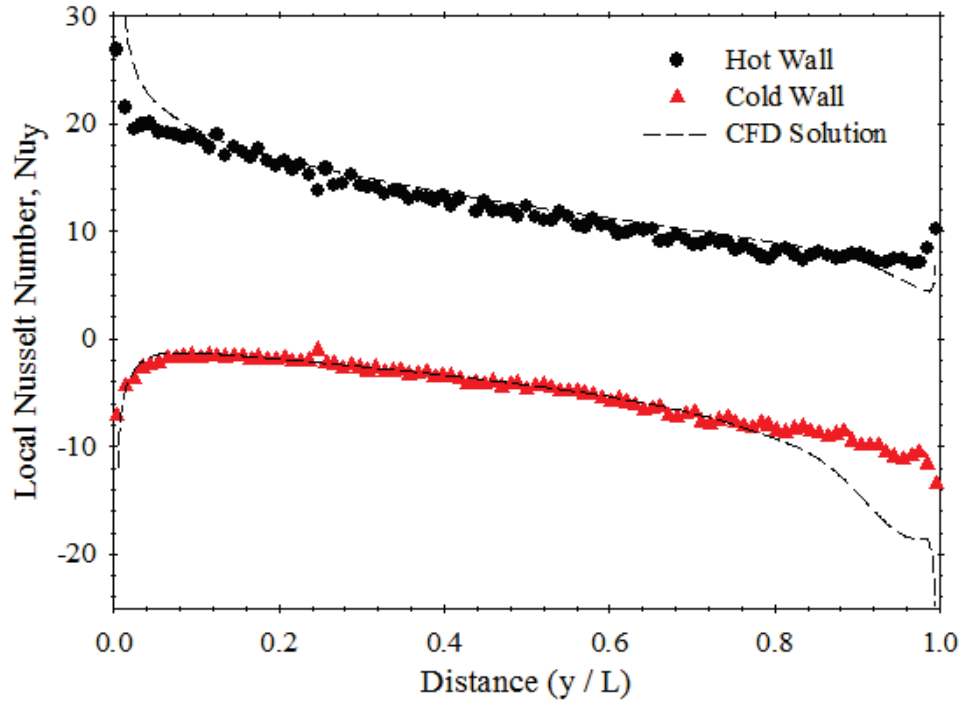
Figure 5.16: Graph of local Nusselt number variation versus distance for $R_T = -0.5$, $A = 13.2$ and
Ra(b/L) = 214. Experimental: $Nu_H = 12.3$, $Nu_C = -5.28$, CFD: $Nu_H = 13.3$, $Nu_C = -6.23$.

slightly different in the upper region of the channel, where the streamlines show a single eddy in the numerical solution, but the experiment was observed to be slightly unsteady. Even though the experiments were observed to be slightly unsteady, a steady analysis was used to obtain the convective heat transfer rates for this case. As discussed in Section 4.3, convergence problems were encountered in the unsteady laminar solutions.

The $R_T = -0.75$ case is shown in Figure 5.18, which corresponds to the interferogram in Figure 5.6(d). This case is similar to the previous one of $R_T = -0.5$. In this graph, two numerical results were added for comparison because this case was observed to be slightly unsteady when taking the interferograms. A steady laminar model and a steady k-ε turbulence model using the enhanced wall functions were both used to obtain the numerical predictions. Both of these numerical results are similar, but the turbulent solution gives better agreement for this case. The laminar results show that there are stable eddies inside the channel because the heat flux is not a straight curve like the experimental data. This suggests that the laminar prediction is not real for

(a)   (b)   (c)
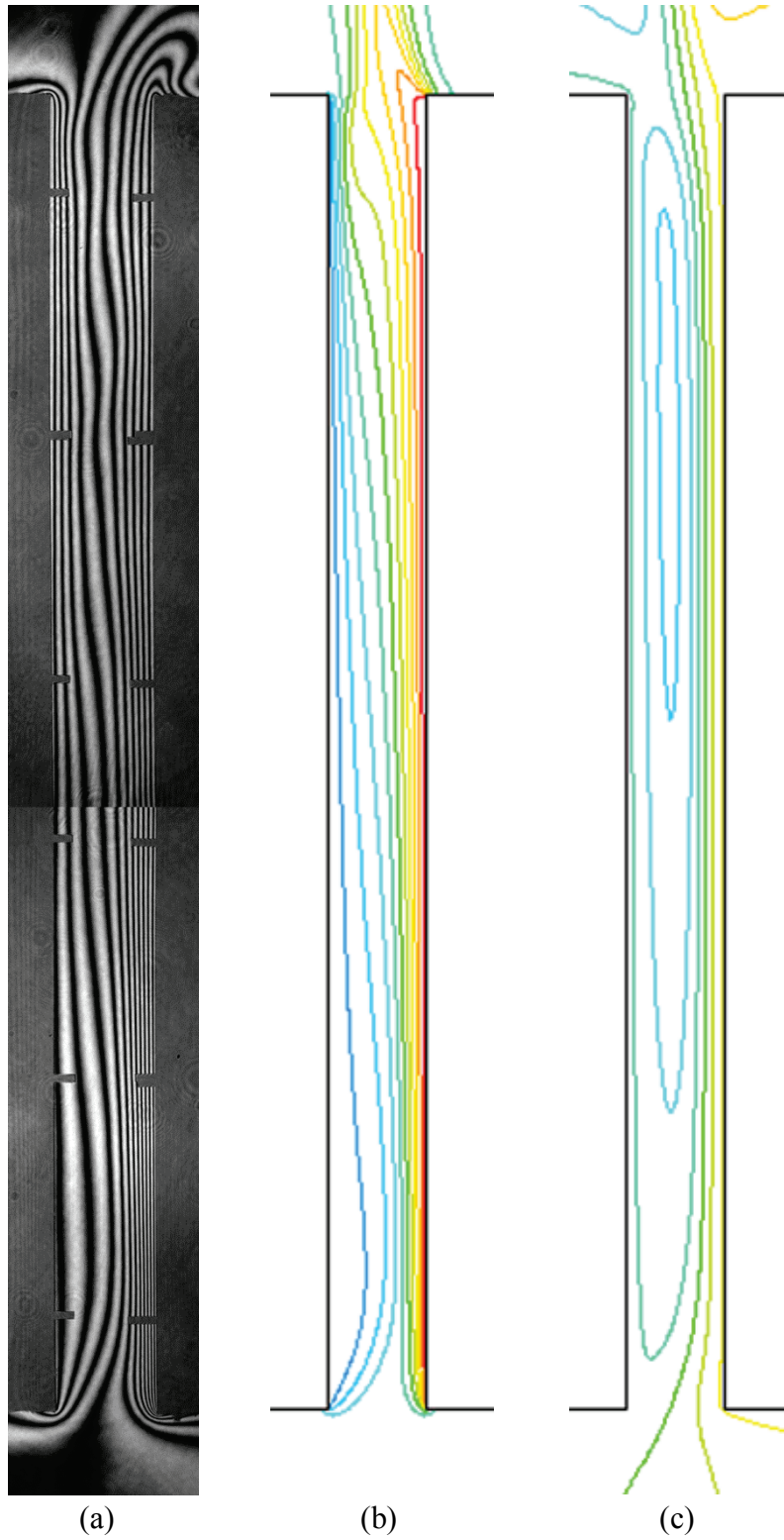
Figure 5.17: Comparison for $R_T = -0.5$ at $A = 13.2$ between the experiment and numerical model: (a) experimental temperature field, (b) numerical temperature field, and (c) numerical streamlines.
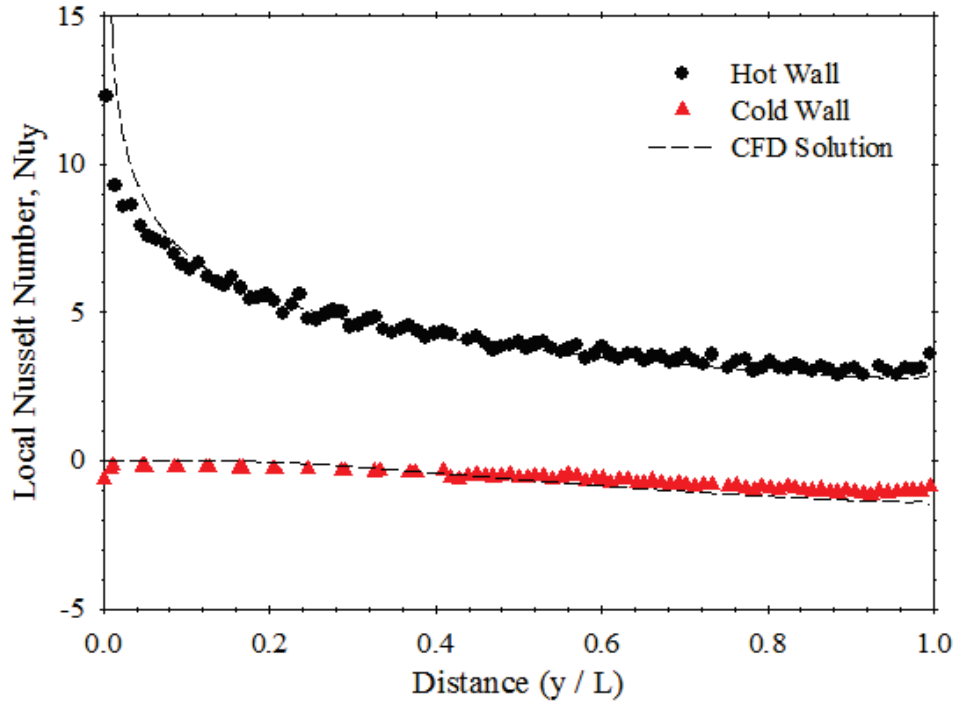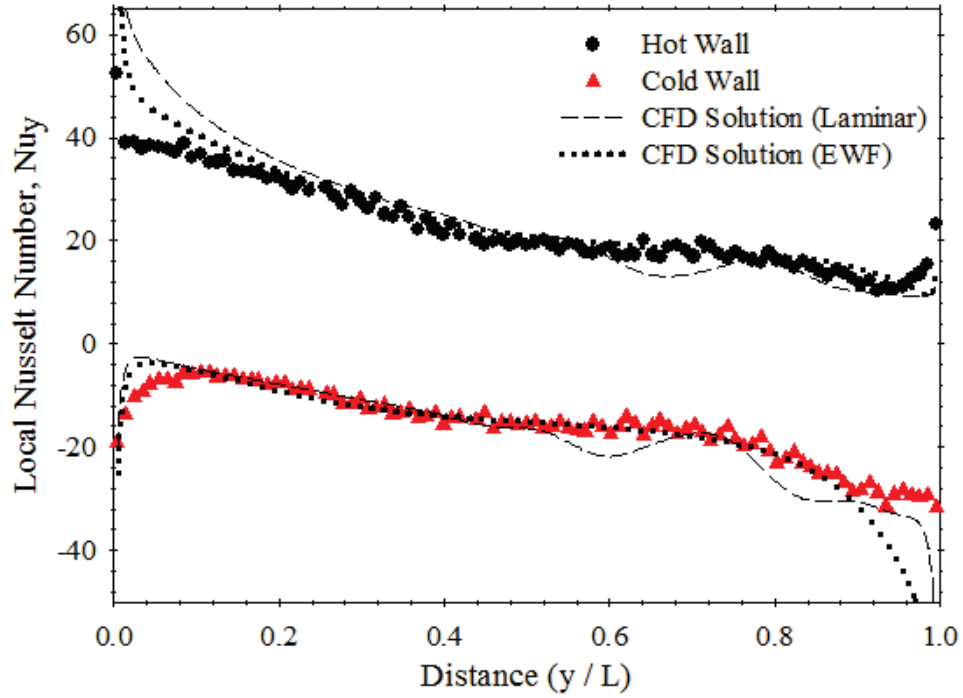
Figure 5.18: Graph of local Nusselt number variation versus distance for $R_T = -0.75$, A = 13.2 and Ra(b/L) = 76.6. Experimental: $Nu_H = 23.0$, $Nu_C = -15.8$, CFD (laminar): $Nu_H = 25.2$, $Nu_C = -17.5$, CFD (EWF): $Nu_H = 25.2$, $Nu_C = -17.8$.

this case. It should be noted that there is a slight error on both walls of the channel near the bottom, which is larger on the hot wall like the previous cases. Figure 5.19 shows a comparison of the streamlines of the two numerical solutions, as well as a comparison of the temperature fields with the interferogram. There are two eddies seen in the laminar prediction, which account for the undulating heat transfer on the graph. The turbulence model does not show these smaller eddies, but instead a single large eddy similar to the earlier cases.

The local Nusselt number distribution for $R_T = -1$ is shown in Figure 5.20, with the corresponding interferogram in Figure 5.6(e). This graph is similar to the previous case of $R_T = -0.75$ and two numerical solutions are added to the graph for comparison. In this case, the numerical results are quite different and the laminar results show better agreement with the experimental data. Again, the laminar solution showed that there were eddies inside the channel because of the wavy heat transfer on the two channel walls. These three cases show that as the
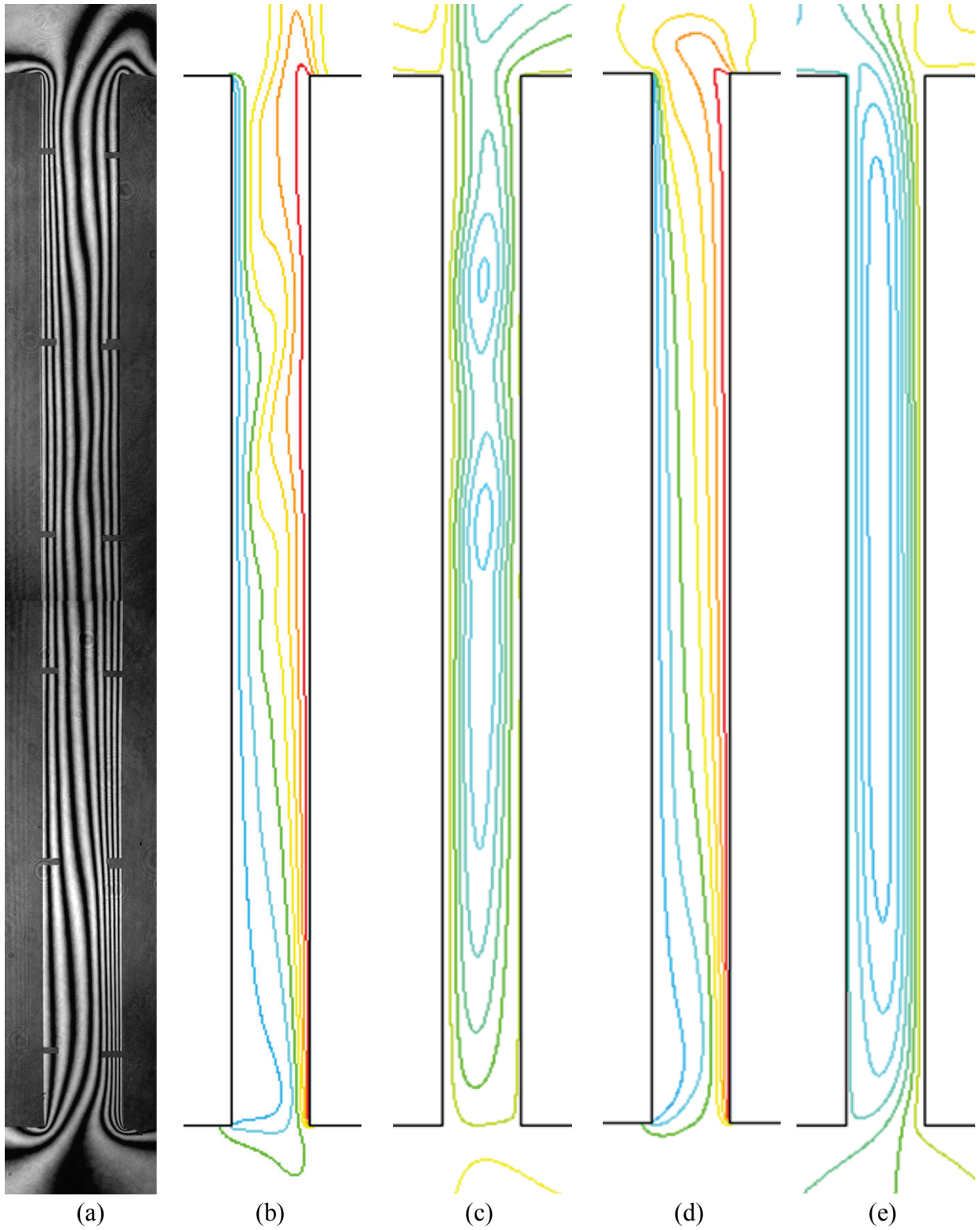
Figure 5.19: Comparison for $R_T = -0.75$ at $A = 13.2$ between the experiment and numerical model: (a) experimental temperature field, (b) laminar temperature field, (c) laminar streamlines, (d) turbulent EWF temperature field, (e) turbulent EWF streamlines.
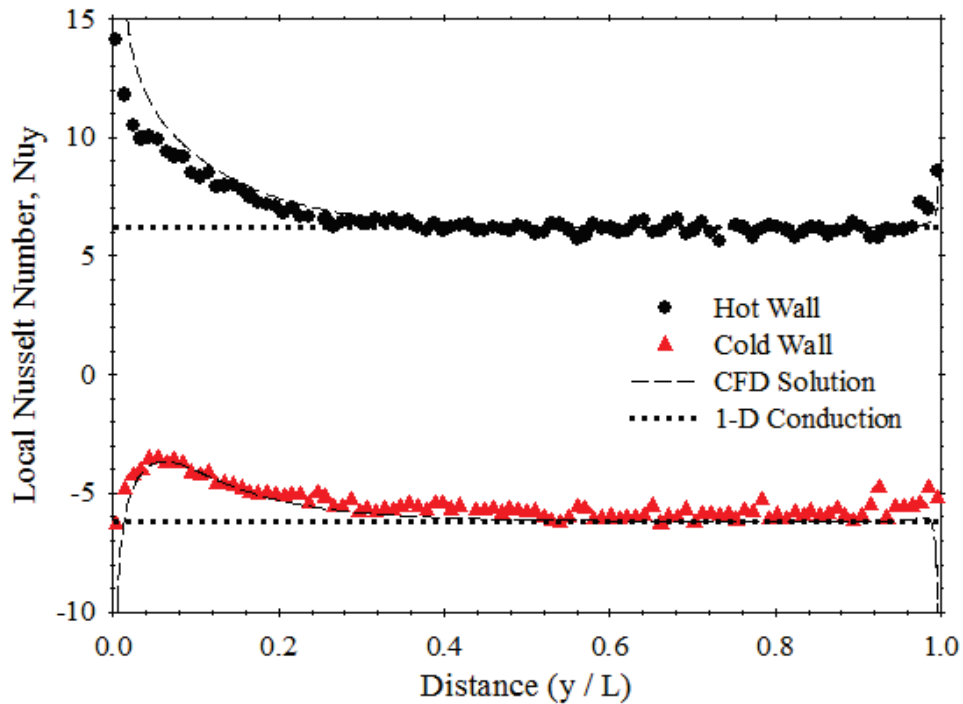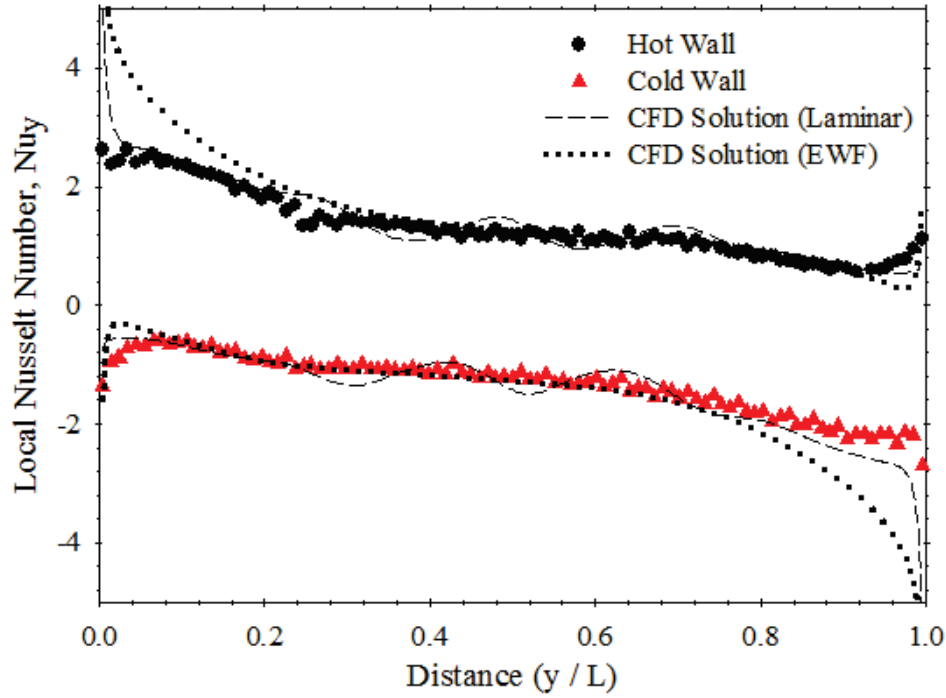
Figure 5.20: Graph of local Nusselt number variation versus distance for $R_T = -1$, $A = 13.2$ and $Ra = 11756$. Experimental: $Nu_H = 1.32$, $Nu_C = -1.32$, CFD (laminar): $Nu_H = 1.40$, $Nu_C = -1.40$, CFD (EWF): $Nu_H = 1.60$, $Nu_C = -1.60$.

aspect ratio is decreased (Rayleigh number increased), the temperature field is less conduction dominated. The interferograms also show that the flow quickly becomes unsteady as the temperature ratio is decreased.

The overall channel average Nusselt numbers for both the experimental data and numerical solution are compared in Table 5.3 for $R_T = -0.5$ and -0.75. The numerical predictions presented in this table were all solved with the steady laminar model. The Nusselt numbers agree quite well for $A = 13.2$, even though these cases were observed to be slightly unsteady experimentally. Overall the numerically predicted overall channel average Nusselt numbers are within 7% of the experimental data.

Table 5.4 shows a comparison of the hot wall average Nusselt numbers between the experimental data, numerical data and the ElSherbiny et al. (1982) correlation for $R_T = -1$. This empirical correlation is for a tall enclosure, not an open-ended channel. As noted previously, for

Table 5.3: Comparison of experimental and numerical overall channel average Nusselt numbers for three aspect ratios at $R_T = -0.5$ and -0.75.

	$R_T = -0.5$				$R_T = -0.75$			
	Rayleigh Number	Experimental Data	Numerical Solution		Rayleigh Number	Experimental Data	Numerical Solution	
Aspect Ratio	Ra(b/L)	Nu	Nu	Error	Ra(b/L)	Nu	Nu	Error
26.4	12.3	0.673	0.697	3.6%	4.74	0.680	0.658	−3.2%
17.6	66.6	2.19	2.27	3.7%	22.9	2.17	2.27	4.6%
13.2	214	3.51	3.53	0.6%	76.6	3.62	3.85	6.4%

Table 5.4: Comparison of experimental data, numerical predictions, and ElSherbiny et al. (1982) correlation of the hot wall average Nusselt numbers for the anti-symmetrical ($R_T = -1$) cases.

	$R_T = -1$				Enclosure	
	Rayleigh Number	Experimental Data	Numerical Solution		ElSherbiny et al. Correlation (1982)	
Aspect Ratio	Ra	Nu_H	Nu_H	Error	Nu_H	Error
26.4	1482	0.972	1.02	4.9%	1.00	2.9%
17.6	4787	1.03	1.11	7.8%	1.11	7.8%
13.2	11750	1.32	1.40	6.1%	1.60	21.2%

the anti-symmetrical case, the open-ended channel has some temperature field and flow features that are similar to an enclosure. Overall, the numerical model is within 8% of the experimental data, which shows that the laminar numerical prediction compares favorably. At the lowest Rayleigh number, the correlation is within 3%, but as the Rayleigh number increases, the correlation over-predicts the experimental data by about 21%. This shows that the enclosure correlation is adequate for a quick estimation of the heat transfer for the anti-symmetrical cases, but its accuracy decreases as the Rayleigh number increases.

Table 5.5 shows a comparison of the different numerical models used with the experimental data for $R_T = -0.5$, -0.75 and -1 at A = 13.2. Note that for the $R_T = -0.5$ and -0.75 case, the modified Rayleigh number and overall channel average Nusselt number is presented in this table and the non-modified Rayleigh number and hot wall average Nusselt number is presented for

Table 5.5: Comparison of the different numerical models with the experimental data for an aspect ratio of 13.2 and $R_T = -0.5, -0.75$ and -1.

	Experimental Data		Laminar Numerical Solution		Turbulent Numerical Solution with EWF		Turbulent Numerical Solution with SWF	
R_T	Ra(b/L)	Nu	Nu	Error	Nu	Error	Nu	Error
-0.5	214	3.51	3.53	0.6%	3.48	-0.9%	2.68	-23.6%
-0.75	76.6	3.62	3.85	6.4%	3.66	1.1%	2.67	-26.2%
-1	11750	1.32	1.40	6.1%	1.60	21.2%	1.70	28.8%

the $R_T = -1$ case. These cases show that the laminar numerical predictions generally are in good agreement with the experimental data. The turbulent numerical solution with the standard wall functions is not a good model for this type of flow. The enhanced wall functions used in the turbulent numerical model were in agreement with the $R_T = -0.5$ and -0.75 case, but were not as accurate for the $R_T = -1$ case.

Two unsteady cases were studied experimentally with a high speed movie camera. Data was obtained for two temperature ratios of $R_T = -0.5$ and $R_T = -1$ at an aspect ratio of 8.8 (b = 30 mm). As mentioned in Section 3.4, studying unsteady flow was labour intensive and time consuming, which is why only two cases were studied. A sequence of images was recorded at 120 fps for 20 seconds. After some initial analysis, it was determined that a frame rate of 30 fps was sufficient and this reduced the time required for image processing. A low frame rate was sufficient because the MZI beam averages along the z-direction, so the beam averaged frequency is much less than the local frequency at any given point in the channel. Each case consisted of 12 captures in order to examine the entire channel. Using these 12 images, the local heat transfer data was obtained for approximately 100 locations on each channel wall. A numerical simulation was solved for each case for comparison with the experimental data.

Figure 5.21(a) shows a comparison of the instantaneous heat fluxes on the hot walls of the two cases and Figure 5.21(b) shows the instantaneous heat flux on the cold walls. These measurements were made a height of y/L = 0.67 on the hot and cold walls over a 20 second interval at a frame rate of 30 fps. These graphs show the fluctuations which were typical over most of the channel. The RMS fluctuation is 10% or less for these cases and the peak-to-peak fluctuation is between 7% and 21% about the mean. It can be seen from this graph that the

$R_T = -0.5$ case has more fluctuation in the instantaneous heat fluxes than the $R_T = -1$ case. Figure 5.21 also shows the running time average for these locations. This graph shows that time-averaged heat flux becomes nearly stationary after about 10 seconds, but the full 20 seconds was used for analysis.

Figure 5.22 shows the time-averaged local heat transfer rates for the $R_T = -0.5$ case at an aspect ratio of 8.8. In this graph, two numerical results were added for comparison. This case was observed to be unsteady and was analyzed using the high speed movie camera to capture the fluctuations in the heat flux. The numerical model was first solved using a steady k-ε turbulence model with enhanced wall functions because it was an unsteady case. A steady laminar solution was able to reach convergence, so the laminar numerical results were also added for comparison. Both numerical models show poor agreement near the top of the channel, with the laminar prediction showing worse agreement. The isotherms of the laminar numerical prediction showed that the plume curved abruptly at the top of the channel to the cold wall side. This suggests that the laminar numerical solution is not valid for this case. The turbulence model with enhanced
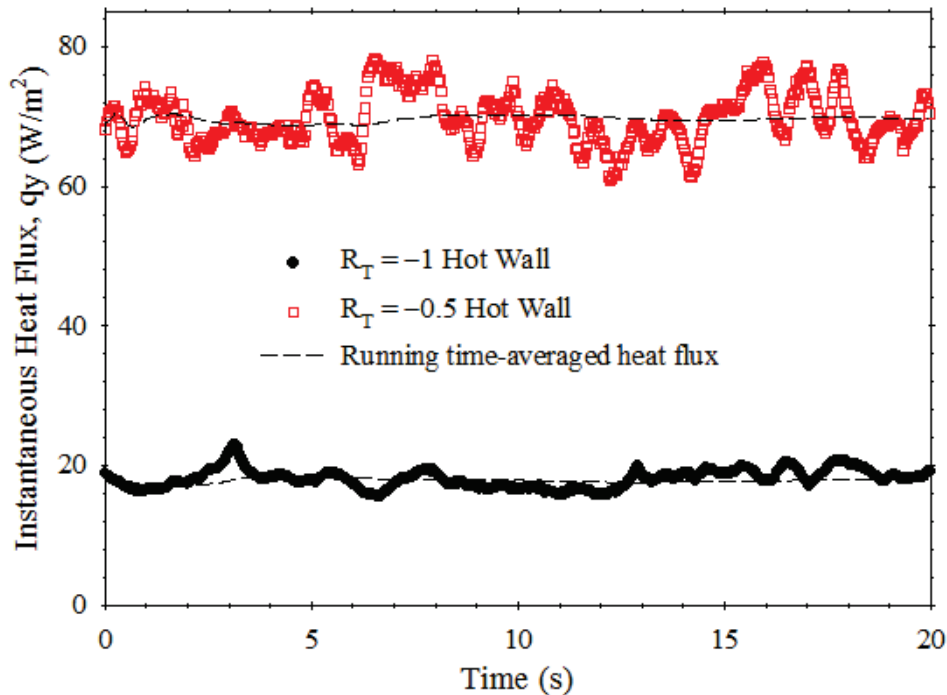
Figure 5.21(a): Instantaneous and running time-averaged local heat fluxes on the hot wall for the $R_T = -0.5$ and $R_T = -1$ cases with A = 8.8 at y/L = 0.67.
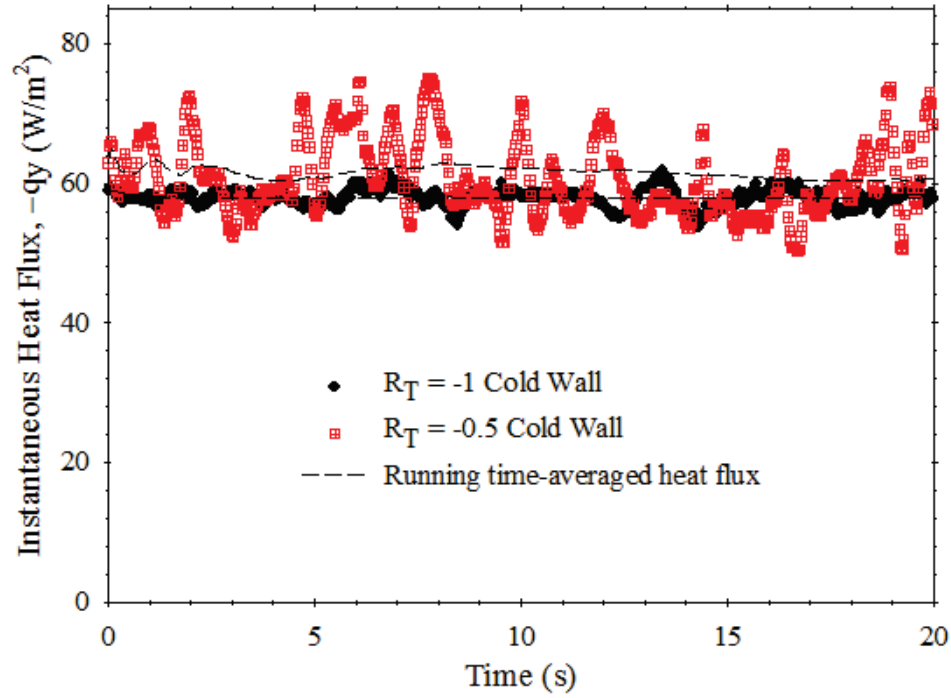
Figure 5.21(b): Instantaneous and running time-averaged local heat fluxes on the cold wall for the $R_T = -0.5$ and $R_T = -1$ cases with A = 8.8 at y/L = 0.67.
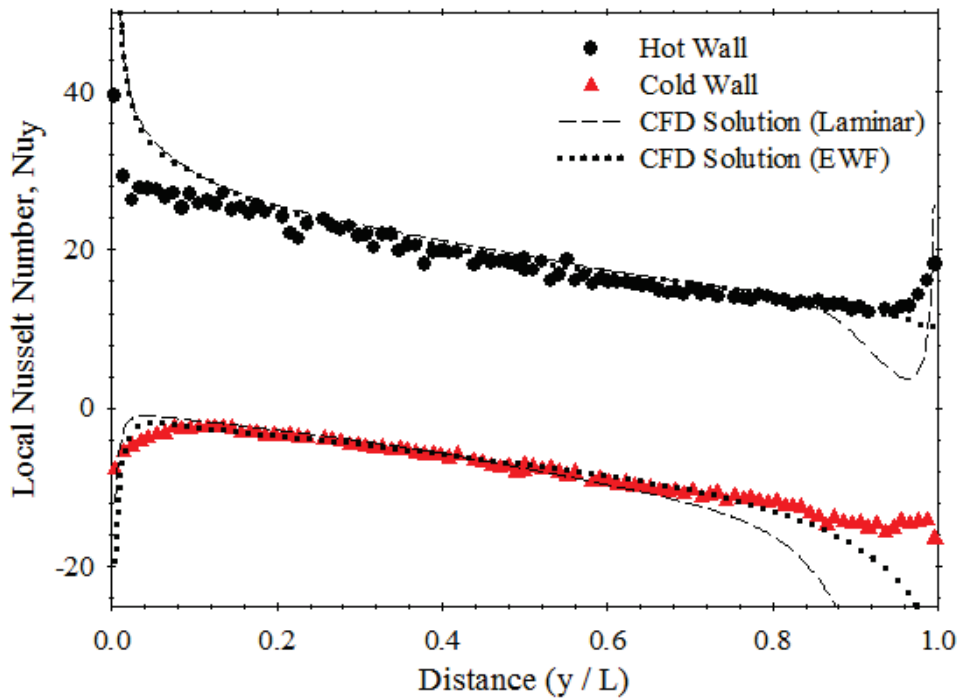

Figure 5.22: Graph of time-averaged local Nusselt number variation versus distance for $R_T = -0.5$, A = 8.8 and Ra(b/L) = 1084. Experimental: $Nu_H = 18.9$, $Nu_C = -8.10$, CFD (laminar): $Nu_H = 20.2$, $Nu_C = -11.5$, CFD (EWF): $Nu_H = 20.5$, $Nu_C = -9.11$.

wall functions compared more favorably with the experimental data. As observed with the laminar cases, there is some slight error between the numerical results and the experimental data in the entrance and exit regions of the channel.

The $R_T = -1$ case at an aspect ratio of 8.8 is shown in Figure 5.23. Again, two numerical models were added to the graph for comparison. In this case, the laminar model predictions show better agreement with the experimental data than the turbulence model with enhanced wall functions. A possible explanation can be made by examining the instantaneous heat fluxes in Figure 5.18. The graph shows that instantaneous heat fluxes have less fluctuation in the $R_T = -1$ case than the $R_T = -0.5$ case. This shows that the $R_T = -1$ case might be unsteady laminar flow, which would be why the turbulence model does not give an accurate prediction. The k-ε turbulence model is more appropriate for fully turbulent flows and does not give good results for unsteady laminar flow. The higher fluctuations in the $R_T = -0.5$ case show that the flow might be turbulent and not unsteady laminar, which is why the turbulence model showed better agreement.
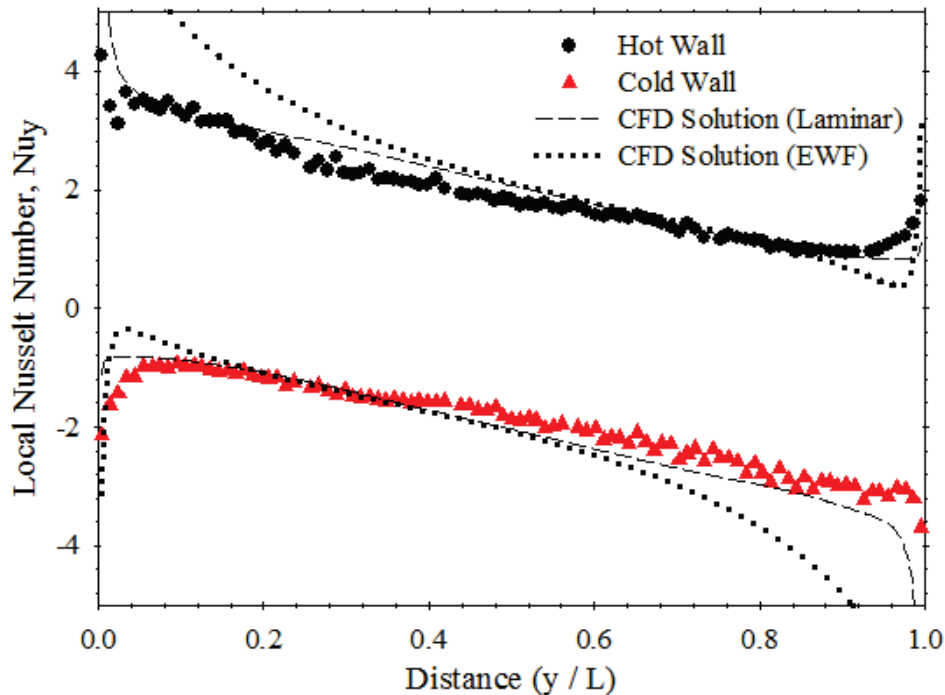
Figure 5.23: Graph of time-averaged local Nusselt number variation versus distance for $R_T = -1$, A = 8.8 and Ra = 39430. Experimental: $Nu_H = 1.98$, $Nu_C = -1.96$, CFD (laminar): $Nu_H = 2.10$, $Nu_C = -2.08$, CFD (EWF): $Nu_H = 2.52$, $Nu_C = -2.50$.

Table 5.6 shows a comparison of the two unsteady cases of $R_T = -0.5$ and -1 at A = 8.8. The modified Rayleigh number and overall channel average Nusselt number is presented for the $R_T = -0.5$ case in this table and the non-modified Rayleigh number and hot wall average Nusselt number is presented for the $R_T = -1$ case. The laminar numerical results were within 7% of the experimental data for the $R_T = -1$ case and the turbulence model with enhanced wall functions predictions were within 5% for the $R_T = -0.5$ case.

The hot and cold wall average Nusselt numbers have been added to captions of all the local Nusselt number distribution graphs. Both the experimental data and numerically predicted values have been added for comparison. The numerical and experimental hot and cold wall average Nusselt numbers are within 10% across all the cases studied.

5.5 Numerical Predictions of Average Nusselt Number

The numerical model was validated against the experimental data and some data from the literature in previous sections. The streamlines, temperature field and heat fluxes have been compared over a range of variables and generally show good qualitative agreement with the experimental data. So, the numerical model was used to conduct a parametric study of opposing buoyancy forces inside an asymmetrically heated vertical channel. The numerical results were obtained over multiple temperature ratios of $R_T = 0, -0.25, -0.5, -0.75,$ and -1 and solved over a Rayleigh number range of $0.1 < Ra(b/L) < 10^4$. Initially a steady laminar model was used to determine the average Nusselt numbers of the overall channel, but the numerical model was unable to be solved over the entire modified Rayleigh number range, so a steady k-ε turbulence model was used at higher Rayleigh numbers.

Table 5.6: Comparison of the different numerical models with the experimental data for an aspect ratio of 8.8 and $R_T = -0.5$ and -1.

	Rayleigh Number	Experimental Data	Laminar Numerical Solution		Turbulent Numerical Solution with EWF	
R_T	Ra(b/L)	Nu	Nu	Error	Nu	Error
-0.5	1084	5.42	4.31	-20.5%	5.69	5.0%
-1	39430	1.97	2.10	6.6%	2.51	27.4%

Figure 5.24 shows a graph of the overall channel average Nusselt number versus modified Rayleigh number for $R_T = 0$. These numerical predictions were solved with a steady laminar model as discussed in Chapter 4 using a vertical channel with an aspect ratio of 50. This solution was obtained to validate the numerical model with existing data from the literature. This graph shows good agreement with the empirical correlation of Raithby and Hollands (1998). The average Nusselt numbers from two experimental cases studied at $R_T = 0$ were also added to this graph for comparison. These two data points fit on the curve of numerical results. (Note that the experimental model cases used aspect ratios of 17.6 and 13.2, but by using Ra(b/L), all aspect ratio data falls on the same curve.)

Figures 5.25, 5.26 and 5.27 show the numerically predicted overall channel average Nusselt numbers for $R_T = -0.25$, -0.5, and -0.75 respectively using an aspect ratio of 50. All three of these graphs show that the steady laminar model was unable to be solved over the entire Rayleigh number range of $0.1 < Ra(b/L) < 10^4$. With air flowing up the hot wall and down the cold wall, there is a region where these two flows interact in the center of the channel. As the
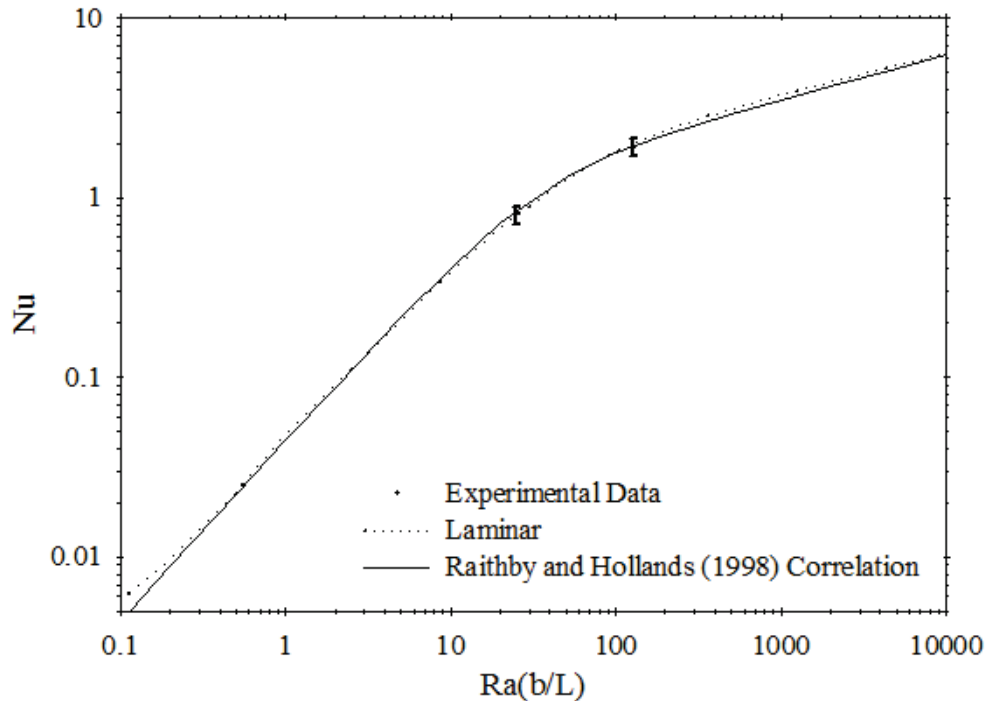
Figure 5.24: Overall channel average Nusselt number variation with modified Rayleigh number for $R_T = 0$.

101
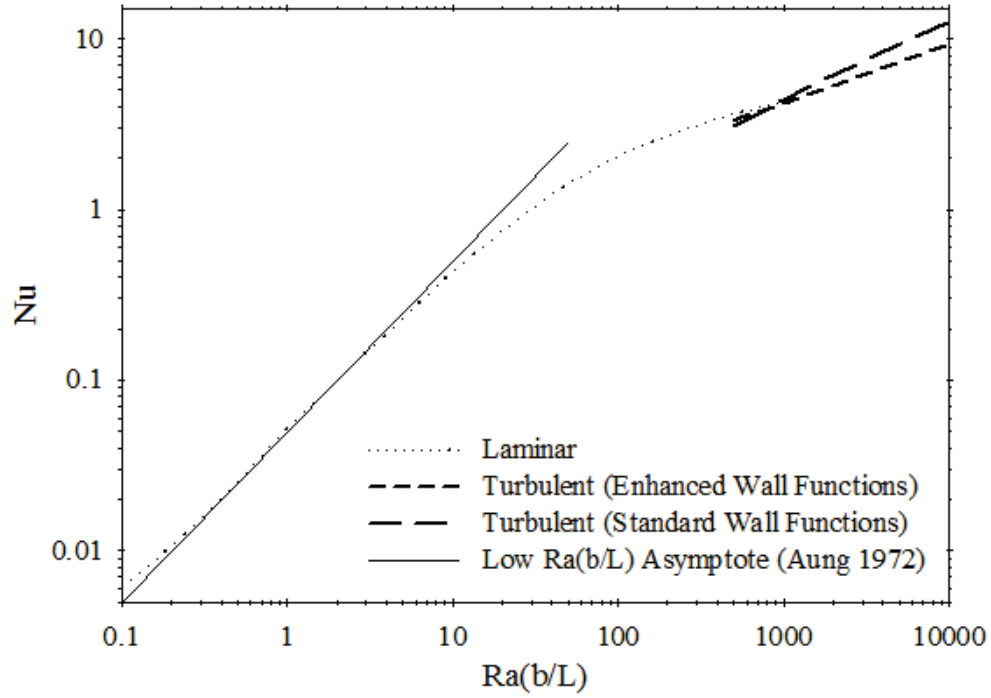
Figure 5.25: Overall channel average Nusselt number variation with modified Rayleigh number for $R_T = -0.25$.
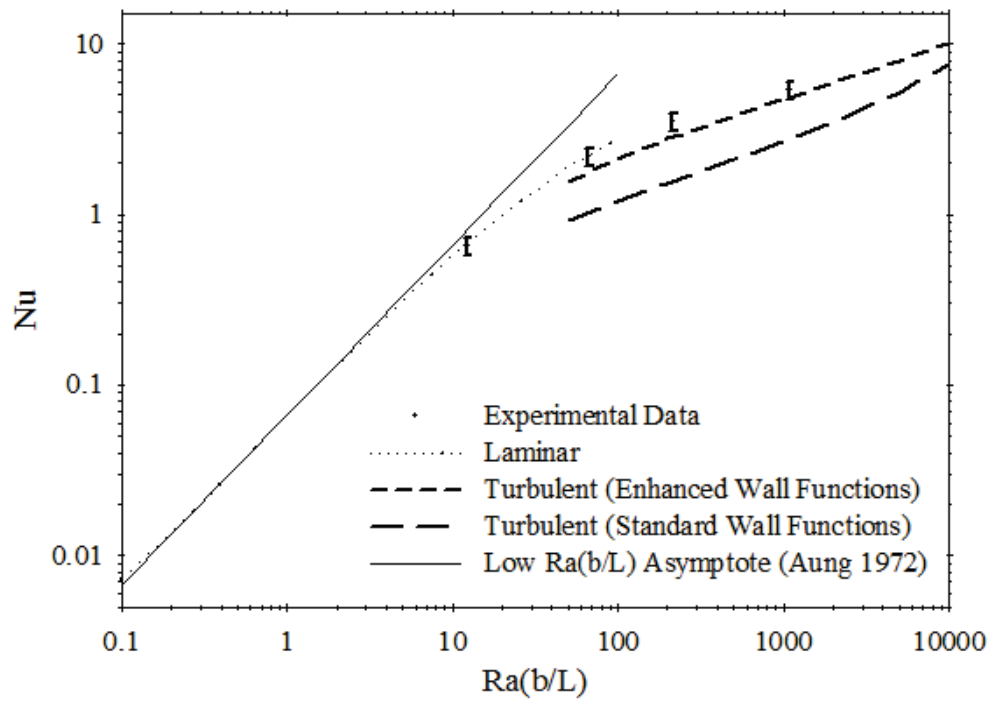
Figure 5.26: Overall channel average Nusselt number variation with modified Rayleigh number for $R_T = -0.5$.
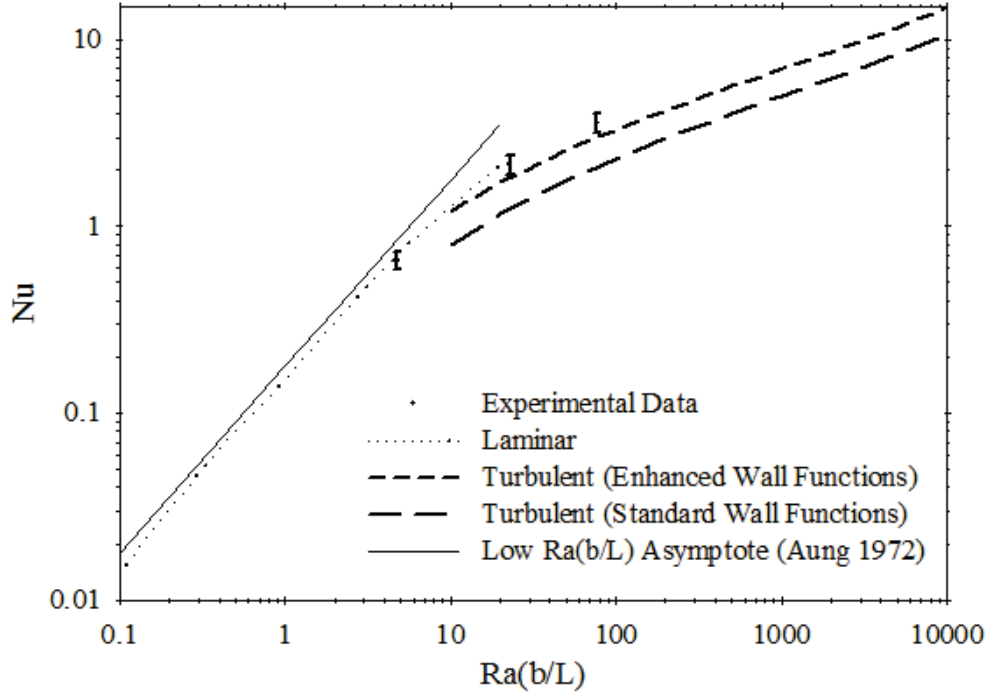
Figure 5.27: Overall channel average Nusselt number variation with modified Rayleigh number for $R_T = -0.75$.

Rayleigh number is increased, where these two flows interact causes instability inside the channel and a steady laminar numerical solution was unable to reach convergence. In order to obtain predictions up to a $Ra(b/L) = 10^4$, a steady k-ε turbulence model was used with two different wall functions: standard wall functions and enhanced wall functions. Figure 5.25 shows that laminar results for $R_T = -0.25$ were only obtained for $0.1 < Ra(b/L) < 1000$ and turbulence results were solved over the range $500 < Ra(b/L) < 10^4$. For $R_T = -0.5$, Figure 5.26 shows that laminar predictions were solved for $0.1 < Ra(b/L) < 100$, so the turbulence model was used for $50 < Ra(b/L) < 10^4$. Finally, for $R_T = -0.75$, the turbulent solutions were obtained for $10 < Ra(b/L) < 10^4$ because the laminar solutions only converged for $0.1 < Ra(b/L) < 20$ as shown in Figure 5.27. The average Nusselt number for fully developed flow that was developed by Aung (1972) and given in Equation (1.12) was added to these graphs for comparison. This analytical asymptote correlation was developed for positive R_T values, but as can be seen in these graphs, the numerical solutions for negative R_T values also follow this asymptote. Aung's (1972) solution was developed using fully developed flow assumptions, where there is no diffusion at the channel ends. The flow was derived based on the net buoyancy force relative to

the ambient inside the channel, so it is also valid for negative R_T values. On each graph, there is a critical Rayleigh number where the laminar numerical model was unable to reach convergence. As the temperature ratio was decreased, this critical Rayleigh number also decreased.

The experimental data points are plotted with error bars on these graphs as well for comparison (note that the experimental data are for different aspect ratios of 26.4, 17.6, 13.2, and 8.8, but they all fall on the same curve when plotted using Ra(b/L)). The experimental data and the laminar numerical results are in agreement with each other and the enhanced wall function results agree better with the experimental data than the standard wall functions. Therefore, for free convection in a heated vertical channel with a negative temperature ratio, a steady k-ε turbulence model with enhanced wall functions is suggested to be used.

Figure 5.28 shows the overall channel average Nusselt number data for the anti-symmetric case of $R_T = -1$ using a channel with A = 50. This graph has laminar results over the range $100 < Ra < 5000$ and turbulent predictions for $5000 < Ra < 10^6$. The correlation developed by ElSherbiny et al. (1982) for tall vertical enclosures is used to compare the hot wall average Nusselt numbers because the flow and temperature fields look similar as shown in the previous sections. Four experimental data points are added to this graph to compare with the numerical results (Again, using four different aspect ratios of 26.4, 17.6, 13.2, and 8.8). The first experimental data point is slightly below the laminar results and the correlation at Ra = 1482. The next data point at Ra = 4788 agrees with the laminar solution, enhanced wall function results and the correlation. This area of the graph shows that the enhanced wall functions show better agreement than the standard wall functions. These results are also in agreement with Wright et al. (2006), where they determined that under Ra = 6220, the flow was stable inside a tall enclosure. The critical Rayleigh number predicted by Korpela et al. (1982) is $Ra_C = 6274$ for an aspect ratio of 50. This is where the onset of secondary cells takes places in the conduction regime inside a tall enclosure. Figure 5.28 shows that this critical Rayleigh number agrees with the heat flux data for an open ended channel with an aspect ratio of 50 for $R_T = -1$. At Ra = 11760 was in the range where Wright et al (2006) observed the flow pattern inside a tall vertical cavity became unsteady and the beginning of 3-dimensional flow was exhibited. This was in
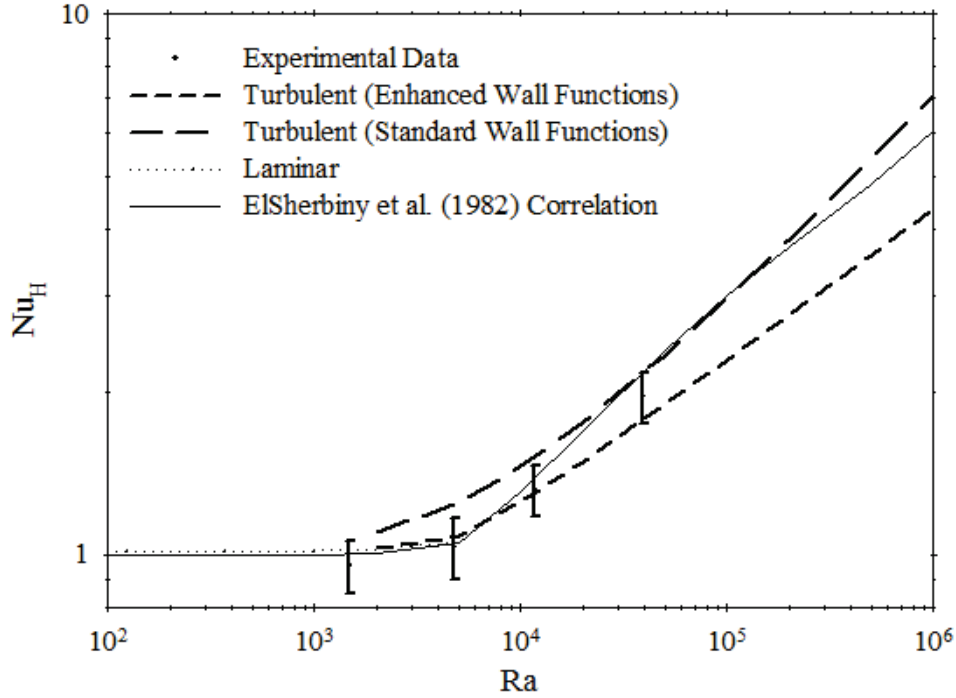
Figure 5.28: Hot wall average Nusselt number variation with Rayleigh number for $R_T = -1$.

agreement with what was observed in the present study, where the flow was slightly unsteady at this Rayleigh number for an open-ended channel. The experimental data point at Ra = 11750compares favorably with the enhanced wall functions and the correlation in Figure 5.28. For Ra = 39430, Wright et al. (2006) found that in this range of Rayleigh number the flow began to transition to fully turbulent flow inside a tall enclosure. The magnitude of the 3-D fluctuations increased, with the flow becoming more chaotic and turbulent. The current experimental results showed that at Ra = 39430, the flow was unstable, but it was not transitioning to turbulent flow, as the laminar results showed better agreement than the turbulent predictions. The experimental data point at Ra = 39430 is slightly higher than the enhanced wall function results, but below the standard wall functions and the ElSherbiny et al. (1982) correlation. Some more experimental data is required at higher Rayleigh numbers in order to determine which wall functions are appropriate for this type of flow. This graph shows that an enclosure correlation can be used as an estimate of the hot wall average Nusselt number for an open channel when $R_T = -1$, which is a significant finding.

Chapter 6

Conclusions and Recommendations

6.1 Summary and Conclusions

The results of an interferometric study of an asymmetrically, isothermally heated vertical channel with opposing buoyancy forces have been presented. Finite fringe interferograms were obtained for five different temperature ratios using four different channel spacings. The local and average heat transfer data were determined from these interferograms. Infinite fringe interferograms were taken for temperature field visualization inside the vertical channel. Flow visualization was also preformed for several cases.

Numerical solutions were developed and compared with the experimental data and correlations from the literature. A steady laminar model and a steady k-ε turbulence model with two different wall functions were used. A parametric study was conducted with the numerical model to obtain heat transfer data over a wide range of Rayleigh numbers and negative temperature ratios. The conclusions are as follows:

i)   Symmetrical heating of $R_T = 1$ and asymmetrical heating of $R_T = 0$ showed similar results to the literature. The average heat transfer rates were in agreement with correlations from the literature for these cases. The local heat flux distribution showed good agreement between the numerical results and the experimental data. The numerical model was solved for $R_T = 0$ over a wide range of Rayleigh numbers and compared favourably with the Raithby and Hollands (1998) correlation.

ii)   The results showed that as the temperature ratio was decreased, the flow pattern inside the channel became more complex. Air can enter the channel from both the top and bottom of the channel and it can exit the channel from the top and bottom. This sometimes causes the air to recirculate inside the channel. For $R_T = -1$, the flow pattern was observed to be similar to flow inside a tall vertical cavity, with a recirculaitng cell present in the center of the channel. This recirculating cell causes the isotherms to pull away from the surfaces, creating a region of low local heat flux. The interferograms of the anti-symmetrical cases showed this phenomenon at the top of the hot wall and the

bottom of the cold wall. For $R_T < 0$ but not equal to-1 , a recirculating cell of air was also present, with a separation point on the cold wall near the bottom of the channel. The isotherms pulled away from the cold wall due to the separation point, creating a region of low heat flux.

iii)   The experimental results showed that the plume of air did not exit the channel straight vertically, except in the symmetrically heated cases. This was in contrast to the numerical predictions, which showed the plume exiting the channel straight vertically. This disagreement is most likely due to the imperfect boundary conditions on the pre-entry plenums in the numerical model. This did cause some discrepancies in the local heat transfer distribution between the numerical results and the experimental data near the top of the channel, especially as the channel spacing was increased.

iv)   As expected, as the Rayleigh number is increased, the flow becomes unsteady. The opposing buoyancy forces cause the flow to become unstable at a much lower Rayleigh number when compared with a channel with a buoyancy force in a single direction.

v)   The local heat transfer results showed that as the temperature ratio is decreased below zero, for the same aspect ratio, the net buoyancy force is reduced and the flow becomes increasingly conduction dominated.

vi)   In general, the numerical solutions were found to be in good agreement with the experimental data. As was found experimentally, the opposing buoyancy forces produce instability inside the channel. A steady laminar model and a steady k-ε turbulence model were both used to obtain solutions over the entire Rayleigh number range of interest. In general, a k-ε turbulence model with enhanced wall functions shows better agreement than the k-ε turbulence model with standard wall functions for this type of flow at higher Rayleigh numbers. The streamlines, temperature field, and local heat transfer data predicted by the numerical model are qualitatively similar to those from the experiment.

vii)   The numerical solutions showed some slight error in the local heat flux distribution at the bottom of the hot wall. This error was, in part, because the numerical model assumed that the horizontal surfaces in the entrance and exit regions of the channel were adiabatic. On the experimental model, these surfaces were not perfectly adiabatic.

viii) In fully developed flow, the numerical predictions of the velocity and temperature profiles across the channel showed good agreement with the analytical solutions presented by Aung (1972). Even though the analytical solution was developed based on positive temperature ratios inside a vertical channel, the solutions are applicable for negative temperature ratios.

ix) The numerical solutions followed the asymptote of the average Nusselt number for fully developed flow that was developed by Aung (1972). Again, this analytical asymptote correlation was developed for positive R_T values, but is applicable to negative R_T values.

x) In the anti-symmetrical cases ($R_T = -1$), the net buoyancy force is zero and has a similar flow and temperature field as a tall enclosure (i.e. A > 20). In fact, it was shown that an enclosure correlation can be used to estimate the average Nusselt number for the anti-symmetrical case.

6.2 Recommendations

The following recommendations are made for future studies:

i) The numerical and experimental data can be used to develop empirical correlations for negative temperature ratios inside a heated vertical channel. Empirical correlations can be developed to predict the average Nusselt numbers for the overall channel, as well as correlations for the hot wall and cold wall local and average Nusselt numbers. These correlations can then be used for predicting the heat transfer in a variety of engineering problems. There is a need for these correlations in a simplified model of a fenestration system, as discussed in Section 1.4.

ii) This study has shown that more experimental data at higher Rayleigh numbers would be useful in further validating the numerical model. More data in the transition and fully turbulent regimes would be helpful for further testing of which turbulence model and wall functions are more accurate as the flow becomes increasingly unsteady and turbulent. In the anti-symmetrical case, this data would be useful in determining how

close an approximation the enclosure correlations are at higher Rayleigh numbers. When studying higher Rayleigh numbers, a taller channel would be beneficial.

iii) More flow visualization would be useful to further investigate the velocity field. Since only a preliminary study of flow visualization was presented here, flow visualization experiments could be made with the existing experimental model. Using the same technique as in the present thesis, the flow patterns could be observed of some of the cases that were studied with the laser interferometer. Other methods could be used as well, such as Particle Image Velocimetry or Laser-Doppler Anemometry. This could be utilized to obtain more detailed velocity field measurements.

iv) The literature showed that there have been a few numerical studies on turbulent free convection in an asymmetrically heated channel. These studies used a low Reynolds number k-ε turbulence model. The current study used a standard k-ε turbulence model, so different turbulence models, such as the low Reynolds number k-ε turbulence model, could be used with negative temperature ratios inside a vertical channel. Other turbulence models, such as Large Eddy Simulation (LES) and Direct Numerical Simulation (DNS), could also be tested.

v) Isothermal walls were used in this study, but there are many applications where a uniform heat flux is applied to the walls. For negative temperature ratios, using a uniform heat flux on the hot wall and isothermal conditions on the cold wall could be considered.

vi) In the literature, there have been numerous studies with various heated, unheated, or cooled objects inside a channel with positive temperature ratios. It could be of interest to see the effect of these objects on the heat transfer and flow patterns in a channel with negative temperature ratios.

vii) In the present study, the channel walls are parallel to each other and vertical with respect to gravity. The effects of angle of inclination, converging or diverging channel walls could also be studied. These cases have been investigated in the literature with buoyancy forces in a single direction ($R_T > 0$), but the effects of opposing buoyancy forces ($R_T < 0$) could be examined.

Appendix A

Specifications of Interferometer and Instruments

A.1 Mach-Zehnder Interferometer Specifications

Tables A.1 through A.5 show the specifications of all the optics used in the Mach-Zehnder Interferometer.

Table A.1: Specifications of the two beam splitters in the interferometer.

BK-7 Custom Beam Splitter Plates (Coated)		
Size	8" diameter	±0.005"
Thickness	1.50"	±0.005"
Flatness	1/20 λ (632.8 nm)	Both surfaces over central 90%
Surface Finish	40-20	
Parallelism	1 arc second	
Coated	1 side 50% reflective, 50% transmittive for 632.8 nm 1 side anti-reflective for 632.8 nm	±5% Incidence angle of 30°
Edges ground and safety beveled 0.020" max		

Table A.2: Specifications of the two flat Mirrors in the interferometer.

PYREX Front Surface Mirrors		
Size	8" diameter	±0.050"
Thickness	1.50"	±0.050"
Flatness	1/20 λ (632.8 nm)	Mirrored surface over central 90%
Surface Finish	40-20, other side finely ground	
Coated	Enhanced aluminum	95% reflective at 632.8 nm
Edges ground and safety beveled 0.020" max		

Table A.3: Specifications of the parabolic mirror in the interferometer.

Edmund Precision Parabolic Mirrors NT32-075-533		
Size	8" diameter	+0.006"/−0
Thickness	1.37"	
Focal Length	64"	±1.5%
Surface Finish	60-40, back surface ground	
Surface Accuracy	1/8 λ (632.8 nm)	
Coating	Enhanced aluminum	
Aperture	f/8.00	
Substrate	Pyrex 7740	

Table A.4: Specifications of the spherical mirror in the interferometer.

Edmund Precision Spherical Mirrors NT43-590		
Size	8" diameter	+0.006"/-0
Thickness	1.37"	+0%/-10%
Focal Length	24"	±2%
Surface Finish	60-40, back surface ground	
Surface Accuracy	1/4 λ (632.8 nm)	
Coating	Enhanced aluminum	
Aperture	f/3.00	
Substrate	Pyrex 7740	

Table A.5: Specifications of the two optical windows in the interferometer.

ESCO ZF280150C BK-7 Grade A Double Sided Optical Flat (Coated)		
Size	8" diameter	±0.005"
Thickness	1.50"	±0.005"
Flatness	1/20 λ (632.8 nm)	Both surfaces over central 90%
Surface Finish	40-20	
Parallelism	5 arc seconds	
Coated	AR-MgF$_2$ (both surfaces)	For visible light (400 nm to 700 nm) at normal angle of incidence (NAOI)
Edges ground and safety beveled 0.020" max		

A.2 Instrumentation Specifications

Tables A.6 through A.10 show the specifications of the two digital cameras and any other instrumentation used.

Table A.6: Specifications of the Phase One P45 digital back.

Resolution	39 mega pixels
Active Pixels	7216 × 5412 pixels
CCD Size effective	49.1 × 36.8 mm
Image Bit Depth	16 bit per colour
Pixel Size	6.8 × 6.8 micron
Image Ratio	4:3
ISO	50, 100, 200, 400, 800
Software	Capture One Pro version 4.5

Table A.7: Specifications of the Integrated Designs Inc. MotionPro X-3
Monochrome high speed digital movie camera.

Resolution	1.3 mega pixels
Active Pixels	1280 × 1024 pixels
Image Bit Depth	8-bit mono
Pixel Size	12 × 12 micron
Image Ratio	5:4
Max Frame Rate at max resolution	1040 fps
On-board Memory	4 GB
Software	MotionPro X version 2.03

Table A.8 Specifications of the Lauda Proline RP 1845 constant temperature water baths.

Working temperature range	-50°C to 200°C
Temperature control	± 0.01°C
Heater Power	3.5 kW
Cooling capacity at 20°C	1.60 kW
Pump pressure / suction	0.7 / 0.4 bar
Pump flow at max. pressure / suction	25 / 23 L/min
Size of bath	300 × 200 × 200 mm
Overall Dimension	400 × 540 × 770 mm

Table A.9: Specifications of the Omega DP97 high accuracy platinum resistance thermometers with two DP97-PROBE1 precision Pt100 probes.

Temperature Range	-199.99°C to 849.99°C
Instrument accuracy	±0.02°C ±1 digit for range -200°C to 500°C ±0.005% reading ±1 digit for range 500°C to 850°C
Overall System accuracy	Better than ±0.04°C from -50°C to 250°C
Display resolution	0.01°C, K, °F, Ω
Measurement Units	°C, K, °F, Ω (user selectable)
Measurement Modes	Input A or B, or A-B
Display	14 mm LED, 5 DIGIT, 999.99 range
Dimensions	145 × 66 × 240 mm

Table A.10 Specifications of the Fluke 8846A digital multimeter.

Maximum Input	1000 V DC
Input Range Resolution	100 mV 100 nV
Accuracy	± 0.0025% measurement + 0.0035% of range at 100 mV range at ≈ 23°C
Display	6.5 digits
Dimensions	3.46 × 8.56 × 11.7 in

Appendix B

Mechanical Drawings

B.1 Mechanical Drawings for Miscellaneous Parts for the Interferometer

A few new parts were designed and installed on the interferometer prior to conducting the experiments. As mentioned in Section 2.2, the extensions under two of the optics were modified to provide more clearance for the experimental model. The mechanical drawings of these extensions are shown in Figure B.1. A new extension was also constructed for the small mirror assembly, also shown in Figure B.1. A new mounting system was designed for the small mirror that reflects the image from the spherical mirror to the camera. Figure B.2 shows a mechanical drawing and a 3-D view of the entire assembly. The system is mounted on a 65 mm square metric low profile magnetic base (Edmund Industrial Optics #NT55-527). The magnet in this base can be turned on or off so that the assembly can be moved easily around the extension plate or optical table. The small mirror is attached to a thin steel rod with glue, which is mounted through a hole to a larger rod (rod #1) with a set screw. This larger rod is attached to a horizontal to vertical adapter, which is attached to a vertical rod (rod #2) that is threaded into the magnetic base. With this new mirror mounting system, the small mirror can be translated and rotated in any direction necessary for alignment. The mechanical drawings of rod #1 and rod #2 are given in Figures B.3 and B.4.

B.2 Mechanical Drawings for the Experimental Model

In Chapter 2, the experimental model is explained in detail. The mechanical drawings for the hot and cold plates were given in Figures 2.4, 2.5 and 2.6. The support structure was designed to hold these plates vertically, with the ability to adjust the channel spacing. The mechanical drawings of the other parts that were machined for the experimental model are presented in Figure B.5 through B.13.

B.3 Mechanical Drawings for the Optical Windows

New optical windows were purchased, as explained in Section 2.3.2 with the specifications given in Table A.5. These optical windows had new mounts constructed out of Plexiglas. The drawings for these new optical window mounts are given in Figure B.14. The Plexiglas panels that were attached to the optical window mounts in order to close off the sides of the experimental model are shown in Figures B.15 and B.16.
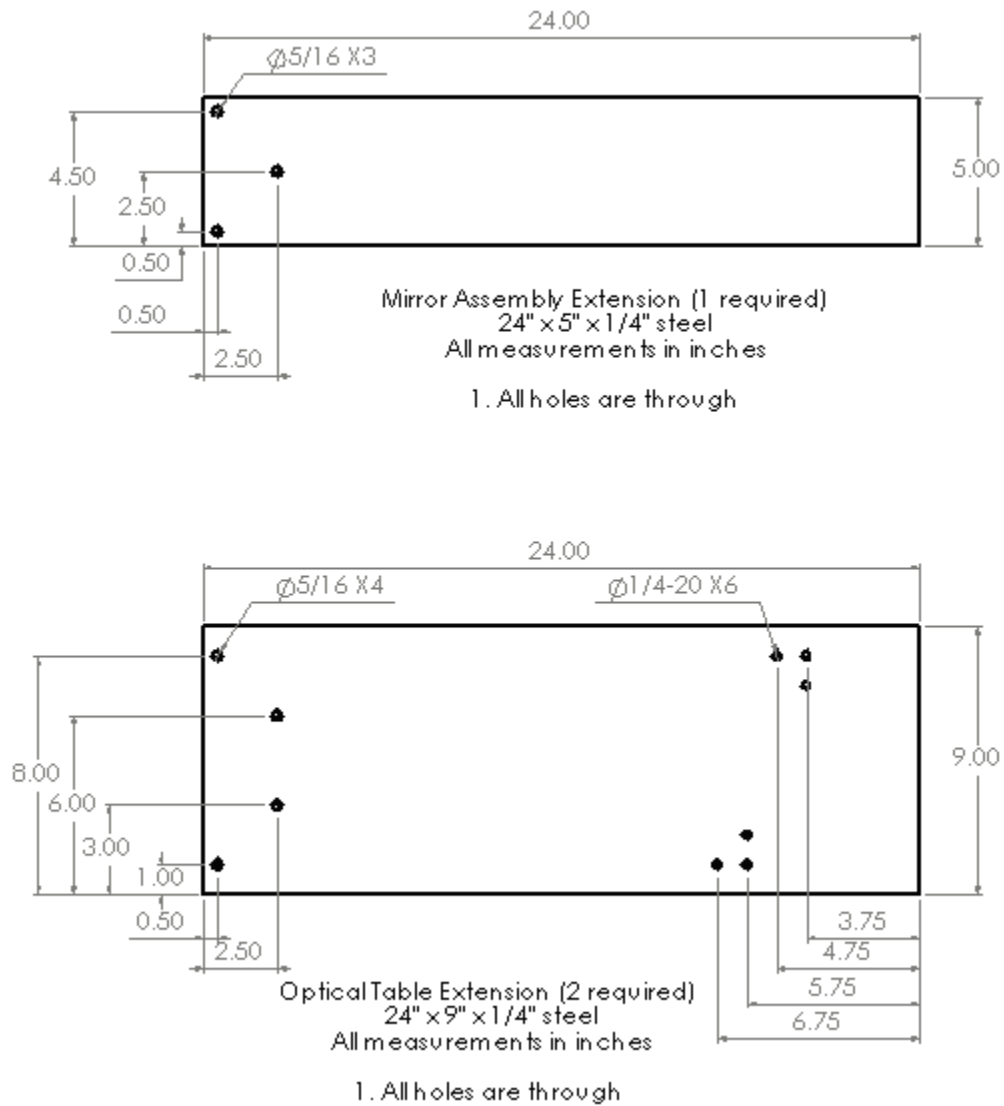
Figure B.1: Mechanical drawings of the optical table extensions for the small mirror assembly and the optics.
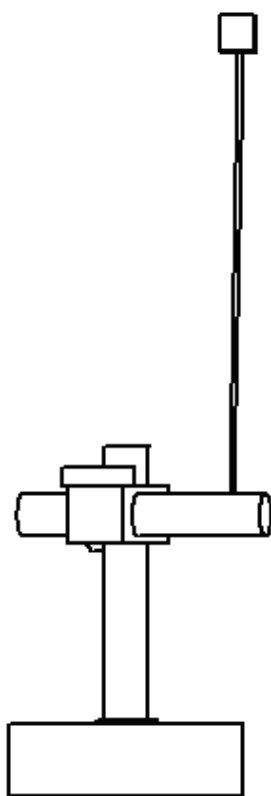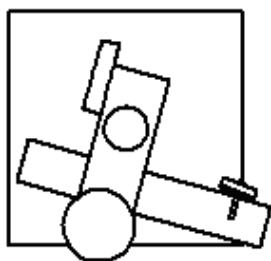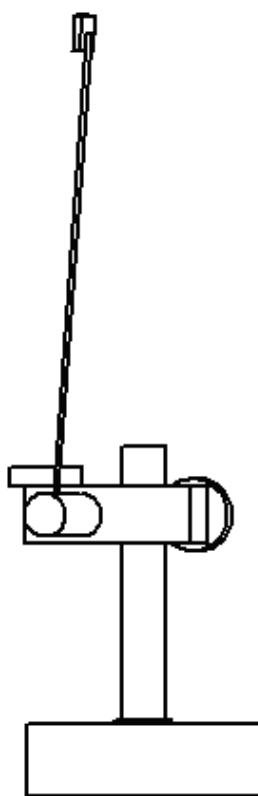
(a)   (b)
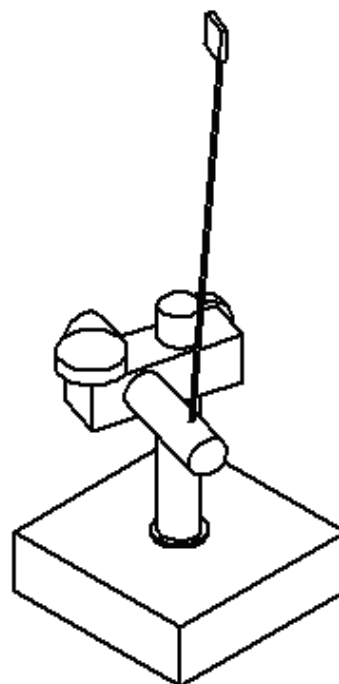
Figure B.2: (a) Mechanical drawings of the small mirror mounting system and (b) an isotropic 3-D view.
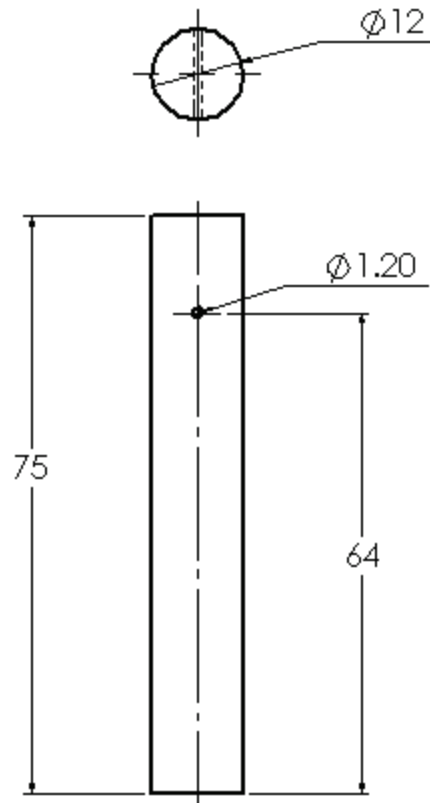
Mirror Mounting Rod #1 (Horizontal Rod)
All measurements in millimeters

1. All holes are through
2. A set screw was added to the 1.2 mm hole to hold the tiny mirror in place

Figure B.3: Mechanical drawings of mirror mounting rod #1 (horizontal rod).

Mirror Mounting Rod #2 (Veritcal Rod)
All measurements are in millimeters

1. Thread at the bottom of the rod is M16x1
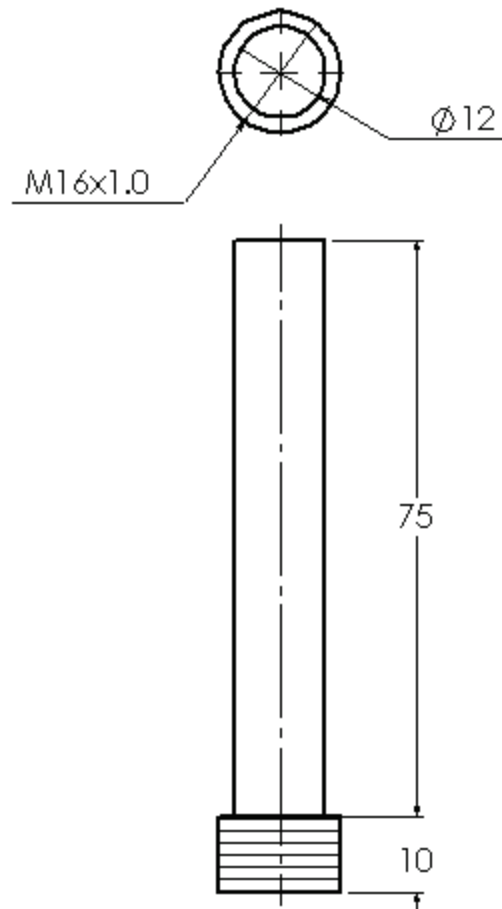
Figure B.4: Mechanical drawings of mirror mounting rod #2 (vertical rod).

Figure B.5: Mechanical drawing of the base plate.
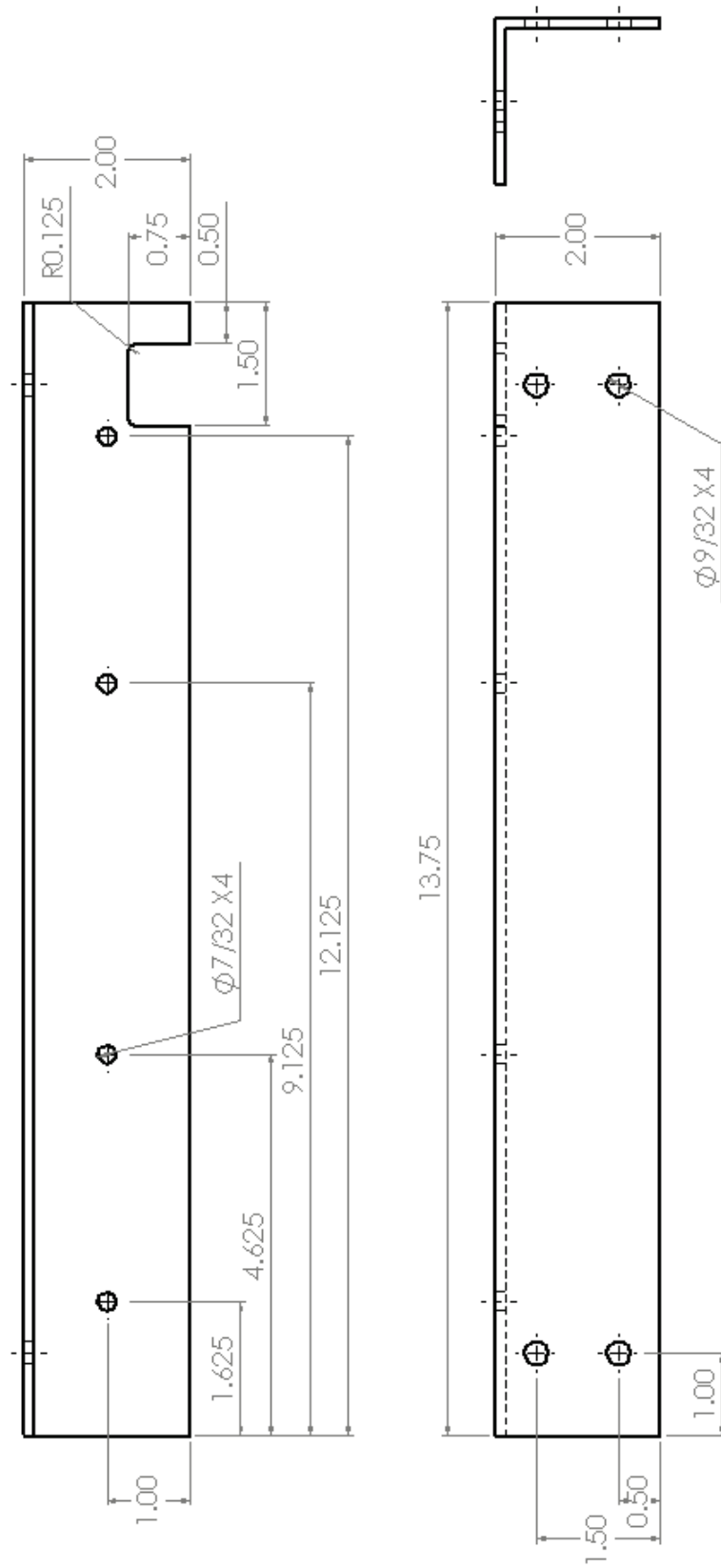
Figure B.6: Mechanical drawing of the bottom horizontal support brackets.

Horizontal Support Top (2 Required)
2" x 2" x 1/8" angle aluminum
All measurements in inches

1. All holes through
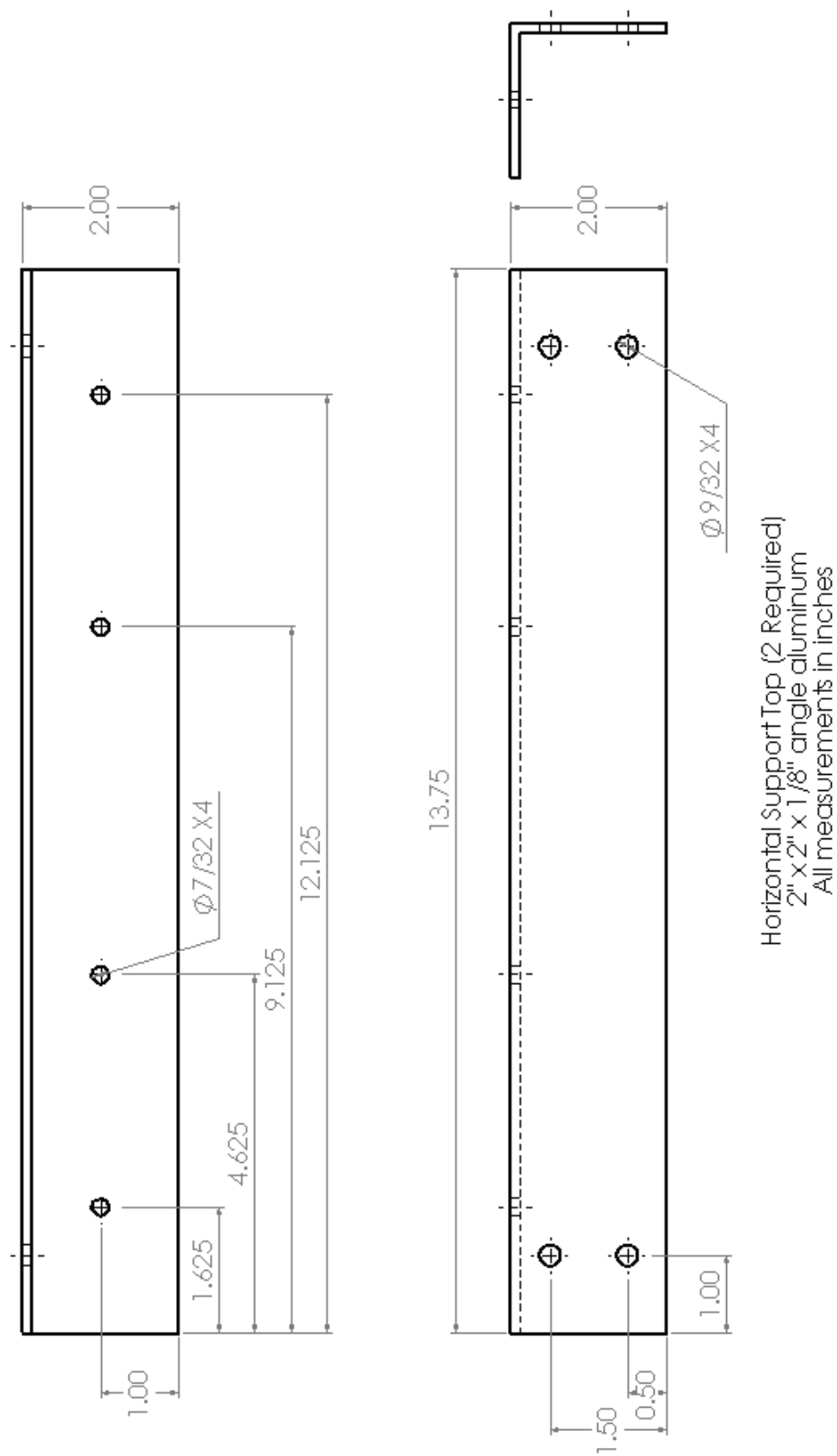
Figure B.7: Mechanical drawing of the top horizontal support brackets.
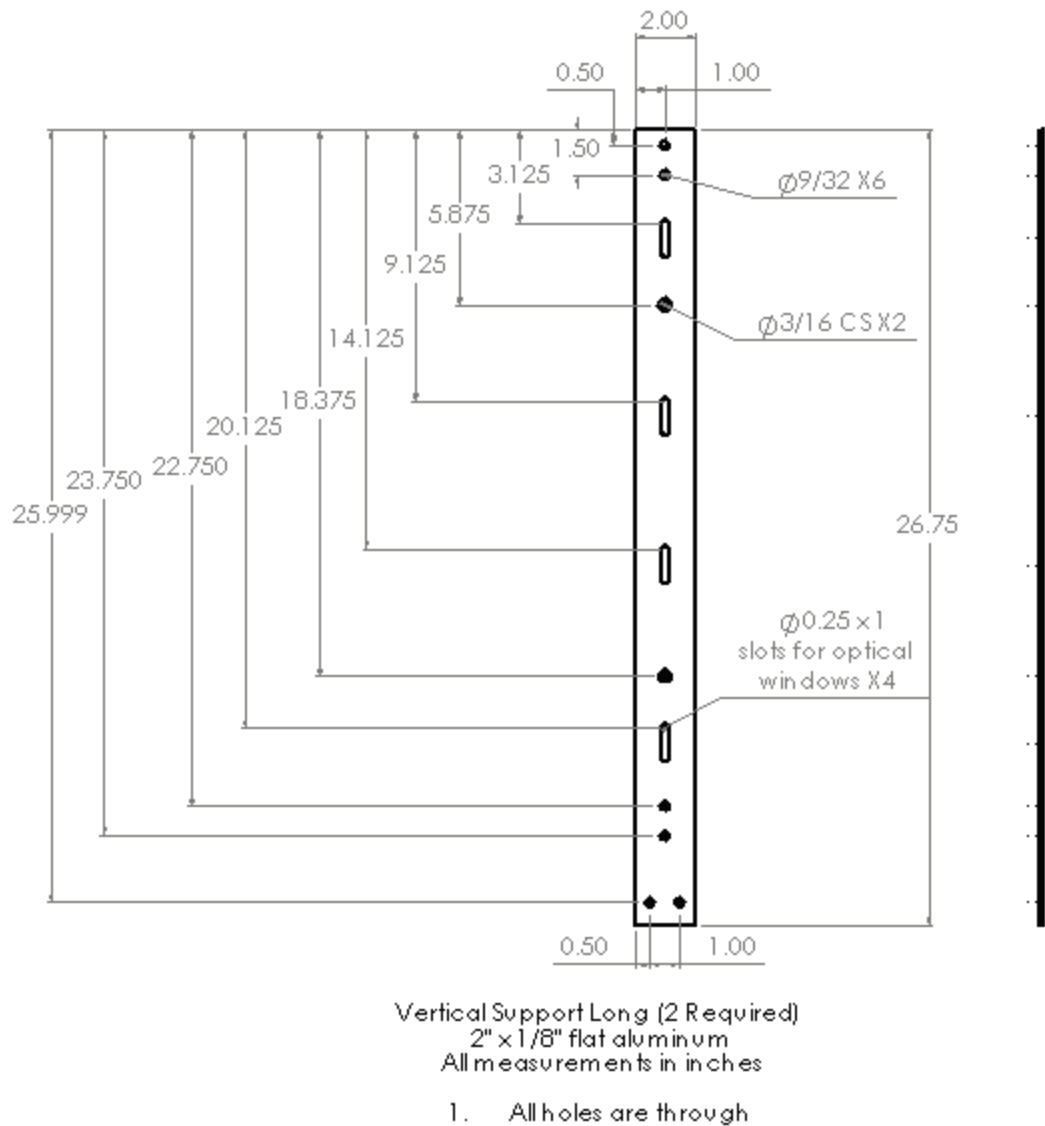
Figure B.8: Mechanical drawing of the longer vertical support brackets.
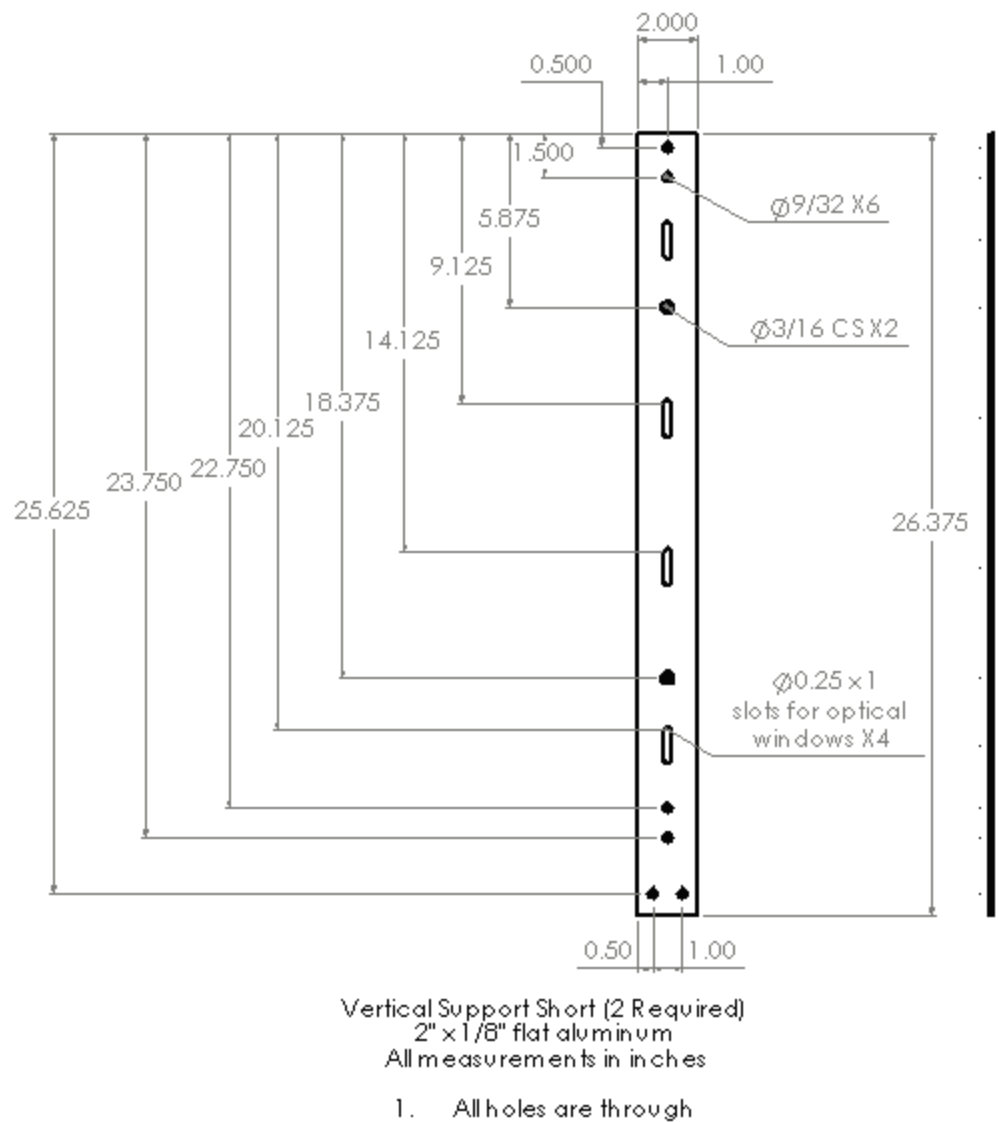
Figure B.9: Mechanical drawing of the shorter vertical support brackets.

Angle Bracket with 1/4" holes (10 required)
2" x 2" x 1/4" angle aluminum
All measurements in inches

1. All holes are through

Ø9/32 X3

2.00

2.00

1.00

1.00

2.00

1.50

0.50

1.00
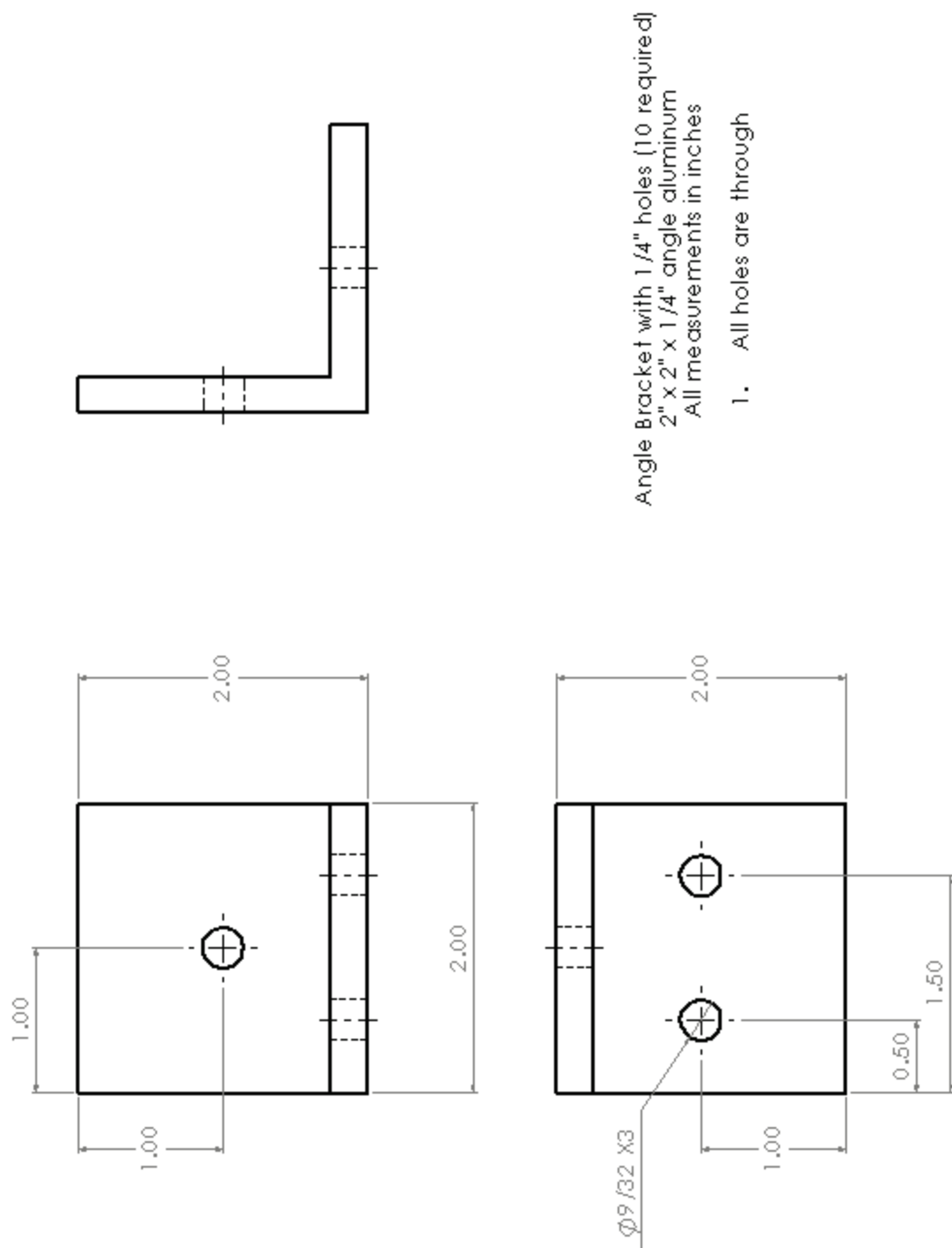
Figure B.10: Mechanical drawing of angle brackets with 1/4 inch holes.

Angle Bracket for Slider (2 required)
2" x 1.5" x 1/4" angle aluminum
All measurements are in inches

1. All holes are through
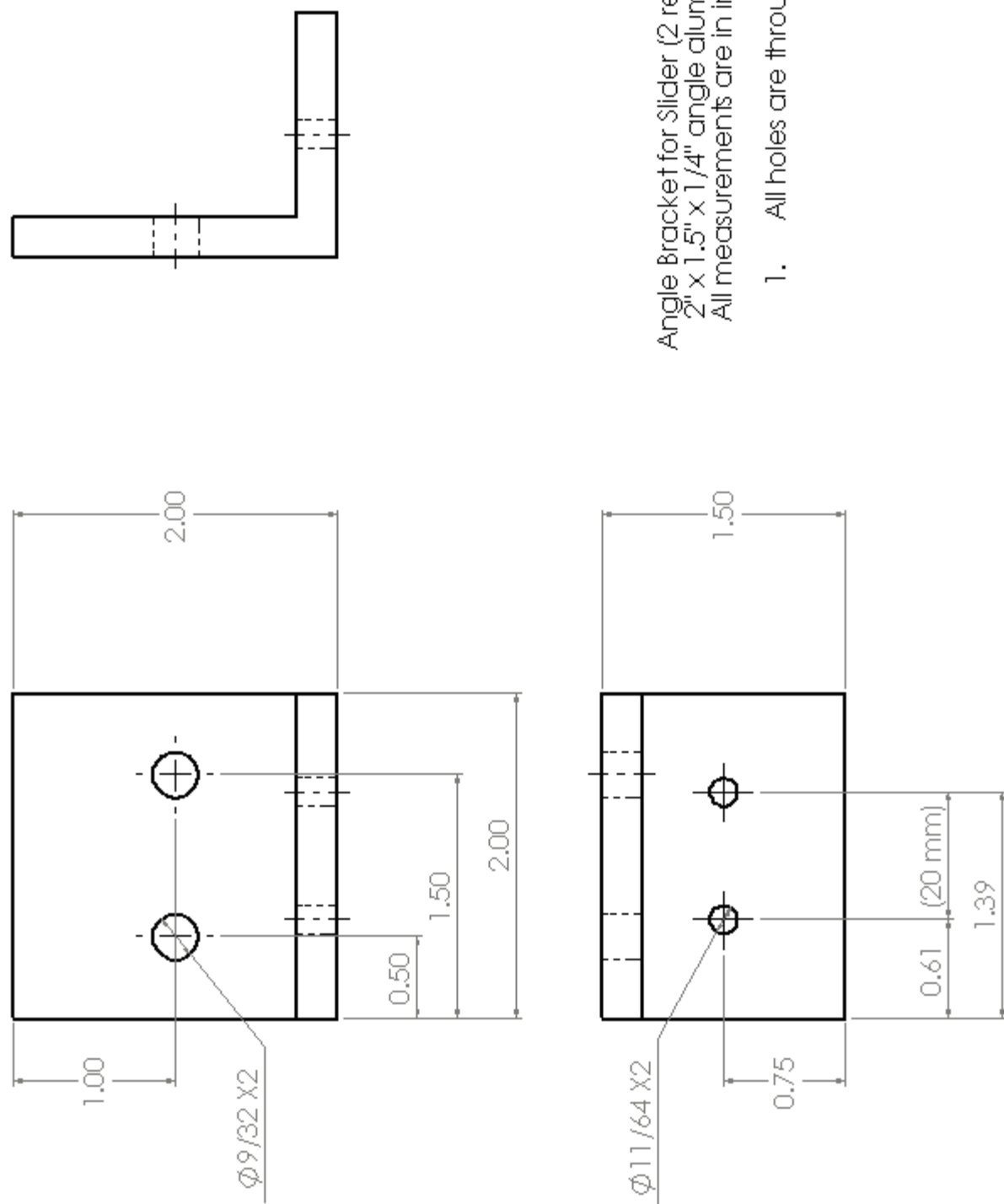
Figure B.11: Mechanical drawing of angle brackets for the sliders on base plate.

126
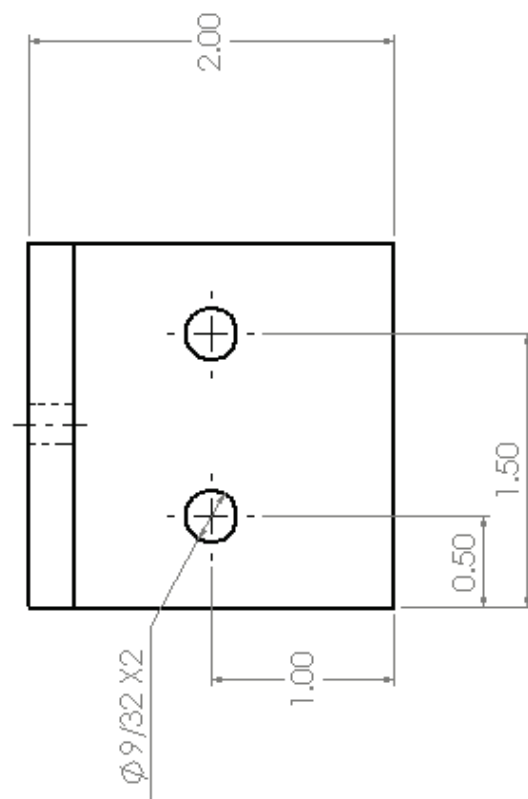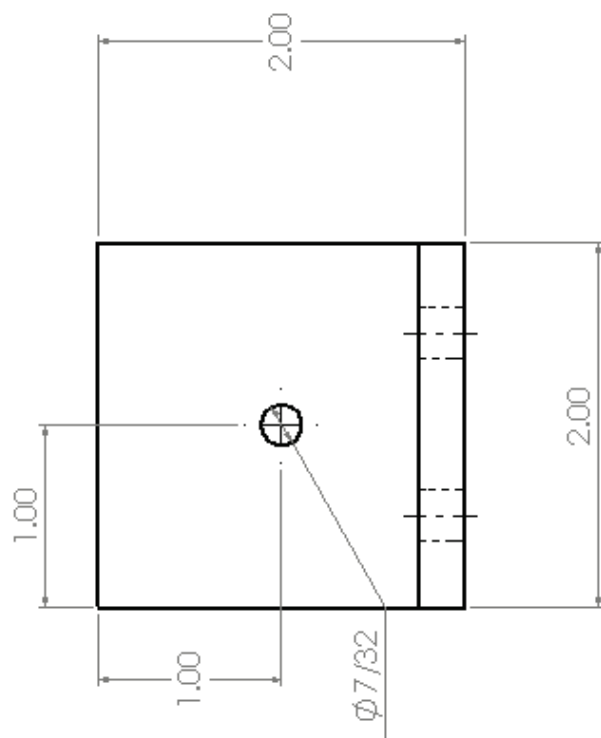
Angle Bracket for Horizontal Supports (8 required)
2" x 2" x 1/4" angle aluminum
All measurements in inches

1. All holes are through

2.00

2.00

2.00

1.00

1.00

Ø 7/32

1.50

0.50

1.00

Ø 9/32 X2

Figure B.12: Mechanical drawing of angle brackets for the horizontal support brackets.

127

Figure B.13: Mechanical drawing of the wood backing plates.

128
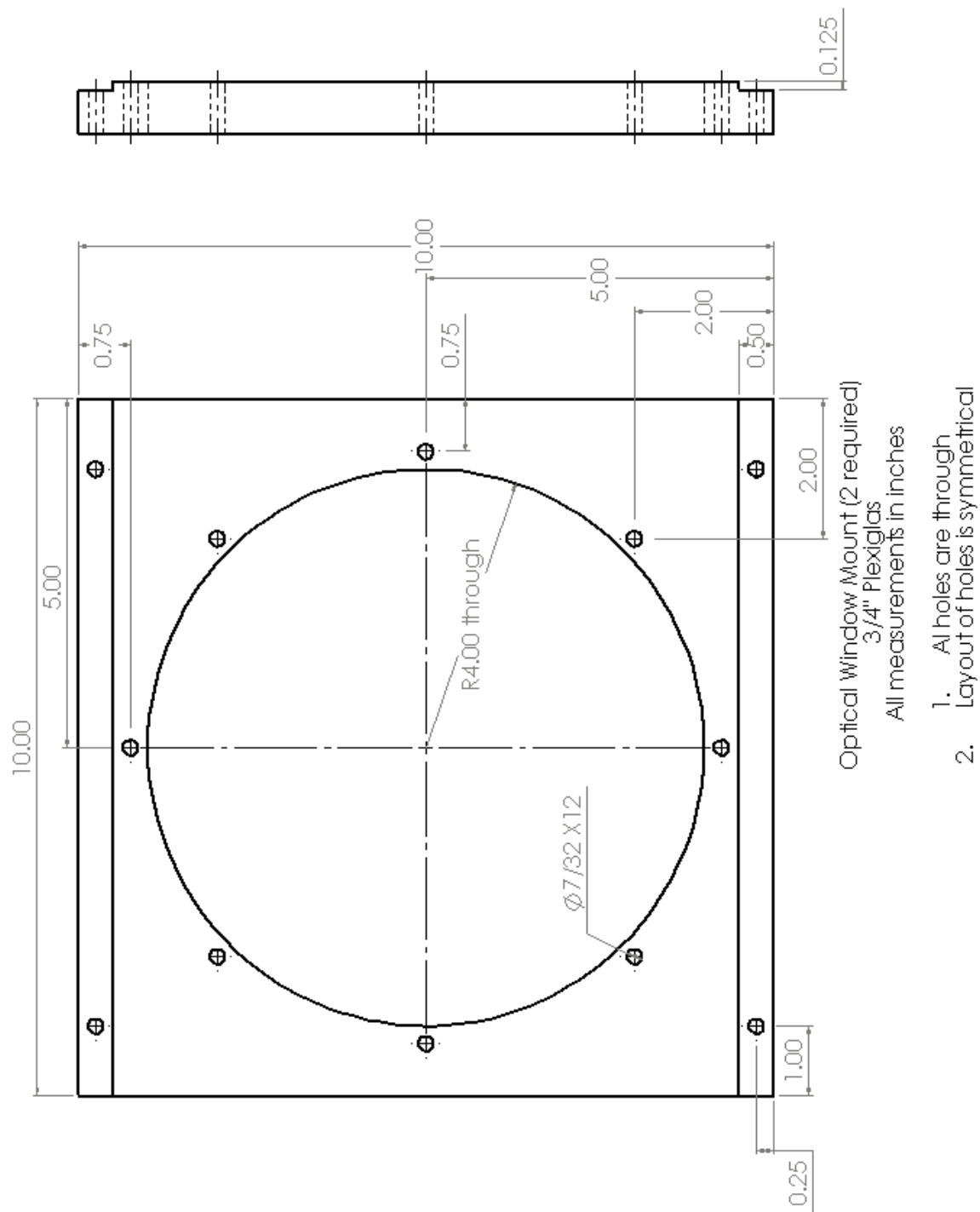
Figure B.14: Mechanical drawing of the optical window mounts.
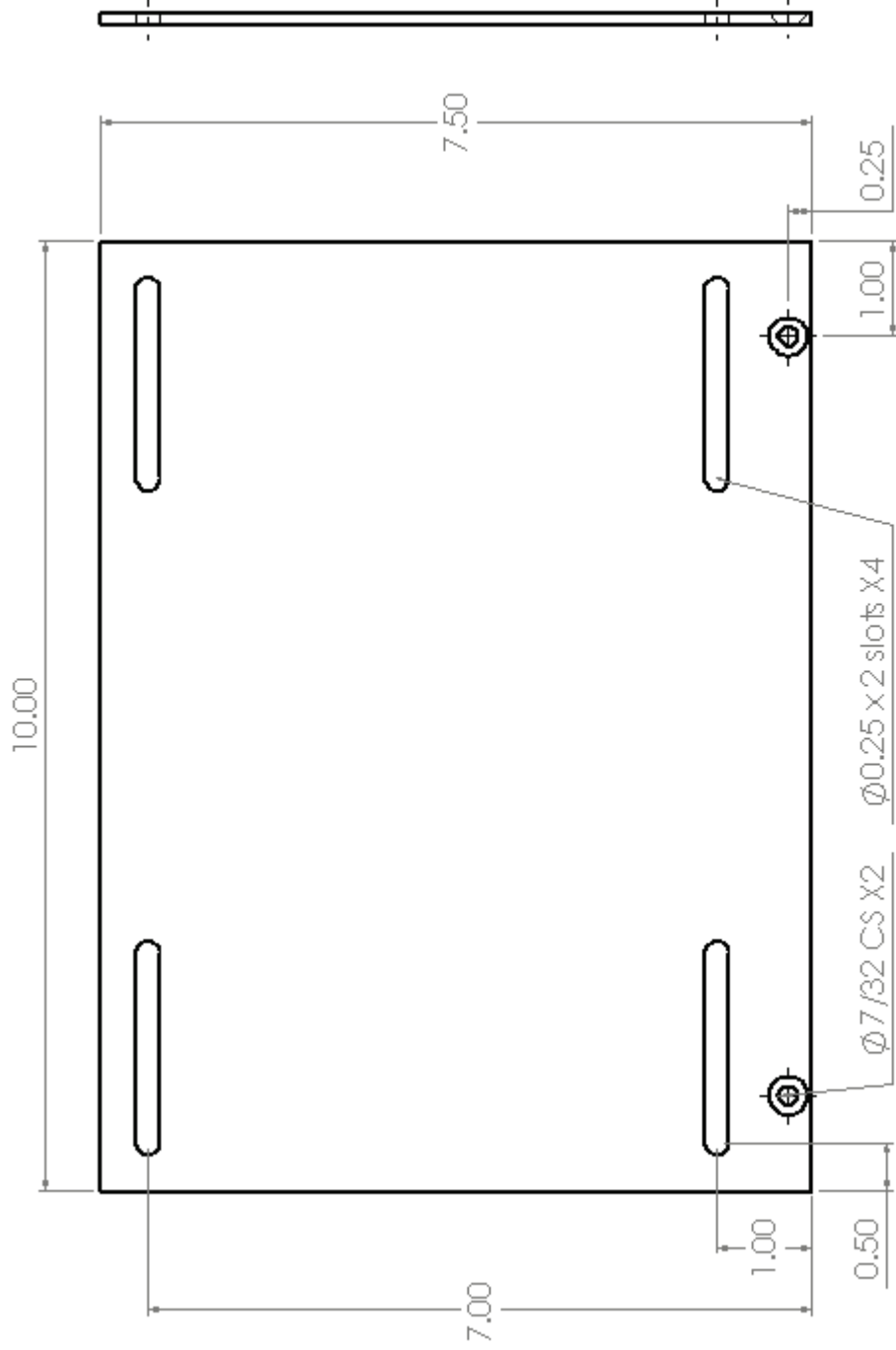
Figure B.15: Mechanical drawing of the long Plexiglas panels.

130

Figure B.16: Mechanical drawing of the short Plexiglas panels.

Appendix C

Experimental Procedure

C.1 Sample Experimental Checklist

Experiment Number: _____ Picture: Top / Bottom of Channel R_T: _____ Channel Spacing: _____

Approximate: T_H: _____ T_C: _____ T_∞: _____ Ra(b/L): _____ Date: _____

Experimental Procedure

1. Level the optical bench via the air bags

2. Collimate the beam

   a. This can be obtained in two ways.

3. Align the optics

   a. Using a paper cut-out of a circle, cover each optic individually starting with BS_1 and finishing with BS_2 to ensure that the optics are aligned properly.

4. Prepare the experimental Model

   a. Adjust the channel spacing to the desired distance and check with gauge blocks

   b. Install the optical windows and align them with each other

   c. Make sure thermocouples, thermopiles, and platinum resistance thermometers are plugged in. Make sure constant temperature water bath (CTWB) hoses are clamped onto the model.

   d. If model is not already at ambient temperature, set CTWB to ambient. Adjust CTWB to make sure both thermopiles read below 0.02 mV (≈ 0.1 °C).

   e. Turn on digital multi-meters, thermocouple reader, platinum resistance thermometers, and computer

5. Place the experimental model in the test beam

6. Block the reference beam

   a. Adjust the height of the table to the desired shot and to align the optical windows

   b. Align the experimental model using the plumb bob and level

   c. Carefully install the eddy tent over the experimental model

   d. Move the table and model to roughly align the test beam by using the reflections off the channel walls

e. Align the test beam more precisely by using a white card beyond the experimental model, inclined sharply to the beam to magnify the locating pins and reflections off the channel walls

f. After these steps do not touch BS_1, M_{TEST}, or the experimental model

7. Unblock the reference beam and cover the spherical mirror with a white card for "near field – far field focusing"

   a. Place an object in the far field between the parabolic mirror and BS_1

   b. Place an object in the near field between BS_2 and the spherical mirror

   c. Using M_{REF} and BS_2 focus the two objects on the white card. This is an iterative process that may take several adjustments.

   d. Once both objects are in focus, carefully adjust BS_2 until the desired finite fringe or infinite fringe pattern is achieved

   e. After these steps do not touch M_{REF} or BS_2

8. Camera positioning

   a. Remove the white card from in front of the spherical mirror

   b. Adjust the small mirror so that it reflects the image from the spherical mirror 90° towards the camera and so that the shadow of the mirror is in the center line of the optics

   c. Measure the height off the floor of the small mirror

   d. Measure the height of the shadow of the small mirror on the wall

   e. Adjust the angle of the small mirror so these two are the same distance

   f. Place the camera in position parallel with the output from the small mirror

   g. Maximize the area on the frosted screen of the camera and level the camera.

   h. Plug camera into computer

   i. Turn off the laser and focus the camera on a light placed at ½ the length of the experimental model

   j. Turn laser back on. Do not move camera. It is crucial that the camera, optics, and experimental model are not bumped beyond this step.

9. Taking Pictures

   a. Start Capture One Pro on computer. Ensure the capture name and job name are set and that the camera is using ISO 50

b. Block the reference beam once again and place the horizontal reference into the beam. Put the NDX4 neutral density filter in place in front of the laser. Slide digital back over on camera, close the shutter and cock the camera. Turn off the lights (including computer monitor) and take a scale photo of the unheated model. Turn on lights and check picture on computer

c. Unblock the reference beam, ensure the model is still aligned with the desired fringe pattern. Check that finite fringes bend up on hot surface – check with hand

d. Cock camera, turn off lights and take a picture of the preheated experimental model fringe pattern. Turn on lights and check picture on camera   Time: _____

e. Set the CTWB to the desired temperatures and allow them to come to steady state. Make periodic checks and adjustments to the CTWB to ensure the thermopiles / thermocouples are reading the desired temperatures

f. Cock camera, move into position, and wait five minutes for air in room to settle. Turn off the lights and take picture of the heated model. Turn lights on and check picture.

g. Repeat step f to create a second/third photo.   Time: _____

h. Record data from the thermopiles, thermocouples, room temperature, room pressure, and platinum resistance thermometer (PRT):
TP_1: _____ TP_2: _____ T_∞: _____   Uncorrected Pressure: _____ T_{bar}: _____
Thermocouples 1: _____   2: _____   3: _____   4: _____   5: _____   6: _____
PRT A: _____   B: _____   A – B: _____

i. Set the CTWB to ambient temperature and allow them to come to steady state. Again make periodic checks and adjustments to make sure both thermopiles read below 0.02 mV

j. Cock the camera, turn off the lights, and take a picture of the post-heated experimental model. Turn lights on and check photo.   Time: _____

10. Post processing
   a. Ensure all the proper settings in Capture One Pro
      i. Starting with the Quick Tab: make sure the following are set
         1. ICC Profile – Phase One P 45 B&W
         2. Curve – Linear Response

3. Mode – Custom

4. Kelvin – 1155 K

5. Tint – 0

 ii. The Exposure Tab: leave all settings at 0

 iii. The Lens Tab: do not use any lens correction

 iv. The Details Tab: Sharpening can be ignored as it will be disabled and leave the Noise Reduction settings at default

  1. Luminance – 25

  2. Color – 40

 v. The Output Tab: Make sure the sharpening tick box is checked to disabled and the ICC profile is set to Embedded Camera Profile. Set the output name and click the process button. The picture is exported as an 8 bit TIFF format

b. Use photo-editing software to convert the photo to grayscale. Re-save the file (usually into a portable drive).

c. Run picture through custom MATLAB image processing code

d. Extract the fringe gradient spacing information and determine temperature and heat transfer data

C.2 Coarse Alignment of the Interferometer

Normally the interferometer is left in a state that is close to this coarse alignment, so depending on how long the interferometer has sat idle, this can take as little as a few minutes, or up to 3 or 4 hours to complete even for an experienced operator. In the current case, the primary optical components were upgraded (as discussed in Section 2.2). So, a full alignment was necessary. The general procedure is outlined below:

1)   The optical bench is leveled via the airbags underneath the table, using a large carpenter's level.

2)   Next the beam is collimated, which can be performed by two methods.

(i)   One method is to place a white board behind the reflecting beam of the first beam splitter (BS_1). Move the laser forward or backwards in its mount until no "ghost fringes" appear in the output on the white board. These "ghost fringes" are low intensity wedge fringes that appear by light reflecting off the back surface of the beam splitter interfering with the light reflecting of the front surface. A uniform field guarantees that the laser is at the focal point of the parabolic mirror and the reflected light beams are parallel.

(ii)   The second method uses a commercial collimation tester in the light beam after the parabolic mirror, but it is not as accurate as the first method.

3)   Once the beam has been collimated, the optics can be aligned to each other. Using a paper cut-out and starting with BS_1, cover each optic to ensure that the beam is aligned in the center of the optic. Adjust the parabolic mirror to align the beam to BS_1 and rotate BS_1 to align the beam to M_{TEST}. For M_{REF}, move the optic to align it to the beam passing through BS_1. For BS_2, rotate M_{TEST} to align the beam to the front surface and rotate M_{REF} to align the beam to the back surface. Then move the spherical mirror to align the beam for output to the camera.

4)   Once all the optics have been aligned to the light beam, they need near field – far field focusing. Place an object in the far field between BS_1 and the parabolic mirror (Point A in Figure 2.1) and place an object in the near field between BS_2 and the spherical mirror (Point B in Figure 2.1). Cover the spherical mirror with a white card in order to view the shadows. Using either (or both) BS_1 and M_{REF}, focus the far field object on the white card. Then use BS_2 to focus the near field object on the white card. This is an iterative process and may take several adjustments, as focusing the near field object can cause the far field object to be out of focus and vice versa. Once both objects are in focus, a fringe pattern should be visible on the white card. Adjust BS_2 until the desired finite or infinite fringe pattern is achieved.

Now the interferometer is setup and ready for the experimental model. Step 4 is not necessary because it will need to be repeated when the experimental model is placed in the interferometer, but it helps keep the optics close to alignment when setting up the experimental model in the

interferometer. It is advised to avoid bumping the optical table, although it is not critical at this point.

C.3 Fine Alignment of the Interferometer

1)   The experimental model is placed in the test beam, levelled and roughly aligned. The model is leveled horizontally using a spirit level and vertically using a plumb bob.

2)   The reference beam is blocked. A white card is placed at an inclined angle (to magnify the output) just beyond the experimental model. The flat mirror of the test beam (M_{TEST}) is rotated to align the model. The model is aligned horizontally when the reflections off of both channel walls are eliminated. It is aligned vertically by lining up two locating pins (one at the front and one at the back of one of the channel walls). Once these steps are completed, M_{TEST} and BS_1 are not moved.

3)   The reference beam is unblocked and the white card removed. The far field – near field focusing needs to be revisited because aligning the beam to the experimental model has caused the reference beam to be out of alignment. Using the same method as in step 4 in Appendix C.2, the desired fringe pattern is set. For this fine alignment, only M_{REF} is rotated to adjust the far field and only BS_2 is used to adjust the near field. At this point, M_{REF} and BS_2 were not moved.

C.4 Still Image Camera Procedure

This is the procedure for taking pictures with the still image camera. It also includes some of the post processing required of the images.

1)   The spherical mirror is aligned with the output from BS_2 and levelled. It is then focused onto a small flat mirror that reflects the image roughly 90° from the optical table towards the camera. The height of the mirror is measured and checked with the output on the wall to ensure the beam is reflecting off the small mirror parallel to the floor.

2) The camera is moved into position to capture the output from the small flat mirror. It is aligned with the output beam and levelled, while ensuring the output is maximized on the frosted screen of the still image camera.

3) The laser is turned off and a light source is placed at ½ the length of the experimental model (Hauf and Grigull 1970). The camera is then focused on this light source to reduce refraction error. (This camera can be focused by adjusting the bellows.) The laser is then turned back on. (It should be noted that some researchers focus the camera at 1/3 the length of the model (Mehta and Black 1977).)

4) The computer is turned on and the camera is connected to the computer. A neutral density filter (NDX4) is placed and aligned in front of the laser. A test image is then taken to ensure that the output is aligned properly and that there are no large imperfections visible. (One of the minor problems that occurs is the small flat mirror has some imperfections. These can be avoided by moving the spherical mirror slightly to reflect off of a different spot on the flat mirror.) If there are any problems with the output at this point, corrections are made and some of the previous steps may need to be repeated. Note that the optical bench, experimental model, and camera should not be touched after this point.

5) The two constant temperature water baths (CTWB) are set to the ambient temperature and all the measurement instruments are turned on. The digital multimeters are used to ensure the two channel walls are at ambient temperature. The software Capture One Pro (2008) is started on the computer and double checked to make sure that the camera is using ISO 50.

6) A scale photo of the unheated model is taken first. The reference beam is blocked and the horizontal scale reference is placed into the beam and aligned so that it is visible between the channel walls. The digital back is slid over on the camera mount and the shutter is closed and cocked. All the lights are turned off, including the monitor of the computer, and a photograph is taken.

7) The reference beam is unblocked and the horizontal scale is removed. A white card with horizontal reference lines is placed in front of the spherical mirror and BS$_2$ is rotated to

align the finite fringes horizontally. Once the desired finite fringe pattern is achieved, the white card is removed. The camera is cocked, the lights are turned off and a photograph is taken of the finite fringe pattern.

8)   The constant temperature water baths are set to the desired temperatures and allowed to settle for 20 – 30 minutes. The operator enters the room slowly, sits down, and waits 5 minutes to allow any disturbances caused by entering the room to settle. The camera is then cocked, the lights turned off and a photograph taken of the heated model. (Two or three pictures are taken.)

9)   The thermopiles, thermocouples, and platinum resistance thermometers are recorded. The ambient temperature is recorded using a precision glass thermometer and the absolute room pressure is recorded using a mercury barometer. (The absolute room pressure is also corrected for both room temperature and gravity.) Once all the data is recorded, the CTWBs are set to the ambient temperature again.

10) Once the CTWBs are at room temperature, the camera is cocked, the lights turned off and a photograph taken of the finite fringe pattern. This photograph and the photograph of the preheated model are used to apply a small correction due to fringe shift error in the calculations.

11) The pictures need to be processed and exported in Capture One Pro. Under the "Quick" tab, the "ICC Profile" needs to be set at "Phase One P 45 B&W", the "curve" to "Linear Response", "Kelvin" at 1155K, and "Tint" to 0. Then on the "Output" Tab, set the "Sharpening" checkbox to "disabled" and set the job name. The "process" button exports an 8-bit TIFF image.

12) The exported picture file is then converted to a black & white image using photo editing software. The image is then processed through a custom MATLAB image processing code to extract the fringe spacing data. This fringe spacing data is then used to determine the heat transfer rate using a spreadsheet.

C.5 High Speed Camera Procedure

When using the high-speed camera, the procedure is slightly different from the still camera. This is mostly due to differences in the resolution of the two cameras. The high-speed camera has a lower resolution, which means that multiple captures will be needed to analyze the entire channel. This also affects determining the scale factor and adds extra calculations to determine the location of each capture.

1)   When using the high-speed camera, some minor modifications need to be made to the interferometer. The focal plane was adjusted inwards so that the scale factor was similar to the still image camera. So the spherical mirror and small mirror need to be moved further away from BS_2 and the experimental model may need to be moved closer to M_{TEST}. This will involve redoing the fine alignment of the interferometer (Appendix C.3).

2)   The spherical mirror is aligned with the output from BS_2 and levelled. It is then focused onto a small flat mirror that reflects the image roughly 90° from the optical table towards the camera. The height of the small mirror is measured and checked with the output on the wall to ensure the beam is reflecting off the small mirror parallel to the floor.

3)   There is no output screen on the high speed camera, so the computer is turned on and the camera is connected to the computer. Also the camera power cord is plugged in. Motion Pro X is started, so the output of the camera is visible on the monitor. The laser is turned off and a light source is placed at ½ the length of the experimental model. Using a white card, the focal point of the light source reflecting off the small flat mirror is found and the distance measured from the small mirror.

4)   The camera is moved into position at roughly the distance measured to the small mirror. It is aligned with the output beam and levelled. Using the translating device and the output on the monitor, fine adjustments are made to focus the camera. The camera is focused on this light source to reduce refraction error. The laser is then turned back on.

5)   The camera is then translated up and down the output to ensure that the entire area of interest can be captured and there are no large imperfections visible. If there are any

problems with the output at this point, corrections are made and some of the previous steps may need to be repeated.

6) Once the camera is in position, the CTWBs are set to the ambient temperature and all the measurement devices are turned on.

7) Again, the reference beam is blocked and the horizontal scale is placed and aligned in the beam. The camera is positioned such that the horizontal scale is visible in the output using the translating device. The lights are turned off and the exposure settings in Motion Pro X are adjusted properly. Then a single frame is captured.

8) This single frame is then analyzed in either photo editing software or MATLAB to determine the pixel distance between the two pins on the horizontal scale. This is then used to calculate the horizontal scale factor.

9) The high speed camera is moved vertically until the top locating pin in aligned with the top of the output in the software. The counter on the vertical component of the translating device is recorded. The camera is then moved down the channel until the top of the output is aligned with the bottom locating pin. Again the counter is recorded. The two counter numbers are then used to calculate the vertical scale factor. It is compared to the horizontal scale factor to ensure that the camera is reasonably aligned and square with the output beam. (Normally the scale factors are within less than 1% of each other.)

10) Using the scale factors and counter numbers, calculations are made to determine how many captures are needed and the locations of these captures. The high-speed camera is then moved into position for the first capture (usually either top or bottom of the channel).

11) The reference beam is unblocked and the horizontal scale is removed. A white card with horizontal lines is placed in front of the spherical mirror and the finite fringe pattern is set. The white card is removed and the lights are turned off. A single frame is captured of the unheated model fringe pattern.

12) The CTWBs are set to the desired temperature and allowed to settle for 20 to 30 minutes. The room pressure is recorded. The operator enters the room slowly and then waits 5

minutes for the disturbances to settle. The software is then set to the desired frame rate and total time for the capture. The exposure setting is adjusted to make sure the pixel intensity values were not saturated in the intensity histogram. The lights are turned off and the images are recorded with the software and then saved.

13) The thermopiles, thermocouples, PRTs, and room temperature are recorded. The camera is then moved into the next capture position.

14) Steps 12 and 13 are repeated until all the necessary captures are completed. The room total pressure is then recorded again and the CTWBs are set to the ambient temperature and allowed to settle for 20 – 30 minutes.

15) The lights are turned off and a single frame is recorded of the unheated model. This image and the image of the preheated model are used as a correction due to fringe shift in the calculations.

16) Each capture is processed through a custom MATLAB image processing code to extract the fringe spacing data. This data is then used in a spreadsheet to determine the heat transfer rates. Each frame is analyzed giving local heat transfer data at each time step. A time average can then be calculated in the spreadsheet. (The high speed camera only takes black and white photographs, so the images do not need to be converted through photo editing software.)

Appendix D

Sample Calculations

D.1: Measured Data

A typical set of experimental calculations is provided to demonstrate how the heat transfer results were obtained. The case analyzed here is for $R_T = -0.5$ at $A = 176$. The composite infinite fringe interferogram is given in Figure 5.4(c), but the finite fringe interferogram was used for analysis, which is shown in Figure D.1.

The dimensions of the experimental model are given in Table D.1. The dimensions of the channel plates were given in inches and are converted to meters. The thermocouples in the cold wall of the channel, the two thermopiles and the absolute room pressure were recorded immediately after the interferogram was taken. These values are recorded in Table D.2. The barometers pressure and temperature were recorded because the pressure needs to be corrected for temperature and gravity. The calculations also use some constants in the various equations, so they are given in Table D.3.

Table D.1: Dimensions of the experimental model.

Plate width in beam direction	W	13.980 inches	0.355 m
Plate length	L	10.400 inches	0.264 m
Channel spacing	b		0.015 m

Table D.2: Recorded data from the experiment.

Cold wall temperature	T_C	17.9 °C
Thermopile 1 (hot and cold walls of channel)	TP_1	5.5389 mV
Thermopile 2 (hot wall and ambient)	TP_2	3.7218 mV
Barometric pressure	P	750.7 mm Hg
Lab temperature (for barometer)	T_{bar}	24 °C
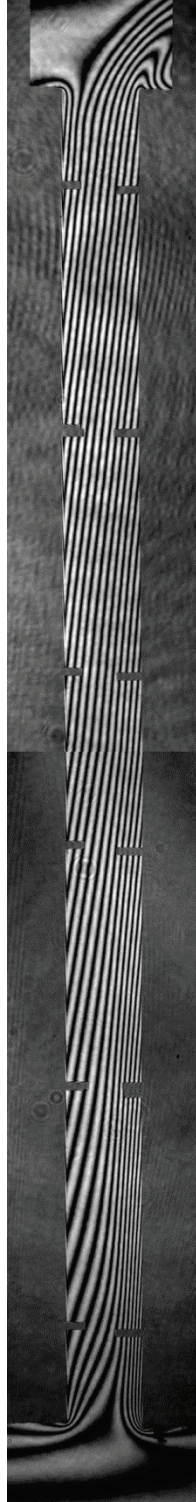
Figure D.1: Composite finite fringe interferogram of $R_T = -0.5$ at $A = 17.6$.

Table D.3: Constants used for the sample calculations.

Gravity	g	9.805 m/s^2
Laser wavelength	λ_0	632.8×10^{-9} m
Gladstone-Dale constant	G	0.226×10^{-3} m^3/kg
Gas constant for air	R	287.1 J/kgK

D.2: Thermopile Calculations

The cold wall temperature was measured using thermocouples as the reference temperature for the thermopile calculations. First, the cold wall temperature $T_C = 17.9$ °C needs to be converted from a temperature to a voltage using (Burns et al. 1993):

$$E = C_0 + C_1 T + C_2 T^2 + C_3 T^3 + C_4 T^4 + C_5 T^5 + C_6 T^6 + C_7 T^7 + C_8 T^8 \tag{D.1}$$

$$E_C = 705.2\mu V$$

where T is T_C and is expressed in °C, E_C is the voltage of the cold wall temperature and the constants C_0 through C_8 are listed in Table D.4.

The voltages of the hot wall temperature and ambient temperature need to be determined using the thermopile voltages. The thermopile works by combining the voltages of each bead:

$$TP = NE_1 + NE_2 \tag{D.2}$$

Table D.4: Constants for Equation (D.1).

C_0	0
C_1	3.875×10^{1}
C_2	3.329×10^{-2}
C_3	2.062×10^{-4}
C_4	-2.188×10^{-6}
C_5	1.100×10^{-8}
C_6	-3.082×10^{-11}
C_7	4.548×10^{-14}
C_8	-2.751×10^{-17}

where TP is the thermopile voltage, N is the number of thermopile pairs, and E_1 and E_2 are the voltages of the two temperatures being measured by the thermopile. In this study, there were 6 thermopile pairs on each thermopile (this gives a total of 12 beads). The hot wall temperature voltage E_H can be determined with the first thermopile voltage by:

$$E_H = \frac{TP_1}{N} - E_C = \frac{5538.9}{6} - 705.2 = 1628.4 \mu V$$

And similarly using the second thermopile voltage, the ambient temperature voltage can be found:

$$E_\infty = E_H - \frac{TP_2}{N} = 1628.4 - \frac{3.7218}{6} = 1008.1 \mu V$$

Next, these voltages need to be converted to a temperature using (Burns et al. 1993):

$$T = C_0 + C_1 E + C_2 E^2 + C_3 E^3 + C_4 E^4 + C_5 E^5 + C_6 E^6 \tag{D.3}$$

where the constants are given in Table D.5.

So, T_H = 40.69 °C and T_∞ = 25.41 °C. These temperatures can be converted to Kelvin, T_H = 313.5 K, T_C = 291.1 K and T_∞ = 298.6 K.

Table D.5: Constants for Equation (D.3).

C_0	0
C_1	2.593×10^{-2}
C_2	-7.603×10^{-7}
C_3	4.638×10^{-11}
C_4	-2.165×10^{-15}
C_5	6.048×10^{-20}
C_6	-7.293×10^{-25}

D.3 Air Properties

Film Temperature

The film temperature is calculated from the hot wall, cold wall and ambient temperatures. This is consistent with studies from the literature on natural convection in vertical channels (Raithby and Hollands 1998). The film temperature is used to determine most of the air properties.

$$T_f = \left(\frac{(T_H + T_C)}{2} + T_\infty\right) \Big/ 2 = \left(\frac{(40.69 + 17.9)}{2} + 25.41\right) \Big/ 2 = 27.28°C = 300.43K$$

Total Pressure

The barometric reading needs to be corrected for local gravity and temperature, and converted to Pascal. The gravity correction for latitude of 43° (Toronto, Ontario) is−0.000234 mm Hg and the temperature correction for 24 °C is−0.003905 mm Hg. These need to be multiplied by the pressure and added:

$$P = 750.7 + (-0.000234 \cdot 750.7) + (-0.003905 \cdot 750.7) = 747.6\text{mm Hg}$$

The total pressure is 99,671 Pa.

Volumetric Expansion Coefficient

$$\beta = \frac{1}{T_f} = \frac{1}{300.43} = 3.329 \times 10^{-3} \frac{1}{K}$$

Density

The density is determined using the incompressible ideal gas law:

$$\rho = \frac{P}{RT_f} = \frac{99671}{287.1 \cdot 300.43} = 1.156 \frac{\text{kg}}{\text{m}^3}$$

Dynamic Viscosity

The dynamic viscosity is determined by linear interpolation of the data of Touloukian et al. (1975) using $T_f = 300.43$ K, which gives $\mu = 1.855 \times 10^{-5}$ kg/ms

Thermal Conductivity

The thermal conductivity is determined by linear interpolation of the data of Touloukian et al. (1970). The thermal conductivity at $T_f = 300.43$ K is $K = 0.02617$ W/mK and at the cold wall temperature, $K_s = 0.02546$ W/mK.

Specific Heat

The specific heat is determined using Equation (D.4) from Touloukian and Makita (1970) with $T = T_f = 300.43$ K:

$$c_p = \left(0.250 - 7.552 \times 10^{-5} T^1 + 1.692 \times 10^{-7} T^2 - 6.461 \times 10^{-11} T^3\right) \cdot 4184$$

(D.4)

$$c_p = 1006.3 \frac{J}{kgK}$$

Prandtl Number

$$Pr = \frac{c_p \mu}{K} = \frac{1006.3 \cdot 1.855 \times 10^{-5}}{0.02617} = 0.713$$

D.4 Modified Rayleigh Number

The characteristic temperature difference is:

$$\overline{\Delta T} = \frac{(T_H + T_C)}{2} - T_\infty = \frac{(40.39 + 17.90)}{2} - 25.41 = 3.73 K$$

From Equation (1.5)

$$Ra(b/L) = \frac{g \beta \overline{\Delta T} \rho^2 b^3}{\mu^2} Pr \frac{b}{L}$$

$$Ra(b/L) = \frac{9.805 \cdot 3.329 \times 10^{-3} \cdot 3.73 \cdot (1.156)^2 \cdot (0.015)^3}{(1.855 \times 10^{-5})^2} 0.713 \frac{0.015}{0.2642} = 64.7$$

150

D.5 Local Heat Transfer

The pixel dimensions used to determine the scale factors were measured from the scale factor image taken before the experiment using photo editing software. The horizontal scale factor is:

$$SF_H = \frac{D_{actual}}{N_{pixels}} = \frac{0.2744(0.0254)}{242} = 2.880 \times 10^{-5} \frac{m}{pixels}$$

and the vertical scale factor is:

$$SF_V = \frac{D_{actual}}{N_{pixels}} = \frac{3.809(0.0254)}{3386} = 2.858 \times 10^{-5} \frac{m}{pixels}$$

The percent difference between these two scale factors is 0.7%. The scale factor used was the average of the horizontal and vertical scale factors $SF = 2.866 \times 10^{-5}$ m/pixels. The fringe gradient was obtained from a custom MATLAB image processing code using the regression technique described in Section 3.5. For this sample, a point was picked at roughly 25% from the bottom of the channel. The MATLAB code returned the fringe gradient and the location of this scan. The scan is 3008 pixels from the top of the image and the fringe gradient is 75.095 pixels/fringe. The fringe gradient needs to be converted to fringes per meter and a correction due to fringe shift error (e_{fs}) can be applied:

$$\frac{\partial \varepsilon}{\partial x}\bigg|_{x=0} = \frac{1}{75.095 \frac{pixels}{fringe} \cdot SF} + \frac{1}{e_{fs} \cdot SF}$$

$$\frac{\partial \varepsilon}{\partial x}\bigg|_{x=0} = \frac{1}{75.095 \cdot 2.866 \times 10^{-5}} + \frac{1}{(-4500) \cdot 2.866 \times 10^{-5}} = 456.86 \frac{fringes}{m}$$

An image was taken before the experiment of the unheated model finite fringe pattern and an image was taken after the experiment of the unheated model finite fringe pattern. These two images were compared to calculate how much the fringes shifted between the two images and applied as the fringe shift error. The temperature gradient was determined using Equation (3.19):

$$\frac{\partial T}{\partial x}\bigg|_{x=0} = \frac{R\lambda_0 T_S^2}{LPG} \frac{\partial \varepsilon}{\partial x}\bigg|_{x=0} = \frac{287.1 \cdot 632.8 \times 10^{-9} \cdot 291.1^2}{0.3551 \cdot 99671 \cdot 0.226 \times 10^{-3}} 456.86 = 879.0 \frac{K}{m}$$

So the local heat flux on the cold wall of the channel is:

$$q_C = -K_s \frac{\partial T}{\partial x}\bigg|_{x=0} = -0.02546 \cdot 879.0 = -22.38 \frac{W}{m^2}$$

And the local Nusselt number is:

$$Nu_y = \frac{q_C b}{\Delta T K_f} = \frac{-22.38 \cdot 0.015}{3.73 \cdot 0.02617} = -3.43$$

The location of this scan was 0.0625 m, which is y/L = 0.237. This was determined using the scale factor and locating pins in the image.

D.6 Average Nusselt Number

The average Nusselt number is determined by integrating the local Nusselt numbers over the length of the channel.

$$Nu = \frac{1}{L} \int_0^L Nu_y \, dy$$

This was calculated by using the trapezoidal rule:

$$Nu = \frac{1}{L} \sum_{i=1}^{N-1} \left[\frac{(y_i - y_{i+1})}{2} \left(Nu_{y,i} + Nu_{y,i+1} \right) \right]$$

This gives an average Nusselt number of 4.50 for the cold wall. The overall channel average Nusselt number was determined by averaging the average Nusselt numbers for the hot and cold walls. For this case, the overall channel average Nusselt number is Nu = 2.17.

Appendix E

Experimental Error Analysis

E.1 Introduction

With any experiment, there is always a certain degree of unavoidable uncertainty. An attempt is made in this Appendix to indicate the major sources of error. Uncertainty estimates are made for the primary measured and calculated quantities.

The uncertainty analysis was conducted based on the Kline and McClintock (1953) method and also using Coleman and Steele (1999). Consider an experimental result R calculated from n independent variables x_1, x_2, ... , x_n. Each variable has an total uncertainty of δx_1, δx_2, ... , δx_n. If the uncertainty in each variable were given the same odds, then the uncertainty of the result δR at these odds is:

$$\delta R = \sqrt{\left(\frac{\delta R}{\delta x_1}\delta x_1\right)^2 + \left(\frac{\delta R}{\delta x_2}\delta x_2\right)^2 + ... + \left(\frac{\delta R}{\delta x_n}\delta x_n\right)^2} \qquad (E.1)$$

This analysis can be simplified in cases where R can be expressed as a product of the variables, each raised to some power. If R is expressed as:

$$R = x_1^a x_2^b ... x_n^z \qquad (E.2)$$

Then, the relative uncertainty can be calculated as:

$$\frac{\delta R}{R} = \sqrt{\left(a\frac{\delta x_1}{x_1}\right)^2 + \left(b\frac{\delta x_2}{x_2}\right)^2 + ... + \left(z\frac{\delta x_n}{x_n}\right)^2} \qquad (E.3)$$

In the present study, the uncertainties of four parameters are of interest: Ra, Ra(b/L), Nu_H and Nu.

E.2 Measured Values Uncertainties

It is important to note that the total uncertainty of each variable contains two components: bias (or systematic) uncertainty and random (or precision) uncertainty. These two components are related to the overall uncertainty using:

$$\delta x_{total} = \sqrt{\left(\delta x_{bias}\right)^2 + \left(\delta x_{random}\right)^2} \qquad (E.4)$$

Table E.1 shows the typical measured values and the associated bias, random and total uncertainty. The channel height, channel width, channel spacing, and pressure measurements all have a bias error with no random component. The fringe gradient error has both a bias and random error and will be discussed in further detail in Section E.2.1. The temperatures also have a bias and random error component in both the cold wall temperature and the two thermopiles. This will be discussed in Section E.2.2. The fluid properties (c_p, μ, and K) have two bias errors associated with them, and will be discussed in Section E.2.3.

The channel width bias error is estimated at ± 0.125 inches because of the end effects between the channel walls and the optical window. When the optical windows are added to ends of the channel, there is a total gap of 0.25 inches on both sides between the optical windows and the edge of the channel walls. This gap is caused by the foam padding that is used to protect the glass from scratching. This gap increases the optical path length of the channel, but there are a few factors to consider. The flow is complex in the end regions due to the different temperatures between the optical windows, and the hot and cold walls. Another factor is that the flow interacts with a third surface (the optical window), which also affects the flow pattern in this region (possibly the speed and direction of the flow). These factors affect the optical path length of the channel that is measured by the interferometer. Therefore the error associated with this gap is estimated to be half of the 0.25 inch gap or ± 0.125 inches to account for these end effects.

E.2.1 Uncertainty in the Fringe Gradient

A detailed analysis of the error associated with the fringe gradient (error due to the optics) was performed because the Mach-Zehnder interferometer had new optics installed before the

Table E.1: Measured values and the estimated total uncertainties.

Parameter	Symbol	Measured Value	Bias Error	Random Error	Total Uncertainty
Channel Height	L	10.40 inches	±0.01 inch		±0.01 inch
Channel Width	W	13.98 inches	±0.125 inch		±0.125 inch
Channel Spacing	b	15 mm	±0.1 mm		±0.1 mm
Specific Heat	c_p		±0.25% and due to T_f		±0.8%
Dynamic Viscosity	μ		±0.5% and due to T_f		±0.5%
Thermal Conductivity	K, K_s		±1% and due to T_f		±1%
Pressure	P	747.6 mm Hg	±0.2 mm Hg		±0.2 mm
Cold Wall Temperature	T_C	291.0 K	±0.3 K ±0.1%	±0.1 K	±0.32 K
Thermopile	TP_1, TP_2	5538.9 µV, 3721.8 µV	±10 µV ±0.5%	±5 µV	±11 µV
Fringe Gradient	$\left.\dfrac{\partial \varepsilon}{\partial x}\right|_{x=0, x=b}$		±10%	±2.0%	±10.2%

experiments were conducted. A finite fringe pattern with vertical fringes spaced approximately one millimeter apart was photographed for analysis. This image is shown in Figure E.1. This pattern was selected because it was determined that the experiments would have an average fringe spacing of 1 mm. The custom MATLAB image processing code was used to determine the fringe gradient at approximately 400 points over the center 90% of the output pattern. The fringe gradient was converted to fringe spacing and the average was calculated. Using the average fringe spacing, the error at each of the 400 points was determined and the sum-squared error was used to calculate the bias error. The bias error in the fringe gradient was determined to be ±10% at 20:1 odds. The random error was determined by setting up the same finite fringe pattern in the interferometer with an average fringe spacing of 1 mm. This was then recorded with the high speed camera over 5 seconds and the random error was determined to be ±2%. Using Equation (E.4), the total uncertainty was calculated to be:

$$\delta x_{total} = \sqrt{\left(\delta x_{bias}\right)^2 + \left(\delta x_{random}\right)^2} = \sqrt{\left(0.10\right)^2 + \left(0.02\right)^2} = 0.102 = 10.2\%$$
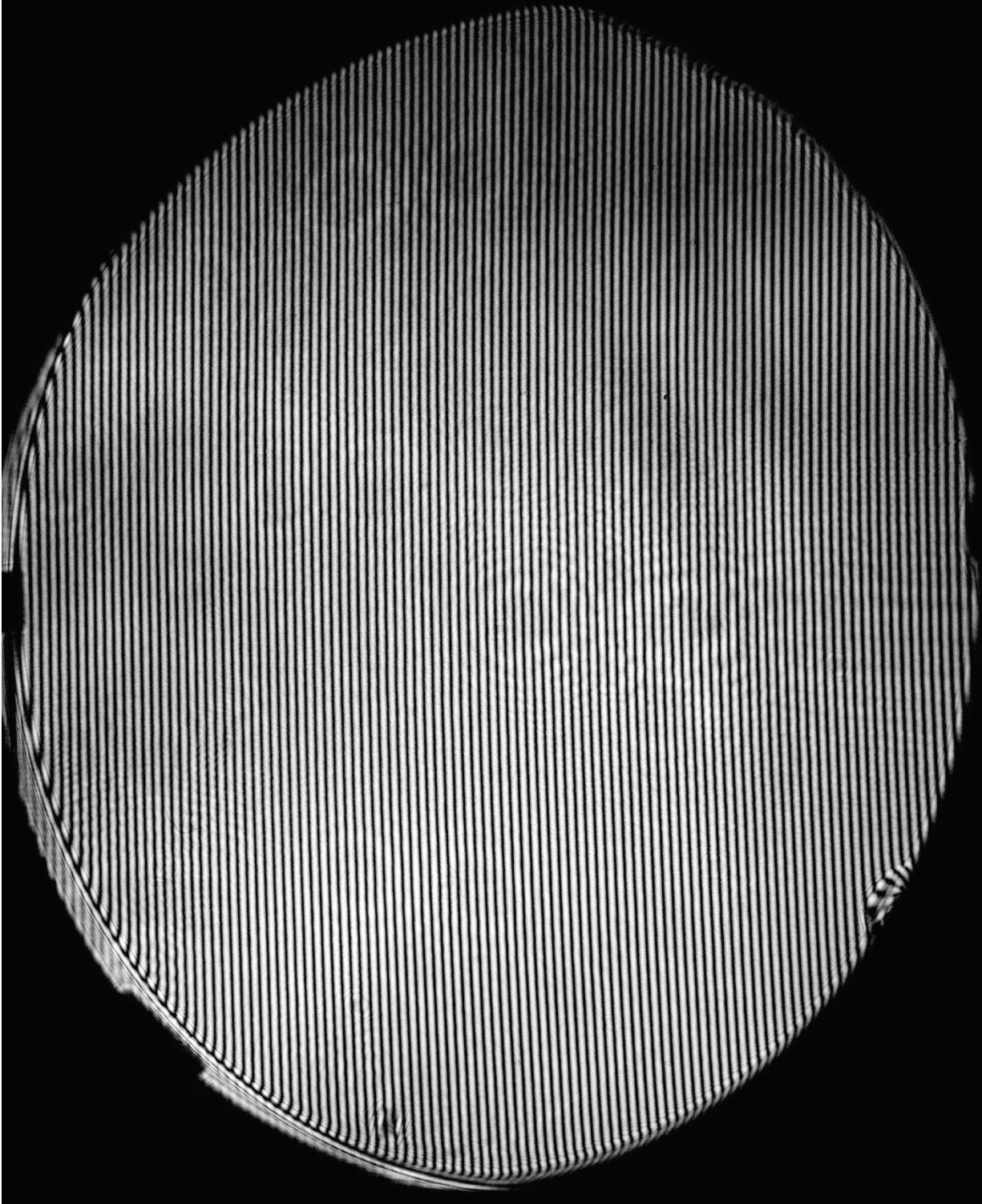
Figure E.1: Finite fringe interferogram with vertical fringes at approximately 1 mm spacing used for optical error analysis of the Mach-Zehnder interferometer.

The total uncertainty is a combination of a few different factors, with the main factor being the optical imperfections of the MZI. It also includes the error associated with the CCD array of the digital back camera and the regression algorithm used in the custom MATLAB image processing code. It is shown in Table E.1 that the total uncertainty of the fringe gradient is the highest source of error in these experiments.

E.2.2 Uncertainty in the Temperatures

The cold wall temperature and the thermopiles both have a bias and random component to the total uncertainty. The cold wall temperature is measured using type T thermocouples using copper and constantan wire with special limits of error. The bias error is estimated to be ±0.3 K and the random error is estimated to be ±0.1 K on the cold wall temperature. The two thermopiles were constructed using the same copper and constantan wire with special limits of error as the thermocouple wire. The bias error of the thermopiles is estimated to be ±10 μV and the random error is estimated to be ±5 μV. Using Equation (E.4), the total uncertainty of the cold wall temperature is ±0.32 K and the total uncertainty of the thermopiles is ±11 μV.

As shown in the sample calculation in Appendix D.2, the hot wall and ambient temperatures are calculated from the two thermopiles using the cold wall temperature as a reference. Using Equations (D.1), (D.2) and (D.3) with the coefficients from Tables D.4 and D.5, an expression to calculate the hot wall temperature can be determined. Substituting this expression into Equation (E.1), the total uncertainty in the hot wall temperature can be determined:

$$\delta T_H = \sqrt{\left(\frac{\delta T_H}{\delta T_C}\delta T_C\right)^2 + \left(\frac{\delta T_H}{\delta TP_1}\delta TP_1\right)^2} = \sqrt{(-1.027\cdot 0.32)^2 + (0.004267\cdot 11)^2} = \pm 0.33K$$

where MATLAB was used to calculate $\dfrac{\delta T_H}{\delta T_C}$ and $\dfrac{\delta T_H}{\delta TP_1}$ from the expression for the hot wall temperature. Similarly, an expression can be determined to calculate the ambient temperature.

Again, using Equation (E.1), the total uncertainty in the ambient temperature can be determined:

$$\delta T_\infty = \sqrt{\left(\frac{\delta T_\infty}{\delta T_C}\delta T_C\right)^2 + \left(\frac{\delta T_\infty}{\delta TP_1}\delta TP_1\right)^2 + \left(\frac{\delta T_\infty}{\delta TP_2}\delta TP_2\right)^2}$$

$$= \sqrt{(-1.065\cdot 0.32)^2 + (0.004427\cdot 11)^2 + (-0.004427\cdot 11)^2} = \pm 0.35\text{K}$$

where MATLAB was used to calculate $\dfrac{\delta T_\infty}{\delta T_C}$, $\dfrac{\delta T_\infty}{\delta TP_1}$, and $\dfrac{\delta T_\infty}{\delta TP_2}$. Therefore the total uncertainty in the hot wall temperature is ± 0.33 K and the ambient temperature is ± 0.35 K.

These temperatures are then implemented into the temperature differences that are used to calculate the Rayleigh numbers and Nusselt numbers. The two temperature differences used in this study were $\overline{\Delta T} = \dfrac{T_H + T_C}{2} - T_\infty$ and $T_H - T_C$. The uncertainty in $\overline{\Delta T}$ is:

$$\delta\overline{\Delta T} = \sqrt{\left(\frac{\delta\overline{\Delta T}}{\delta T_C}\delta T_C\right)^2 + \left(\frac{\delta\overline{\Delta T}}{\delta T_H}\delta T_H\right)^2 + \left(\frac{\delta\overline{\Delta T}}{\delta T_\infty}\delta T_\infty\right)^2} =$$

$$\sqrt{\left(\frac{1}{2}\cdot 0.32\right)^2 + \left(\frac{1}{2}\cdot 0.33\right)^2 + (-1\cdot 0.35)^2} = \pm 0.42\text{K}$$

And the uncertainty in $T_H - T_C$ is:

$$\delta(T_H - T_C) = \sqrt{\left(\frac{\delta(T_H - T_C)}{\delta T_H}\delta T_H\right)^2 + \left(\frac{\delta(T_H - T_C)}{\delta T_C}\delta T_C\right)^2}$$

$$= \sqrt{(1\cdot 0.32)^2 + (-1\cdot 0.33)^2} = \pm 0.46\text{K}$$

Another temperature that is used is the film temperature, which is calculated from Equation (1.2):

$$T_f = \left(\frac{T_H + T_C}{2} + T_\infty\right)\bigg/ 2$$

The uncertainty in the film temperature is:

$$\delta T_f = \sqrt{\left(\frac{\delta \overline{\Delta T}}{\delta T_H} \delta T_H\right)^2 + \left(\frac{\delta \overline{\Delta T}}{\delta T_C} \delta T_C\right)^2 + \left(\frac{\delta \overline{\Delta T}}{\delta T_\infty} \delta T_\infty\right)^2} =$$

$$\sqrt{\left(\frac{1}{4} \cdot 0.32\right)^2 + \left(\frac{1}{4} \cdot 0.33\right)^2 + \left(\frac{1}{2} \cdot 0.35\right)^2} = \pm 0.21K$$

In summary, the uncertainty in T_H is ±0.33 K, T_∞ is ±0.35 K, $\overline{\Delta T}$ is ±0.42 K, $T_H - T_C$ is ±0.46 K and T_f is ±0.21 K.

E.2.3 Uncertainty in the Fluid Properties

The fluid properties have two different sources of bias error. The error caused by the uncertainty in the fluid property measurements, estimated from the scatter charts in the literature are: ±0.25% for the specific heat from Touloukian and Makita (1970), ±0.5% for the dynamic viscosity from Touloukian et al. (1975), and ±1% for the thermal conductivity from Touloukian et al. (1970). The other source of bias error is due to the film temperature error. These two bias errors are combined to give the total uncertainty:

$$\delta c_p = \sqrt{\left(\delta c_{p,scatter}\right)^2 + \left(\frac{\delta c_p}{\delta T_f} \delta T_f\right)^2} = \sqrt{(0.0025)^2 + (0.0362 \cdot 0.21)^2} = 0.008 = 0.8\%$$

$$\delta \mu = \sqrt{\left(\delta \mu_{scatter}\right)^2 + \left(\frac{\delta \mu}{\delta T_f} \delta T_f\right)^2} = \sqrt{(0.005)^2 + \left(4.7 \times 10^{-8} \cdot 0.21\right)^2} = 0.005 = 0.5\%$$

$$\delta K = \sqrt{\left(\delta K_{scatter}\right)^2 + \left(\frac{\delta K}{\delta T_f} \delta T_f\right)^2} = \sqrt{(0.01)^2 + \left(7.3 \times 10^{-4} \cdot 0.21\right)^2} = 0.010 = 1.0\%$$

The error due to the film temperature error has a very small effect on the total uncertainty of the fluid properties.

159

E.3 Uncertainty in the Rayleigh Number

The modified Rayleigh number is given in Equation (1.5):

$$Ra(b/L) = \frac{g\beta\overline{\Delta T}\rho^2 b^3}{\mu^2} Pr \frac{b}{L}$$

But some of the variables in this equation have also been calculated, not measured. Therefore the Rayleigh number needs to be expanded into only measured variables. The Prandtl number can be expressed as:

$$Pr = \frac{c_p \mu}{K}$$

The density is calculated using the incompressible ideal gas law:

$$\rho = \frac{P}{RT_f}$$

and the thermal expansion coefficient is:

$$\beta = \frac{1}{T_f}$$

Substituting these equations into the modified Rayleigh number gives:

$$Ra(b/L) = \frac{g\overline{\Delta T}P^2 b^4 c_p}{T_f^3 R^2 \mu L K} \tag{E.4}$$

The accuracy of the calculated Rayleigh number depends upon the accuracy of the thermocouple and thermopile readings, barometric pressure, channel spacing, channel length and fluid properties.

Applying Equation (E.3) gives the uncertainty in the Rayleigh number:

$$\frac{\delta Ra}{Ra} = \left[\left(\frac{\delta\overline{\Delta T}}{\overline{\Delta T}}\right)^2 + \left(2\frac{\delta P}{P}\right)^2 + \left(4\frac{\delta b}{b}\right)^2 + \left(\frac{\delta c_p}{c_p}\right)^2 + \right.$$

$$\left. \left(3\frac{\delta T_f}{T_f}\right)^2 + \left(\frac{\delta\mu}{\mu}\right)^2 + \left(\frac{\delta K}{K}\right)^2 + \left(\frac{\delta L}{L}\right)^2 \right]^{\frac{1}{2}} \qquad (E.5)$$

The uncertainties in the gravity g and gas constant R have been neglected. Solving this equation with the values from Table E.1 gives an error in the modified Rayleigh number Ra(b/L) of ±5%. A similar calculation can be made to determine the uncertainty in the non-modified Rayleigh number, which was determined to be ±4%.

E.4 Uncertainty in the Nusselt Number

In order to calculate the uncertainty in the overall channel average Nusselt number, the uncertainty in the local Nusselt numbers must first be calculated. The hot wall local Nusselt numbers are determined using:

$$Nu_{y,H} = \frac{q_H b}{\Delta T K}$$

where in this case, $\Delta T = \overline{\Delta T}$. The heat flux q_H is defined as:

$$q_H = K_s \frac{\partial T}{\partial x}\bigg|_{x=b}$$

The temperature gradient is given by:

$$\frac{\partial T}{\partial x}\bigg|_{x=b} = \frac{R\lambda_0 T_s^2}{WPG}\frac{\partial \varepsilon}{\partial x}\bigg|_{x=b}$$

where T_s is the hot wall temperature T_H.

Substituting these equations into the Nusselt number gives:

$$\mathrm{Nu}_{y,H} = \frac{\mathrm{K_s} b R \lambda_0 T_H^2}{\overline{\Delta T} K W P G} \left. \frac{\partial \varepsilon}{\partial x} \right|_{x=b}$$

(E.6)

The accuracy of the local Nusselt number depends on the fluid properties, channel spacing, channel width, thermocouple and thermopile readings, barometric pressure, and the fringe gradient. The uncertainty in the local hot wall Nusselt number is calculated from:

$$\frac{\partial \mathrm{Nu}_{y,H}}{\mathrm{Nu}_{y,H}} = \sqrt{\left(\frac{\delta b}{b}\right)^2 + \left(2\frac{\delta T_H}{T_H}\right)^2 + \left(\frac{\delta\left(\left.\frac{\partial \varepsilon}{\partial x}\right|_{x=0}\right)}{\left.\frac{\partial \varepsilon}{\partial x}\right|_{x=0}}\right)^2 + \left(\frac{\delta(\overline{\Delta T})}{(\overline{\Delta T})}\right)^2 + \left(\frac{\delta W}{W}\right)^2 + \left(\frac{\delta P}{P}\right)^2}$$

(E.7)

where the uncertainty of K_s/K, the gas constant R, the wavelength of the laser λ_0, and the Gladstone-Dale constant have been assumed to be negligible. A similar calculation can be done for the local cold wall Nusselt numbers. Using the values from Table E.1, the uncertainty in the local Nusselt numbers is estimated to be ±11%.

The local Nusselt numbers were integrated using the trapezoidal rule in order to obtain the average Nusselt numbers. The integration process averages out the "noise" in the local Nusselt number data. For this reason, the average Nusselt number is more accurate than the individual local Nusselt number data. Using a Monte Carlo simulation, the uncertainty in the fringe gradient can be reduced to ±2%. Substituting this value into Equation (E.7), the total uncertainty in the average Nusselt numbers is estimated at ±6%. Using the formula in Equation (3.22), the error in the overall channel average Nusselt number can be estimated at ±8%

The error in the hot wall average Nusselt number as used in the anti-symmetrical ($R_T = -1$) cases is also estimated at ±6%. It should be noted that when studying the $R_T = -1$ cases, the temperature difference $\Delta T = T_H - T_C$.

APPENDIX F

Richardson Extrapolation

F.1 Introduction

The Richardson extrapolation (Celik et al., 2008) is used in Chapter 4 to report the discretization error estimation of the grid that is used in the numerical solution. This method is calculated in this appendix for two different temperature difference ratios, $R_T = 0$ and $R_T = -0.5$. Both these cases are analyzed to ensure that the numerical solution is reasonable over the range of temperature difference ratios of interest in this study.

F.2 Calculation of the Estimation of Discretization Error for $R_T = 0$

This is the Richardson extrapolation calculation for $R_T = 0$, with $A = 50$ and $Ra(b/L) = 14.8$:

Step 1: The first step of the Richardson extrapolation is to determine three representative grid sizes: h_1, h_2, and h_3 such that $h_1 < h_2 < h_3$. Note that N is the number of cells and ΔA_i is the area of the ith cell.

$$h_1 = \left[\frac{1}{N}\sum_{i=1}^{N}\Delta A_i\right]^{\frac{1}{2}} = \left[\frac{1}{49387}4.00\times10^{-8}\right]^{\frac{1}{2}} = 9.00\times10^{-7}$$

$$h_2 = \left[\frac{1}{N}\sum_{i=1}^{N}\Delta A_i\right]^{\frac{1}{2}} = \left[\frac{1}{30389}6.25\times10^{-8}\right]^{\frac{1}{2}} = 1.43\times10^{-6} \tag{F.1}$$

$$h_3 = \left[\frac{1}{N}\sum_{i=1}^{N}\Delta A_i\right]^{\frac{1}{2}} = \left[\frac{1}{16671}1.11\times10^{-7}\right]^{\frac{1}{2}} = 2.58\times10^{-6}$$

Step 2: These three grids are then used to solve for the critical variable, ϕ, which is Nu in this case.

$$\phi_1 = Nu = 0.53221$$
$$\phi_2 = Nu = 0.53230$$
$$\phi_3 = Nu = 0.53232$$

Step 3:   The apparent order, p, of the method is calculated next using an iterative method.

$$p = \frac{1}{\ln(r_{21})} \left| \ln\left|\frac{\varepsilon_{32}}{\varepsilon_{21}}\right| + q(p) \right| \tag{F.2}$$

$$q(p) = \ln\left(\frac{r_{21}^p - s}{r_{32}^p - s}\right) \tag{F.3}$$

$$s = 1 \cdot \text{sign}\left(\frac{\varepsilon_{32}}{\varepsilon_{21}}\right) \tag{F.4}$$

where

$$\varepsilon_{32} = \phi_3 - \phi_2 = 1.93 \times 10^{-5}, \tag{F.5a}$$

$$\varepsilon_{21} = \phi_2 - \phi_1 = 9.55 \times 10^{-5}, \tag{F.5b}$$

$$r_{21} = \frac{h_2}{h_1} = 1.594, \text{ and} \tag{F.6a}$$

$$r_{32} = \frac{h_3}{h_2} = 1.800. \tag{F.6b}$$

 It should also be noted that:

$$\text{sign}(x) = \begin{cases} -1 & \to & x < 0 \\ 0 & \to & x = 0 \\ 1 & \to & x > 0 \end{cases} \tag{F.7}$$

The apparent order of this grid: p = 0.274.

Step 4:   The extrapolated values are:

$$\phi_{ext}^{21} = \frac{r_{21}^p \phi_1 - \phi_2}{r_{21}^p - 1} = 0.5315$$

$$\phi_{ext}^{32} = \frac{r_{32}^p \phi_2 - \phi_3}{r_{32}^p - 1} = 0.5322 \tag{F.8}$$

Step 5: The approximate relative error:

$$e_a^{21} = \left| \frac{\phi_1 - \phi_2}{\phi_1} \right| = 0.0002 \rightarrow 0.02\% \tag{F.9}$$

The Extrapolated relative error:

$$e_{ext}^{21} = \left| \frac{\phi_{ext}^{21} - \phi_1}{\phi_{ext}^{21}} \right| = 0.0013 \rightarrow 0.13\% \tag{F.10}$$

The fine grid convergence index:

$$GCI_{fine}^{21} = \frac{1.25 e_a^{21}}{r_{21}^p - 1} = 0.0016 \rightarrow 0.16\% \tag{F.11}$$

The approximate relative error, the extrapolated relative error, the fine grid convergence index, and the apparent order of the method are all reported. For $R_T = 0$, the numerical uncertainty is 0.2%.

F.3 Calculation of the Estimation of Discretization Error for $R_T = -0.5$

This is the Richardson extrapolation calculation for $R_T = -0.5$, with A = 50 and Ra(b/L) = 7.61:

Step 1: The first step of the Richardson extrapolation is to determine three representative grid sizes: h_1, h_2, and h_3:

$$h_1 = 9.00 \times 10^{-7}$$
$$h_2 = 1.43 \times 10^{-6}$$
$$h_3 = 2.58 \times 10^{-6}$$

Step 2: These three grids are then used to solve for the critical variable, ϕ, which is Nu in this case.

$$\phi_1 = Nu = 0.22516$$
$$\phi_2 = Nu = 0.22533$$
$$\phi_3 = Nu = 0.22566$$

Step 3: The apparent order, p, of the method is calculated next using an iterative method as mentioned in the previous section, which is p = 0.274.

Step 4: The extrapolated values are:

$$\phi_{ext}^{21} = \frac{r_{21}^p \phi_1 - \phi_2}{r_{21}^p - 1} = 0.2239$$

$$\phi_{ext}^{32} = \frac{r_{32}^p \phi_2 - \phi_3}{r_{32}^p - 1} = 0.2235$$

(F.8)

Step 5: The approximate relative error:

$$e_a^{21} = \left| \frac{\phi_1 - \phi_2}{\phi_1} \right| = 0.0008 \rightarrow 0.08\%$$

(F.9)

The Extrapolated relative error:

$$e_{ext}^{21} = \left| \frac{\phi_{ext}^{21} - \phi_1}{\phi_{ext}^{21}} \right| = 0.0056 \rightarrow 0.56\%$$

(F.10)

The fine grid convergence index:

$$GCI_{fine}^{21} = \frac{1.25 e_a^{21}}{r_{21}^p - 1} = 0.0070 \rightarrow 0.70\%$$

(F.11)

For $R_T = -0.5$, the numerical uncertainty is 0.7%.

Appendix G

Experimental Data

G.1 Experimental Data

Table G.1: Cold plate thermocouple calibration.

Actual (°C)	Thermocouple Readings (°C)					
	1	2	3	4	5	6
15.1	15.0	15.0	15.0	15.0	15.0	15.0
20.1	20.1	20.1	20.1	20.1	20.1	20.1
25.2	25.1	25.2	25.2	25.1	25.2	25.2
30.1	30.2	30.1	30.1	30.1	30.1	30.2
35.1	35.2	35.2	35.2	35.2	35.2	35.2
40.1	40.2	40.2	40.2	40.2	40.2	40.2
35.1	35.2	35.2	35.2	35.2	35.2	35.2
30.1	30.1	30.1	30.1	30.1	30.1	30.1
25.2	25.2	25.1	25.2	25.1	25.1	25.2
20.1	20.1	20.1	20.1	20.1	20.1	20.1
15.1	15.1	15.1	15.1	15.1	15.1	15.1
Correction	+0.0	+0.0	+0.0	+0.0	+0.0	+0.0

Table G.2: Hot wall, cold wall and ambient temperature averages for A = 27.6.

R_T	Section	T_H	T_C	T_∞
0	Bottom	312.2 K	297.2 K	297.1 K
	Top	311.9 K	297.0 K	297.0 K
−0.5	Bottom	310.1 K	289.2 K	296.2 K
	Top	311.2 K	288.8 K	296.4 K
−0.75	Bottom	306.5 K	289.0 K	296.5 K
	Top	306.9 K	289.5 K	296.9 K
−1	Bottom	303.7 K	288.7 K	296.2 K
	Top	304.3 K	289.3 K	296.8 K

Table G.3: Hot wall, cold wall and ambient temperature averages for A = 17.6.

R_T	Section	T_H	T_C	T_∞
1	Bottom	314.5 K	314.5 K	299.6 K
	Top	312.6 K	312.6 K	297.8 K
0	Bottom	314.9 K	300.0 K	300.0 K
	Top	312.6 K	312.7 K	297.6 K
−0.5	Bottom	313.5 K	291.1 K	298.6 K
	Top	311.9 K	289.4 K	296.9 K
−0.75	Bottom	308.7 K	291.2 K	298.6 K
	Top	306.9 K	289.4 K	296.9 K
−1	Bottom	306.7 K	291.7 K	299.1 K
	Top	304.4 K	289.5 K	297.0 K

Table G.4: Hot wall, cold wall and ambient temperature averages for A = 13.2.

R_T	Section	T_H	T_C	T_∞
1	Bottom	311.9 K	311.9 K	297.0 K
	Top	312.2 K	312.2 K	297.3 K
−0.5	Bottom	311.9 K	289.4 K	297.0 K
	Top	312.2 K	289.7 K	297.1 K
−0.75	Bottom	307.0 K	289.5 K	296.9 K
	Top	307.1 K	289.6 K	297.0 K
−1	Bottom	304.4 K	289.4 K	296.9 K
	Top	304.4 K	289.4 K	296.9 K

Table G.5: Hot wall, cold wall and ambient temperature averages for $R_T = -0.5$ and A = 8.8.

Section	T_H	T_C	T_∞
1 (Bottom)	311.1 K	288.6 K	296.0 K
2	311.0 K	288.6 K	296.0 K
3	311.0 K	288.5 K	296.0 K
4	311.0 K	288.5 K	296.1 K
5	311.0 K	288.5 K	296.1 K
6	311.0 K	288.5 K	296.2 K
7	311.1 K	288.7 K	296.1 K
8	311.1 K	288.6 K	296.1 K
9	311.1 K	288.7 K	296.1 K
10	311.1 K	288.6 K	296.0 K
11	310.9 K	288.4 K	296.0 K
12 (Top)	310.9 K	288.5 K	295.9 K

Table G.6: Hot wall, cold wall and ambient temperature averages for $R_T = -1$ and A = 8.8.

Section	T_H	T_C	T_∞
1 (Bottom)	303.8 K	288.8 K	296.2 K
2	303.7 K	288.7 K	296.1 K
3	303.8 K	288.8 K	296.2 K
4	303.8 K	288.8 K	296.2 K
5	303.8 K	288.8 K	296.3 K
6	303.8 K	288.8 K	296.2 K
7	303.7 K	288.7 K	296.2 K
8	303.7 K	288.7 K	296.2 K
9	303.7 K	288.7 K	296.2 K
10	303.7 K	288.7 K	296.1 K
11	303.7 K	288.7 K	296.1 K
12 (Top)	303.9 K	288.7 K	296.3 K

Table G.7: Local Nusselt numbers for bottom section, $R_T = 1$, A = 17.6, P = 100.67 kPa, Ra(b/L) = 237.

Cold Wall				Hot Wall			
y/L	$Nu_{y,C}$	y/L	$Nu_{y,C}$	y/L	$Nu_{y,H}$	y/L	$Nu_{y,H}$
0.004	6.781	0.267	2.493	0.004	7.022	0.267	2.274
0.014	5.371	0.277	2.546	0.014	5.157	0.277	2.505
0.024	5.006	0.287	2.570	0.024	4.799	0.287	2.515
0.034	4.937	0.297	2.438	0.034	4.548	0.297	2.544
0.044	4.753	0.307	2.316	0.044	4.538	0.307	2.401
0.054	4.420	0.318	2.418	0.054	4.454	0.318	2.260
0.064	4.229	0.328	2.282	0.065	3.944	0.328	2.336
0.075	4.180	0.338	2.330	0.075	3.949	0.338	2.286
0.085	3.877	0.348	2.227	0.085	3.946	0.348	2.223
0.095	3.588	0.358	2.248	0.095	3.870	0.358	2.141
0.105	3.607	0.368	2.227	0.105	3.381	0.368	2.170
0.115	3.634	0.378	2.113	0.115	3.409	0.378	2.211
0.125	3.457	0.388	2.098	0.125	3.487	0.388	2.063
0.135	3.261	0.399	2.100	0.135	3.475	0.398	2.043
0.145	3.261	0.409	2.102	0.145	3.093	0.409	2.106
0.156	3.208	0.419	2.062	0.156	3.149	0.419	2.031
0.166	3.201	0.439	1.959	0.166	3.158	0.439	1.915
0.176	2.900	0.449	1.947	0.176	3.082	0.449	2.009
0.186	2.978	0.459	1.820	0.186	2.830	0.459	1.881
0.196	2.999	0.469	1.816	0.196	2.876	0.469	1.777
0.206	2.822	0.480	1.839	0.206	2.874	0.479	1.888
0.216	2.712	0.490	1.871	0.216	2.854	0.490	1.879
0.226	2.584			0.226	2.640		
0.237	2.642			0.237	2.655		
0.257	2.637			0.257	2.600		

Table G.8: Local Nusselt numbers for top section, $R_T = 1$, A = 17.6, P = 101.16 kPa, Ra(b/L) = 245.

Cold Wall				Hot Wall			
y/L	$Nu_{y,C}$	y/L	$Nu_{y,C}$	y/L	$Nu_{y,H}$	y/L	$Nu_{y,H}$
0.500	1.863	0.763	1.383	0.500	1.803	0.763	1.355
0.510	1.839	0.773	1.301	0.510	1.873	0.773	1.296
0.520	1.882	0.783	1.279	0.520	1.830	0.783	1.277
0.530	1.815	0.793	1.328	0.530	1.800	0.793	1.364
0.540	1.761	0.803	1.268	0.540	1.775	0.803	1.304
0.550	1.793	0.813	1.246	0.550	1.774	0.813	1.202
0.560	1.750	0.824	1.240	0.560	1.821	0.824	1.203
0.571	1.710	0.834	1.254	0.571	1.709	0.834	1.279
0.581	1.679	0.844	1.203	0.581	1.626	0.844	1.263
0.591	1.694	0.854	1.172	0.591	1.659	0.854	1.149
0.601	1.708	0.864	1.200	0.601	1.673	0.864	1.154
0.611	1.579	0.874	1.164	0.611	1.664	0.874	1.148
0.621	1.534	0.884	1.145	0.621	1.635	0.884	1.156
0.631	1.625	0.894	1.094	0.631	1.592	0.894	1.118
0.641	1.656	0.905	1.137	0.641	1.604	0.905	1.096
0.652	1.555	0.915	1.196	0.651	1.607	0.915	1.084
0.662	1.489	0.925	0.937	0.662	1.517	0.925	1.156
0.672	1.527	0.935	1.064	0.672	1.501	0.935	1.040
0.682	1.530	0.945	1.052	0.682	1.562	0.945	0.998
0.692	1.433	0.955	1.057	0.692	1.480	0.955	1.026
0.702	1.429	0.965	1.027	0.702	1.408	0.965	1.098
0.712	1.446	0.975	1.012	0.712	1.451	0.975	1.059
0.722	1.430	0.986	0.944	0.722	1.520	0.985	1.017
0.733	1.386	0.996	0.872	0.732	1.354	0.996	0.970
0.753	1.371			0.753	1.367		

Table G.9: Local Nusselt numbers for bottom section, $R_T = 1$, A = 13.2, P = 100.97 kPa, Ra(b/L) = 788.

Cold Wall				Hot Wall			
y/L	$Nu_{y,C}$	y/L	$Nu_{y,C}$	y/L	$Nu_{y,H}$	y/L	$Nu_{y,H}$
0.004	8.316	0.257	3.474	0.004	8.342	0.257	3.445
0.014	6.699	0.267	3.386	0.014	6.086	0.267	3.421
0.024	6.335	0.277	3.381	0.024	5.507	0.277	3.386
0.034	5.959	0.287	3.415	0.034	5.761	0.287	3.267
0.044	5.700	0.297	3.346	0.044	5.353	0.297	3.296
0.054	5.624	0.307	3.330	0.054	5.364	0.307	3.216
0.065	5.445	0.318	3.282	0.065	5.103	0.317	3.174
0.075	5.230	0.328	3.244	0.075	4.925	0.328	3.204
0.085	5.212	0.338	3.168	0.085	5.096	0.338	3.186
0.095	4.905	0.348	3.089	0.095	4.738	0.348	3.061
0.105	4.676	0.358	3.158	0.105	4.613	0.358	3.104
0.115	4.692	0.368	2.994	0.115	4.572	0.368	2.996
0.125	4.486	0.378	3.115	0.125	4.484	0.378	2.962
0.135	4.419	0.388	3.077	0.135	4.378	0.388	2.885
0.145	4.248	0.398	2.968	0.145	4.206	0.398	2.873
0.156	4.076	0.409	2.987	0.156	4.108	0.409	2.965
0.166	4.110	0.419	2.909	0.166	4.135	0.419	2.891
0.176	4.104	0.429	3.025	0.176	3.974	0.439	2.763
0.186	3.994	0.439	2.884	0.186	4.014	0.449	2.753
0.196	3.998	0.449	2.897	0.196	3.896	0.459	2.767
0.206	3.793	0.459	2.783	0.206	3.732	0.469	2.797
0.216	3.819	0.469	2.744	0.216	3.839	0.479	2.683
0.226	3.881	0.479	2.745	0.226	3.685	0.490	2.667
0.237	3.596	0.490	2.807	0.237	3.585	0.500	2.684
0.247	3.770			0.247	3.321		

Table G.10: Local Nusselt numbers for top section, $R_T = 1$, A = 13.2, P = 101.19 kPa, Ra(b/L) = 785.

Cold Wall				Hot Wall			
y/L	$Nu_{y,C}$	y/L	$Nu_{y,C}$	y/L	$Nu_{y,H}$	y/L	$Nu_{y,H}$
0.500	2.719	0.753	2.053	0.510	2.630	0.763	2.048
0.510	2.674	0.763	2.048	0.520	2.709	0.773	2.179
0.520	2.613	0.773	2.114	0.530	2.626	0.783	2.091
0.530	2.687	0.783	2.132	0.540	2.607	0.793	2.066
0.540	2.485	0.793	2.061	0.550	2.626	0.803	2.154
0.550	2.502	0.803	2.005	0.560	2.531	0.813	2.154
0.560	2.648	0.813	2.141	0.571	2.417	0.824	1.939
0.571	2.453	0.824	2.015	0.581	2.545	0.834	1.984
0.581	2.413	0.834	1.994	0.591	2.456	0.844	2.079
0.591	2.498	0.844	2.041	0.601	2.392	0.854	2.032
0.601	2.429	0.854	2.034	0.611	2.357	0.864	1.890
0.611	2.406	0.864	1.918	0.621	2.365	0.874	1.944
0.621	2.323	0.874	1.897	0.631	2.380	0.884	2.053
0.631	2.442	0.884	2.006	0.641	2.409	0.894	1.882
0.641	2.456	0.894	1.996	0.652	2.368	0.905	1.871
0.652	2.419	0.905	1.831	0.662	2.258	0.915	1.916
0.662	2.294	0.915	1.831	0.672	2.405	0.935	1.885
0.672	2.302	0.925	1.976	0.682	2.202	0.945	1.852
0.682	2.285	0.935	1.805	0.692	2.230	0.955	1.904
0.692	2.272	0.945	1.805	0.702	2.370	0.965	1.865
0.702	2.263	0.955	1.783	0.712	2.220	0.975	1.779
0.712	2.368	0.965	1.871	0.722	2.198	0.985	1.808
0.722	2.310	0.975	1.860	0.732	2.186	0.996	1.819
0.732	2.192	0.985	1.760	0.743	2.040		
0.743	2.233	0.996	1.727	0.753	2.091		

Table G.11: Local Nusselt numbers for bottom section, $R_T = 0$, A = 26.4, P = 99.76 kPa, Ra(b/L) = 25.5.

Cold Wall				Hot Wall			
y/L	$Nu_{y,C}$	y/L	$Nu_{y,C}$	y/L	$Nu_{y,H}$	y/L	$Nu_{y,H}$
0.019	-0.335	0.338	-1.194	0.004	9.486	0.267	2.973
0.020	-0.333	0.348	-1.339	0.014	7.597	0.277	2.972
0.051	-0.385	0.358	-1.459	0.024	6.692	0.287	3.101
0.051	-0.383	0.368	-1.286	0.034	6.351	0.297	2.786
0.081	-0.454	0.378	-1.348	0.044	5.617	0.307	2.982
0.082	-0.451	0.388	-1.563	0.054	5.739	0.317	3.115
0.112	-0.530	0.398	-1.409	0.064	5.562	0.328	2.840
0.113	-0.522	0.409	-1.394	0.075	4.656	0.338	2.843
0.144	-0.623	0.419	-1.521	0.085	5.056	0.348	3.004
0.145	-0.612	0.429	-1.427	0.095	4.923	0.358	2.743
0.175	-0.746	0.439	-1.421	0.105	4.193	0.368	2.657
0.177	-0.723	0.449	-1.596	0.115	4.559	0.378	2.817
0.206	-0.729	0.459	-1.553	0.125	4.353	0.388	2.902
0.216	-0.869	0.469	-1.475	0.135	3.849	0.398	2.523
0.226	-0.966	0.479	-1.532	0.145	4.192	0.409	2.632
0.237	-0.853	0.490	-1.583	0.156	3.652	0.419	2.689
0.247	-1.141			0.166	3.821	0.439	2.478
0.257	-1.062			0.176	3.679	0.449	2.574
0.267	-1.036			0.186	3.797	0.459	2.327
0.277	-1.058			0.196	3.668	0.469	2.550
0.287	-1.190			0.206	3.381	0.479	2.473
0.297	-1.207			0.216	3.489	0.490	2.335
0.307	-1.135			0.226	3.398	0.500	2.425
0.318	-1.237			0.237	3.281		
0.328	-1.301			0.257	3.151		

Table G.12: Local Nusselt numbers for top section, $R_T = 0$, A = 26.4, P = 97.18 kPa, Ra(b/L) = 24.1.

Cold Wall				Hot Wall			
y/L	$Nu_{y,C}$	y/L	$Nu_{y,C}$	y/L	$Nu_{y,H}$	y/L	$Nu_{y,H}$
0.500	-1.569	0.753	-1.514	0.510	2.286	0.763	2.050
0.510	-1.583	0.763	-1.745	0.520	2.359	0.773	2.096
0.520	-1.602	0.773	-1.664	0.530	2.334	0.783	2.202
0.530	-1.459	0.783	-1.796	0.540	2.316	0.793	2.265
0.540	-1.573	0.793	-1.653	0.550	2.126	0.803	2.220
0.550	-1.744	0.803	-1.708	0.560	2.276	0.813	2.027
0.560	-1.669	0.813	-1.752	0.571	2.328	0.824	2.146
0.571	-1.538	0.824	-1.858	0.581	2.273	0.834	2.297
0.581	-1.577	0.834	-1.748	0.591	2.208	0.844	2.222
0.591	-1.611	0.844	-1.545	0.601	2.178	0.854	2.100
0.601	-1.766	0.854	-1.743	0.611	2.307	0.864	2.020
0.611	-1.628	0.864	-1.816	0.621	2.452	0.874	2.200
0.621	-1.518	0.874	-1.772	0.631	2.284	0.884	2.083
0.631	-1.833	0.884	-1.651	0.641	2.089	0.894	2.145
0.641	-1.769	0.894	-1.704	0.651	2.201	0.905	1.948
0.652	-1.768	0.905	-1.779	0.662	2.246	0.915	2.063
0.662	-1.594	0.915	-1.755	0.672	2.224	0.935	2.089
0.672	-1.806	0.925	-1.665	0.682	2.075	0.945	1.998
0.682	-1.783	0.935	-1.701	0.692	2.190	0.955	2.211
0.692	-1.762	0.945	-1.767	0.702	2.268	0.965	2.232
0.702	-1.664	0.955	-1.727	0.712	2.235	0.975	2.319
0.712	-1.728	0.965	-1.689	0.722	2.102	0.986	2.392
0.722	-1.781	0.975	-1.517	0.732	2.138	0.996	2.563
0.732	-1.776	0.985	-1.606	0.743	1.860		
0.743	-1.687	0.996	-1.378	0.753	2.120		

Table G.13: Local Nusselt numbers for bottom section, $R_T = 0$, A = 17.6, P = 100.62 kPa, Ra(b/L) = 125.

Cold Wall				Hot Wall			
y/L	$Nu_{y,C}$	y/L	$Nu_{y,C}$	y/L	$Nu_{y,H}$	y/L	$Nu_{y,H}$
0.009	-0.304	0.459	-0.510	0.004	12.297	0.257	4.743
0.011	-0.171	0.469	-0.544	0.014	9.254	0.267	4.924
0.047	-0.202	0.479	-0.511	0.024	8.541	0.277	5.042
0.050	-0.194	0.490	-0.444	0.034	8.631	0.287	5.014
0.086	-0.220	0.500	-0.561	0.044	7.919	0.297	4.515
0.090	-0.212			0.054	7.562	0.307	4.566
0.124	-0.237			0.064	7.416	0.318	4.748
0.127	-0.232			0.075	7.316	0.328	4.833
0.165	-0.256			0.085	6.975	0.338	4.434
0.168	-0.251			0.095	6.622	0.348	4.318
0.204	-0.275			0.105	6.440	0.358	4.409
0.207	-0.271			0.115	6.686	0.368	4.527
0.246	-0.295			0.125	6.194	0.378	4.373
0.247	-0.300			0.135	6.027	0.388	4.162
0.286	-0.326			0.145	5.892	0.398	4.283
0.291	-0.324			0.156	6.192	0.409	4.340
0.326	-0.366			0.166	5.811	0.419	4.236
0.334	-0.357			0.176	5.408	0.439	4.075
0.368	-0.404			0.186	5.468	0.449	4.191
0.376	-0.399			0.196	5.582	0.459	3.950
0.409	-0.352			0.206	5.363	0.469	3.744
0.419	-0.583			0.216	4.966	0.479	3.853
0.429	-0.646			0.226	5.249	0.490	3.897
0.439	-0.509			0.237	5.618		
0.449	-0.442			0.247	4.780		

Table G.14: Local Nusselt numbers for top section, $R_T = 0$, A = 17.6, P = 101.09 kPa, Ra(b/L) = 131.

Cold Wall				Hot Wall			
y/L	$Nu_{y,C}$	y/L	$Nu_{y,C}$	y/L	$Nu_{y,H}$	y/L	$Nu_{y,H}$
0.510	-0.574	0.763	-0.837	0.500	3.980	0.763	3.367
0.520	-0.514	0.773	-0.937	0.510	3.799	0.773	3.431
0.530	-0.505	0.783	-0.973	0.520	3.921	0.783	3.036
0.540	-0.618	0.793	-0.878	0.530	4.008	0.793	3.144
0.550	-0.563	0.803	-0.943	0.540	3.763	0.803	3.339
0.560	-0.495	0.813	-0.978	0.550	3.645	0.813	3.130
0.571	-0.505	0.824	-0.884	0.560	3.739	0.824	3.087
0.581	-0.680	0.834	-0.924	0.571	3.901	0.834	3.261
0.591	-0.573	0.844	-1.007	0.581	3.449	0.844	3.127
0.601	-0.617	0.854	-1.027	0.591	3.570	0.854	2.996
0.611	-0.746	0.864	-0.962	0.601	3.846	0.864	3.193
0.621	-0.619	0.874	-1.036	0.611	3.574	0.874	3.081
0.631	-0.648	0.884	-1.087	0.621	3.417	0.884	2.885
0.641	-0.758	0.894	-0.981	0.631	3.607	0.894	3.049
0.652	-0.759	0.905	-1.057	0.641	3.606	0.905	3.105
0.662	-0.667	0.915	-1.104	0.652	3.381	0.915	2.892
0.672	-0.766	0.925	-1.172	0.662	3.513	0.935	3.184
0.682	-0.823	0.935	-1.030	0.672	3.513	0.945	2.995
0.692	-0.775	0.945	-1.080	0.682	3.312	0.955	2.905
0.702	-0.796	0.955	-1.057	0.692	3.394	0.965	3.123
0.712	-0.881	0.965	-0.998	0.702	3.583	0.975	3.072
0.722	-0.810	0.975	-1.026	0.712	3.357	0.986	3.130
0.732	-0.799	0.986	-1.017	0.722	3.237	0.996	3.577
0.000	-0.655	0.996	-0.870	0.733	3.571		
0.753	-0.860			0.753	3.123		

Table G.15: Local Nusselt numbers for bottom section, $R_T = -0.5$, $A = 26.4$, $P = 100.02$ kPa, $Ra(b/L) = 12.2$.

Cold Wall				Hot Wall			
y/L	$Nu_{y,C}$	y/L	$Nu_{y,C}$	y/L	$Nu_{y,H}$	y/L	$Nu_{y,H}$
0.003	-6.301	0.257	-5.183	0.004	14.094	0.267	6.247
0.014	-4.849	0.267	-5.581	0.014	11.792	0.277	6.438
0.024	-4.237	0.277	-5.605	0.024	10.515	0.287	6.526
0.034	-4.011	0.287	-5.261	0.034	9.947	0.297	6.434
0.044	-3.542	0.297	-5.800	0.044	10.016	0.307	6.359
0.054	-3.535	0.307	-5.651	0.054	9.908	0.318	6.573
0.064	-3.758	0.317	-5.812	0.064	9.402	0.328	6.449
0.074	-3.633	0.328	-5.643	0.075	9.197	0.338	6.533
0.085	-3.750	0.338	-5.715	0.085	9.187	0.348	6.341
0.095	-4.141	0.348	-5.558	0.095	8.491	0.358	6.496
0.105	-4.254	0.358	-5.457	0.105	8.317	0.368	6.197
0.115	-4.149	0.368	-5.588	0.115	8.485	0.378	6.073
0.125	-4.596	0.378	-5.735	0.125	7.900	0.388	6.345
0.135	-4.591	0.388	-5.436	0.135	7.936	0.398	6.099
0.145	-4.665	0.398	-5.454	0.145	7.974	0.409	6.205
0.155	-4.816	0.409	-5.699	0.156	7.783	0.419	6.294
0.166	-5.008	0.419	-5.536	0.166	7.504	0.429	6.332
0.176	-5.025	0.439	-5.733	0.176	7.244	0.439	6.073
0.186	-5.007	0.449	-5.718	0.186	7.190	0.449	6.056
0.196	-5.087	0.459	-5.680	0.196	7.072	0.459	6.193
0.206	-5.164	0.469	-5.842	0.206	6.824	0.469	6.146
0.216	-5.055	0.479	-5.681	0.216	7.023	0.479	6.037
0.226	-5.086	0.490	-5.711	0.226	6.672	0.490	6.287
0.236	-5.408			0.237	6.648		
0.247	-4.992			0.257	6.543		

Table G.16: Local Nusselt numbers for top section, $R_T = -0.5$, A = 26.4, P = 98.17 kPa, Ra(b/L) = 12.4.

Cold Wall				Hot Wall			
y/L	$Nu_{y,C}$	y/L	$Nu_{y,C}$	y/L	$Nu_{y,H}$	y/L	$Nu_{y,H}$
0.500	-5.796	0.753	-6.141	0.500	6.207	0.763	6.164
0.510	-5.767	0.763	-5.714	0.510	5.962	0.773	5.807
0.520	-6.030	0.773	-5.777	0.520	5.979	0.783	6.115
0.530	-6.160	0.783	-5.299	0.530	6.336	0.793	6.284
0.540	-6.231	0.793	-6.100	0.540	6.314	0.803	6.210
0.550	-6.002	0.803	-5.907	0.550	6.097	0.813	6.107
0.560	-5.564	0.813	-6.095	0.560	5.725	0.824	5.769
0.571	-5.633	0.824	-5.792	0.571	5.881	0.834	6.028
0.581	-6.089	0.834	-5.943	0.581	6.318	0.844	6.224
0.591	-6.058	0.844	-5.773	0.591	6.164	0.854	6.165
0.601	-5.940	0.854	-5.959	0.601	6.165	0.864	5.842
0.611	-6.100	0.864	-5.866	0.611	6.036	0.874	6.058
0.621	-6.033	0.874	-5.670	0.621	6.072	0.884	6.045
0.631	-6.040	0.884	-5.947	0.631	6.391	0.894	6.428
0.641	-5.962	0.894	-6.156	0.641	6.512	0.905	6.209
0.651	-5.540	0.904	-5.974	0.652	5.995	0.915	5.810
0.662	-6.280	0.915	-5.489	0.662	6.084	0.925	5.769
0.672	-5.992	0.925	-4.777	0.672	6.429	0.935	6.116
0.682	-6.029	0.935	-6.059	0.682	6.533	0.945	6.086
0.692	-5.685	0.945	-5.596	0.692	5.918	0.955	6.095
0.702	-6.265	0.955	-5.580	0.702	6.093	0.965	6.208
0.712	-5.876	0.965	-5.537	0.712	6.406	0.975	7.268
0.722	-5.902	0.975	-5.435	0.722	6.014	0.985	6.985
0.732	-5.940	0.985	-4.762	0.732	5.645	0.996	8.583
0.743	-5.854	0.996	-5.212	0.753	6.293		

Table G.17: Local Nusselt numbers for bottom section, $R_T = -0.5$, A = 17.6, P = 99.67 kPa, Ra(b/L) = 64.7.

Cold Wall				Hot Wall			
y/L	$Nu_{y,C}$	y/L	$Nu_{y,C}$	y/L	$Nu_{y,H}$	y/L	$Nu_{y,H}$
0.004	-9.000	0.257	-3.282	0.004	19.912	0.257	9.966
0.014	-6.405	0.267	-3.245	0.014	16.445	0.267	9.754
0.024	-4.936	0.277	-3.502	0.024	14.310	0.277	9.721
0.034	-4.198	0.287	-3.855	0.034	14.283	0.287	9.927
0.044	-3.650	0.297	-3.723	0.044	14.991	0.297	10.246
0.054	-2.966	0.307	-3.549	0.054	14.431	0.307	9.746
0.065	-2.669	0.318	-3.831	0.064	13.416	0.318	9.329
0.075	-2.630	0.328	-4.197	0.075	13.439	0.328	9.406
0.085	-2.564	0.338	-3.956	0.085	13.952	0.338	9.779
0.095	-2.214	0.348	-3.718	0.095	13.552	0.348	9.338
0.105	-2.160	0.358	-3.964	0.105	12.452	0.358	8.911
0.115	-2.398	0.368	-4.364	0.115	12.615	0.368	8.931
0.125	-2.417	0.378	-4.299	0.125	12.613	0.378	9.055
0.135	-2.252	0.388	-4.148	0.135	12.470	0.388	8.867
0.145	-2.323	0.398	-4.114	0.145	11.906	0.398	8.379
0.156	-2.548	0.409	-4.611	0.156	12.066	0.409	8.348
0.166	-2.619	0.419	-4.639	0.166	12.251	0.419	8.700
0.176	-2.521	0.439	-4.405	0.176	12.091	0.429	8.398
0.186	-2.518	0.449	-4.747	0.186	11.068	0.439	7.776
0.196	-2.774	0.459	-4.735	0.196	11.063	0.449	8.258
0.206	-2.991	0.469	-4.574	0.206	11.085	0.459	8.393
0.216	-2.869	0.479	-4.676	0.216	10.920	0.469	7.855
0.226	-2.988	0.490	-4.930	0.226	10.088	0.479	7.710
0.237	-3.310	0.500	-4.778	0.237	10.623	0.490	7.925
0.247	-3.047			0.247	10.080	0.500	8.045

Table G.18: Local Nusselt numbers for top section, $R_T = -0.5$, A = 17.6, P = 100.99 kPa, Ra(b/L) = 68.6.

Cold Wall				Hot Wall			
y/L	$Nu_{y,C}$	y/L	$Nu_{y,C}$	y/L	$Nu_{y,H}$	y/L	$Nu_{y,H}$
0.510	-4.839	0.763	-5.082	0.510	7.897	0.773	6.559
0.520	-4.684	0.773	-5.332	0.520	7.913	0.783	6.881
0.530	-4.852	0.783	-5.037	0.530	7.564	0.793	6.717
0.540	-5.180	0.793	-4.916	0.540	7.477	0.803	6.626
0.550	-4.968	0.803	-5.190	0.550	7.629	0.813	6.638
0.560	-4.907	0.813	-5.306	0.560	7.615	0.824	6.824
0.571	-4.608	0.824	-5.328	0.571	7.519	0.834	6.692
0.581	-5.127	0.834	-5.130	0.581	7.384	0.844	7.068
0.591	-5.338	0.844	-5.122	0.591	7.163	0.854	6.368
0.601	-5.058	0.854	-5.526	0.601	7.434	0.864	6.635
0.611	-4.817	0.864	-5.576	0.611	7.291	0.874	6.611
0.621	-4.890	0.874	-5.129	0.621	7.565	0.884	6.501
0.631	-5.282	0.884	-5.250	0.631	7.222	0.894	6.673
0.641	-5.552	0.894	-5.311	0.641	7.219	0.905	6.307
0.651	-5.158	0.905	-5.598	0.651	7.373	0.915	6.739
0.662	-5.028	0.915	-5.662	0.662	7.195	0.935	6.457
0.672	-5.262	0.925	-6.010	0.672	6.967	0.945	6.106
0.682	-5.469	0.935	-6.108	0.682	6.933	0.955	6.631
0.692	-5.163	0.945	-6.509	0.692	7.255	0.965	6.804
0.702	-4.936	0.955	-7.053	0.702	7.112	0.975	6.563
0.712	-4.912	0.965	-7.270	0.712	6.893	0.986	7.001
0.722	-5.353	0.975	-6.926	0.722	6.642	0.996	8.144
0.732	-5.406	0.986	-7.876	0.732	6.958		
0.722	-5.766	0.996	-8.643	0.753	6.567		
0.753	-4.947			0.763	6.564		

Table G.19: Local Nusselt numbers for bottom section, $R_T = -0.5$, A = 13.2, P = 100.91 kPa, Ra = 211.

Cold Wall				Hot Wall			
y/L	$Nu_{y,C}$	y/L	$Nu_{y,C}$	y/L	$Nu_{y,H}$	y/L	$Nu_{y,H}$
0.004	-7.144	0.257	-2.327	0.004	26.837	0.257	15.783
0.014	-4.420	0.267	-2.385	0.014	21.472	0.267	14.183
0.024	-3.734	0.277	-2.719	0.024	19.470	0.277	14.442
0.034	-2.686	0.287	-2.447	0.034	19.848	0.287	15.182
0.044	-2.470	0.297	-2.695	0.044	19.983	0.297	14.214
0.054	-2.216	0.307	-2.999	0.054	19.175	0.307	14.023
0.065	-1.777	0.318	-2.693	0.065	19.069	0.318	14.025
0.075	-1.816	0.328	-3.107	0.075	18.894	0.328	13.478
0.085	-1.707	0.338	-3.038	0.085	18.666	0.338	13.701
0.095	-1.536	0.348	-2.905	0.095	18.854	0.348	13.568
0.105	-1.769	0.358	-3.329	0.105	18.434	0.358	12.882
0.115	-1.539	0.368	-3.257	0.115	17.721	0.368	13.264
0.125	-1.581	0.378	-3.146	0.125	18.950	0.378	13.063
0.135	-1.716	0.388	-3.603	0.135	17.003	0.388	12.845
0.145	-1.626	0.399	-3.486	0.145	17.851	0.398	13.249
0.156	-1.669	0.409	-3.514	0.156	17.376	0.409	12.344
0.166	-1.908	0.419	-3.706	0.166	16.825	0.419	13.000
0.176	-1.717	0.429	-4.222	0.176	17.644	0.439	11.779
0.186	-1.923	0.439	-4.079	0.186	16.495	0.449	12.675
0.196	-1.926	0.449	-4.254	0.196	15.985	0.459	11.902
0.206	-1.793	0.459	-3.984	0.206	16.481	0.469	11.854
0.216	-2.163	0.469	-4.469	0.216	15.680	0.479	11.915
0.226	-2.154	0.479	-4.212	0.226	16.188	0.490	11.388
0.237	-2.060	0.490	-4.154	0.237	15.210		
0.247	-1.079	0.500	-4.687	0.247	13.771		

Table G.20: Local Nusselt numbers for top section, $R_T = -0.5$, A = 13.2, P = 100.94 kPa, Ra = 218.

Cold Wall				Hot Wall			
y/L	$Nu_{y,C}$	y/L	$Nu_{y,C}$	y/L	$Nu_{y,H}$	y/L	$Nu_{y,H}$
0.510	-4.369	0.763	-8.181	0.500	12.247	0.753	8.199
0.520	-4.317	0.773	-8.290	0.510	11.273	0.763	8.611
0.530	-4.588	0.783	-7.818	0.520	10.975	0.773	8.241
0.540	-4.908	0.793	-8.034	0.530	11.028	0.783	7.682
0.550	-4.937	0.803	-8.514	0.540	11.722	0.793	7.430
0.560	-4.843	0.813	-8.693	0.550	11.292	0.803	8.152
0.571	-5.121	0.824	-8.354	0.560	10.446	0.813	8.415
0.581	-5.264	0.834	-8.229	0.571	10.402	0.824	7.806
0.591	-5.583	0.844	-8.642	0.581	11.132	0.834	7.234
0.601	-5.850	0.854	-8.749	0.591	10.515	0.844	7.699
0.611	-5.620	0.864	-9.128	0.601	10.518	0.854	8.076
0.621	-5.918	0.874	-8.885	0.611	9.765	0.864	7.683
0.631	-6.152	0.884	-8.670	0.621	9.799	0.874	7.505
0.641	-6.619	0.894	-9.527	0.631	10.169	0.884	7.541
0.652	-6.499	0.904	-9.905	0.641	10.113	0.894	7.861
0.662	-6.374	0.915	-9.929	0.652	10.209	0.904	7.914
0.672	-7.180	0.925	-9.970	0.662	9.022	0.915	7.479
0.682	-7.355	0.935	-10.543	0.672	9.117	0.925	7.122
0.692	-7.033	0.945	-10.965	0.682	9.639	0.935	7.063
0.702	-6.834	0.955	-11.238	0.692	9.190	0.945	7.383
0.712	-7.729	0.965	-10.906	0.702	8.670	0.955	7.374
0.722	-7.886	0.975	-10.614	0.712	8.811	0.965	6.901
0.732	-7.541	0.985	-11.601	0.722	9.302	0.975	7.108
0.743	-7.306	0.996	-13.500	0.732	8.821	0.985	8.403
0.753	-7.757			0.743	9.088	0.996	10.120

Table G.21: Local Nusselt numbers for bottom section, $R_T = -0.75$, A = 26.4, P = 99.79 kPa, Ra = 4.71.

Cold Wall				Hot Wall			
y/L	$Nu_{y,C}$	y/L	$Nu_{y,C}$	y/L	$Nu_{y,H}$	y/L	$Nu_{y,H}$
0.004	-15.826	0.257	-12.362	0.004	23.720	0.267	13.397
0.014	-10.773	0.267	-13.576	0.014	18.040	0.277	13.935
0.024	-10.010	0.277	-12.916	0.024	19.416	0.287	13.108
0.034	-8.952	0.287	-12.989	0.034	20.244	0.297	14.243
0.044	-10.239	0.297	-13.883	0.044	18.158	0.307	13.539
0.054	-10.550	0.307	-12.765	0.054	18.607	0.318	13.021
0.064	-10.891	0.318	-13.283	0.065	16.856	0.328	14.046
0.075	-11.540	0.328	-13.670	0.075	16.733	0.338	13.293
0.085	-11.585	0.338	-12.589	0.085	16.214	0.348	13.268
0.095	-11.865	0.348	-13.156	0.095	14.662	0.358	14.279
0.105	-12.685	0.358	-13.210	0.105	15.631	0.368	13.111
0.115	-12.170	0.368	-12.451	0.115	15.157	0.378	13.794
0.125	-12.202	0.378	-13.515	0.125	13.726	0.388	13.874
0.135	-12.855	0.388	-12.670	0.135	14.843	0.398	13.263
0.145	-11.979	0.399	-12.845	0.146	14.684	0.409	13.660
0.156	-12.615	0.409	-13.325	0.156	14.224	0.419	13.299
0.166	-12.649	0.419	-12.765	0.166	15.112	0.439	13.359
0.176	-12.143	0.439	-13.190	0.176	13.397	0.449	13.264
0.186	-13.495	0.449	-12.276	0.186	14.102	0.459	13.626
0.196	-13.221	0.459	-13.228	0.196	14.116	0.469	12.634
0.206	-12.912	0.469	-12.842	0.206	12.910	0.479	12.886
0.216	-13.737	0.479	-13.101	0.216	13.943	0.490	13.193
0.226	-12.683	0.490	-12.940	0.226	13.589		
0.237	-13.614	0.500	-12.933	0.237	13.554		
0.247	-11.587			0.257	12.707		

Table G.22: Local Nusselt numbers for top section, $R_T = -0.75$, A = 26.4, P = 101.06 kPa, Ra = 4.76.

Cold Wall				Hot Wall			
y/L	$Nu_{y,C}$	y/L	$Nu_{y,C}$	y/L	$Nu_{y,H}$	y/L	$Nu_{y,H}$
0.510	-13.343	0.763	-11.628	0.500	13.183	0.763	12.238
0.520	-12.505	0.773	-12.831	0.510	13.889	0.773	13.548
0.530	-12.406	0.783	-13.036	0.520	13.408	0.783	13.897
0.540	-13.344	0.793	-12.215	0.530	12.830	0.793	11.929
0.550	-12.862	0.803	-12.725	0.540	13.795	0.803	13.554
0.560	-12.574	0.813	-13.319	0.550	13.820	0.813	13.651
0.571	-13.278	0.824	-12.567	0.560	12.748	0.824	12.734
0.581	-13.436	0.834	-11.985	0.571	13.193	0.834	13.056
0.591	-12.251	0.844	-12.877	0.581	13.733	0.844	12.873
0.601	-12.548	0.854	-12.748	0.591	13.309	0.854	13.055
0.611	-13.490	0.864	-11.833	0.601	12.929	0.864	12.524
0.621	-13.002	0.874	-12.571	0.611	14.101	0.874	13.508
0.631	-12.428	0.884	-12.715	0.621	13.805	0.884	13.581
0.641	-12.912	0.894	-12.269	0.631	12.909	0.894	12.194
0.652	-13.220	0.905	-12.652	0.641	13.551	0.904	13.262
0.662	-12.101	0.915	-13.401	0.651	14.238	0.915	13.376
0.672	-12.637	0.925	-13.886	0.662	13.528	0.935	12.967
0.682	-13.849	0.935	-12.240	0.672	13.350	0.945	13.545
0.692	-12.522	0.945	-13.137	0.682	14.072	0.955	13.273
0.702	-12.715	0.955	-12.344	0.692	13.239	0.965	13.389
0.712	-13.489	0.965	-12.130	0.702	13.110	0.975	14.574
0.722	-12.377	0.975	-13.011	0.712	14.720	0.985	14.884
0.733	-12.384	0.986	-12.856	0.722	13.686	0.996	16.593
0.743	-12.744	0.996	-12.716	0.732	12.944		
0.753	-12.866			0.753	13.287		

Table G.23: Local Nusselt numbers for bottom section, $R_T = -0.75$, A = 17.6, P = 100.25 kPa,

Ra = 22.6.

Cold Wall				Hot Wall			
y/L	$Nu_{y,C}$	y/L	$Nu_{y,C}$	y/L	$Nu_{y,H}$	y/L	$Nu_{y,H}$
0.004	-12.724	0.257	-11.623	0.004	35.253	0.287	15.665
0.014	-8.195	0.267	-12.389	0.034	29.871	0.297	16.434
0.024	-6.630	0.277	-11.467	0.044	29.332	0.307	16.584
0.034	-5.952	0.287	-10.861	0.054	29.229	0.318	16.449
0.044	-5.419	0.297	-11.870	0.065	28.360	0.328	15.390
0.054	-5.634	0.307	-12.264	0.075	27.399	0.338	16.259
0.064	-6.341	0.317	-11.426	0.085	26.777	0.348	15.578
0.075	-6.686	0.328	-11.512	0.095	26.002	0.358	15.498
0.085	-7.080	0.338	-12.215	0.105	25.692	0.368	14.906
0.095	-7.119	0.348	-11.954	0.115	25.845	0.378	15.587
0.105	-7.872	0.358	-11.652	0.125	24.315	0.388	15.690
0.115	-8.520	0.368	-11.430	0.135	22.744	0.399	14.545
0.125	-8.613	0.378	-12.488	0.145	22.986	0.409	14.484
0.135	-8.985	0.388	-12.392	0.156	22.903	0.419	14.686
0.145	-9.776	0.398	-11.537	0.166	21.349	0.439	13.328
0.156	-10.243	0.409	-12.306	0.176	19.938	0.449	15.171
0.166	-9.604	0.429	-13.267	0.186	21.750	0.459	14.880
0.176	-9.790	0.439	-11.725	0.196	20.045	0.469	14.121
0.186	-10.842	0.449	-12.870	0.206	18.688	0.479	14.364
0.196	-11.076	0.459	-12.804	0.216	19.066	0.490	15.638
0.206	-10.561	0.469	-12.109	0.226	18.674		
0.216	-11.297	0.479	-12.647	0.237	17.968		
0.226	-12.048	0.490	-13.290	0.257	17.079		
0.237	-11.144			0.267	17.398		
0.247	-10.999			0.277	16.392		

Table G.24: Local Nusselt numbers for top section, $R_T = -0.75$, $A = 17.6$, $P = 101.03$ kPa, Ra = 23.1.

Cold Wall				Hot Wall			
y/L	$Nu_{y,C}$	y/L	$Nu_{y,C}$	y/L	$Nu_{y,H}$	y/L	$Nu_{y,H}$
0.500	-12.403	0.763	-12.517	0.500	14.835	0.763	13.653
0.510	-13.395	0.773	-13.480	0.510	14.256	0.773	13.874
0.520	-13.439	0.783	-14.480	0.520	15.024	0.783	15.457
0.530	-13.530	0.793	-13.510	0.530	14.868	0.793	14.572
0.540	-12.880	0.803	-13.152	0.540	14.887	0.803	13.961
0.550	-13.000	0.813	-14.696	0.550	13.966	0.813	14.609
0.560	-13.785	0.824	-14.438	0.560	15.431	0.824	14.019
0.571	-13.692	0.834	-13.552	0.571	14.630	0.834	13.923
0.581	-12.683	0.844	-14.322	0.581	13.654	0.844	13.001
0.591	-13.209	0.854	-15.697	0.591	14.092	0.854	15.066
0.601	-13.919	0.864	-15.675	0.601	15.159	0.864	14.007
0.611	-12.651	0.874	-14.753	0.611	14.566	0.874	13.163
0.621	-13.087	0.884	-15.574	0.621	13.456	0.884	13.445
0.631	-14.560	0.894	-17.130	0.631	14.300	0.894	14.868
0.641	-14.226	0.905	-17.149	0.641	14.698	0.905	13.100
0.652	-13.526	0.915	-16.272	0.652	14.400	0.915	12.607
0.662	-13.006	0.925	-17.784	0.662	13.530	0.935	12.888
0.672	-13.853	0.935	-19.993	0.672	15.426	0.945	12.738
0.682	-13.414	0.945	-20.229	0.682	15.491	0.955	11.801
0.692	-12.501	0.955	-19.980	0.692	14.061	0.965	12.883
0.702	-13.756	0.965	-21.675	0.702	14.221	0.985	12.957
0.712	-13.572	0.975	-21.757	0.712	15.205	0.996	16.302
0.722	-12.835	0.985	-20.503	0.722	14.110		
0.732	-12.839	0.996	-22.358	0.732	13.197		
0.753	-13.020			0.753	14.309		

Table G.25: Local Nusselt numbers for bottom section, $R_T = -0.75$, A = 13.2, P = 100.93 kPa, Ra = 74.7.

Cold Wall				Hot Wall			
y/L	$Nu_{y,C}$	y/L	$Nu_{y,C}$	y/L	$Nu_{y,H}$	y/L	$Nu_{y,H}$
0.004	-19.213	0.267	-9.810	0.004	52.529	0.267	28.620
0.014	-13.623	0.277	-11.750	0.014	39.017	0.277	26.983
0.024	-10.249	0.287	-11.783	0.024	39.071	0.287	29.476
0.034	-9.285	0.297	-10.750	0.034	37.934	0.297	27.797
0.044	-7.735	0.307	-12.731	0.044	38.389	0.307	26.189
0.054	-6.980	0.318	-12.289	0.054	38.061	0.318	28.388
0.064	-6.849	0.328	-11.882	0.065	37.833	0.328	25.053
0.075	-7.417	0.338	-13.566	0.075	37.195	0.338	24.451
0.085	-5.711	0.348	-13.393	0.085	38.720	0.348	26.486
0.095	-6.005	0.358	-12.793	0.095	36.108	0.358	24.511
0.105	-5.626	0.368	-14.360	0.105	36.900	0.368	22.305
0.115	-5.646	0.378	-14.056	0.115	35.160	0.378	24.123
0.125	-6.442	0.388	-13.434	0.125	35.226	0.388	22.381
0.135	-6.136	0.399	-15.706	0.135	35.627	0.399	21.241
0.145	-6.290	0.409	-14.381	0.146	33.582	0.409	23.278
0.156	-6.927	0.419	-14.169	0.156	33.318	0.419	21.199
0.166	-6.934	0.439	-14.822	0.166	33.461	0.439	20.351
0.176	-7.116	0.449	-13.276	0.176	33.229	0.449	19.344
0.186	-7.979	0.459	-16.358	0.186	32.020	0.459	19.718
0.196	-7.698	0.469	-15.212	0.196	32.562	0.469	20.254
0.206	-7.691	0.479	-15.234	0.206	31.344	0.479	19.036
0.216	-9.025	0.490	-15.826	0.216	30.203	0.490	19.942
0.226	-8.610	0.500	-15.315	0.226	31.347	0.500	19.050
0.237	-8.756			0.237	29.769		
0.257	-9.597			0.257	30.450		

Table G.26: Local Nusselt numbers for top section, $R_T = -0.75$, $A = 13.2$, $P = 101.03$ kPa, Ra = 78.4.

Cold Wall				Hot Wall			
y/L	$Nu_{y,C}$	y/L	$Nu_{y,C}$	y/L	$Nu_{y,H}$	y/L	$Nu_{y,H}$
0.510	-15.041	0.763	-19.802	0.510	19.642	0.763	16.800
0.520	-16.377	0.773	-19.474	0.520	20.090	0.773	16.244
0.530	-16.097	0.783	-18.193	0.530	19.311	0.783	15.655
0.540	-15.056	0.793	-20.849	0.540	18.024	0.793	17.558
0.550	-16.219	0.803	-23.027	0.550	19.475	0.803	16.240
0.560	-16.731	0.813	-22.126	0.560	19.200	0.813	15.860
0.571	-16.898	0.824	-21.009	0.571	17.869	0.824	14.834
0.581	-15.075	0.834	-23.016	0.581	17.617	0.834	16.189
0.591	-16.012	0.844	-23.996	0.591	18.005	0.844	15.149
0.601	-17.429	0.854	-25.117	0.601	18.850	0.854	14.214
0.611	-16.113	0.864	-25.062	0.611	17.054	0.864	13.219
0.621	-14.213	0.874	-25.222	0.621	17.026	0.874	14.448
0.631	-15.502	0.884	-27.035	0.631	17.304	0.884	13.782
0.641	-17.578	0.894	-28.623	0.641	20.224	0.894	12.724
0.652	-15.902	0.905	-28.207	0.652	17.214	0.905	11.479
0.662	-14.934	0.915	-27.054	0.662	16.802	0.915	12.327
0.672	-16.144	0.925	-28.804	0.672	18.780	0.925	10.265
0.682	-17.353	0.935	-31.539	0.682	19.237	0.935	10.942
0.692	-16.542	0.945	-29.176	0.692	18.111	0.945	10.543
0.702	-15.662	0.955	-28.357	0.702	16.912	0.955	11.154
0.712	-17.207	0.965	-29.320	0.712	19.738	0.965	12.674
0.722	-18.793	0.975	-29.749	0.722	18.970	0.975	13.527
0.732	-17.858	0.985	-29.303	0.732	17.382	0.985	15.466
0.743	-16.046	0.996	-31.761	0.743	16.549	0.996	23.321
0.753	-18.347			0.753	17.868		

Table G.27: Local Nusselt numbers for top section, $R_T = -1$, A = 26.4, P = 101.14 kPa, Ra = 1489.

Cold Wall				Hot Wall			
y/L	$Nu_{y,C}$	y/L	$Nu_{y,C}$	y/L	$Nu_{y,H}$	y/L	$Nu_{y,H}$
0.004	-1.030	0.257	-0.917	0.004	1.283	0.257	0.922
0.014	-0.906	0.267	-0.941	0.014	1.189	0.267	0.985
0.024	-0.807	0.277	-1.010	0.024	1.142	0.277	0.992
0.034	-0.906	0.287	-0.898	0.034	1.101	0.287	0.930
0.044	-1.001	0.297	-0.944	0.044	1.098	0.297	0.995
0.054	-0.927	0.307	-0.985	0.054	1.025	0.307	1.054
0.064	-0.917	0.318	-0.903	0.065	1.010	0.318	0.962
0.075	-0.975	0.328	-0.954	0.075	1.077	0.328	0.944
0.085	-0.939	0.338	-0.997	0.085	1.022	0.338	1.052
0.095	-0.904	0.348	-0.945	0.095	0.938	0.348	0.985
0.105	-0.956	0.358	-0.907	0.105	0.973	0.358	0.930
0.115	-0.955	0.368	-0.987	0.115	1.000	0.368	1.003
0.125	-0.876	0.378	-0.944	0.125	0.911	0.378	1.028
0.135	-0.944	0.388	-0.873	0.135	0.987	0.388	0.890
0.145	-0.938	0.398	-0.915	0.146	0.993	0.399	0.972
0.156	-0.865	0.409	-1.002	0.156	0.916	0.409	1.051
0.166	-0.946	0.419	-0.911	0.166	0.970	0.419	0.912
0.176	-0.960	0.439	-0.997	0.176	0.976	0.429	1.040
0.186	-0.890	0.449	-0.932	0.186	0.943	0.439	1.066
0.196	-0.963	0.459	-0.921	0.196	0.959	0.449	0.986
0.206	-1.040	0.469	-0.980	0.206	0.981	0.459	0.951
0.216	-0.938	0.479	-0.949	0.216	0.922	0.469	0.998
0.226	-0.895	0.490	-0.946	0.226	0.975	0.480	0.959
0.237	-0.979	0.500	-0.974	0.237	1.036	0.490	0.919
0.247	-0.834			0.247	1.064	0.500	0.976

Table G.28: Local Nusselt numbers for top section, $R_T = -1$, A = 26.4, P = 101.08 kPa, Ra = 1475.

Cold Wall				Hot Wall			
y/L	$Nu_{y,C}$	y/L	$Nu_{y,C}$	y/L	$Nu_{y,H}$	y/L	$Nu_{y,H}$
0.510	-0.979	0.763	-0.914	0.510	0.997	0.763	0.937
0.520	-0.936	0.773	-0.918	0.520	0.954	0.773	0.967
0.530	-0.947	0.783	-0.949	0.530	0.958	0.783	1.004
0.540	-1.008	0.793	-0.939	0.540	0.988	0.793	0.918
0.550	-0.988	0.803	-0.940	0.550	0.919	0.803	0.930
0.560	-0.916	0.813	-0.962	0.560	0.935	0.813	1.006
0.000	-0.879	0.824	-0.952	0.571	0.954	0.824	0.911
0.581	-0.947	0.834	-0.930	0.581	0.949	0.834	0.921
0.591	-0.916	0.844	-0.964	0.591	0.927	0.844	0.972
0.601	-1.004	0.854	-0.970	0.601	0.998	0.854	0.924
0.611	-0.958	0.864	-0.936	0.611	0.990	0.864	0.936
0.621	-0.960	0.874	-0.983	0.621	0.937	0.874	0.976
0.631	-0.985	0.884	-0.979	0.631	0.984	0.884	0.964
0.641	-0.970	0.894	-0.962	0.641	0.959	0.894	0.935
0.651	-0.959	0.905	-1.003	0.652	0.961	0.905	0.952
0.662	-0.973	0.915	-1.003	0.662	1.008	0.915	0.898
0.672	-0.923	0.925	-0.989	0.672	0.982	0.935	0.935
0.682	-0.942	0.935	-1.066	0.682	0.945	0.945	0.885
0.692	-1.005	0.945	-1.065	0.692	1.008	0.955	0.846
0.702	-0.938	0.955	-1.110	0.702	0.969	0.965	0.890
0.712	-0.918	0.965	-1.168	0.712	0.975	0.975	0.822
0.722	-0.966	0.975	-1.199	0.722	1.020	0.985	0.851
0.732	-0.947	0.985	-1.221	0.732	0.913	0.996	1.086
0.743	-0.942	0.996	-1.277	0.743	0.875		
0.753	-0.949			0.753	0.971		

Table G.29: Local Nusselt numbers for top section, $R_T = -1$, A = 17.6, P = 99.52 kPa, Ra = 4654.

Cold Wall				Hot Wall			
y/L	$Nu_{y,C}$	y/L	$Nu_{y,C}$	y/L	$Nu_{y,H}$	y/L	$Nu_{y,H}$
0.004	-0.763	0.257	-0.899	0.004	1.828	0.267	1.041
0.014	-0.640	0.267	-0.955	0.014	1.723	0.277	0.988
0.024	-0.659	0.277	-0.916	0.024	1.826	0.287	1.046
0.034	-0.652	0.287	-0.902	0.034	1.797	0.297	1.070
0.044	-0.691	0.297	-0.960	0.044	1.820	0.307	0.987
0.054	-0.760	0.307	-0.896	0.054	1.810	0.318	1.021
0.064	-0.761	0.318	-0.912	0.065	1.620	0.328	1.030
0.075	-0.759	0.328	-0.959	0.075	1.584	0.338	0.959
0.085	-0.817	0.338	-0.901	0.085	1.570	0.348	0.999
0.095	-0.798	0.348	-0.889	0.095	1.398	0.358	1.060
0.105	-0.841	0.358	-0.991	0.105	1.391	0.368	0.956
0.115	-0.867	0.368	-0.922	0.115	1.428	0.378	0.977
0.125	-0.864	0.378	-0.937	0.125	1.253	0.388	1.064
0.135	-0.866	0.388	-0.974	0.135	1.268	0.399	0.937
0.145	-0.917	0.398	-0.952	0.146	1.321	0.409	0.973
0.156	-0.902	0.409	-0.928	0.156	1.167	0.419	1.031
0.166	-0.865	0.419	-1.005	0.166	1.165	0.439	0.920
0.176	-0.936	0.429	-0.964	0.176	1.110	0.449	1.075
0.186	-0.888	0.439	-0.900	0.186	1.132	0.459	0.977
0.196	-0.876	0.449	-0.986	0.196	1.144	0.469	0.959
0.206	-0.947	0.459	-0.967	0.206	1.148	0.480	1.036
0.216	-0.900	0.469	-0.959	0.216	1.060	0.490	0.946
0.226	-0.914	0.479	-0.993	0.226	1.067		
0.237	-0.931	0.490	-0.998	0.237	1.013		
0.247	-0.894	0.500	-0.929	0.257	1.045		

Table G.30: Local Nusselt numbers for top section, $R_T = -1$, $A = 17.6$, $P = 100.95$ kPa, Ra = 4922.

Cold Wall				Hot Wall			
y/L	$Nu_{y,C}$	y/L	$Nu_{y,C}$	y/L	$Nu_{y,H}$	y/L	$Nu_{y,H}$
0.510	-1.053	0.773	-1.103	0.500	0.980	0.763	0.989
0.520	-0.969	0.783	-1.019	0.510	1.024	0.773	0.919
0.530	-0.956	0.793	-1.124	0.520	0.913	0.783	0.896
0.540	-0.996	0.803	-1.144	0.530	0.966	0.793	0.960
0.550	-1.001	0.813	-1.084	0.540	0.997	0.803	0.916
0.560	-0.903	0.824	-1.201	0.550	0.954	0.813	0.851
0.571	-0.954	0.834	-1.245	0.560	0.915	0.824	0.930
0.581	-1.059	0.844	-1.222	0.571	1.003	0.834	0.906
0.591	-0.940	0.854	-1.279	0.581	0.944	0.844	0.826
0.601	-0.964	0.864	-1.354	0.591	0.877	0.854	0.915
0.611	-1.027	0.874	-1.363	0.601	1.000	0.864	0.853
0.621	-0.936	0.884	-1.290	0.611	0.912	0.874	0.761
0.631	-0.945	0.894	-1.538	0.621	0.880	0.884	0.853
0.641	-1.045	0.905	-1.466	0.631	0.975	0.894	0.817
0.652	-0.957	0.915	-1.430	0.641	0.972	0.905	0.739
0.662	-0.950	0.925	-1.488	0.652	0.911	0.915	0.760
0.672	-1.058	0.935	-1.636	0.662	0.958	0.935	0.654
0.682	-0.983	0.945	-1.595	0.672	0.936	0.945	0.658
0.692	-0.934	0.955	-1.669	0.682	0.864	0.955	0.652
0.702	-1.077	0.965	-1.660	0.692	0.945	0.965	0.615
0.712	-0.997	0.975	-1.551	0.702	0.977	0.975	0.649
0.722	-1.000	0.986	-1.731	0.712	0.886	0.986	0.769
0.732	-1.054	0.996	-1.964	0.722	0.948	0.996	0.877
0.753	-0.940			0.733	0.981		
0.763	-1.061			0.753	0.911		

Table G.31: Local Nusselt numbers for top section, $R_T = -1$, $A = 13.2$, $P = 100.93$ kPa, $Ra = 11743$.

Cold Wall				Hot Wall			
y/L	$Nu_{y,C}$	y/L	$Nu_{y,C}$	y/L	$Nu_{y,H}$	y/L	$Nu_{y,H}$
0.004	-1.361	0.257	-1.005	0.004	2.618	0.257	1.349
0.014	-0.951	0.267	-1.068	0.014	2.366	0.267	1.514
0.024	-0.886	0.277	-1.077	0.024	2.421	0.277	1.424
0.034	-0.732	0.287	-0.980	0.034	2.625	0.287	1.336
0.044	-0.659	0.297	-1.082	0.044	2.401	0.297	1.453
0.054	-0.697	0.307	-1.083	0.054	2.468	0.307	1.442
0.064	-0.610	0.317	-0.996	0.064	2.557	0.318	1.398
0.075	-0.590	0.328	-1.068	0.075	2.413	0.328	1.404
0.085	-0.653	0.338	-1.080	0.085	2.432	0.338	1.411
0.095	-0.625	0.348	-1.043	0.095	2.361	0.348	1.345
0.105	-0.608	0.358	-1.089	0.105	2.354	0.358	1.370
0.115	-0.704	0.368	-1.098	0.115	2.282	0.368	1.371
0.125	-0.716	0.378	-1.059	0.125	2.224	0.378	1.303
0.135	-0.657	0.388	-1.114	0.135	2.211	0.388	1.334
0.145	-0.795	0.398	-1.164	0.145	2.157	0.398	1.289
0.156	-0.781	0.409	-1.082	0.156	2.110	0.409	1.203
0.166	-0.771	0.419	-1.156	0.166	1.944	0.419	1.284
0.176	-0.908	0.429	-0.991	0.176	2.021	0.429	1.243
0.186	-0.925	0.439	-1.131	0.186	1.890	0.439	1.120
0.196	-0.863	0.449	-1.172	0.196	1.784	0.449	1.265
0.206	-0.960	0.459	-1.233	0.206	1.880	0.459	1.170
0.216	-0.976	0.469	-1.129	0.216	1.815	0.469	1.155
0.226	-0.858	0.479	-1.230	0.226	1.589	0.479	1.275
0.237	-1.080	0.490	-1.186	0.237	1.696	0.490	1.169
0.247	-1.030			0.247	1.345		

Table G.32: Local Nusselt numbers for top section, $R_T = -1$, A = 13.2, P = 100.98 kPa, Ra = 11769.

Cold Wall				Hot Wall			
y/L	$Nu_{y,C}$	y/L	$Nu_{y,C}$	y/L	$Nu_{y,H}$	y/L	$Nu_{y,H}$
0.500	-1.217	0.753	-1.677	0.500	1.186	0.763	0.899
0.510	-1.122	0.763	-1.720	0.510	1.098	0.773	0.873
0.520	-1.244	0.773	-1.639	0.520	1.243	0.783	0.906
0.530	-1.246	0.783	-1.803	0.530	1.211	0.793	0.818
0.540	-1.175	0.793	-1.810	0.540	1.132	0.803	0.816
0.550	-1.320	0.803	-1.790	0.550	1.220	0.813	0.826
0.560	-1.268	0.813	-1.956	0.560	1.175	0.824	0.745
0.571	-1.340	0.824	-1.877	0.571	1.078	0.834	0.749
0.581	-1.314	0.834	-1.843	0.581	1.256	0.844	0.730
0.591	-1.300	0.844	-2.024	0.591	1.078	0.854	0.673
0.601	-1.226	0.854	-2.026	0.601	1.074	0.864	0.701
0.611	-1.380	0.864	-1.921	0.611	1.149	0.874	0.668
0.621	-1.310	0.874	-2.087	0.621	1.085	0.884	0.612
0.631	-1.221	0.884	-2.141	0.631	1.038	0.894	0.658
0.641	-1.448	0.894	-2.037	0.641	1.235	0.905	0.620
0.652	-1.387	0.905	-2.252	0.652	1.047	0.915	0.569
0.662	-1.395	0.915	-2.162	0.662	1.099	0.935	0.606
0.672	-1.558	0.925	-2.171	0.672	1.193	0.945	0.591
0.682	-1.408	0.935	-2.260	0.682	1.104	0.955	0.668
0.692	-1.448	0.945	-2.162	0.692	1.103	0.965	0.737
0.702	-1.560	0.955	-2.168	0.702	1.121	0.975	0.770
0.712	-1.464	0.965	-2.329	0.712	0.977	0.986	0.945
0.722	-1.572	0.975	-2.148	0.722	1.097	0.996	1.111
0.732	-1.656	0.986	-2.185	0.732	0.997		
0.743	-1.510	0.996	-2.705	0.753	0.970		

Table G.33: Local Nusselt numbers for section 1 (bottom of channel),
$R_T = -0.5$, A = 8.8, P = 100.08 kPa, Ra(b/L) = 1121.

Cold Wall		Hot Wall	
y/L	$Nu_{y,C}$	y/L	$Nu_{y,C}$
0.004	-7.745	0.004	39.479
0.014	-5.547	0.014	29.268
0.024	-4.756	0.024	26.247
0.034	-4.177	0.034	27.874
0.044	-3.784	0.044	27.739
0.054	-3.316	0.054	27.670

Table G.34: Local Nusselt numbers for section 2, $R_T = -0.5$, A = 8.8,
P = 100.08 kPa, Ra(b/L) = 1093.

Cold Wall		Hot Wall	
y/L	$Nu_{y,C}$	y/L	$Nu_{y,C}$
0.065	-3.223	0.065	26.621
0.075	-2.446	0.075	27.189
0.085	-2.586	0.085	25.298
0.095	-2.617	0.095	27.045
0.105	-2.443	0.105	25.879
0.115	-2.426	0.115	26.330
0.125	-2.437	0.125	25.731
0.135	-2.511	0.135	27.208
0.146	-2.550	0.146	25.100

Table G.35: Local Nusselt numbers for section 3, $R_T = -0.5$, $A = 8.8$, P = 100.08 kPa, Ra(b/L) = 1079.

Cold Wall		Hot Wall	
y/L	$Nu_{y,C}$	y/L	$Nu_{y,C}$
0.156	-3.082	0.156	25.412
0.166	-3.062	0.166	24.588
0.176	-3.082	0.176	25.502
0.186	-3.404	0.186	24.683
0.196	-3.338	0.206	24.169
0.206	-3.483	0.216	22.021
0.216	-3.458	0.227	21.375
0.227	-3.650	0.237	23.291
0.237	-3.732		

Table G.36: Local Nusselt numbers for section 4, $R_T = -0.5$, $A = 8.8$, P = 100.08 kPa, Ra(b/L) = 1061.

Cold Wall		Hot Wall	
y/L	$Nu_{y,C}$	y/L	$Nu_{y,C}$
0.257	-3.871	0.257	23.793
0.267	-3.994	0.267	22.921
0.277	-4.281	0.277	22.560
0.287	-4.605	0.287	22.928
0.297	-4.648	0.297	21.720
0.308	-4.875	0.308	21.917
0.318	-5.091	0.318	20.305
0.328	-5.004	0.328	21.961
0.338	-5.309	0.338	21.982

Table G.37: Local Nusselt numbers for section 5, $R_T = -0.5$, A = 8.8, P = 100.08 kPa, Ra(b/L) = 1055.

Cold Wall		Hot Wall	
y/L	$Nu_{y,C}$	y/L	$Nu_{y,C}$
0.348	-5.159	0.348	19.895
0.358	-5.259	0.358	20.529
0.368	-5.643	0.368	20.605
0.378	-5.889	0.378	18.192
0.389	-5.699	0.389	19.743
0.399	-6.036	0.399	19.788
0.409	-6.324	0.409	19.578
0.419	-5.890	0.419	19.716
		0.439	18.152

Table G.38: Local Nusselt numbers for section 6, $R_T = -0.5$, A = 8.8, P = 100.08 kPa, Ra(b/L) = 1041.

Cold Wall		Hot Wall	
y/L	$Nu_{y,C}$	y/L	$Nu_{y,C}$
0.439	-6.655	0.449	19.112
0.449	-6.805	0.459	18.328
0.459	-7.343	0.470	18.520
0.470	-7.467	0.480	18.401
0.480	-7.301	0.490	18.154
0.490	-8.107	0.500	18.908
0.500	-8.020		

Table G.39: Local Nusselt numbers for section 7, $R_T = -0.5$, A = 8.8, P = 100.07 kPa, Ra(b/L) = 1088.

Cold Wall		Hot Wall	
y/L	$Nu_{y,C}$	y/L	$Nu_{y,C}$
0.501	-7.181	0.501	17.398
0.511	-7.455	0.511	17.465
0.521	-7.805	0.521	18.477
0.531	-7.579	0.531	16.122
0.541	-8.094	0.541	16.848
0.551	-8.505	0.551	18.703

Table G.40: Local Nusselt numbers for section 8, $R_T = -0.5$, A = 8.8, P = 100.07 kPa, Ra(b/L) = 1101.

Cold Wall		Hot Wall	
y/L	$Nu_{y,C}$	y/L	$Nu_{y,C}$
0.561	-8.116	0.561	16.108
0.582	-9.280	0.571	16.837
0.592	-8.868	0.582	15.603
0.602	-9.347	0.592	16.257
0.612	-9.633	0.602	15.969
0.622	-9.440	0.612	15.873
0.632	-9.891	0.622	15.879
0.642	-9.955	0.632	15.729
0.653	-10.096	0.642	15.493
		0.653	15.566

Table G.41: Local Nusselt numbers for section 9, $R_T = -0.5$, A = 8.8, P = 100.07 kPa, Ra(b/L) = 1112.

Cold Wall		Hot Wall	
y/L	$Nu_{y,C}$	y/L	$Nu_{y,C}$
0.663	-10.371	0.663	14.868
0.673	-10.576	0.673	14.547
0.683	-10.412	0.683	14.760
0.693	-10.912	0.693	14.356
0.703	-10.460	0.703	15.191
0.713	-11.318	0.713	14.395
0.723	-10.944	0.723	14.828
0.734	-10.765	0.734	14.133
0.744	-11.797		

Table G.42: Local Nusselt numbers for section 10, $R_T = -0.5$, $A = 8.8$,

P = 100.07 kPa, Ra(b/L) = 1122.

Cold Wall		Hot Wall	
y/L	$Nu_{y,C}$	y/L	$Nu_{y,C}$
0.754	-11.091	0.754	13.984
0.764	-11.539	0.764	13.922
0.774	-11.318	0.774	13.642
0.784	-11.732	0.784	14.290
0.794	-11.984	0.794	14.096
0.804	-11.788	0.804	13.708
0.815	-12.370	0.815	13.611
0.825	-12.346	0.825	13.039
0.835	-12.488	0.835	13.374
0.845	-13.321	0.845	13.248

Table G.43: Local Nusselt numbers for section 11, $R_T = -0.5$, $A = 8.8$,

P = 100.07 kPa, Ra(b/L) = 1053.

Cold Wall		Hot Wall	
y/L	$Nu_{y,C}$	y/L	$Nu_{y,C}$
0.855	-13.777	0.855	13.666
0.865	-14.862	0.865	13.001
0.875	-13.860	0.875	13.142
0.885	-14.429	0.885	13.111
0.896	-14.548	0.896	12.476
0.906	-14.485	0.906	12.770
0.916	-15.202	0.916	12.103
0.926	-14.680	0.936	12.576
0.936	-15.654		

Table G.44: Local Nusselt numbers for section 12 (top of channel),
$R_T = -0.5$, A = 8.8, P = 100.07 kPa, Ra(b/L) = 1086.

Cold Wall		Hot Wall	
y/L	$Nu_{y,C}$	y/L	$Nu_{y,C}$
0.946	-15.184	0.946	12.170
0.956	-14.298	0.956	12.738
0.966	-14.684	0.966	12.893
0.977	-14.320	0.977	14.352
0.987	-14.244	0.987	16.030
0.997	-16.509	0.997	18.183

Table G.45: Local Nusselt numbers for section 1 (bottom of channel),
$R_T = -1$, A = 8.8, P = 100.03 kPa, Ra = 39333.

Cold Wall		Hot Wall	
y/L	$Nu_{y,C}$	y/L	$Nu_{y,C}$
0.004	-2.131	0.004	4.269
0.014	-1.623	0.014	3.405
0.024	-1.426	0.024	3.110
0.034	-1.165	0.034	3.638
0.044	-1.151	0.044	3.423
		0.054	3.511

Table G.46: Local Nusselt numbers for section 2, $R_T = -1$, A = 8.8,
P = 100.03 kPa, Ra = 39418.

Cold Wall		Hot Wall	
y/L	$Nu_{y,C}$	y/L	$Nu_{y,C}$
0.054	-0.969	0.065	3.420
0.065	-0.983	0.075	3.351
0.075	-0.954	0.085	3.496
0.085	-0.999	0.095	3.340
0.095	-0.924	0.105	3.225
0.105	-0.973	0.115	3.364
0.115	-0.959	0.125	3.132
0.125	-0.997	0.135	3.155
0.135	-1.030	0.146	3.151
0.146	-1.066		

Table G.47: Local Nusselt numbers for section 3, $R_T = -1$, A = 8.8,

P = 100.03 kPa, Ra = 39376.

Cold Wall		Hot Wall	
y/L	$Nu_{y,C}$	y/L	$Nu_{y,C}$
0.156	-1.051	0.156	3.151
0.166	-1.106	0.166	2.956
0.176	-1.041	0.176	2.995
0.186	-1.145	0.186	2.918
0.196	-1.170	0.196	2.744
0.206	-1.182	0.206	2.811
0.216	-1.155	0.216	2.630
0.227	-1.315	0.227	2.742
0.237	-1.241	0.237	2.611
		0.247	1.294

Table G.48: Local Nusselt numbers for section 4, $R_T = -1$, A = 8.8,

P = 100.03 kPa, Ra = 39356.

Cold Wall		Hot Wall	
y/L	$Nu_{y,C}$	y/L	$Nu_{y,C}$
0.247	-0.420	0.257	2.362
0.257	-1.342	0.267	2.483
0.267	-1.295	0.277	2.329
0.277	-1.395	0.287	2.541
0.287	-1.470	0.297	2.286
0.297	-1.373	0.308	2.252
0.308	-1.489	0.318	2.272
0.318	-1.502	0.328	2.340
0.328	-1.489	0.338	2.167
0.338	-1.530		

Table G.49: Local Nusselt numbers for section 5, $R_T = -1$, $A = 8.8$,
P = 100.03 kPa, Ra = 39356.

Cold Wall		Hot Wall	
y/L	$Nu_{y,C}$	y/L	$Nu_{y,C}$
0.348	-1.568	0.348	2.202
0.358	-1.511	0.358	2.178
0.368	-1.545	0.368	2.128
0.378	-1.592	0.378	2.131
0.389	-1.566	0.389	2.080
0.399	-1.587	0.399	2.066
0.409	-1.584	0.409	2.174
0.419	-1.565	0.419	2.012
0.429	-0.753	0.429	0.375
		0.439	1.930

Table G.50: Local Nusselt numbers for section 6, $R_T = -1$, $A = 8.8$,
P = 100.03 kPa, Ra = 39356.

Cold Wall		Hot Wall	
y/L	$Nu_{y,C}$	y/L	$Nu_{y,C}$
0.439	-1.629	0.449	1.905
0.449	-1.648	0.459	1.920
0.459	-1.710	0.470	1.899
0.470	-1.717	0.480	1.803
0.480	-1.666	0.490	1.855
0.490	-1.816	0.500	1.821
0.500	-1.780		

Table G.51: Local Nusselt numbers for section 7, $R_T = -1$, $A = 8.8$,
P = 100.07 kPa, Ra = 39395.

Cold Wall		Hot Wall	
y/L	$Nu_{y,C}$	y/L	$Nu_{y,C}$
0.500	-1.872	0.500	1.810
0.510	-1.890	0.510	1.733
0.520	-1.840	0.520	1.763
0.530	-1.888	0.530	1.711
0.541	-2.025	0.541	1.789
0.551	-1.999	0.551	1.687

Table G.52: Local Nusselt numbers for section 8, $R_T = -1$, A = 8.8, P = 100.07 kPa, Ra = 39395.

Cold Wall		Hot Wall	
y/L	$Nu_{y,C}$	y/L	$Nu_{y,C}$
0.561	-1.944	0.561	1.672
0.571	-0.946	0.571	1.724
0.581	-2.009	0.581	1.722
0.591	-2.063	0.591	1.629
0.601	-2.029	0.601	1.570
0.611	-2.213	0.611	1.551
0.622	-2.160	0.622	1.593
0.632	-2.185	0.632	1.561
0.642	-2.290	0.642	1.512
		0.652	1.563

Table G.53: Local Nusselt numbers for section 9, $R_T = -1$, A = 8.8, P = 100.07 kPa, Ra = 39406.

Cold Wall		Hot Wall	
y/L	$Nu_{y,C}$	y/L	$Nu_{y,C}$
0.652	-2.099	0.662	1.513
0.662	-2.255	0.672	1.491
0.672	-2.401	0.682	1.432
0.682	-2.269	0.692	1.369
0.692	-2.290	0.703	1.278
0.703	-2.543	0.713	1.422
0.713	-2.450	0.723	1.340
0.723	-2.358	0.733	1.178
0.733	-2.586		
0.743	-2.379		

Table G.54: Local Nusselt numbers for section 10, $R_T = -1$, A = 8.8,
P = 100.07 kPa, Ra = 39443.

Cold Wall		Hot Wall	
y/L	$Nu_{y,C}$	y/L	$Nu_{y,C}$
0.753	-2.526	0.753	1.167
0.763	-2.532	0.763	1.236
0.773	-2.586	0.773	1.185
0.784	-2.789	0.784	1.155
0.794	-2.604	0.794	1.143
0.804	-2.771	0.804	1.128
0.814	-2.932	0.814	1.030
0.824	-2.709	0.824	1.056
0.834	-2.876	0.834	1.031
0.844	-3.042	0.844	0.964

Table G.55: Local Nusselt numbers for section 11, $R_T = -1$, A = 8.8,
P = 100.07 kPa, Ra = 39449.

Cold Wall		Hot Wall	
y/L	$Nu_{y,C}$	y/L	$Nu_{y,C}$
0.854	-2.846	0.854	1.014
0.865	-3.059	0.865	0.967
0.875	-2.914	0.875	0.977
0.885	-2.924	0.885	0.948
0.895	-2.987	0.895	0.943
0.905	-2.962	0.905	0.933
0.915	-2.987	0.915	0.952
0.925	-3.231	0.925	0.536
0.935	-3.093	0.935	0.955

Table G.56: Local Nusselt numbers for section 12 (top of channel),

$R_T = -1$, A = 8.8, P = 100.07 kPa, Ra = 39889.

Cold Wall		Hot Wall	
y/L	$Nu_{y,C}$	y/L	$Nu_{y,C}$
0.946	-3.081	0.946	0.997
0.956	-3.182	0.956	1.066
0.966	-3.026	0.966	1.158
0.976	-3.047	0.976	1.225
0.986	-3.198	0.986	1.425
0.996	-3.694	0.996	1.809

Table G.57: Comparison of the overall channel, hot wall, and cold wall average Nusselt numbers

for A = 27.6 using a laminar numerical model.

R_T	Ra(b/L)	Experimental			Laminar Numerical			Error		
		Nu	Nu_H	Nu_C	Nu	Nu_H	Nu_C	Nu	Nu_H	Nu_C
0	24.8	0.818	2.96	−1.33	0.788	3.00	−1.42	−3.7%	1.4%	6.8%
−0.5	12.3	0.673	6.81	−5.46	0.697	7.25	−5.86	3.6%	6.5%	7.3%
−0.75	4.74	0.680	14.0	−12.7	0.658	14.6	−13.3	−3.2%	4.4%	5.2%
−1	1482		0.973	−0.970		1.02	−1.02		4.8%	5.2%

(Note that Ra is used for $R_T = -1$.)

Table G.58: Comparison of the overall channel, hot wall, and cold wall average Nusselt numbers

for A = 17.3 using a laminar numerical model.

R_T	Ra(b/L)	Experimental			Laminar Numerical			Error		
		Nu	Nu_H	Nu_C	Nu	Nu_H	Nu_C	Nu	Nu_H	Nu_C
1	241	2.16	2.15	2.17	2.24	2.24	2.24	3.7%	4.2%	3.2%
0	128	1.93	4.46	−0.605	1.99	4.63	−0.648	3.1%	3.8%	7.1%
−0.5	66.6	2.19	8.95	−4.57	2.27	9.56	−5.02	3.7%	6.8%	9.9%
−0.75	22.9	2.17	17.1	−12.7	2.26	18.7	−14.0	4.2%	9.7%	9.9%
−1	4787		1.04	−1.03		1.11	−1.11		6.7%	7.8%

(Note that Ra is used for $R_T = -1$.)

Table G.59: Comparison of the overall channel, hot wall, and cold wall average Nusselt numbers for A = 13.2 using a laminar numerical model.

R_T	Ra(b/L)	Experimental			Laminar Numerical			Error		
		Nu	Nu_H	Nu_C	Nu	Nu_H	Nu_C	Nu	Nu_H	Nu_C
1	787	3.04	3.07	3.01	3.11	3.11	3.11	2.3%	1.3%	3.3%
−0.5	214	3.51	12.3	−5.28	3.53	13.3	−6.23	0.6%	8.1%	18.0%
−0.75	76.6	3.62	23.0	−15.8	3.85	25.2	−17.5	6.4%	9.4%	10.8%
−1	11750		1.32	−1.32		1.40	−1.40		6.1%	6.1%

(Note that Ra is used for $R_T = -1$.)

Table G.60: Comparison of the overall channel, hot wall, and cold wall average Nusselt numbers for A = 13.2 using a turbulent numerical model with enhanced wall functions.

R_T	Ra(b/L)	Experimental			Turbulent Numerical (EWF)			Error		
		Nu	Nu_H	Nu_C	Nu	Nu_H	Nu_C	Nu	Nu_H	Nu_C
1	787	3.04	3.07	3.01						
−0.5	214	3.51	12.3	−5.28	3.48	13.3	−6.34	0.9%	8.1%	20.1%
−0.75	76.6	3.62	23.0	−15.8	3.66	25.2	−17.8	−1.1%	9.6%	12.7%
−1	11750		1.32	−1.32		1.60	−1.60		21.2%	21.2%

(Note that Ra is used for $R_T = -1$.)

Table G.61: Comparison of the overall channel, hot wall, and cold wall average Nusselt numbers for A = 8.8 using a laminar numerical model.

R_T	Ra(b/L)	Experimental			Laminar Numerical			Error		
		Nu	Nu_H	Nu_C	Nu	Nu_H	Nu_C	Nu	Nu_H	Nu_C
−0.5	1084	5.42	18.9	−8.10	4.31	20.2	−11.5	−20.5%	6.9%	42.0%
−1	39430		1.98	−1.96		2.10	−2.08		6.1%	6.1%

(Note that Ra is used for $R_T = -1$.)

Table G.62: Comparison of the overall channel, hot wall, and cold wall average Nusselt numbers for A = 8.8 using a turbulent numerical model with enhanced wall functions.

R_T	Ra(b/L)	Experimental			Turbulent Numerical (EWF)			Error		
		Nu	Nu_H	Nu_C	Nu	Nu_H	Nu_C	Nu	Nu_H	Nu_C
−0.5	1084	5.42	18.9	−8.10	5.69	20.5	−9.11	5.0%	8.5%	12.5%
−1	39430		1.98	−1.96		2.52	−2.50		27.3%	27.6%

(Note that Ra is used for $R_T = -1$.)

Figure G.1: Graph of local Nusselt number variation versus distance for $R_T = 1$, A = 13.2 and Ra(b/L) = 787. Experimental: $Nu_H = 3.07$, $Nu_C = 3.01$, CFD: $Nu_H = 3.11$, $Nu_C = 3.11$.

Figure G.2: Graph of local Nusselt number variation versus distance for $R_T = 0$, $A = 26.4$ and $Ra(b/L) = 24.8$. Experimental: $Nu_H = 2.96$, $Nu_C = -1.33$, CFD: $Nu_H = 3.00$, $Nu_C = -1.42$.

Figure G.3: Graph of local Nusselt number variation versus distance for $R_T = -0.75$, $A = 26.4$ and $Ra(b/L) = 4.73$. Experimental: $Nu_H = 14.0$, $Nu_C = -12.7$, CFD: $Nu_H = 14.6$, $Nu_C = -13.3$.
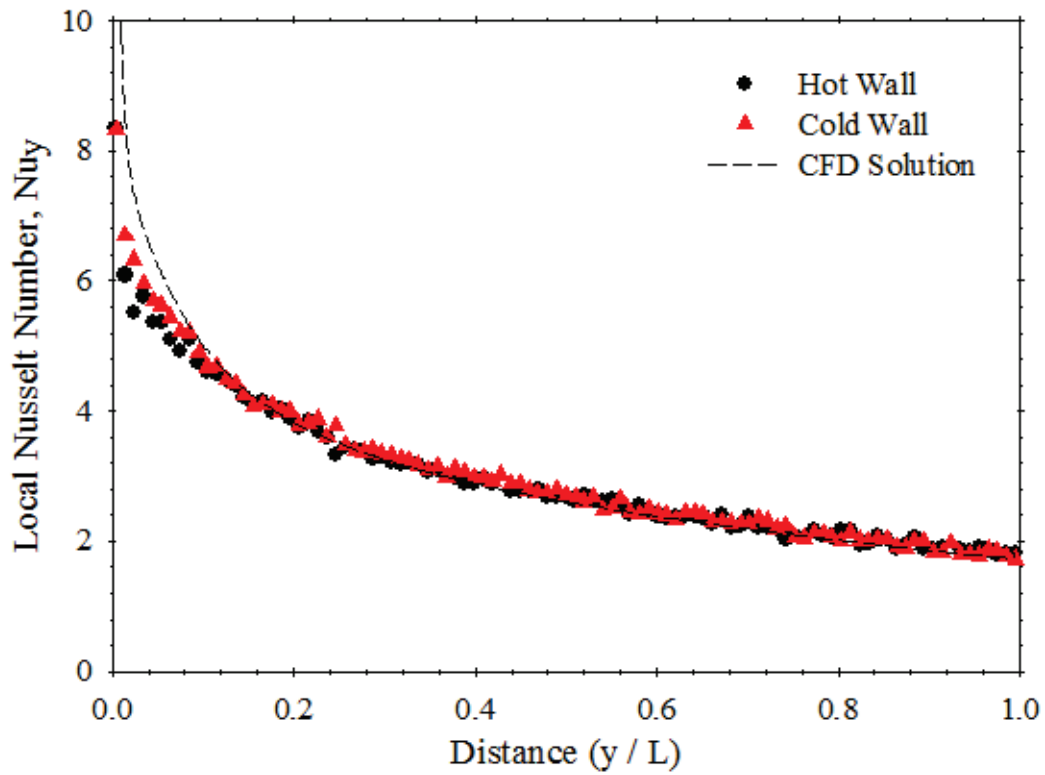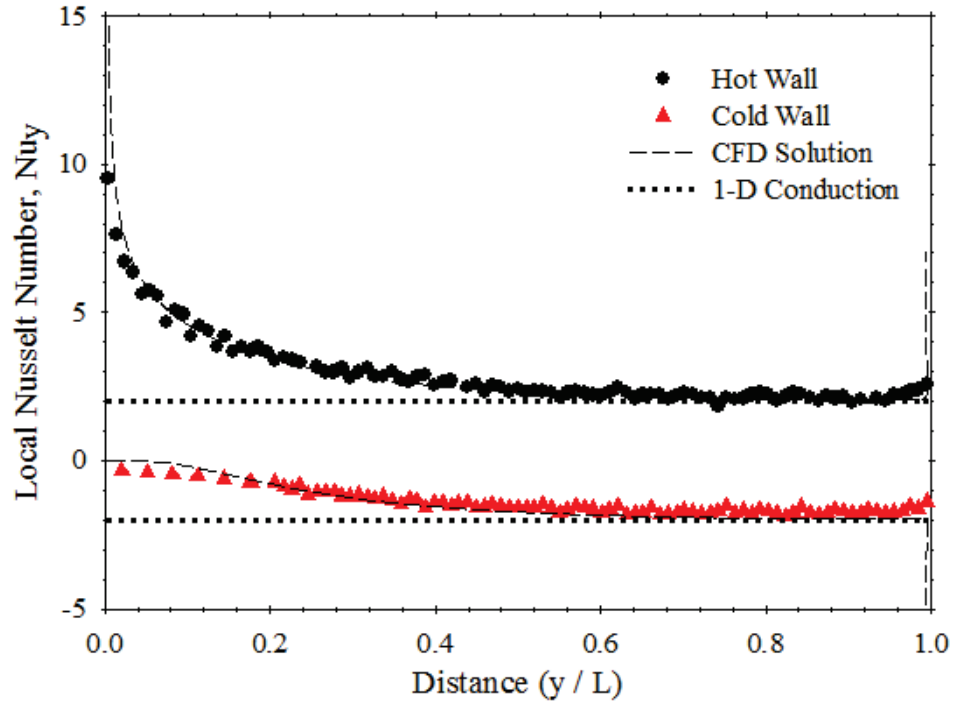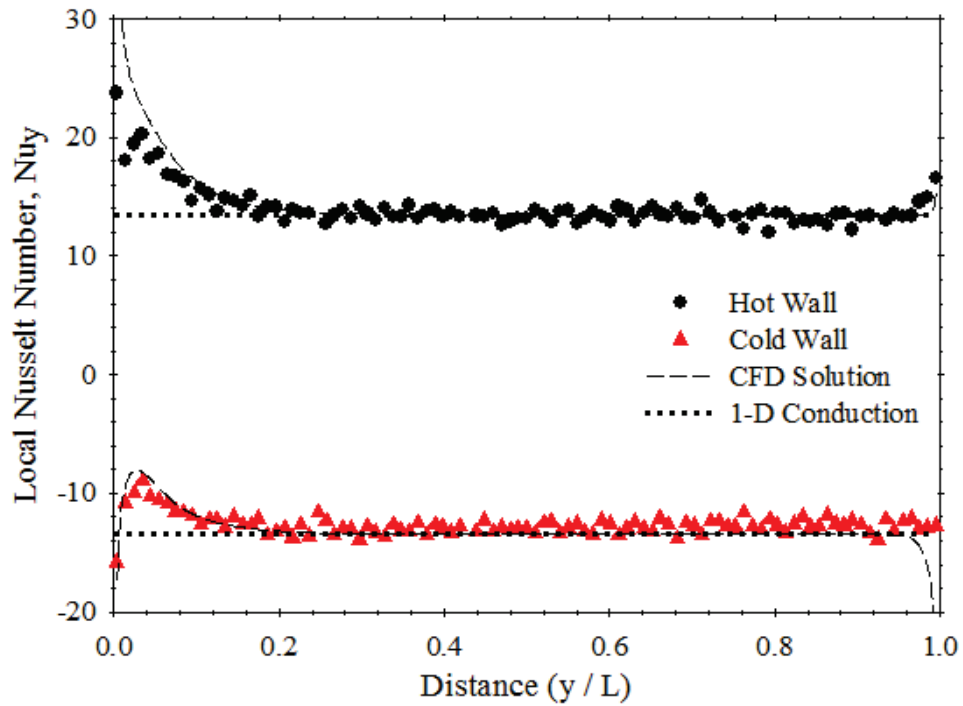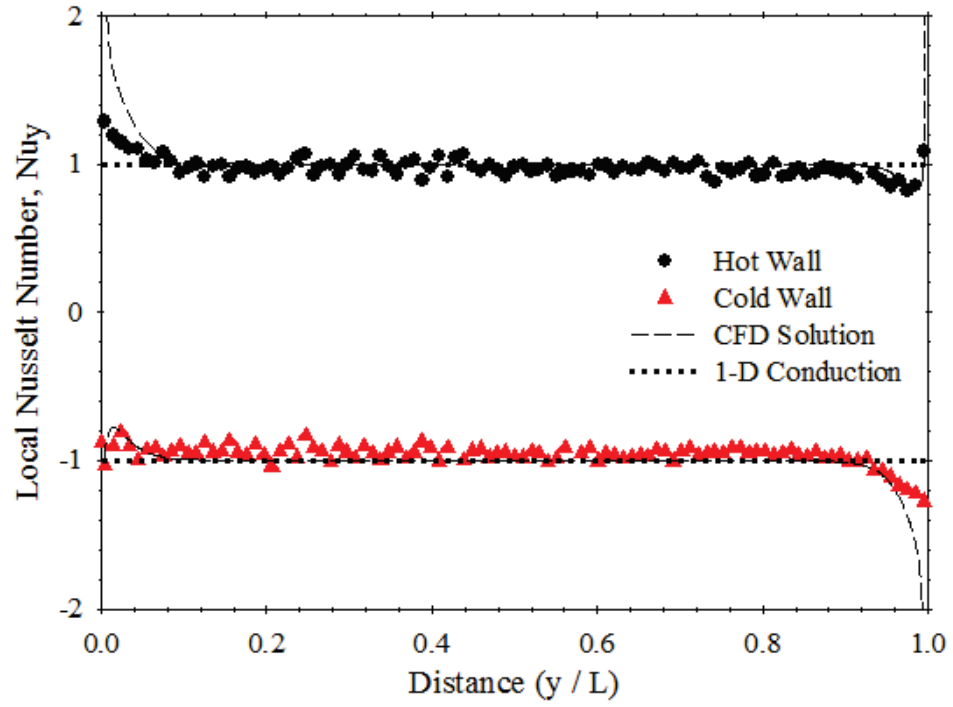
Figure G.4: Graph of local Nusselt number variation versus distance for $R_T = -1$, $A = 26.4$ and Ra = 1482. Experimental: $Nu_H = 0.973$, $Nu_C = -0.970$, CFD: $Nu_H = 1.02$, $Nu_C = -1.02$.

References

Andreozzi, A., Manca, O., and Naso, V., 2002, Natural Convection in Vertical Channels with an Auxiliary Plate, *International Journal of Numerical Methods for Heat and Fluid Flow*, Vol. 12, No. 6, pp. 716 – 734.

ANSYS FLUENT (Version 13.0) [computer software], 2010, ANSYS, Inc..

ANSYS FLUENT Theory Guide, 2011, Section 4.13: Near-Wall Treatments for Wall-Bounded Turbulent Flows, ANSYS, Inc., Canonsburg, United States, pp. 119 – 136.

ANSYS FLUENT User's Guide, 2010, Chapter 13: Modelling Turbulence, ANSYS, Inc., Canonsburg, United States, pp. 643 – 690.

Auletta, A., Manca, O., Morrone, B., and Naso V., 2001, Heat Transfer by the Chimney Effect in a Vertical Isoflux Channel, *International Journal of Heat and Mass Transfer*, Vol. 44, pp. 4345 – 4357.

Aung, W., 1972, Fully Developed Laminar Free Convection between Vertical Parallel Plates Heated Asymmetrically, *International Journal of Heat and Mass Transfer*, Vol. 15, pp. 1577 – 1580.

Aung, W., Flecther, L.S., and Sernas, V., 1972, Developing Laminar Free Convection between Vertical Flat Plates with Asymmetric Heating, *International Journal of Heat and Mass Transfer*, Vol. 15, pp. 2293 – 2308.

Ayinde, T.F. and Said, S.A.M., 2008, Turbulent Natural Convection Flow in a Vertical Channel with Anti-Symmetric Heating, *Heat and Mass Transfer*, Vol. 44, pp. 1207 – 1216.

Badr, H.M., Habib, M.A., Anwar, S., Ben-Mansour, R., and Said, S.A.M., 2006, Turbulent Natural Convection in Vertical Parallel-Plate Channels, *Heat and Mass Transfer*, Vol. 43, pp. 73 – 84.

Bar-Cohen, A. and Rohsenow, W.M., 1984, Thermally Optimum Spacing of Vertical, Natural Convection Cooled, Parallel Plates, *Journal of Heat Transfer*, Vol. 106, pp. 116 – 123.

Bianco, N. And Nardini, S., 2005, Numerical Analysis of Natural Convection in Air in a Vertical Convergent Channel with Uniformly Heated Conductive Walls, *International Communications in Heat and Mass Transfer*, Vol. 32, pp. 758 – 769.

Bodia, J.R. and Osterle, J.F., 1962, The Development of Free Convection Between Heated Vertical Plates, *Journal of Heat Transfer*, Vol. 84, pp. 40 – 44.

Boudebous, S., Nemouchi, Z., and Meniai, A.H., 2001, Numerical Study of Developing Natural Laminar Convection in a Vertical Hyperbolic Duct of Fixed Length and with a Constant Wall Temperature, *Numerical Heat Transfer*, Vol. 40, pp. 783 – 800.

Burch, T., Rhodes, T., and Acharya, S., 1985, Laminar Natural Convection between Finitely Conducting Vertical Plates, *International Journal of Heat and Mass Transfer*, Vol. 28, No. 6, pp. 1173 – 1186.

Burns, G.W., Scroger, M.G., and Strouse, G.F., 1993, Temperature-Electromotive Force Reference Functions and Tables for the Letter-Designated Thermocouple Types Based on ITS-90, *National Institute of Standards and Technology*, Washington, United States, pp. 249 – 280.

Campo, A., Manco, O., and Morrone, B., 2005, Natural Convection in Vertical, Parallel-Plate Channels with Appended Unheated Entrances, *International Journal for Numerical Methods in Heat and Fluid Flow*, Vol. 15, No. 2, pp. 183 – 204.

Campo, A., Manca, O., and Morrone, B., 2006, Numerical Investigation of the Natural Convection Flows for Low-Prandtl Fluids in Vertical Parallel-Plates Channels, *Journal of Applied Mechanics*, Vol. 73, pp. 96 – 107.

Capture One Pro (version 4.5.1) [computer software], 2008, Denmark: Phase One.

Celik, I.B., Ghia, U., Roache, P.J., Freitas, C.J., Coleman, H., and Raad, P.E., 2008, Procedure for Estimation and Reporting of Uncertainty Due to Discretization in CFD Applications, *Journal of Fluids Engineering*, Vol. 130, pp. 1 – 4.

Chappidi, P.R. and Eno, B.E., 1990, A Comparative Study of the Effect of Inlet Conditions on a Free Convection Flow in a Vertical Channel, *Journal of Heat Transfer*, Vol. 112, pp. 1082 – 1085.

Churchill, S.W. and Usagi, R., 1972, A General Expression for the Correlation of Rates of Transfer and Other Phenomena, *AIChE Journal*, Vol. 18, No. 6, pp. 1121 – 1128.

Coleman, H.W. and Steele, W.G., 1999, *Experimentation and Uncertainty Analysis for Engineers*, John Wiley and Sons, Inc., New York, United States.

Collins, M., 2001, Analysis of Solar Heat Gain and Thermal Transmission for Windows with Louvered Shade Systems, Department of Mechanical Engineering, Queen's University, Kingston, Canada.

Currie, I.G. and Newman, W.A., 1970, Natural Convection between Isothermal Vertical Surfaces, *Fourth International Heat Transfer Conference*, Paris-Versailles, France, pp. NC 2.7: 1 – 8.

Desarayaud, G. And Fichera, A., 2002, Laminar Natural Convection in a Vertical Isothermal Channel with Symmetric Surface-Mounted Rectangular Ribs, *International Journal of Heat and Fluid Flow*, Vol. 23, pp. 519 – 529.

Dyer, J.R., 1978, Natural-Convective Flow through a Vertical Duct with a Restricted Entry, *International Journal of Heat and Mass Transfer*, Vol. 21, pp. 1341 – 1354.

Eckert, E.R.G. and Carlson, W.O., 1961, Natural Convection in an Air Layer Enclosed Between Two Vertical Plates with Different Temperatures, *International Journal of Heat and Mass Transfer*, Vol. 2, pp. 106 – 120.

Elenbaas, W., 1942, Heat Dissipation of Parallel Plates by Free Convection, *Physica*, Vol. 9, No. 1, pp. 1 – 28.

ElSherbiny, S.M., Raithby, G.D., and Hollands, K.G.T., 1982, Heat Transfer across Vertical and Inclined Air Layers, *Journal of Heat Transfer*, Vol. 104, pp. 96 – 102.

ESP-r Software, Building Energy Simulation Code (Version 10.12) [computer software], 2005, University of Stratchclyde, Glasgow, United Kingdom.

Fedorov, A.G. and Viskanta, R., 1997, Turbulent Natural Convection Heat Transfer in an Asymmetrically Heated, Vertical Parallel-Plate Channel, *International Journal of Heat and Mass Transfer*, Vol. 40, No. 16, pp. 3849 – 3860.

Goldstein, R.J., 1976, Optical Temperature Measurement in: *Measurement Techniques in Heat Transfer*, ed. Eckert, E.R.G. and Goldstein, R.J., Technivision Services, Slough, England, pp. 177 – 228.

Guo, Z.Y., Song, Y.Z., and Zhao, X.W., 1988, Experimental Investigation of Natural Convection in Channel by Laser Speckle Photography, *Proceedings of the First World Conference on Experimental Heat Transfer, Fluid Mechanics, and Thermodynamics*, Dubrovnik, Yugoslavia, pp. 412 – 418.

Habib, M.A., Said, S.A.M., Ahmed, S.A., and Asghar, A., 2002, Velocity Characteristics of Turbulent Natural Convection in Symmetrically and Asymmetrically Heated Vertical Channels, *Experimental Thermal and Fluid Science*, Vol. 26, pp. 77 – 87.

Hauf, W. and Grigull, U., 1970, Optical Methods in Heat Transfer, in: *Advances in Heat Transfer*, ed. Harnett, J.P. and Irvine, T.F., Academic Press, New York, United States, pp. 133 – 366.

Higuera, F.J. and Ryazantsev, Y.S., 2002, Natural Convection Flow Due to a Heat Source in a Vertical Channel, *International Journal of Heat and Mass Transfer*, Vol. 45, pp. 2207 – 2212.

Incropera, F.P. and DeWitt, D.P., 2002, *Introduction to Heat Transfer: Fourth Edition*, John Wiley and Sons, Inc., New York, United States.

Karim, F., Farouk, B., and Namer, I., 1986, Natural Convection Heat Transfer from a Horizontal Cylinder between Vertical Confining Adiabatic Walls, *Journal of Heat Transfer*, Vol. 108, pp. 291 – 298.

Kazeminejad, H., 2005, Laminar Free Convection in a Vertical Channel with Asymmetrical Heating, *2005 ASME Summer Heat Transfer Conference,* San Francisco, United States, pp. 521 – 530.

Kettlebourough, C.F., 1972, Transient Laminar Free Convection between Heated Vertical Plates including Entrance Effects, *International Journal of Heat and Mass Transfer*, Vol. 15, pp. 883 – 896.

Khodary, K. And Bhattacharyya, T.K., 2006, Optimum Natural Convection from Square Cylinder in Vertical Channel, *International Journal of Heat and Fluid Flow*, Vol. 27, pp. 167 – 180.

Kim, S.H., Anand, N.K., and Aung, W., 1990, Effect of Wall Conduction on Free Convection between Asymmetrically Heated Vertical Plates: Uniform Wall Heat Flux, *International Journal of Heat and Mass Transfer*, Vol. 33, No. 5, pp. 1013 – 1023.

Kline, S.J. and McClintock, F.A., 1953, Describing Experimental Uncertainties in Single-Sample Experiments, *Mechanical Engineering*, Vol. 75, pp. 3 – 8.

Korpela, S.A., Lee, Y., and Drummond, J.E., 1982, Heat Transfer through a Double Pane Window, *Journal of Heat Transfer*, Vol. 104, pp. 539 – 544.

Kotey, N.A., Collins, M.R., Wright, J.L., and Jiang, T., 2009, A Simplified Method for Calculating the Effective Solar Optical Properties of a Venetian Blind Layer for Building Energy Simulation, *Journal of Solar Energy Engineering*, Vol. 131, No. 2, pp. 0210021 – 0210029.

Lai, B., 2004, An Interferometric Study of Free Convective Heat Transfer in a Double Glazed Window with a Between-Panes Venetian Blind, Department of Mechanical & Industrial Engineering, Ryerson University, Toronto, Canada.

Lau, G.E., Yeoh, G.H., Timchenko, V., and Reizes, J.A., 2012, Numerical Investigation of Passive Cooling in Open Vertical Channels, *Applied Thermal Engineering*, Vol. 39, pp. 121 – 131.

Lauber, T.S. and Welch, A.U., 1966, Natural Convection Heat Transfer between Vertical Flat Plates with Uniform Heat Flux, *Proceedings of the Third International Heat Transfer Conference*, Chicago, United States, pp. 126 – 131.

Lee, T.S., Parikh, P.G., Acrivos, A., and Bershader, D., 1982, Natural Convection in a Vertical Channel with Opposing Buoyancy Forces, *International Journal of Heat and Mass Transfer*, Vol. 25, No. 3, pp. 499 – 511.

Lomanowski, B. A. and Wright, J. L., 2007, Heat Transfer Analysis of Windows with Venetian Blinds: A Comparative Study, *Proceedings of the 2nd Canadian Solar Buildings Conference*, Calgary, Canada, pp. 1 – 9.

Machin, A., 1997, An Experimental Study of Free Convective Heat Transfer from a Vertical Flat Plate in the Presence of Louvers, Department of Mechanical Engineering, University of Western Ontario, London, Ontario.

Marcondes, M., Melo, V.S., and Gurgel, J.M., 2006, Numerical Analysis of Natural Convection in Parallel, Convergent, and Divergent Open-Ended Channels, *International Journal of Numerical Methods for Heat and Fluid Flow*, Vol. 16, No. 3, pp. 304 – 323.

Marsters, G.F., Natural Convective Heat Transfer from a Horizontal Cylinder in the Presence of Nearby Walls, *Canadian Journal of Chemical Engineering*, Vol. 53, pp. 144 – 149.

Martin, L., Raithby, G.D., and Yovanovich, M.M., 1991, On the Low Rayleigh Number Asymptote for Natural Convection through an Isothermal, Parallel-Plate Channel, *Journal of Heat Transfer*, Vol. 113, pp. 899 – 905.

MATLAB (version R2010a) [computer software], 2010, USA: The Mathworks, Inc.

Mehta, J.M. and Black, W.Z., 1977, Errors Associated with Interferometric Measurement of Convective Heat Transfer Coefficients, *Applied Optics*, Vol. 16, No. 6, pp. 120 – 1726.

Merzkirch, M., 1987, *Flow Visualization*, Academic Press, Inc., Orlando, United States.

Miyatake, O. and Fujii, T., 1973a, Natural Convection Heat Transfer between Vertical Parallel Plates at Unequal Uniform Temperature, *Heat Transfer: Japanese Research*, Vol. 2, pp. 79 – 88.

Miyatake, O. and Fujii, T., 1973b, Natural Convective Heat Transfer between Vertical Parallel Plates at Unequal Heat Fluxes, *Heat Transfer: Japanese Research*, Vol. 3, pp. 29 – 33.

Nakamura, H., Asako, Y., and Naitou, T., 1982, Heat Transfer by Free Convection between Two Parallel Flat Plates, *Numerical Heat Transfer*, Vol. 5, pp. 95 – 106.

Naylor, D., 2003, Recent Developments in the Measurement of Convective Heat Transfer Rates by Laser Interferometry, *International Journal of Heat and Mass Transfer*, Vol. 24, pp. 345 – 355.

Naylor, D., Floryan, J.M., and Tarasuk, J.D., 1991, A Numerical study of Developing Free Convection Between Isothermal Vertical Plates, *Journal of Heat Transfer*, Vol. 113, pp. 620 – 626.

Ospir, D., Popa, C, Chereches, C., Polidori, G., and Fohanno, S., 2012, Flow Visualization of Natural Convection in a Vertical Channel with Asymmetric Heating, *International Communications in Heat and Mass Transfer*, Vol. 39, pp. 486 – 493.

Ostrach, S., 1953, An Analysis of Laminar Free Convection Flow and Heat Transfer About a Flat Plate Parallel to the Direction of the Generating Body Force, *National Advisory Committee for Aeronautics Report*, No. 1111.

Patankar, S.V., 1980, *Numerical Heat Transfer and Fluid Flow*, Hemisphere Publishing Corp., New York, United States.

Poulad, M.E., Naylor, D., and Oosthuizen, P.H., 2011, Turbulent Free Convection in a Tall Enclosure Using Interferometery, *Journal of Heat Transfer*, Vol. 133, pp. 042501-1 – 042501-8.

Raithby, G.D. and Hollands, K.G.T., 1998, Natural Convection, in: *Handbook of Heat Transfer*, ed. Rohsenow, W.M., Harnett, J.P., and Cho, Y.I., McGraw-Hill, New York, United States, pp. 4.32 – 4.35.

Ramanathan, S. And Kumar, R., 1991, Correlations for Natural Convection between Heated Plates, *Journal of Heat Transfer*, Vol. 113, pp. 97 – 107.

Roeleveld, D., Naylor, D., and Oosthuizen, P.H., 2009, Empirical Correlations for Free Convection in an Isothermal, Asymmetrically Heated Vertical Channel, *Heat Transfer Engineering*, Vol. 30, No. 3, pp. 189 – 196.

Roeleveld, D., Naylor, D., and Oosthuizen, P.H., 2010, A Simplified Model of Heat Transfer at an Indoor Window Glazing Surface with a Venetian Blind, *Journal of Building Performance Simulation*, Vol. 3, No. 2, pp. 121 – 128.

Sahoo, R.K. and Sastri, V.M.K., 1997, Numerical Investigation of Free Convective Flow in Divergent Channels, *Computational Methods in Applied Mechanics and Engineering*, Vol. 146, pp. 31 – 41.

Shewen, E., Hollands, K.G.T., and Raithby, G.D., 1996, Heat Transfer by Natural Convection across a Vertical Air Cavity of Large Aspect Ratio, *Journal of Heat Transfer*, Vol. 118, pp. 993 – 995.

Slepicka, S.S. and Cha, S.S., 1995, Stabilized Nonlinear Regression for Interferogram Analysis, *Applied Optics*, Vol. 34, No. 23, pp. 5039 – 5044.

SolidWorks (version 2008 SP5.0) [computer software], 2008, USA: Dassault Systems.

Sparrow, E.M. and Azevedo, L.F.A., 1985, Vertical-Channel Natural Convection Spanning between the Fully-Developed Limit and the Single-Plate Boundary-Layer Limit, *International Journal of Heat and Mass Transfer*, Vol. 29, No. 10, pp. 1847 – 1857.

Sparrow, E.M., Chrysler, G.M., and Azevedo, L.F., 1984, Observed Flow Reversals and Measured-Predicted Nusselt Numbers for Natural Convection in a One-Sided Heated Vertical Channel, *Journal of Heat Transfer*, Vol. 106, pp. 325 – 332.

Sparrow, E.M. and Ruiz, R., 1988, Experiments on Natural Convection in Divergent Vertical Channels and Correlation of Divergent, Convergent, and Parallel-Channel Nusselt Numbers, *International Journal of Heat and Mass Transfer*, Vol. 31, No. 11, pp. 2197 – 2205.

Suárez, C., Joubert, P., Molina, J.L., and Sánchez, F.J., 2011, Heat Transfer and Mass Flow Correlations for Ventilated Facades, *Energy and Buildings*, Vol. 43, pp. 3696 – 3703.

Terekhov, V.I. and Ekaid, A.L., 2011, Laminar Natural Convection between Vertical Isothermal Heated Plates with Different Temperatures, *Journal of Engineering Thermophysics*, Vol. 20, No. 4, pp. 416 – 433.

Touloukian, Y.S., Liley, P.E., and Hestermans, P., 1975, Viscosity: Nonmetallic Liquids and Gases, *Thermophysical Properties of Matter*, Vol. 11, Thermophysical Properties Research Center (TPRC), Purdue University, Plenum Publishing Corp..

Touloukian, Y.S., Liley, P.E., and Saxena, S.C., 1970, Thermal Conductivity: Nonmetallic Liquids and Gases, *Thermophysical Properties of Matter*, Vol. 3, Thermophysical Properties Research Center (TPRC), Purdue University, Plenum Publishing Corp..

Touloukian, Y.S. and Makita, T., 1970, Specific Heat: Nonmetallic Liquids and Gases, *Thermophysical Properties of Matter*, Vol. 6, Thermophysical Properties Research Center (TPRC), Purdue University, Plenum Publishing Corp..

TRNSYS: A Transient Simulation Program (Version 1.5) [computer software], 2000, Solar Energy Laboratory, University of Wisconsin-Madison, Madison, United States.

Van Doormaal, J.P. and Raithby, G.D., 1984, G.D. Enhancement of the Simple Method for Predicting Incompressible Flows, *Numerical Heat Transfer*, Vol. 7, No. 2, pp. 147 – 163.

Versteeg, H.K. and Malalasekera, W., 1995, *An Introduction to Computational Fluid Dynamics: The Finite Volume Method*, Longman Group Ltd., Essex, England.

Walsh, P.C. and Leong, W.H., 2004, Effectiveness of Several Turbulence Models in Natural Convection, *International Journal of Methods for Heat and Fluid Flow*, Vol. 14, pp. 633 – 648.

Wang, X. And Pepper, D.W., 2009, Numerical Simulation for Natural Convection in Vertical Channels, *International Journal of Heat and Mass Transfer*, Vol. 52, pp. 4096 – 4102.

Webb, B.W. and Hill, D.P., 1989, High Rayleigh Number Laminar Natural Convection in a Asymmetrically Heated Vertical Channel, *Journal of Heat Transfer*, Vol. 111, pp. 649 – 656.

Wirtz, R.A. and Stutzman, R.J., 1982, Experiments on Free Convection between Vertical Plates with Symmetric Heating, *Journal of Heat Transfer*, Vol. 104, pp. 501 – 507.

Wright, J.L., 1992, Glazing System Thermal Analysis, CANMET, Advanced System Laboratory, VISION3, Minister of Supply Services Canada, University of Waterloo, Waterloo, Canada.

Wright, J.L., 1996, A Correlation to Quantify Convective Heat Transfer between Vertical Window Galzings, *ASHRAE Transactions: Technical and Symposium Papers*, pp. 940 – 946.

Wright, J.L., Jin, H., Hollands, K.G.T., and Naylor, D., 2006, Flow Visualization of Natural Convection in a Tall, Air-Filled Vertical Cavity, *International Journal of Heat and Mass Transfer*, Vol. 49, pp. 889 – 904.

Yilmaz, T. And Gilchrist, A., 2007, Temperature and Velocity Field Characteristics of Turbulent Natural Convection in a Vertical Parallel-Plate Channel with Asymmetric Heating, *Heat and Mass Transfer*, Vol. 43, pp. 707 – 719.